

**WIND TURBINE CONTROLS FOR FARM AND
OFFSHORE OPERATION**

by

Zhongzhou Yang

A Dissertation Submitted in
Partial Fulfillment of the
Requirements for the Degree of

Doctor of Philosophy
in Engineering

at

The University of Wisconsin-Milwaukee

December 2013

ABSTRACT

**WIND TURBINE CONTROLS IN WIND FARM AND
OFFSHORE OPERATION**

by

Zhongzhou Yang

The University of Wisconsin-Milwaukee, 2013
Under Supervision of Professor Yaoyu Li and Dr. John E. Seem

Development of advanced control techniques is a critical measure for reducing the cost of energy for wind power generation, in terms of both enhancing energy capture and reducing fatigue load. There are two remarkable trends for wind energy. First, more and more large wind farms are developed in order to reduce the unit-power cost in installation, operation, maintenance and transmission. Second, offshore wind energy has received significant attention when the scarcity of land resource has appeared to be a major bottleneck for next level of wind penetration, especially for Europe and Asia. This dissertation study investigates on several wind turbine control issues in the context of wind farm and offshore operation scenarios.

Traditional wind farm control strategies emphasize the effect of the deficit of average wind speed, i.e. on how to guarantee the power quality from grid integration angle by the control of the electrical systems or maximize the energy capture of the whole wind farm

by optimizing the setting points of rotor speed and blade pitch angle, based on the use of simple wake models, such as Jensen wake model. In this study, more complex wake models including detailed wind speed deficit distribution across the rotor plane and wake meandering are used for load reduction control of wind turbine. A periodic control scheme is adopted for individual pitch control including static wake interaction, while for the case with wake meandering considered, both a dual-mode model predictive control and a multiple model predictive control is applied to the corresponding individual pitch control problem, based on the use of the computationally efficient quadratic programming solver qpOASES. Simulation results validated the effectiveness of the proposed control schemes.

Besides, as an innovative nearly model-free strategy, the nested-loop extremum seeking control (NLESC) scheme is designed to maximize energy capture of a wind farm under both steady and turbulent wind. The NLESC scheme is evaluated with a simple wind turbine array consisting of three cascaded variable-speed turbines using the SimWindFarm simulation platform. For each turbine, the torque gain is adjusted to vary/control the corresponding axial induction factor. Simulation under smooth and turbulent winds shows the effectiveness of the proposed scheme. Analysis shows that the optimal torque gain of each turbine in a cascade of turbines is invariant with wind speed if the wind direction does not change, which is supported by simulation results for smooth wind inputs. As changes of upstream turbine operation affects the downstream turbines with significant delays due to wind propagation, a cross-covariance based delay estimate is proposed as adaptive phase compensation between the dither and demodulation signals.

Another subject of investigation in this research is the evaluation of an innovative scheme of actuation for stabilization of offshore floating wind turbines based on actively controlled aerodynamic vane actuators. For offshore floating wind turbines, underactuation has become a major issue and stabilization of tower/platform adds complexity to the control problem in addition to the general power/speed regulation and rotor load reduction controls. However, due to the design constraints and the significant power involved in the wind turbine structure, a unique challenge is presented to achieve low-cost, high-bandwidth and low power consumption design of actuation schemes. A recently proposed concept of vertical and horizontal vanes is evaluated to increase damping in roll motion and pitch motion, respectively. The simulation platform FAST has been modified including vertical and horizontal vane control. Simulation results validated the effectiveness of the proposed vertical and horizontal active vane actuators.

ACKNOWLEDGEMENT

First and foremost I would like to express my sincerest gratitude to my advisor, Dr. Yaoyu Li, who has always supported me with his patience and knowledge during my PhD study, especially in the beginning when I jumped into control application field from my previous major fluid dynamics. Thanks for Dr. Li's guidance and suggestion which make my research much more interesting and meaningful.

Special thanks go to my co-advisor Dr. John Seem, who provided lots of constructive suggestions and comments on my work with his patience, knowledge and rich research experience during my doctoral study. Especially, Dr. Seem provided the original general idea of nested-loop extremum seeking control of a wind farm, which gave me the opportunity to solve this challenging wind farm control issue.

Special thanks also go to my co-advisor Dr. David C. Yu for his precious time, discussion and suggestion.

I would like to thank other committee members: Dr. Tien-Chien Jen, and Dr. Ron A. Perez for their precious time and comments.

Thanks also go to NREL Researchers, Dr. Jason Jonkman and Mrs. Bonnie Jonkman, who help me use and modify FAST software and Mr. Neil Kelly for help in using TurbSim.

I gratefully acknowledge the financial support from Johnson Controls Inc., We Energies and the University of Texas at Dallas, which let me concentrate on my research.

Finally I would like to express my deep gratitude to my wife and parents for their love and support, which is the impetus making me move forward.

TABLE OF CONTENTS

LIST OF FIGURES	xiii
LIST OF TABLES	xxvii
Nomenclature	xxviii
Chapter 1. Introduction	1
1.1. Wind Turbine Types.....	2
1.2. Wind Turbine Control Strategy.....	4
1.3. Wind Farm Control	6
1.3.1. Load Reduction Control for Turbines in Farm Operation.....	7
1.3.2. Energy Capture Control in Wind Farm Level.....	10
1.3.3. Summary of Load Reduction and Energy Capture Control of Farm Operated Turbines	11
1.4. Floating Offshore Wind Turbine Control.....	11
1.5. Problem Statements.....	14
1.6. Organization of Thesis	14
Chapter 2. Literature Review	16
2.1. Review of Individual Pitch Control of Wind Turbine.....	16
2.2. Wind Turbine Wake Model.....	20

2.3.	Wind Turbine Meandering Wake Modeling	22
2.4.	Model Predictive Control for Wind Turbine.....	25
2.5.	Dynamic Modeling and Control of Floating Offshore Wind Turbine	29
2.6.	Wind Farm Control	36
Chapter 3. Modeling of Wind Turbine Wake and Wake Meandering.....		42
3.1.	Jensen Wake Model	42
3.2.	Larsen Wake Model	43
3.3.	Wind Shear	46
3.4.	Wind Profile of Downstream Turbine Rotor Disc with Wake Interaction included	47
3.5.	Wake Meandering	49
3.6.	Algorithms for Wake Interaction and Wake Meandering in TurbSim....	53
Chapter 4. Individual Pitch Control of Wind Turbine Including Wake Interaction ...		58
4.1.	Controller Switching Strategy.....	58
4.2.	Determination of Local Pitch Reference along Azimuth	59
4.3.	Disturbance Accommodating Control.....	62
4.4.	Periodic Control	64
4.5.	Simulation Results.....	65

4.5.1.	Simulation Platform	65
4.5.2.	Wind Profile with Wind Shear and Wake Effect	66
4.5.3.	ECWP and Different Pitch Reference along Azimuth	67
4.5.4.	Model Linearization for Individual Pitch Control.....	70
4.5.5.	Rotor Disc Segmentation	70
4.5.6.	Comparison of Switching and Non-switching Controller.....	72
4.6.	Summary	77
Chapter 5. Model Predictive Control of Wind Turbine Including Wake Meandering		78
5.1.	Multi-Blade Coordinate Transformation.....	79
5.2.	Dual-Mode Model Predictive Control.....	85
5.3.	Multiple-Model Predictive Control.....	91
5.4.	Simulation Study.....	97
5.4.1.	Simulation Platform	97
5.4.2.	Simulated Wake Meandering Model.....	97
5.4.3.	Model Linearization and MBC Transformation.....	101
5.4.4.	Simulation Results for Dual-Mode MPC Based IPC	102
5.4.5.	Simulation Results for MMPC Based IPC	105

5.5.	Summary	110
Chapter 6. Maximizing Wind Energy Capture via Nested-loop Extremum Seeking		
	Control	111
6.1.	Nested Optimization of Cascaded Wind Turbine Array	112
6.2.	NLESC Based Wind Farm Control Design	113
6.2.1.	Steady Wind	115
6.2.2.	Turbulent Wind	115
6.2.3.	Cross-Covariance Based Adaptive Delay Compensation	117
6.3.	Simulation Study	117
6.3.1.	Simulation for Steady Wind	118
6.3.2.	Turbulent Wind	132
6.4.	Conclusion.....	137
Chapter 7. Active Vane Control for Stabilization of Floating Offshore Wind		
	Turbine.....	138
7.1.	Vertical Vane Design	139
7.1.1.	Design Approach.....	139
7.2.	Horizontal Vane Design	144
7.3.	Simulation Results.....	146

7.3.1.	Simulation Results for Vertical Vane.....	146
7.3.1.1.	Vertical Vane and NACA 0012 with Different Measurements and Upwind Design as Benchmark	146
7.3.1.2.	Vertical Vane and NACA 0012 with Different Measurements and Downwind Design as Benchmark	155
7.3.1.3.	Vertical Vane and NACA 0012 with Different Vane Area and Downwind Design as Benchmark	163
7.3.1.4.	High Lift Airfoil and Vertical Vane with Different Measurements and Downwind Design as Benchmark	171
7.3.1.5.	High Lift airfoil and Vertical Vane with Different Vane Area and Downwind Design as Benchmark	179
7.3.1.6.	Damage Equivalent Loads	187
7.3.1.7.	Power Assumption by Vertical Vane Actuator	187
7.3.2.	Simulation Results for Horizontal Vane	189
7.4.	Summary	194
Chapter 8.	Contribution and Future Work	195
8.1.	Summary of Research Contribution.....	195
8.1.1.	Individual Pitch Control of Wind Turbine Load Reduction by Including Wake Interaction	195

8.1.2.	Model Predictive Control of Wind Turbines including Wake	
	Meandering.....	196
8.1.3.	Maximizing Wind Farm Energy Capture via Nested-loop Extremum	
	Seeking Control	196
8.1.4.	Active Vane Control for Stabilization of Floating Offshore Wind	
	Turbine	197
8.2.	Future Work	197
Appendix A. Justification of Nested-loop Optimization for Maximizing Energy		
	Capture of A Cascade of Wind Turbines.....	198
Appendix B. Specifications of NREL 5MW Turbine Model		
		207
Appendix C. Codes of MMPC and dual-mode MPC		
		213
C.1	Multiple Model Predictive Control	213
C.2	Dual Mode MPC	222
Appendix D. Codes for Jensen Wake Model, Larsen Wake Model and Wake		
	Meandering	227
D.1	Jensen Wake Model	227
D.2	Larsen Wake Model.....	231
Appendix E. Codes and Simulink Diagram for Active Vane		
		263
E.1	Modified Codes for Building Simulink Interface of FAST.....	263

E.2 Simulink Diagram	272
Appendix F. Simulation Programs for NLESC Wind Farm Control.....	273
F.1. Simulink Layout of ESC Implementation	274
F.2 Simulink Layout for NLESC	275
F.3 Simulink Layout Template Generated by SimWindFarm	276
Appendix G. Default Wind Farm Controller in SimWindFarm	277
Reference	278

LIST OF FIGURES

Fig. 1.1 Horizontal Axis Wind Turbine [5].....	3
Fig. 1.2 A Darrieus Type Vertical Axis Wind Turbine [6].....	4
Fig. 1.3 Operation Regions for Wind Turbine	5
Fig. 1.4 Relationship between Power Coefficient, TSR and Pitch Angle [7].....	6
Fig. 1.5 Atmospheric Boundary Layer.....	8
Fig. 1.6 Wake Overlap at Downstream Turbines.....	8
Fig. 1.7 Status of Offshore Wind Energy Technology [28].....	12
Fig. 2.1. Floating Deepwater Platform Concepts: 1) Semisubmersible Dutch Tri-Floater [132] 2) Spar buoy with two tiers of guy wires [130] 3) Three-arm mono-hull tension-leg platform (TLP) [128]; 4) Concrete TLP with gravity anchor [129]; 5) SWAY [131].....	30
Fig. 2.2 Reduction of Tower Fore-aft Damage Equivalent Load by use of TMD [33]	34
Fig. 2.3 Reduction Percent of Tower Fore-aft Damage Equivalent Load by use of TMD [33].....	35
Fig. 2.4 Comparison of the TMD Stroke for the optimal passive control case and a selected active control case [33].....	35
Fig. 3.1: Illustration of Jensen wake model	43

Fig. 3.2: Illustration of Larsen wake model	44
Fig. 3.3: Illustration of Wake Interaction at the Downstream Turbine	47
Fig. 3.4: Illustration for Wind Turbine Wake Meandering.....	49
Fig. 3.5: Spectral Method to Generate Turbulent Wind [176].....	50
Fig. 3.6 Grid Points for Wind Profile in TurbSim [176].....	53
Fig. 3.7: Coordinates in TurbSim [176].....	55
Fig. 4.1 Switching IPC Controller Strategy	60
Fig. 4.2 Equivalent Circular Wind Profile (ECWP)	61
Fig. 4.3 Wind Speed Distributions within Rotor Disc due to Wind Shear	68
Fig. 4.4 Wind Profile with Wind Shear and General Wake Interaction	68
Fig. 4.5 Equivalent Circular Wind Profile for The Simulation Example.....	69
Fig. 4.6 Pitch Reference along Azimuth Obtained with ECWP	69
Fig. 4.7 Maximum Singular Value Difference within Rotor Disc.....	71
Fig. 4.8 Sixteen Segments of Rotor Disc after Segment Merge	72
Fig. 4.9 Tower-base Fore-aft Bending Moment using the Proposed Method (Switch) and DAC (No Switch)	73
Fig. 4.10 Tower-base Side-to-side Bending Moment using the Proposed Method (Switch) and DAC (No Switch).....	74

Fig. 4.11 Rotor Speed using the Proposed Method (switch) and DAC (no switch)	75
Fig. 4.12 Blade-tip Displacement Difference using the Proposed Method (Switch) and DAC (No Switch)	76
Fig. 5.1 Blade Coordinate System [140].....	79
Fig. 5.2 Nacelle Coordinate System [140].....	79
Fig. 5.3 Tower-base Coordinate System [140]	80
Fig. 5.4 Multi-Blade Coordinates for Controller Design	85
Fig. 5.5. Block Diagram of Dual-mode MPC based IPC control	89
Fig. 5.6. Illustration for Wake Center Positions for Controller Switching	91
Fig. 5.7 Controller Switching for Dual-mode MPC based IPC Control under Wake Meandering.....	91
Fig. 5.8 Algorithm for Multiple-Model Predictive Control	92
Fig. 5.9 Illustration of MMPC based Wind Turbine Control Incorporating MBC Transformation	95
Fig. 5.10 Illustration of wake meandering for two turbines in a wind farm	98
Fig. 5.11. Wake Center Trajectory at the Downstream Wind Turbine	99
Fig. 5.12 Wind Profiles at the Downstream Wind Turbine for Different Wake-Center Positions.....	100

Fig. 5.13. MPC Controlled Rotor Speed with and without Considering Wake Meandering	103
Fig. 5.14: MPC Controlled Flapwise Moment at the Root of Blade-1 with and without Considering Wake Meandering	104
Fig. 5.15. Rotor Speed with and without Considering Wake Meandering.	106
Fig. 5.16. Flapwise Bending Moment at the Root of Blade-1.	107
Fig. 5.17: Temporal Profile for the Pitch Angle Rate for the MMPC IPC	108
Fig. 5.18: Temporal Profile of Pitch Angle for the MMPC IPC	109
Fig. 5.19: Weighting and Model Mode in MMPC	109
Fig. 6.1 NLESC Control for A Cascaded Array of Wind Turbines	113
Fig. 6.2 Block Diagram of Dither ESC Algorithms	114
Fig. 6.3 ESC of Three Turbines under Steady Wind	115
Fig. 6.4 Power Coefficient of NREL 5MW with Pitch Angle 0°	119
Fig. 6.5 Static Map of Power Capture for Two Cascaded Turbines at 6m/s	119
Fig. 6.6 Step Response of NREL 5MW Power	121
Fig. 6.7 Estimation of Time Constant of for Torque Based Power Regulation	122
Fig. 6.8 Illustration of ESC Dither Frequency and Phase Compensation for Turbine #3	123

Fig. 6.9 Illustration of ESC Dither Frequency and Phase Compensation for Turbine #1	125
Fig. 6.10 Illustration of ESC Dither Frequency and Phase Compensation for Turbine #2	126
Fig. 6.11 Torque Gain Profiles for NLESC Search under 6m/s Smooth Wind	127
Fig. 6.12 Wind Speed at Each Turbine for NLESC Search under 6m/s Smooth Wind	128
Fig. 6.13. Generator Speed Profiles for NLESC Search under 6m/s Smooth Wind..	128
Fig. 6.14. Total Power Profiles for NLESC Search under 6m/s Smooth Wind.....	129
Fig. 6.15. Torque Gain Profiles for NLESC Search under 10 m/s Smooth Wind	130
Fig. 6.16. Effective Wind Speed at Each Turbine for NLESC Search under 10 m/s Smooth Wind.....	130
Fig. 6.17 Generator Speed Profiles for NLESC Search under 10 m/s Smooth Wind	131
Fig. 6.18 Total Power Profiles for ESC Search for Smooth 10 m/s Wind.....	132
Fig. 6.19. Effective Wind Speed Profile at Turbine #1 under 8 m/s 5% Turbulent Wind	133
Fig. 6.20 Effective Wind Speed Profile at Turbine #2 under 8 m/s 5% Turbulent Wind	134

Fig. 6.21. Effective Wind Speed Profile at Turbine #3 under 8 m/s 5% Turbulent Wind	134
Fig. 6.22. Torque Gains under 8 m/s 5% Turbulent Wind.....	135
Fig. 6.23 Generator Speed at Turbine 1 under 8 m/s 5% Turbulent Wind	135
Fig. 6.24 Generator Speed at Turbine 2 under 8 m/s 5% Turbulent Wind	136
Fig. 6.25 Generator Speed at Turbine 3 under 8 m/s 5% Turbulent Wind	136
Fig. 6.26. Total Power under 8 m/s 5% Turbulent Wind.....	137
Fig. 7.1. Vertical Vane Design a) Side View; b) Top View 1; c) Top View 2.....	140
Fig. 7.2. Configuration of Tail-Furling	141
Fig. 7.3. Simulink Interface of FAST including Vertical Vane Pitch Control.....	142
Fig. 7.4. Lift and Drag Coefficients of NACA0012	143
Fig. 7.5. Vertical Vane Control Loop	144
Fig. 7.6. Configuration of Horizontal Vane	145
Fig. 7.7. Generator Power (Vertical Vane, NACA0012, Upwind as Benchmark)	148
Fig. 7.8 Spectra of Generator Power (Vertical Vane, NACA0012, Upwind as Benchmark).....	148
Fig. 7.9. Rotor Speed (Vertical Vane, NACA0012, Upwind as Benchmark).....	149

Fig. 7.10. Spectra of Rotor Speed (Vertical Vane, NACA0012, Upwind as Benchmark)	149
Fig. 7.11. Side-to-Side Velocity (Vertical Vane, NACA0012, Upwind as Benchmark)	150
Fig. 7.12. Spectra of Side-to-Side Velocity (Vertical Vane, NACA0012, Upwind as Benchmark)	150
Fig. 7.13. Vane Pitch Angle (Vertical Vane, NACA0012, Upwind as Benchmark)	151
Fig. 7.14. Spectra of Vane Pitch Angle (Vertical Vane, NACA0012, Upwind as Benchmark)	151
Fig. 7.15. Platform Sway Displacement (Vertical Vane, NACA0012, Upwind as Benchmark)	152
Fig. 7.16. Platform Sway Displacement Spectra (Vertical, NACA0012, Upwind as Benchmark)	152
Fig. 7.17. Platform Roll Displacement (Vertical Vane, NACA0012, Upwind as Benchmark)	153
Fig. 7.18. Platform Roll Displacement Spectra (Vertical, NACA0012, Upwind as Benchmark)	153
Fig. 7.19. Side-to-Side Bending Moment (Vertical Vane, NACA0012, Upwind as Benchmark)	154

Fig. 7.20. Side-to-Side Bending Moment Spectra (Vertical, NACA0012, Upwind as Benchmark).....	154
Fig. 7.21. Generator Power (Vertical Vane, NACA0012, Downwind as Benchmark)	156
Fig. 7.22. Generator Power Spectra (Vertical Vane, NACA0012, Downwind as Benchmark).....	156
Fig. 7.23. Rotor Speed (Vertical Vane, NACA0012, Downwind as Benchmark).....	157
Fig. 7.24. Rotor Speed Spectra (Vertical Vane, NACA0012, Downwind as Benchmark)	157
Fig. 7.25. Vane Pitch Angle (Vertical Vane, NACA0012, Downwind as Benchmark)	158
Fig. 7.26. Vane Pitch Angle Spectra (Vertical Vane, NACA0012, Downwind as Benchmark).....	158
Fig. 7.27. Side-to-Side Velocity (Vertical Vane, NACA0012, Downwind as Benchmark).....	159
Fig. 7.28. Side-to-Side Velocity Spectra (Vertical Vane, NACA0012, Downwind as Benchmark).....	159
Fig. 7.29. Roll Displacement (Vertical Vane, NACA0012, Downwind as Benchmark)	160

Fig. 7.30. Roll Displacement Spectra (Vertical Vane, NACA0012, Downwind as Benchmark).....	160
Fig. 7.31. Sway Displacement (Vertical Vane, NACA0012, Downwind as Benchmark)	161
Fig. 7.32. Sway Displacement Spectra (Vertical Vane, NACA0012, Downwind as Benchmark).....	161
Fig. 7.33. Side-to-Side Bending Moment (Vertical, NACA0012, Downwind as Benchmark).....	162
Fig. 7.34. Side-to-Side Bending Moment Spectra (Vertical, NACA0012, Downwind as Benchmark).....	162
Fig. 7.35. Generator Power (Vertical Vane, NACA0012, Downwind as Benchmark)	164
Fig. 7.36. Generator Power (Vertical Vane, NACA0012, Downwind as Benchmark)	164
Fig. 7.37. Rotor Speed (Vertical Vane, NACA0012, Downwind as Benchmark).....	165
Fig. 7.38. Rotor Speed Spectra (Vertical Vane, NACA0012, Downwind as Benchmark)	165
Fig. 7.39. Vane Pitch Angle (Vertical Vane, NACA0012, Downwind as Benchmark)	166

Fig. 7.40. Vane Pitch Angle Spectra (Vertical Vane, NACA0012, Downwind as Benchmark).....	166
Fig. 7.41. Side-to-Side Velocity (Vertical Vane, NACA0012, Downwind as Benchmark).....	167
Fig. 7.42. Side-to-Side Velocity Spectra (Vertical Vane, NACA0012, Downwind as Benchmark).....	167
Fig. 7.43 Roll Displacement (Vertical Vane, NACA0012, Downwind as Benchmark)	168
Fig. 7.44. Roll Displacement Spectra (Vertical Vane, NACA0012, Downwind as Benchmark).....	168
Fig. 7.45. Sway Displacement (Vertical Vane, NACA0012, Downwind as Benchmark)	169
Fig. 7.46 Sway Displacement Spectra (Vertical Vane, NACA0012, Downwind as Benchmark).....	169
Fig. 7.47. Side-to-Side Bending Moment (Vertical Vane, NACA0012, Downwind as Benchmark).....	170
Fig. 7.48. Side-to-Side Bending Moment (Vertical Vane, NACA0012, Downwind as Benchmark).....	170
Fig. 7.49. Generator Power Comparison (Vertical Vane, Highlift Airfoil, Downwind as Benchmark)	172

Fig. 7.50 Generator Power Spectral (Vertical Vane, Highlift Airfoil, Downwind as Benchmark).....	172
Fig. 7.51 Rotor Speed (Vertical Vane, Highlift Airfoil, Downwind as Benchmark)	173
Fig. 7.52 Rotor Speed Spectra (Vertical Vane, Highlift Airfoil, Downwind as Benchmark).....	173
Fig. 7.53 Side-to-side Velocity on Tower Top (Vertical Vane, Highlift Airfoil, Downwind as Benchmark)	174
Fig. 7.54 Spectra of Side-to-side Velocity on Tower Top (Vertical Vane, Highlift Airfoil, Downwind as Benchmark).....	174
Fig. 7.55 Vane Pitch Angle (Vertical Vane, Highlift Airfoil, Downwind as Benchmark).....	175
Fig. 7.56 Vane Pitch Angle Spectra (Vertical Vane, Highlift Airfoil, Downwind as Benchmark).....	175
Fig. 7.57 Platform Roll Displacement (Vertical Vane, Highlift Airfoil, Downwind as Benchmark).....	176
Fig. 7.58 Platform Roll Displacement Spectra (Vertical Vane, Highlift Airfoil, Downwind as Benchmark)	176
Fig. 7.59 Platform Sway Displacement (Vertical Vane, Highlift Airfoil, Downwind as Benchmark).....	177

Fig. 7.60 Platform Sway Displacement Spectra (Vertical Vane, Highlift Airfoil, Downwind as Benchmark)	177
Fig. 7.61 Side-to-side Bending Moment (Vertical Vane, Highlift Airfoil, Downwind as Benchmark)	178
Fig. 7.62 Side-to-side Bending Moment Spectra (Vertical Vane, Highlift Airfoil, Downwind as Benchmark)	178
Fig. 7.63 Generator Power (Vertical Vane, Highlift Airfoil, Downwind as Benchmark)	180
Fig. 7.64 Generator Power Spectra (Vertical Vane, Highlift Airfoil, Downwind as Benchmark).....	180
Fig. 7.65 Rotor Speed (Vertical Vane, Highlift Airfoil, Downwind as Benchmark)	181
Fig. 7.66 Rotor Speed Spectra (Vertical Vane, Highlift Airfoil, Downwind as Benchmark).....	181
Fig. 7.67 Vane Pitch Angle (Vertical Vane, Highlift Airfoil, Downwind as Benchmark).....	182
Fig. 7.68 Vane Pitch Angle Spectra (Vertical Vane, Highlift Airfoil, Downwind as Benchmark).....	182
Fig. 7.69 Side-to-Side Velocity (Vertical Vane, Highlift Airfoil, Downwind as Benchmark).....	183

Fig. 7.70 Side-to-Side Velocity Spectra (Vertical Vane, Highlift Airfoil, Downwind as Benchmark)	183
Fig. 7.71 Platform Roll Displacement (Vertical Vane, Highlift Airfoil, Downwind as Benchmark).....	184
Fig. 7.72 Platform Roll Displacement Spectra (Vertical Vane, Highlift Airfoil, Downwind as Benchmark)	184
Fig. 7.73 Platform Sway Displacement (Vertical Vane, Highlift Airfoil, Downwind as Benchmark).....	185
Fig. 7.74 Platform Sway Displacement Spectra (Vertical Vane, Highlift Airfoil, Downwind as Benchmark)	185
Fig. 7.75 Side-to-Side Bending Moment (Vertical Vane, Highlift Airfoil, Downwind as Benchmark)	186
Fig. 7.76 Side-to-Side Bending Moment Spectra (Vertical Vane, Highlift Airfoil, Downwind as Benchmark)	186
Fig. 7.77 Vane Pitch Angle for Horizontal Vane Control.....	190
Fig. 7.78 Vane Pitch Angle Spectra for Horizontal Vane Control.....	190
Fig. 7.79 Fore-aft Velocity at Tower Top for Horizontal Vane Control.....	191
Fig. 7.80. Spectra of Fore-aft Velocity at Tower Top for Horizontal Vane Control .	191
Fig. 7.81. Platform Rotational Pitch Displacement for Horizontal Vane Control	192

Fig. 7.82. Spectra of Platform Rotational Displacements for Horizontal Vane Control
..... 192

Fig. 7.83. Fore-Aft Bending Moments at Tower Base for Horizontal Vane Control 193

Fig. 7.84. Spectra of Fore-Aft Bending Moments at Tower Base for Horizontal Vane
Control 193

LIST OF TABLES

Table 4-1: State Description for a 9-state Wind Turbine Model (CART)	70
Table 5-1: STATE DESCRIPTION FOR A 9-STATE WIND TURBINE MODEL (NREL 5MW TURBINE).....	101
Table 5-2: MEASUREMENTS FOR NREL 5MW	102
Table 7-1: List of Status for Tail-Fin Degrees of Freedom for Vertical Vane	140
Table 7-2: FAST Setting for Horizontal Vane.....	145
Table 7-3: Damage Equivalent Loads (DEL) for Vertical Vane	187
Table 7-4: Power Assumption of Vane Pitch.....	188
Table B-1: Properties of the NREL-5MW Baseline	207

Nomenclature

Abbreviations

CFD	Computational Fluid Dynamics
COE	Cost of Energy
CPC	Collective Pitch Control
DAC	Disturbance Accommodating Control
ECWP	Equivalent Circular Wind Profile
ESC	Extremum Seeking Control
IPC	Individual Pitch Control
LQR	Linear Quadratic Regulator
MBC	Multi-blade Coordinates Transformation
MPC	Model Predictive Control
MMPC	Multiple Model Predictive Control
NLESC	Nested-loop Extremum Seeking Control
PI	Proportional-Integral
SWMM	Simplified Wake Meandering Model
LIDAR	Light Detection and Ranging
a	Coherence decrement
a_i	Induction Factor of i th wind turbine
A	The rotor plane area in wake meandering model
A	The state matrix in state-space model
iA	The state matrix in i th state-space model
B	The input matrix in state-space model
iB	The input matrix in i th state-space model

c_k	Control perturbation at the k th sampling instant
\underline{c}_k	The sequence of control perturbation
C	Relates the measurement vector with the state vector in state-space model
C	Damping matrix in wind turbine dynamics
C_t	Thrust coefficient at upstream wind turbine
D_r	The diameter of wind turbines
D_w	The diameter of wake behind wind turbines
F	Frequency in Hz
$F_{wm}(s)$	The first-order low-pass filter
F_d	Parameter for wind disturbance in state-space model
G	The feedback gain for LQR method
\bar{G}	The feedback gain for DAC method
H	The hub height of wind turbines
I_a	The ambient turbulence intensity
L	The distance between two points
L_k	Integral scale parameter for velocity component k
M	Mass matrix in wind turbine dynamics
L_c	A coherence scale parameter
K	The feedback gain in Dual Mode MPC
\bar{K}	The observer gain for DAC method
k	The wake entrainment constant
L_{hub}	The distance between the hub axes of upstream and downstream wind turbines
q_b^j	the j th rotating degree of freedom for the b th blade

Q	Weighting matrix for states in LQR method
R	Weighting matrix for control input in LQR method
R_w	The radius of wake behind wind turbines
R_y	The wake radius in the y direction
R_z	The wake radius in the z direction
r	Radius from the wake centerline
$S_k(f)$	Spectra at frequency f for velocity component k
T	Multi-Blade Coordinates Transformation Matrix
T_d	The downstream traveling time
T_f	Time constant for the first-order low-pass filter
u	Velocity component in x direction
u	The control input vector in state-space model
u_d	The disturbance vector
U	The mean wind speed along incoming wind direction at hub height H
v	Velocity component in y direction
V_c	Characteristic velocity along y direction across the rotor plane at upstream turbine
V_{filt}	Filtered wake center moving velocity in y direction
V_∞	The mean wind speed at the upstream wind turbine
V_w	The mean wind speed in the wake
V_{hub}	The wind speed at hub height
$V_{wcenter}$	The wind speed at the wake center
$V(x,y,z)$	The wind speed distribution in three dimension
$V(z)$	The wind speed distribution along vertical direction
ΔV	The wind speed deficit

w	Velocity component in z direction
W_c	Characteristic velocity along z direction across the rotor plane at upstream turbine
W_{filt}	Filtered wake center moving velocity in z direction
${}^i w_k$	Weighting for i th model at time sampling k in MMPC
x	The coordinate along incoming wind direction for wake model
x	State vector in state-space model
x_k	State vector at the k th sampling instant in state-space model
\hat{x}	Estimator of state vector x
x_1	Location of upstream wind turbine along x direction
x_2	Location of downstream wind turbine along x direction
x_w	The distance between the upstream and downstream wind turbine
X	States of wind turbine dynamics including rotating and fixed vector
X_F	Fixed-frame-referenced degrees of freedom for wind turbine dynamics
X_{NF}	States of wind turbine dynamics in nonrotating frame
y	The coordinate along lateral direction perpendicular with x and z for wake model
y	Measurement vector in state-space model
\hat{y}	Estimator of measurement vector y
z	The vertical coordinate and the origin is at the root of wind turbine tower
z_0	The surface roughness
σ_k	The variance determined by the turbulence intensity
Δ_y	Wake Center Position along y direction at the downstream wind turbine
Δ_z	Wake Center Position along z direction at the downstream wind turbine
Γ	The disturbance gain matrix in state-space model

θ	Parameter for wind disturbance
ψ_i	Azimuth angle of i th blade

Chapter 1. Introduction

Wind energy has become and will remain a critical part of renewable power generation for the upcoming decades. The worldwide wind power installed has exceeded 280 GW by the end of 2012 [1]. According to the US Department of Energy, by 2030, 20% of all U.S. electricity will be likely supplied by wind power including onshore (16%) and offshore (4%) wind power [2]. A major barrier for further development and acceptance of wind power is the relatively higher cost of energy (COE), as compared to that of conventional energy sources. In order to reduce the COE, the wind energy sector has to improve the wind turbine design and operation towards better efficiency and reliability, for which better control strategies are very important for the reduction of COE.

For utility wind turbines, due to the turbulent characteristics of natural wind source and complex dynamic characteristics, feedback control is indispensable for effective energy capture and load reduction, regardless how good a wind turbine structural design could be. Controls for maximizing energy capture is usually focused below rated wind speed (the so-called Region-2 operation as to be described in Section 1.1). Above the rated wind speed (i.e. the so-called Region 3 operation), the primary control objectives are maintaining the power output to the rated level, and minimizing the structural load. Reducing both fatigue and extreme loads helps extending the operating life of wind turbines.

This dissertation study focuses on the advanced wind turbine control design for both load reduction and maximizing energy capture. A major attempt is to investigate this topic with two scenarios that have drawn more attention recently: wind farm and offshore

operations. The remainder of this chapter is organized as follows. To facilitate the understanding of research motivations, typical wind turbine design and conventional wind turbine control strategies will be explained first. Then the wind farm control will be briefly reviewed. For turbines in farm operation, the challenges in both load reduction and energy capture will be described. Next, the significances and challenges of floating offshore wind turbine will be discussed, and especially the issues with load reduction control and stabilization. Finally, the statements of research problems for this dissertation study will be presented: three problems for the farm operated turbine control, and the other for floating turbine.

1.1. Wind Turbine Types

Wind turbines extract energy from wind and convert mechanical rotation into electrical power [3]. Wind turbines are generally classified into the Horizontal Axis Wind Turbine (HAWT) and Vertical Axis Wind Turbine (VAWT). An HAWT rotates about a horizontal axis, as shown in Fig. 1.1; while the VAWT rotates about a vertical axis, as shown in Fig. 1.2. The key advantage of the VAWT is that it does not need to face into the incoming wind direction. VAWT could be built at the sites with frequent change in wind direction, e.g. urban areas. The disadvantages of VAWT include high cost of drive train, low power efficiency, and high dynamic loading on the blades.

For the utility level wind power generation, the HAWT is almost the exclusive choice so far [4]. This dissertation study focuses on the HAWT. Most of the utility wind turbines are 3-bladed upwind HAWTs and 2-bladed downwind HAWTs. In the earlier development of wind power, downwind turbines were popular because active yaw mechanism is not needed and there is no danger for blades to hit the tower. However,

turbulence induced by the tower leads to periodic loads on the blades and power fluctuation, i.e. the so-called “tower shadow” [4]. For upwind turbines, the rotor is placed before the tower along the wind direction, so there is no concern for the tower shadow effect. With the comprehensive benefit of load reduction and energy capture, 3-bladed upwind turbines are currently dominant for utility wind power generation. In the earlier development of wind power, fixed-speed wind turbines were popular due to their simplicity in the control strategy needed. Due to higher energy capture efficiency below rated wind speed, variable-speed wind turbines are commonly used in wind industry now. In this dissertation study, variable-speed variable-pitch upwind turbines are the focus because they are the most popular wind turbine types at present.

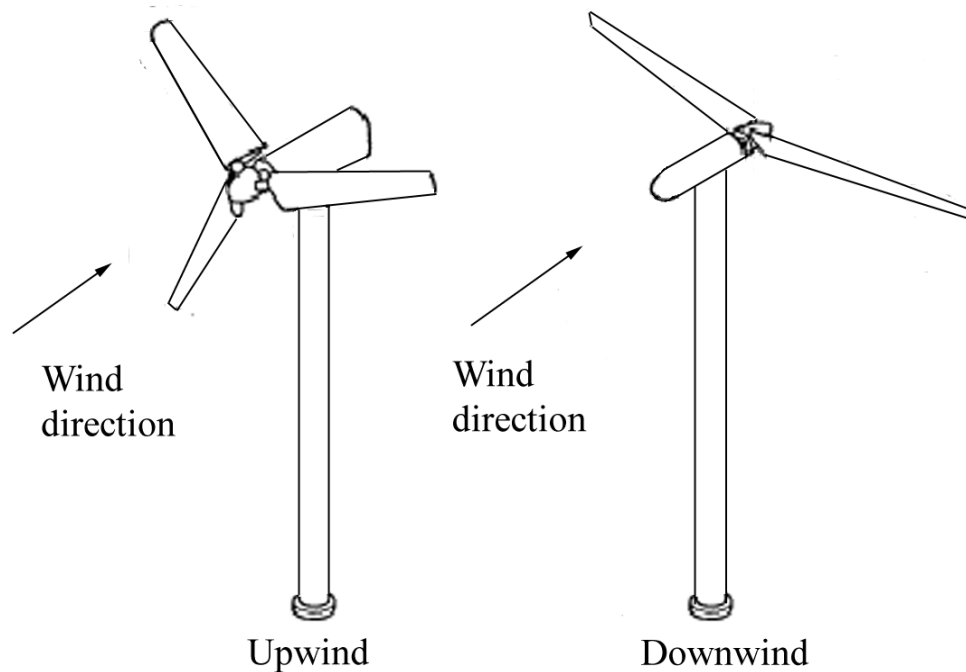


Fig. 1.1 Horizontal Axis Wind Turbine [5]



Fig. 1.2 A Darrieus Type Vertical Axis Wind Turbine [6]

1.2. Wind Turbine Control Strategy

The operation of variable-pitch variable-speed wind turbines can be divided into four regions [4] based on the definition of the cut-in speed V_{in} , the rated wind speed V_{rated} and the cut-out wind speed V_{out} , as shown in Fig. 1.3. For different regions, the objectives of wind turbine control are different.

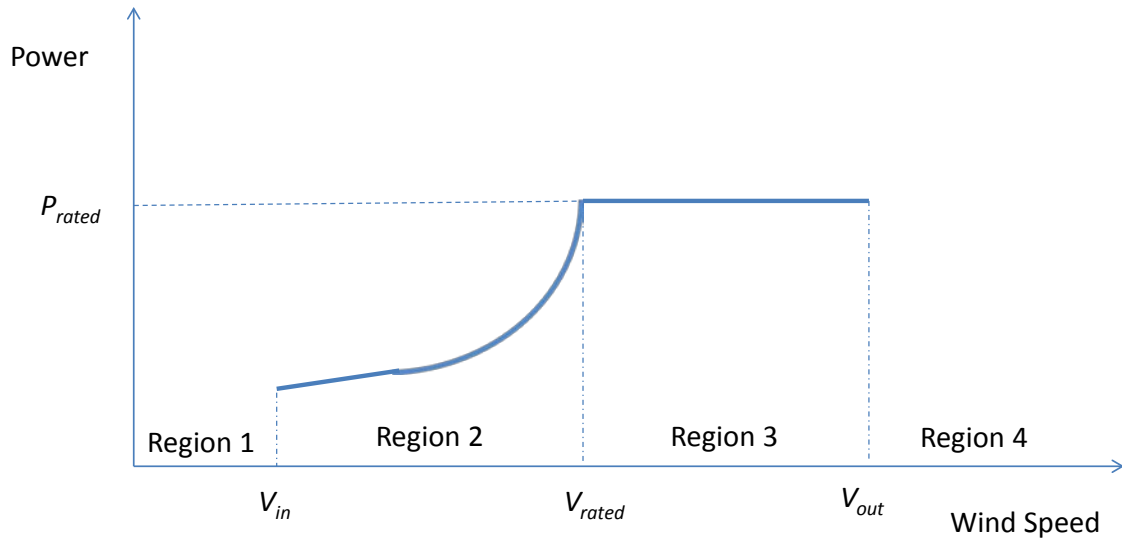


Fig. 1.3 Operation Regions for Wind Turbine

Below the cut-in wind speed V_{in} (Region 1), the wind turbine is not connected to the grid. Above the cut-in wind speed V_{in} and below the rated wind speed V_{rated} (Region 2), the wind turbine is operated to extract the maximum possible energy from the wind by varying rotor speed and/or blade pitching. Above the rated wind speed V_{rated} and below the cut-out wind speed V_{out} (Region 3), the wind turbine maintains at its rated power P_{rated} and the generator speed is restrained to the neighborhood of the rated speed, i.e. the main control objective in Region 3 is to keep the rotor speed near the rated speed while minimizing the wind turbine loads. Above the cut-out wind speed V_{out} (Region 4), the wind turbine is shut down with aerodynamic and disc braking for the sake of safety.

The variable-speed variable-pitch turbines typically feature three actuators: blade pitch, generator torque and yaw. Blade pitch angles are usually fixed at fine pitch angle in Region 2, and are adjusted to limit rotor speed and wind turbine loads in Region 3. The generator side power converters are controlled to vary the electrical torque, which in turn

adjust rotor speed. The relationship between power coefficient, Tip Speed Ratio (TSR) and pitch angle is shown in Fig. 1.4.

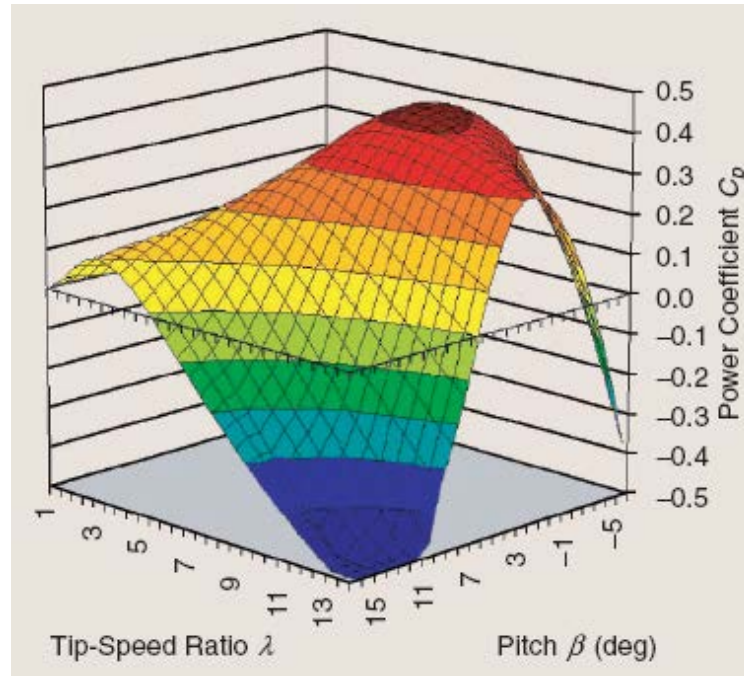


Fig. 1.4 Relationship between Power Coefficient, TSR and Pitch Angle [7]

Advanced control technologies have been studied extensively for energy capture [8, 9] in Region 2 and load reduction [10-12] for Region 3 operations of stand-alone wind turbines. However, energy capture and load reduction control from wind farm level has not been studied as much.

1.3. Wind Farm Control

Appropriate wind farm operation has the benefits of better grid integration, lower maintenance costs, and more energy production [13]. For controls of turbines in wind farm operation, there are also two aspects similar to the stand-alone: energy capture and

load reduction. However, under wind farm operation, both aspects present different challenges than the stand-alone turbine operation.

To the author's best knowledge, the traditional control strategies for wind farm operation emphasize the effect of the deficit of average wind speed, i.e. on how to guarantee the power quality for grid integration by the control of the electrical systems [14, 15] or maximize the energy capture of the whole wind farm [16]. However, wind farm control strategies for maximizing energy capture is still far from mature due to complex wake phenomenon. From another standpoint, it is obvious that the asymmetric nature of wake interaction would bring great impact on structural load. In this study, both load reduction control and maximizing energy capture control are investigated.

1.3.1. Load Reduction Control for Turbines in Farm Operation

For stand-alone wind turbines, controls for energy capture is generally based on mean wind speed (e.g. hub height), while controls for load reduction is concerned more with the asymmetry within the rotor disc. For stand-alone turbines, the incoming wind speed is generally uniform except for the vertical wind shear due to the atmospheric boundary layer (ABL), shown in Fig. 1.5.

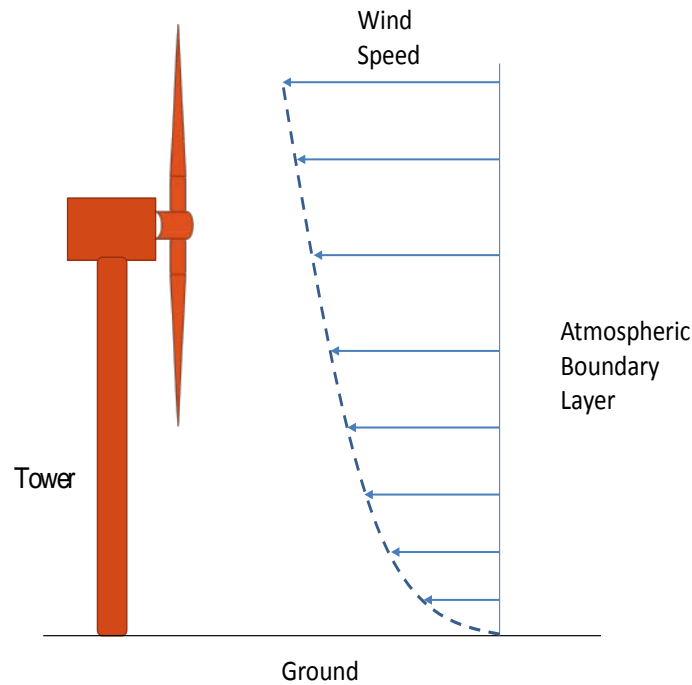


Fig. 1.5 Atmospheric Boundary Layer

For turbines in wind farm operation, however, the downstream turbines are exposed to a different situation. After passing the upstream turbines, the wind speed is determined by the wake characteristics. Thus, the downstream turbines have non-uniform wind distribution within the rotor disc due to the overlap of the wake of the upstream turbines, as shown in Fig. 1.6.

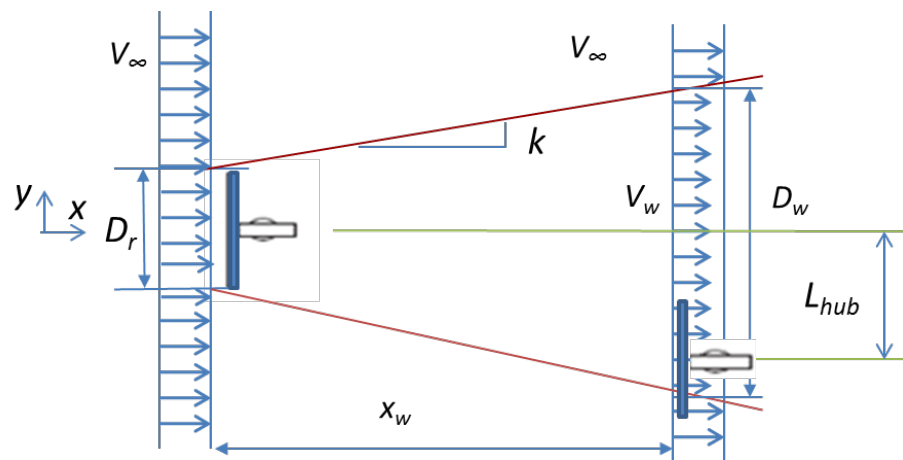


Fig. 1.6 Wake Overlap at Downstream Turbines

Wind turbine wake models play a critical role for wind farm control because wake interaction significantly influences both energy capture and loads of the downstream turbine. In wind farm, average wind speed at the downstream turbine can be predicted by use of simple wake models, such as Jensen wake model [17], which are accurate enough for energy capture calculation. However, wind speed across the whole rotor plane is necessary for load calculation of the downstream wind turbine.

Even worse, the actual wake behavior is not static, i.e. the wind turbine wakes actually move bodily in lateral direction in wind farm. This is the so-called *wake meandering* [18] phenomenon. Wake meandering produces time-varying loading on the downstream wind turbines. Therefore, incorporation of wake meandering model is beneficial for better load reduction control of downstream turbines.

Structural load reduction in the context of wind farm operation was regarded as an opportunity which had not been investigated due to the complexity in predicting the wind speed over the rotor disc of the downstream turbine [13]. In order to achieve better load reduction control for farm operated wind turbines, more accurate wake models are needed to accurately predict wind speed across rotor plane at downstream wind turbines [13]. Based on the above issues, more accurate wake models including wake interaction and wake meandering were built and corresponding controllers were designed for load reduction control of wind turbine in farm operation.

When wake meandering happens, downstream wind turbine dynamics is nonlinear due to varying wind conditions. It is easier to obtain multiple linearized wind turbine dynamic models rather than explicit nonlinear wind turbine dynamic models under wake meandering. At the same time, model predictive control (MPC) [19] is good at

systematically dealing with constraints which are important for wind turbine control, such as limits of blade pitch angle and rate. In this situation, one kind of nonlinear model predictive control, multi-model predictive control (MMPC) [20], was chosen for loads reduction control of wind turbines under wake meandering.

1.3.2. Energy Capture Control in Wind Farm Level

The energy capture control of wind farm has the key difference from that for a stand-alone wind turbine: maximizing the energy capture of individual turbines does not lead to maximizing energy capture of a wind farm due to the velocity deficit and wake interaction. Intuitively speaking, for a wind farm, an upstream turbine should rotate somehow slower than its optimum speed in stand-alone operation, thus extracting less kinetic energy so that more energy may be extracted by the downstream turbines, which eventually increases the total energy capture of a wind farm [21]. There is an interesting observation that the fatigue loads was reduced when energy capture of a cascade of turbines was enhanced [21]. Although the optimal induction factors were obtained for a cascaded array of wind turbines [21, 22], it is difficult to implement wind farm control by use of optimal induction factors.

Model-based control strategies, such as model predictive control [23] and numerical optimization [24], also had been used for wind farm control for maximizing energy capture. The issue for model-based control of wind farm is that wake models may be accurate for flat terrain but inaccurate for complex terrain. Therefore, self-learning or self-optimizing approaches are received as more feasible solutions. Johnson and Thomas [16] proposed a hybrid approach for maximizing the wind farm energy capture by combining the Iterative Learning Control (ILC) and Iterative Feedback Tuning (IFT).

Marden *et al.* [25] proposed a model-free control strategy by use of game theory and cooperative control to optimize the axial induction factors to maximize power production of wind farm.

More recently, one wind farm control strategy had been patented by use of self-optimizing controller to maximize wind farm power output [22]. Its key idea is: the self-optimizing controller for an upstream turbine should be configured to control the upstream turbine in an attempt to maximize the combined total power output of this upstream turbine and downstream turbines in the wake of this upstream turbine. A better choice for self-optimizing controller is ESC. In this thesis, the nest-looped extremum seeking control (NLESC) scheme [22] was investigated for maximizing the wind farm energy capture.

1.3.3. Summary of Load Reduction and Energy Capture Control of Farm

Operated Turbines

This dissertation study investigates both the load reduction control and energy capture control in wind farm level. First, the individual pitch control (IPC) is designed for load reduction to handle the wind variation due to wake interaction via a periodic control scheme. Then, to deal with the wake meandering phenomenon, a model predictive control (MPC) scheme is developed for the IPC of the downstream turbine loads. Thirdly, a novel *Nested-Loop Extremum Seeking Control* (NLESC) strategy is used to maximize energy capture of a wind farm.

1.4. Floating Offshore Wind Turbine Control

Both fixed platform and floating platform can be used for offshore wind turbines. Usually fixed platform is used in shallow water where water depth is usually below 60

meters and floating platform is used in deeper water, as shown in Fig. 1.7. Although Heroneus introduced floating offshore wind turbine in 1972 [26], it was not until 2009 that the first floating wind turbine based on the spar-buoy platform was installed [27].

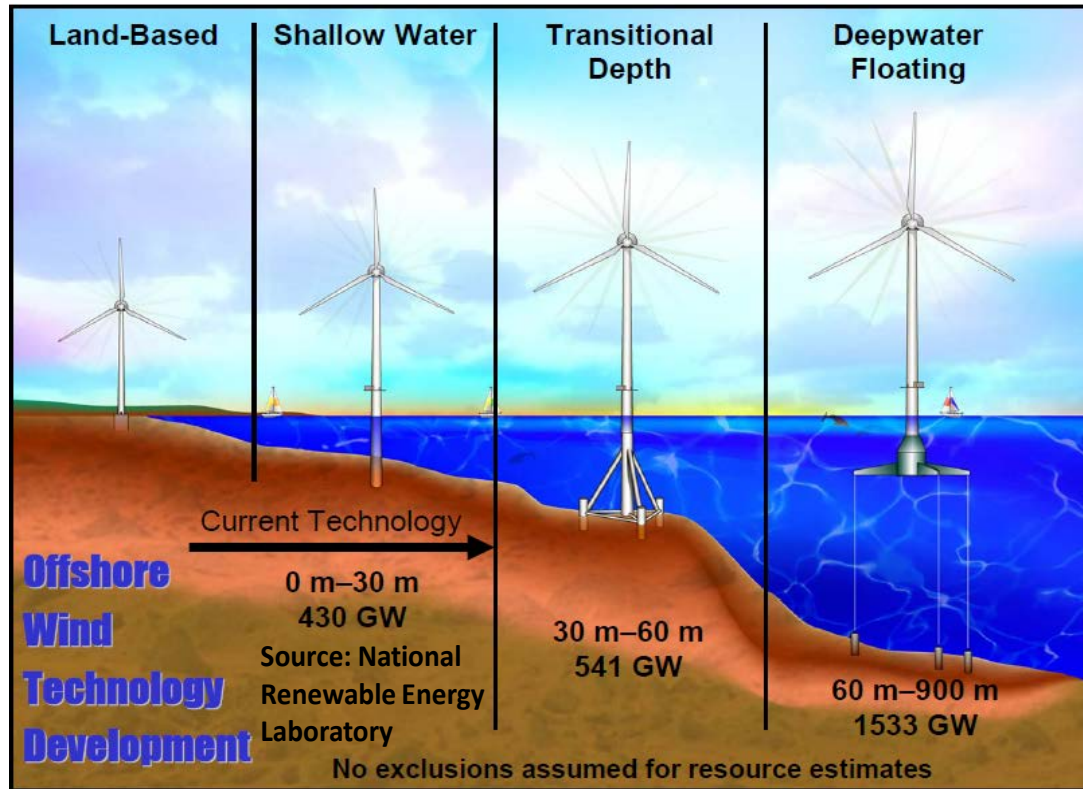


Fig. 1.7 Status of Offshore Wind Energy Technology [28]

Although fixed offshore wind turbines are easily built based on ripe onshore wind turbine technology, offshore wind farms in shallow water near the coastline are usually objected by wildlife groups concerning the effects on avian life along the shores. Coastline dwellers worry that offshore wind farms block the sea view. Floating wind turbines are usually installed some distance from the coast such that floating wind turbines are neither visible nor audible. Sullivan pointed out that “field observations of offshore wind facilities in the United Kingdom revealed that the facilities may be a major

focus of visual attention at distances of up to 10 miles” [29]. Extensive deep water areas exist on the West coast, in Hawaii and the Great Lakes region [30] which are ideal sites to install floating turbines. From the technical side, the marine and offshore oil industries have demonstrated ripe technology to build long-term floating structures. Status of offshore wind energy technology in Fig. 1.7 [28] shows wind resources for deep water floating turbines (1533GW) is 58% more than the sum of that for transitional depth and that for shallow water ($430\text{GW} + 541\text{GW} = 971\text{GW}$).

The wind turbine dynamics has no big difference between onshore turbine and fixed offshore turbine. However, the dynamics of floating turbine is very different from that of fixed turbine due to the floating foundation, which brings lots of engineering challenges. The first question we should ask is how to stabilize floating wind turbine which is a very interesting and challenging one for control field. A greater challenge for floating wind turbine is increasing damping in roll motions which are side to side translation in the plane of rotor rotation [31]. One more problem, negative damping in tower pitch motion exists for floating offshore wind turbines [32].

Lackner and Rotea [33] proposed tuned mass-spring-damper (TMD) actuator for stabilization of floating offshore wind turbines. However, mass of TMD 20,00 kg is too high and TMD stroke (± 18 m for active control) is too long, which prevent the practical applications of TMD. Colwell and Basu [34] proposed a tuned liquid column damper (TLCD) but the size of TLCD 15.2m was also very long.

In this dissertation study, the problem of interest is to investigate on actuation schemes of high bandwidth and low-power consumption with light mass and small size.

1.5. Problem Statements

Based on the discussion in Sections 1.3 and 1.4, four research problems on wind turbine control are addressed in this dissertation study as follows.

- 1) *For Region 3 operation, design individual pitch controllers for wind turbine load reduction with the wake interaction included*
- 2) *For Region 3 operation, design model predictive controller for individual pitch control of wind turbine load reduction with wake meandering considered*
- 3) *For Region 2 operation, investigate a novel Nested-Loop Extremum Seeking Controller to maximize energy capture of a wind farm based on the wind farm control concept from Seem and Li [22]*
- 4) *Investigate the feasibility of an active flow control scheme for stabilization and load reduction of floating offshore wind turbine based on the floating offshore wind turbine control concept from Li [35]*

1.6. Organization of Thesis

In order to provide appropriate solutions to above four problems, the remainder of this thesis is organized as follows.

Chapter 2 provides detailed literature review about IPC, wake models, wake meandering modeling, MPC, wind farm control and control of floating offshore wind turbines. Periodic control was proposed for IPC of a wind turbine to deal with wake interaction. MMPC was proposed to deal with wake meandering of wind turbine. NLESC was proposed to maximize energy capture of a cascade of wind turbines. Vertical and horizontal vanes are proposed to stabilize floating wind turbines in side-to-side and fore-aft directions respectively.

Chapter 3 presents Jensen wake model, Larsen wake model and simplified wake meandering model which are used to generate wind profile at downstream wind turbines. The detailed procedure for implementation is also described.

Chapter 4 presents how to design a periodic controller for wind turbine loads reduction with the influence of wake interaction. Dynamics simulation of a 600kw 2-bladed wind turbine was conducted for verification of the proposed DAC controller.

Chapter 5 presents algorithms of multi-model predictive controller and detailed design for loads reduction of downstream wind turbine under wake meandering. Dynamics simulation of NREL 5MW wind turbine was conducted for MMPC verification.

Chapter 6 presents a nested-loop extremum seeking control for maximizing energy capture of a wind farm. A cascade of 3-turbine were simulated under steady and turbulent wind for verification of proposed NLESC.

Chapter 7 presents the concept of both vertical and horizontal vane. PI-based controllers were designed in order to increase damping and alleviate loads of floating offshore wind turbine in side-to-side and fore-aft directions respectively. Power assumption of vane actuators was also calculated.

Contributions of this dissertation research are presented in the Chapter 8, along with suggested future work.

Chapter 2. Literature Review

In this chapter, previous research in the subjects relevant to this dissertation research is reviewed. Understanding of the limitations of the previous research motivates the research work of this dissertation. First, the work on wind turbine individual pitch control is reviewed, as well as the periodic control because it is chosen in this study to deal with the situation of turbine control with wake interaction. As control of farm operated turbine is a major theme of this dissertation, the state-of-arts wake models and wake meandering models are reviewed. The objective is to set up the ground for choosing appropriate wake and wake meandering models for the simulation study of relevant control designs, which can provide acceptable accuracy of moderate to low computational complexity. Then, model predictive control (MPC) for wind energy application is reviewed. Finally reviewed are the floating offshore wind turbine control schemes and wind farm control strategies for maximizing total energy capture, respectively.

2.1. Review of Individual Pitch Control of Wind Turbine

For Region 3 of wind turbine operation, the expectation is to regulate the power output at the rated level while reducing the structural load [4]. As turbine size grows larger and larger, the wind turbine structure tends to be more flexible due to the adoption of lighter materials and increase in dimension. Load reduction is thus increasingly critical for the reliability and safety of turbine operation. Improvement in both blade design and control development can contribute to the alleviation of the fatigue loads for turbine, drive-train and tower structure. Advanced controller design is considered a relatively cost effective approach to load reduction, which can compensate for the system and environmental variations.

Load reduction control has been implemented and studied via generator torque control, blade pitch control and active flow control [36]. For pitch control based load reduction, both collective pitch control (CPC) and individual pitch control (IPC) have been studied. For CPC, the pitch angles of all turbine blades are adjusted simultaneously, and it is appropriate to control the variations slower than one rotor revolution. Due to its simplicity, CPC has been widely studied and implemented in wind industry [37]. A major drawback of CPC is the inability of dealing with asymmetric load for actual wind turbine. Asymmetric load distribution arises most often when the wind speed varies across the rotor disc due to factors such as vertical wind shear, change in wind direction, yaw error, and wake interaction [10]. Changes in blade characteristics such as surface icing and snow accumulation may also lead to asymmetric loading. Such drawback of CPC becomes a significant limitation nowadays as the turbine diameter becomes increasingly larger.

In comparison, IPC is achieved by controlling the pitching motion of each blade by the virtue of separate actuating mechanism [10], with a primary objective of controlling variations faster than the one rotor revolution. Therefore, IPC aims to deal with asymmetric loading. Typically the actuators for IPC are required to have higher bandwidth, for which high-stiffness electric motor actuators are more advantageous. Various sensing schemes have been investigated, such as strain gage at blade root [10], local blade inflow [12, 38] and LIDAR [39]. Bossanyi [10] designed LQG-based IPC controller to alleviate loads at blade roots by use of linear invariant models obtained through $d-q$ axis. Larsen *et al* [12] designed gain scheduling PI-based IPC for load reduction by use of the local inflow angle and relative velocity on each of the blades.

Olsen *et al.* [38] designed IPC based on inflow angle measurements. In particular, Hand *et al.* [39] designed an IPC through directly measuring the upwind incoming flow field by use of LIDAR system, which appears promising for improving the system performance for feed-forward and model-based feedback control strategies.

Different control design methods have been applied to the IPC development. The IPC design is in principle a multi-input-multi-output control design problem. For industrial applications, Bossanyi [37] designed a multi-loop decentralized PI controller where two separate SISO loops are designed for rotor tilt and yaw moments, respectively. Kanev *et al.* [40] proposed an IPC algorithm for rotor balance within pitch and pitch rate constraints handled by an anti-windup scheme. Jelavic *et al.* [41] proposed a load estimation based IPC scheme. Van Engelen [42] proposed a high harmonics control for wind turbines by use of IPC to reduce loads in high frequency. Specially, a series of field tests had been conducted at the National Renewable Energy Laboratory (NREL) by Bossanyi *et al.* [43-45].

However, the loop coupling is a significant issue, especially among the generator torque, the first tower fore-aft mode and the first tower side-to-side mode control loops. It revealed that loop interaction tends to destabilize the closed-loop system when the size of the wind turbine rotor increases beyond a certain extent [46]. To solve this problem, centralized control design based on the state-space turbine model has appeared a better solution. The state-space model based IPC schemes by use of inflow angle measurements was initially investigated by NREL from 2002 to 2004 [38] and different sensor choices, such as hot wire, laser Doppler velocimetry system *et al.*, are evaluated for inflow angle measurements. By far, the optimal and robust control methods have been widely applied

to the IPC design, such as the Linear Quadratic Gaussian (LQG) [10] and H_∞ controls [47]. Besides, Selvam *et al.* [11] proposed a LQG-based IPC algorithm with feedforward disturbance rejection by use of the estimation of the wind speed. More recently, IPC was combined with flap control for load reduction [48].

It is noteworthy that a particular stream of work on wind turbine control has been developed following Balas' Disturbance Accommodating Control (DAC) scheme [49]. Several control schemes have been studied following this framework, e.g. Stol [50], Hand [51], Wright [52], Wright and Fingersh [53], Wright and Stol [46]. Stol [50] applied Taylor theory to obtain linearized state-space model of wind turbines and applied DAC for periodic control of a wind turbine. Hand [51] built wind turbine models including vortex and applied DAC for wind disturbance cancellation along blades. Wright [52] applied DAC for IPC of a two-bladed turbine. Wright and Fingersh [53] implemented and tested DAC for IPC of the CART wind turbine in NREL. Wright and Stol [54] applied DAC for loads reduction at both blades and tower base of wind turbines by use of IPC. Besides, active yaw control of wind turbine was also achieved through periodic state-space IPC by Zhao *et al.* [55]. Recently, Hazim and Stol [56] applied LQR based periodic control to the IPC for floating offshore wind turbine.

To the author's best knowledge so far, the reported work on IPC design has included only the model of vertical wind shear regarding wind asymmetry. For wind farm operation, the inter-turbine wake interaction is also significant [16]. It is potentially beneficial for further reduction of dynamic load by including wind turbine wake interaction.

2.2. Wind Turbine Wake Model

For wind turbine operation, wake models have been used to predict wind profiles after an operating wind turbine [16]. In the past three decades, various wind turbine wake models have been studied for optimizing wind farm layout, as well as wind turbine load analysis. These wake models can be roughly categorized into three major classes: numerical models, kinematic models and field models. In the past three decades, various wind turbine wake models have been studied for optimizing wind farm layout, as well as wind turbine load analysis. These wake models can be roughly categorized into three major classes: numerical models, kinematic models and field models [57].

In numerical wake models, wind turbines are described as distributed roughness elements, e.g. Templin [58], Newman [59], Crafoord [60] and Moore [61]. Later, these models were further developed by Bossanyi *et al.* [62], Frandsen [63], and Emeis and Frandsen [64]. Although these models are seldom adopted in practice due to the complexity involved, they can describe the overall wind characteristic for large wind farms [57]. Kinematic wake models, also known as explicit wake models, are based on self-similar velocity deficit profiles [57]. The original work of kinematic models for wind turbine was developed by Lissaman [65], and later modified by Vermeulen *et al.* [66]. Jensen [17] and Katic *et al.* [67] built simple explicit formula to predict wind speed in the far wake of wind turbines by use of momentum balance, leading to the so-called Jensen Wake Model. However, linear wake expansion is assumed and initial wake expansion is neglected in the Jensen Wake Model. Frandsen [68] presented a nonlinear wake expansion. The kinematic model derived by Larsen *et al.* [69], known as Larsen Wake Model, was based on classic wake theory [70]. This model includes the thrust

coefficient, the undisturbed wind speed, the rotor diameter, the hub height of wind turbine and the ambient turbulence intensity. Field models provide the flow information everywhere in the wake through solving a simplified version of the Reynolds averaged Navier-Stokes flow equations. The original work on field models was developed by Sforza *et al.* [71], and much more work has followed, e.g. Taylor [72], Liu [73] and Ainslie [74]. A comprehensive coverage of wake models can be found in [57].

Recently Duckworth [75] validated and compared three different wake models by Ainslie [74], Katic [67] and Larsen [69], respectively. Renkema [76] also validated wake models by use of testing data in wind farms and wind tunnels. Renkema used second-order Larsen wake model and pointed out the typo of Larsen wake model in European Wind Turbine Standards II (EWTSII) [77].

One objective of this study is to integrate appropriate wake models into the process of plant derivation for controller design. The choice of wake models should be compatible with both the control-oriented purpose, i.e. capturing the major characteristics of wind turbine wakes while possessing acceptable simplicity. Numerical and field wake models are too complex for control design, while the complexity of kinematic wake models appears appropriate for control design. Therefore, the kinematic wake models are considered in this study. Furthermore, for wake interaction between turbines in wind farm, only the far-wake models are needed. Among the available kinematic far-wake models, the Jensen Wake Model and the Larsen Wake Model have been considered. The Jensen wake model and the Larsen wake model belong to static wake models. This kind of wake models is used to predict the average wind speed at downstream wind turbine and sufficient for wind power prediction and wind farm configuration optimization.

Turbulence intensity and ground effect are considered in the Larsen wake model. The wake diameter in Larsen wake model increases nonlinearly with the distance after upstream wind turbine. In this situation, the Larsen wake model is more accurate and chosen in this study.

However, a common limitation of the Jensen and Larsen wake models is that the wake profile is axisymmetric, while the actual wake profile for the turbines in wind farm operation is typically asymmetric, e.g. due to wind shear. When controllers of downstream wind turbines are designed for load reduction, more accurate asymmetric wake models are needed. For this purpose, an asymmetric wind profile by use of logarithmic vertical wind shear and Gaussian type wake deficit [78] is chosen to improve axisymmetric wake models.

In summary, the Larsen wake model and the asymmetric wake model by Van Leuven [78] are chosen to generate wind profile at downstream wind turbine and for the controller design in this study.

2.3. Wind Turbine Meandering Wake Modeling

The mechanism of wind turbine wake meandering phenomenon has been investigated intensively in the past couple of decades. The existing approaches for wake meandering modeling mainly include Engineering Models [18, 74, 79-83], Computational Fluid Dynamics (CFD) [84] and Spectral Method [85, 86]. The Engineering Models and CFD method are time-domain approaches.

The simplest approach to simulating wake meandering is the Engineering Models, which are built through analytical derivation or analysis of experimental and CFD results. For Engineering Models, Ainslie [74] considered that the large eddy is the cause of wake

meandering and he built the first wake meandering model with the assumption that the wake meandering effect on wake deficit is proportional to the standard deviation of turbulent wind directions. While Högström *et al.* [79] argued that Ainslie's approach is incorrect because the standard deviation of wind direction is caused by eddies of all sizes. Larsen *et al.* [80] considered that the instability of blade-tip vortex may be one of the reasons for wake meandering. They simulated wake meandering by use of the analytical wake model and obtained similar simulation results with the experiment data [81]. Espana [87] proposed that the typical atmospheric length scales may be the reason of wake meandering but did not suggest any approach to simulating wake meandering. Later, Larsen *et al.* [18] (see details on page 381) developed the Pseudo-Lagrangian approach, which assumes that the wake meandering is a process of releasing a series of wake from upstream turbines. Thomsen [82] developed the *Simplified Wake Meandering Model* (SWMM) which can predict the wake center position at the downstream wind turbine via the lateral speed at hub-height of the upstream wind turbine. Trujillo [83] developed the disk-particle model based on the Pseudo-Lagrangian approach.

The most accurate method is via CFD, which however may take very intensive computational effort to get the wind velocity field within the whole wind turbine wake. Recently, Jimenez *et al.* [84] simulated the wind turbine wake meandering by use of large-eddy simulation (LES), and the oscillating wind direction is used as boundary conditions.

For simulating turbulent wind, the most common method may be the spectral method described by Veers [85]. In this method, the spectral model and coherence functions are used to obtain filtered random variables. Then, filtered signals in spectral domain are

converted into real-time turbulent wind by use of Inverse Fast Fourier Transformation (IFFT). However, Veers [85] did not provide an appropriate coherence function along the transversal direction for simulating wake meandering. As comparison, Kristensen [88] provided detailed analysis of lateral coherence which is the critical component of wake meandering model. Recently, Nielsen [86] also presented an approach to simulating inhomogeneous, non-stationary and non-Gaussian turbulent wind including wake meandering, using the coherence model by Davenport [89].

This study aims to use an appropriate wake meandering model which is accurate enough for wake meandering simulation and yet simple enough for wind turbine controller design. Compared to the CFD and Spectral Method, the Engineering Models are simpler approaches that are more suitable for model based controller design. In Engineering Models, the relatively simpler SWMM [82], as a Pseudo Lagrangian approach, is considered both incorporating the transversal wake motion and control-design friendly.

However, SWMM only reflects how the wake is bodily transported along the transversal direction, but does not include how to generate the wind profile at the upstream wind turbine. When the transversal wind profile at the upstream wind turbine is already known, the wake movement at the downstream turbine can be predicted by SWMM. Often the transversal wind profile at the upstream wind turbine may not be known, and thus it has to be generated with CFD or the spectral method. Madsen et al. [90] applied CFD to generate the wind profile at the upstream wind turbine to simulate wake meandering, but with considerable complexity. In this study, the spectral method is

adopted by choosing the Kaimal spectral model [91] and Kristensen's coherence functions [88] for the transversal wind at upstream wind turbine.

2.4. Model Predictive Control for Wind Turbine

Model Predictive Control (MPC) predicts the future response of a plant by use of an explicit model [19] and real-time optimize control inputs with the condition of acceptable constraints of both control inputs and outputs. In MPC algorithms, a control sequence is obtained to optimize the future behavior of a plant at every interval, and then the first input in the optimal control sequence is implemented. MPC has been widely used in process industries, food processing, automotive, and aerospace [19]. Two characteristics differentiate MPC from conventional optimal control. One is that the cost function in MPC is chosen as a finite horizon but in conventional optimal control as an infinite horizon. The other is that optimization is calculated at every time instant to obtain current control action in MPC. However, control gain is pre-computed for conventional optimal control design. The most important advantage of MPC is its capability to deal with hard constraints of control action and states.

MPC has been a hot topic both within academic and industry during the past three decades. There have been several excellent textbooks [92-96] to emphasize different aspects of MPC. An efficient dual mode MPC algorithms and corresponding tuning techniques were well explained by Rossiter [92]. Generalized predictive control and implementation issues of MPC were emphasized by Camacho and Bordons [93]. H_2/H_∞ and LMI-based MPC were well summarized by Kwon *et al.* [94]. Proofs of stability and robustness, and distributed MPC were emphasized by Rawlings and Mayne [95]. The MPC theories for hybrid systems are well described by Borrelli *et al.* [96].

For different MPC algorithms, the foremost issue is stability. Stability was not automatically ensured in early versions of MPC, and not addressed by the proponents of MPC in process control [97]. However, if plants are stable, stability properties can be achieved by use of a larger horizon compared with the settling time of plants. Actually, from 1990s “concern for stability has been a major engine for generating different formulation of MPC” [97]. Bemporad *et al.* [98] summarized that stability of MPC can be ensured through different approaches including terminal constraint [99, 100], infinite output prediction horizon [101-103], invariant terminal set [104] and contraction constraint [105, 106], among others. Mayne *et al.* [97] showed that essential “ingredients” of different stable MPC schemes include a terminal constraint set, a terminal objective function, and a local controller.

For wind turbine control applications, Henriksen [107] first applied dual mode MPC [92] which ensures stability without high computational complexity. Santos [108] developed damage mitigating control where linear wind turbine models, nonlinear damage model and nonlinear MPC scheme were used. Kumar and Stol [109] applied the dual-mode MPC with state-feedback to IPC of wind turbine, and the control input was obtained through interpolation of those from neighboring controllers based on estimated velocity at the hub height. Laks *et al.* [110] designed dual-mode MPC with output feedback for IPC of wind turbines with preview measurements from the LIDAR sensor. Soltani *et al.* [111] designed their wind turbine controller with the LMI (linear matrix inequality) based Fast MPC in [112] without addressing stability issues. MPC was also applied to load reduction control via trailing-edge flaps on turbine blades [113], although,

the stability issue was not addressed. With consideration of stability and computational burden, dual mode MPC [92] is deemed a practical approach for wind turbine controls.

However, MPC switching for wind turbines has not been seriously dealt with. Only Kumar and Stol [114] applied simple interpolation between control inputs from different controllers for controller switching. More advanced switched MPC algorithms rather than simple interpolation-based MPC schemes could be used to ensure smooth switching between MPC controllers. In the initial period of dealing with MPC switching, the interpolation approach was used for switching [115-117]. During the past decade, several switched MPC algorithms were built with stability ensured. For example, softly switched MPC was developed by Wang [118] for application to water supply and distribution systems. A switched MPC algorithm [119] was also built and applied for steering vehicle control. The above switched MPC algorithms [118, 119] were developed for piecewise affine plants, but wind turbine systems impacted by wake meandering do not belong to piecewise affine plants. Nonlinear model predictive control was also proposed for smooth switching in [120]. However, tractable nonlinear dynamics for the wind turbine control under wake meandering is not readily available, which makes the theory difficult to apply. An LMI based multi-model predictive control (MMPC) algorithm [121] was applied to a chemical reactor application. In comparison, the MMPC proposed in [122] was developed without special requirements on state-space models for applications to high temperature fuel cells [122] and drug infusion control [123].

Besides stability, computational load is a big concern for industrial applications. One reason why MPC is popular in process control is that the dynamics in process control are usually very slow (typical time length is several days) which allows enough time to

obtain optimized control sequence at every sampling instant. In comparison, for plants with relatively faster dynamics and high dimensions, such as wind turbine control, computationally efficient optimization algorithms are needed to implement MPC. In addition, this study deal with wind turbine control by use of linearized plant models rather than nonlinear plant models, thus linear MPC methods are considered. In general, quadratic programming (QP) problems are solved in typical linear MPC algorithms. In this way, computational efficiency of QP is emphasized below.

The most common methods to solving QP problems include the active set method (ASM), the interior point method and the Multi Parametric Quadratic Programming (MPQP) [92]. The ASM is widely used because it provides a systematic way of choosing a potential active set and iterating through these potential sets to find the global optimum. Recently more efficient ASM solver was developed for Fast MPC [124]. The interior point method is becoming more popular than ASM within MPC because converge is guaranteed in this method and it is faster than ASM. However, the associated optimization for each iteration requires more computational effort. The toolbox of Fast MPC by use of the interior point method is also available in [112]. MPQP remains an active research area for MPC [125, 126]. In MPQP, online optimization computation is transferred to offline, and all possible control laws are defined offline. In this way, online QP optimization is converted into set membership tests. However, the potentially large number of alternative active sets is still an issue [92].

The fastest online MPC solver may be Fast MPC [112] where the interior point method is used for optimization. However, only open-loop MPC is considered in this tool. MPQP is a very efficient algorithm for MPC optimization [96]. Moreover, existing MPC

algorithms with MPQP are only useful for piecewise affine systems or equivalent systems [96]. The wind turbine dynamics subject to meandering wake does not belong to the piecewise affine system because there are no strict partitions for wind turbine states where wind turbine dynamics can be defined differently when wake meandering exists. For wake meandering phenomenon, the wake center position on downstream wind turbine determines wind turbine dynamics rather than wind turbine states. Based on the above considerations, an active set method [124] is chosen as a QP solver.

In summary, the practical MPC approach, the dual-mode MPC [92], was tested to deal with wake meandering at first. Then, with the consideration of both characteristic of wind turbine plants impacted by wake meandering and lower computational burden of MPC without LMI, the MMPC algorithm [122] was proposed to ensure smooth controllers switching. An active set optimization solver [127] was chosen for quadratic programming.

2.5. Dynamic Modeling and Control of Floating Offshore Wind

Turbine

Two main constraints for design of floating offshore wind turbine are stability and cost. One objective in this study is to invent a new type of floating wind turbine with stability and cost-effectiveness ensured from the aspect of control.

Driven by potential offshore wind market, during the past decade different floating platforms have appeared for floating offshore turbines including Barge Platform, Tension Leg Platform (TLP) [128, 129], Ballast Stabilized Spar Buoy Platform [27, 130], SWAY [131] and Dutch Tri-floater [132], as shown in Fig. 2.1 [133]. In particular, the spar-buoy platform had been used in the first installed floating wind turbine [27]. Butterfield *et al.*

[31] had provided a comprehensive investigation about advantages and disadvantages of three different floating platforms including Barge, TLP and Ballast (spar). They showed that TLP should be the most stable platform. Recently, Principle Power proposed a more practical floating platform, WindFloat [134]. The basic idea follows. The floating turbine with the WindFloat platform was designed to be assembled onshore and then hauled to offshore sites by ships in order to avoid high assembling cost on offshore sites due to undesirable weather and operation difficulties.

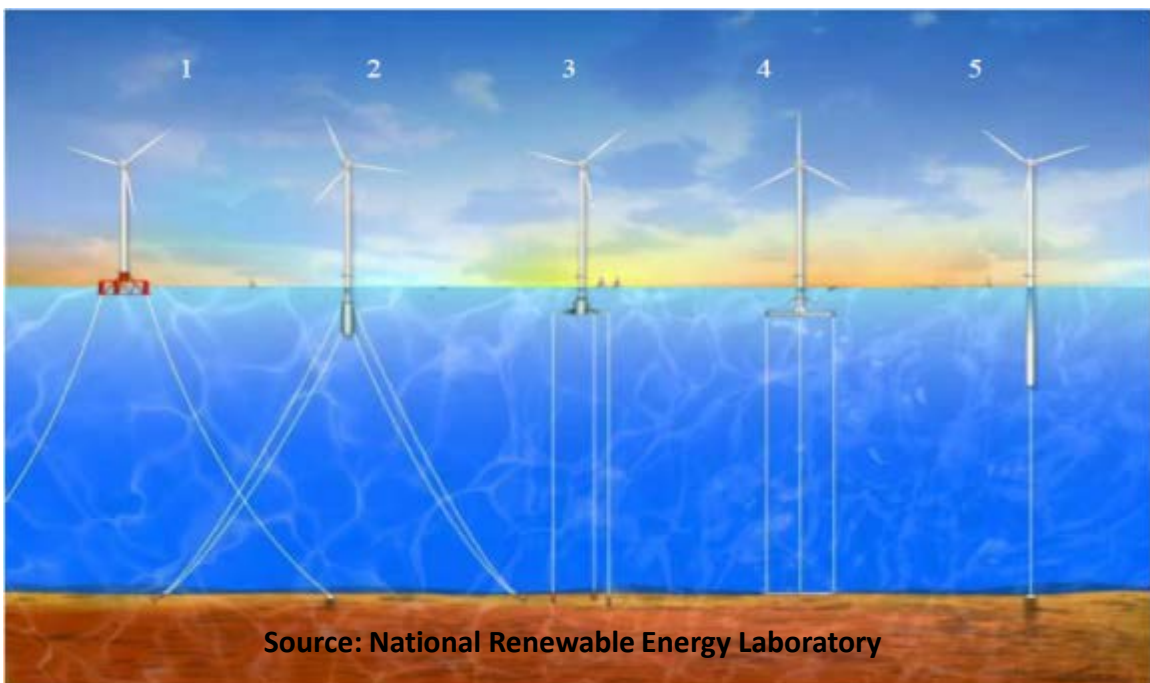


Fig. 2.1. Floating Deepwater Platform Concepts: 1) Semisubmersible Dutch Tri-Floater [132] 2) Spar buoy with two tiers of guy wires [130] 3) Three-arm mono-hull tension-leg platform (TLP) [128]; 4) Concrete TLP with gravity anchor [129]; 5) SWAY [131]

In order to investigate dynamic behavior of new floating wind turbine concepts, three main approaches may be used including numerical dynamic modeling, experimental model-scale testing and full scale prototype testing [135]. From the standing point of both

research and cost saving, numerical modeling of floating wind turbine are very useful in the initial period to verify different new concepts of floating wind turbines.

Withee [136] analyzed the coupled dynamics of a floating wind turbine supported on a floating platform with a tension leg spar buoy [137]. In Withee's thesis, both nonlinear wave loads on floating platforms and the aerodynamic loads on wind turbine rotor were predicted through a coupled way in a stochastic wind and wave environment. The module to calculate nonlinear wave loading on the floater was integrated into ADAMS [137] and aerodynamic forces on the floating wind turbine was obtained by use of AeroDyn module [138]. Finally, both normal operations and extreme wind and wave events were tested to evaluate the floating platform design. Based on Withee's work [136], Wayman [139] optimized parameters of the following platforms: TLP, Tri-Floater platforms, Spar platforms and Barge platforms. Wayman tested the effects of wind speed, water depth and viscous damping on these different platforms. Later, Jonkman [28] extended FAST [140] capability to simulate floating offshore wind turbine through adding the module of floating platform dynamics including TLP, Barge platforms and Spar buoy platforms. Recently, Matha [141] compared loads of TLP with that of other platforms for floating offshore wind turbines. A particular development, the software TimeFloat [142], was used to analyze the motion and calculate hydrodynamic forces of a special platform WindFloat [143], for which WAMIT [144] was used as a preprocessor to compute wave interaction effects. Then, TimeFloat was interfaced with FAST so as to simulate the coupled dynamics of floating wind turbines and passes data of platform motion back to TimeFloat [142].

Except for FAST [140], Nielsen *et al.* [145] extended HWAC2 [146] capability to simulate floating offshore wind turbine through a combination of SIMO/RIFLEX and HAWC2. SIMO [147] is a time domain software used to simulate multibody systems which allow nonlinear effects to be included in the wave-frequency range. RIFLEX [148] is a software of finite element method for static and dynamic analysis of slender marine structures.

The dynamics of a floating turbine is very different from that of a fixed turbine due to the floating foundation, which brings many engineering challenges. The top priority is how to ensure a floating wind turbine's stability, which is a very interesting and challenging one for the control field. A greater challenge for floating wind turbine is increasing damping in the roll motion which is the side-to-side translation in the plane of rotor rotation [31]. Larsen *et al.* [32] also claimed that negative damping of tower pitch motion exists for floating offshore wind turbines and designed PI-based pitch controllers to ensure the desired bandwidth by use of pole placement, which leads to a stable mode of floating offshore wind turbines. Although damping of tower motion was successfully increased, the variations in rotational speed and electrical power are increased 30%.

Jonkman investigated the capability to control floating offshore wind turbine by use of the PID controller and claimed that the barge-pitch-motion problem was not entirely resolved through detuning the gains of blade pitch-to-feather controller [149]. Later, Skaare *et al.* [150] designed an estimator based blade pitch control to increase the fatigue life of floating wind turbines.

In addition to PI controllers, modern control methods by use of state-space models were also investigated to increase tower damping of the floating wind turbine. For

example, based on Jonkman's work [28], Namik and Stol [151] designed periodic control based IPC for floating offshore wind turbines. Later, Namik and Stol [152] designed DAC based IPC for offshore floating turbines with both barge platform and TLP. Their results showed improvement in the regulation of power and rotor speed, as well as reduction in the tower side-to-side bending moment. However, the tower fore-aft bending moment is 24% higher than that of the onshore counterpart.

The aforementioned investigations have all utilize the control actuations available on a typical wind turbine. It is obvious that underactuation is a major issue for floating offshore wind turbine with the tower/platform stabilization issue present. Furthermore, tower/platform motion features large inertia, and thus control authority required is generally significant. Therefore, it is necessary to develop effective and feasible solutions of actuation schemes for stabilizing tower/platform motions.

Lackner and Rotea [33] proposed to use the tuned mass-spring-damper (TMD) actuator for floating turbine stabilization. This technique has been well received for building structure control in earthquake engineering. In this work, the TMD actuator is proposed to reside in the nacelle in order to reduce the fatigue load of the tower-base bending moment of offshore wind turbine with floating barge-type foundation. Fig. 2.2 shows that variation of tower fore-aft damage equivalent load (DEL) was plotted as a function of power consumption of active TMD control. It shows that, with about 20% loads reduction, the power consumption is about 200 kW, which is about 4% of total wind power production (5MW). Fig. 2.3 shows that the passive TMD system reduced the tower fore-aft fatigue load by approximately 10%, as compared to a baseline turbine, while the active TMD control achieved 30% reduction at the expense of about 8% turbine

power generated. However, the TMD mass designed is 20,000 kg in order to achieve the aforementioned performance. This is about 8% of the nacelle mass and 6% of the tower top mass [153], which requires a dramatic redesign of the nacelle, tower and buoyancy units. Besides the significant weight addition, another issue is TMD's large stroke. As shown in Fig. 2.4, the range of stroke for passive control is approximately ± 8 m, while for active control it is about ± 18 m. Because the length of the nacelle is already about 18 m for the wind turbine model considered [153], it is nearly impossible to install TMD in the nacelle in such a large stroke.

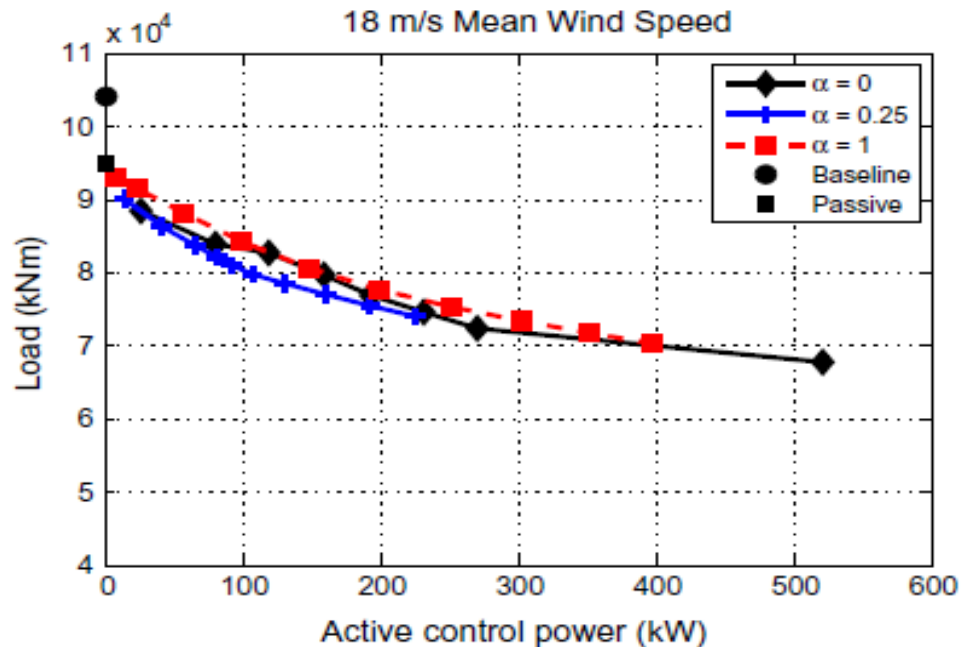


Fig. 2.2 Reduction of Tower Fore-aft Damage Equivalent Load by use of TMD [33]

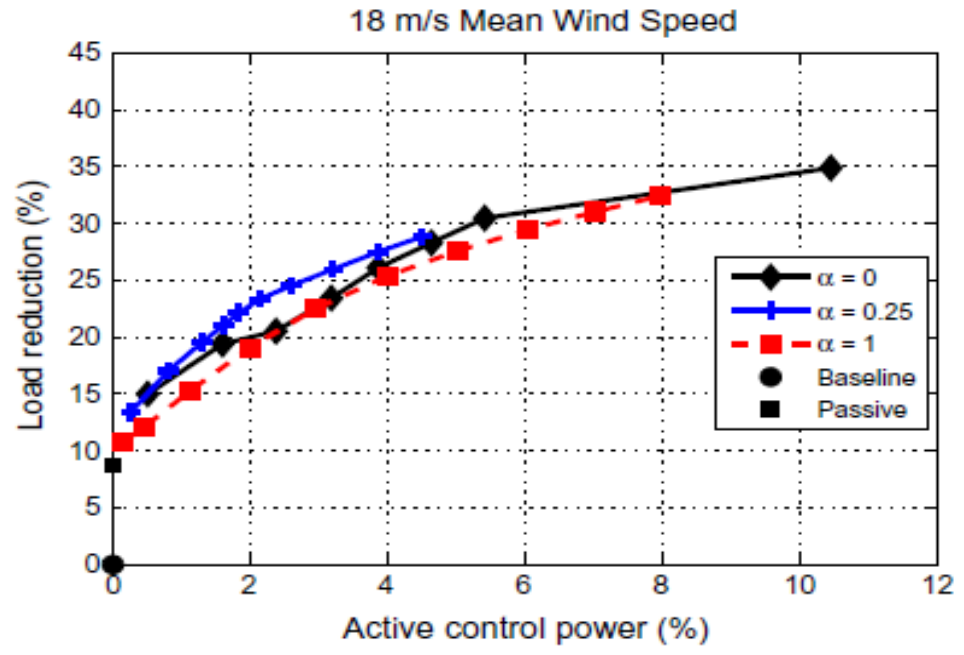


Fig. 2.3 Reduction Percent of Tower Fore-aft Damage Equivalent Load by use of TMD [33]

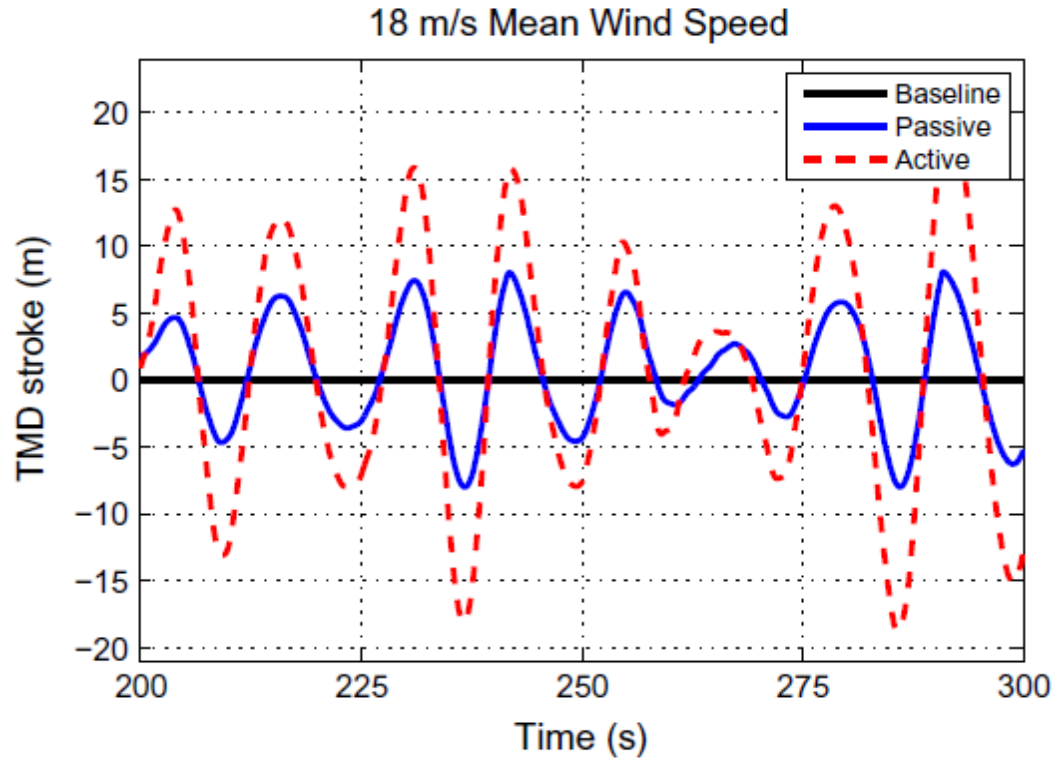


Fig. 2.4 Comparison of the TMD Stroke for the optimal passive control case and a selected active control case [33]

Except for mass-spring-damper actuation, Colwell and Basu [34] and Luo *et al.* [154] designed tuned liquid column damper (TLCD) to stabilize floating offshore wind turbines. Colwell and Basu [34] claimed loads reductions of up to 55% in the peak response by use of TLCD under wind and wave excitation but the TLCD was put at tower top with length of 15.2m, which is too long and brings big troubles for nacelle design. Luo *et al.* [154] put TLCD on a turbine's tower and designed corresponding H_2/H_∞ controllers. However, wind turbine models were too simple and wind and wave conditions were not clarified during simulation.

In this study, a new actuator was added [35] to reduce the floating turbine tower motion and improve stability of a floating turbine. However, tower-top weight should not be increased too much because higher tower-top weight means higher cost for a floating offshore wind turbine from the aspects of maintenance and installation. In this situation, a good choice may be an aerodynamic vane which can take full advantage of aerodynamic forces and its relative weight is lower compared with the TLCD actuator. Based on the comments by Butterfield *et al.*, "A greater challenge for floating wind turbine is increasing damping in roll motions" [31], a vertical vane was used to increase damping of tower motion in side-side direction. A horizontal vane was also used to avoid negative damping and increase damping of floating turbines in the fore-aft direction.

2.6. Wind Farm Control

Wind farm control presents control and optimization challenges in order to maximize the overall power yield or to satisfy the farm level power demand while limiting or minimizing the structural loading. Although the control strategies for stand-alone turbines have been widely investigated, e.g. maximizing energy capture [8, 9] and load reduction

[10, 155, 156], farm-level wind turbine controls have not been mature enough for industrial applications. Due to wake interactions between turbines, optimization of energy capture or load reduction for all the turbines in a wind farm requires globally optimized operation of individual turbines, i.e. this cannot be achieved by merely optimizing the operation of individual turbines.

In 1993, Spruce [157] had systematically conducted simulation and control of wind farms with considering factors including wake interaction, wake transportation delay and fatigue damage. Due to model reliability issues for complex topology of different wind farms, Spruce [157] proposed simple ESC algorithm rather than model-based control method. In his PhD thesis, different cost functions were defined for individual, non-interacting and interacting turbines in a wind farm in order to maximize financial income and minimize the turbines' fatigue damage. Spruce [157] also divided possible wind farm control algorithms into two different categories: hierarchical control and "multivariable control". Hierarchical wind farm control includes plant level control and supervisory level control. However, all turbine inputs are commanded from a central computer in "multivariable control", which should be the same to the concept of centralized control.

Recently various control strategies have been investigated for wind farm controls. Spudic [23] illustrated the idea of hierarchical wind farm control which is based on the mixed-integer quadratic programming (MIQP) for load and power optimization by use of constrained optimal control approach [158] (one type of model predictive control) and the wind farm simulation platform SimWindFarm [159]. In Spudic's work, optimal power reference in a wind farm was obtained for wind farm control and then generator torque

and pitch angle of wind turbines were obtained by defaulted controllers when power references were given.

Soleimanzadeh and Wisniewski [24] conducted wind farm optimization using a wind-flow based farm model via a 2-D finite volume method. Under the rated wind speed, the rotor speed at every turbine is dynamically optimized to maximize the total wind energy capture and the sum of damping factors of wind turbine in both fore-aft and side-to-side directions based on the wind profiles predicted by the wind flow model. Accordingly, above the rated wind speed, the pitch angle and power reference at every turbine are dynamically optimized to meet power demand of a farm while maximizing the sum of the aforementioned damping factors. Soleimanzadeh and Wisniewski [160] improved previous work and designed a centralized controller by use of model predictive controller toolbox and structural loads in low frequency were specially reduced.

Madjidian and Rantzer [161] proposed a stationary turbine interaction model to calculate the wind speed at downstream turbines by use of wind speed, turbulence intensity and thrust coefficients at upstream turbines. It showed that the thrust of downstream turbines can be reduced by decreasing the power production at upstream turbines while maintaining the power of downstream turbines at the same level.

Brand [162] built a quasi-steady wind farm flow model [163], which relates external conditions including wind speed, wind direction, turbulence intensity to states including rotor speed, pitch angle and outputs including power production and mechanical loading of all turbines. Brand [162] also proposed the inverse mode of the quasi-steady wind farm flow model, which means that power is input and all other parameters including

external conditions and mechanical loads of turbines are output. Then the inverse mode is used to calculate the distribution of power references over turbines in a wind farm.

Johnson and Thomas [16] proposed a hybrid approach for maximizing the wind farm energy capture by combining the Iterative Learning Control (ILC) and Iterative Feedback Tuning (IFT). Both pitch angle and tip speed ratio (TSR) are included as control inputs, and the simulation model is developed based on the Park wake model [17] for an array of three turbines.

In 2009, Knudsen *et al* [164] described the basic idea, approach and preliminary results for distributed control of large-scale offshore wind farms in the EU-FP7 project with the objective of wind turbine fatigue loads reduction.

Kristalny and Madjidian [165] proposed a distributed feedforward control scheme for the possibility of cooperation between turbines and the problem was formulated as a decentralized model matching optimization.

Madjidian *et al.* [166] proposed a dynamically distributed power coordination scheme for fatigue load reduction in wind farms when power demand is below the actual power production capacity of a wind farm. The control law only required each turbine to communicate with their neighboring turbines. However, wake model and wind propagation were not considered in this study. Madjidian *et al* [167] also extended their work for reducing structural loads on the turbine tower and the low speed shaft. Recently, Biegel *et al.* [168] applied a similar strategy but designed a distributed low-complexity controller for wind power plant in derated operation for reduction of fatigue loads.

Zhao *et al.* [169] proposed intelligent agent control for fatigue distribution optimization of offshore wind farms and the power reference was distributed for

balancing structure fatigue loads of individual turbines. In this paper, a wind farm was modeled as a multi-intelligent agent network.

Horvat *et al.* [170] showed that power production of a wind farm could be increased through optimizing rotor speed of individual wind turbines when wind speed is below rated wind speed. Horvat *et al.* [170] also showed that the loads at different turbines could be equalized through optimizing power production references for different turbines when wind speed is higher than rated wind speed.

Marden *et al.* [25] suggested a model-free control strategy by use of game theory and cooperative control to optimize the induction factors to maximize power production of the wind farm. The Park wake model was used for wind farm simulation. For an array of three turbines, the resultant axial induction factor for the first upstream turbine was 0.232, instead of the analytical result of $1/7$ in [21].

Bitar and Seiler [171] derived optimal induction factor and total power limit for an array of turbines by use of dynamic programming. They also pointed out that percentage of power improvement on greed policy is 8.33% by use of optimal induction factor. However, in wind field the improvement percentage could be higher than 8.33% because in wind field the power production maximum for an array of turbines is never reached for the benchmark of greed policy with inductor factor $1/3$ for all turbines.

Park *et al.* [172] optimized both yaw offset angle and induction factors in order to maximize wind farm power by use of static game theory. The steepest descent method was used in this study to calculate optimal yaw offset angles and the induction factors.

Guo *et al.* [173] designed a wind farm controller including an outer loop by use of model predictive control and an inner loop by use of adaptive control in order to accurately and smoothly track desired power output reference from a power grid operator.

Most existing studies on wind farm energy capture are model based, except for [16] and [25]. As the existing wind turbine wake model cannot accurately describe the actual wake behavior, a (nearly) model-free approach is still considered more appropriate for wind farm energy capture optimization. Furthermore, since control actuators of wind turbines only include blade pitch angle and generator torque, it is difficult to implement control strategies in wind sites when control input blade tip speed ratio [16], rotor speed [24] or induction factor [25] is used such that in this study generator torque control was proposed to maximize energy capture of wind farm. In this thesis, a nest-looped extremum seeking control (NLESC) scheme was presented for maximizing energy capture of the wind farm [22].

Chapter 3. Modeling of Wind Turbine Wake and Wake

Meandering

As mentioned in Chapter 2, wake and wake meandering modeling is critical for controls of farm operated wind turbines. In this dissertation study, two wake models have been involved, the Jensen wake model and the Larsen wake model. In this chapter, these two wake models are described first. Then the logarithmic vertical wind shear model and Gaussian wake deficit distribution are used to compose the wake profile. Finally a wake meandering model is presented.

3.1. Jensen Wake Model

The Jensen Wake Model [17] is used to predict the mean wind speed at some distance behind wind turbines. An upstream and a downstream wind turbine are shown in Fig. 3.1. The incoming wind speed is V_∞ , D_r is the diameter of both the upstream and downstream turbines, and L_{hub} is the distance between the hub axes of upstream and downstream wind turbines. V_w is the mean wind speed of the downstream turbine rotor which is located at the distance x_w along the incoming wind direction from the upstream one. The wake diameter is assumed to grow linearly from D_r at the upstream turbine to D_w at the downstream turbine, i.e.

$$D_w = D_r + 2kx_w \quad (3.1)$$

where k is the wake entrainment constant. The mean wind speed at the two turbines are related via

$$1 - \frac{V_w}{V_\infty} = \frac{1 - \sqrt{1 - C_t}}{(1 + 2kx_w / D_r)^2} \quad (3.2)$$

where C_t is the thrust coefficient of the upstream turbine.

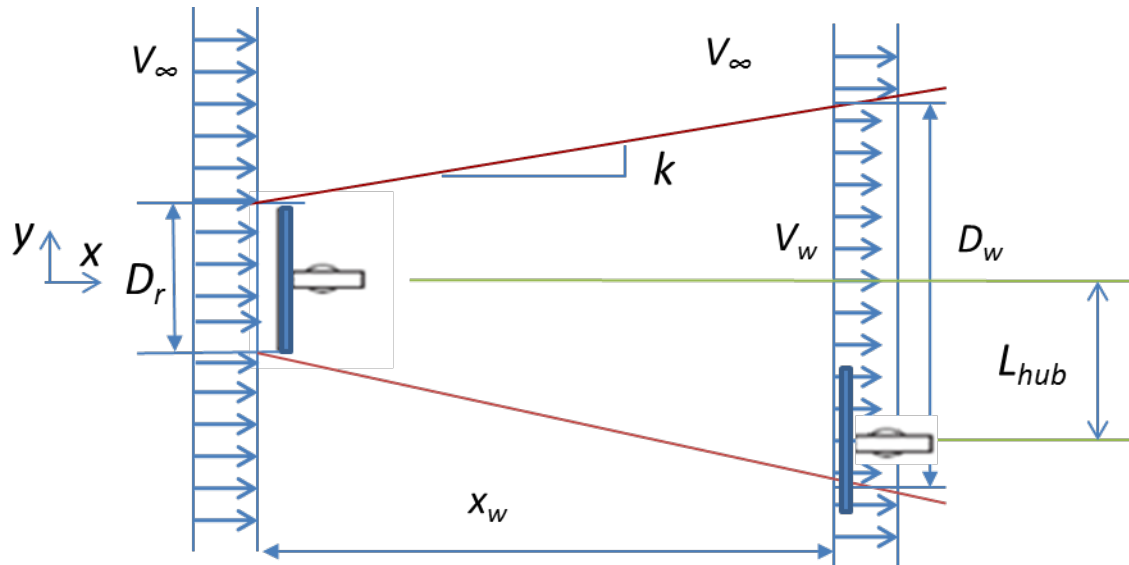


Fig. 3.1: Illustration of Jensen wake model

3.2. Larsen Wake Model

The Larsen Model [69] considers axisymmetric wake profile with nonlinear growth of the wake diameter along the distance after the upstream wind turbine. The Larsen wake model is illustrated in Fig. 3.2, which is a scenario similar to that in Fig. 3.1. In this illustration, both Cartesian and axisymmetric cylindrical coordinates are used for the ease of description. The x coordinate is along the prevailing wind direction, with the origin located at distance x_1 before the upstream turbine. The z coordinate is that perpendicular to the ground surface, with the origin located on the ground. The y coordinate is the other horizontal direction perpendicular to the x coordinate (i.e. the “lateral” direction), with the origin located at the hub axis of the upstream turbine. The origin of axisymmetric

cylindrical coordinate is located at $(0, 0, H)$, where H is the hub height of wind turbines. Along the x direction, the upstream and downstream turbines are located at x_1 and x_2 , respectively, where the difference of x_2 and x_1 is x_w . The definitions of V_∞ , L_{hub} and D_r are same as those in the Jensen model.

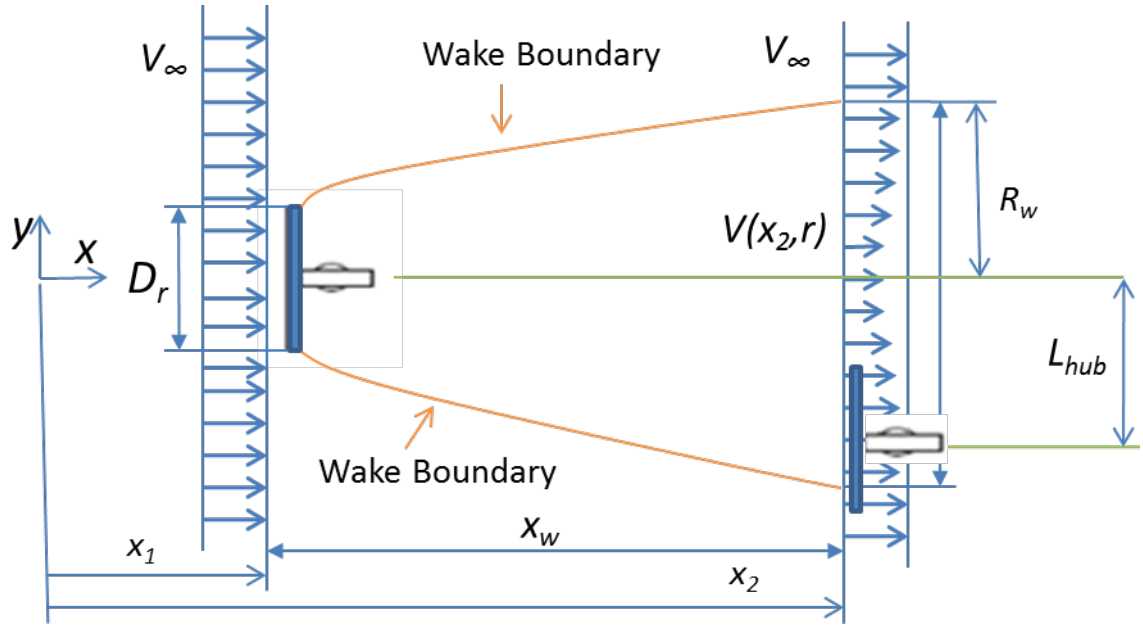


Fig. 3.2: Illustration of Larsen wake model

The Larsen wake model is recommended by the EWTS II (European Wind Turbine Standards) [77], which has been developed based on the Prandtl turbulent boundary layer equations. Based on the assumptions include that the flow is incompressible and stationary, wind shear is neglected, and the velocity profile is self-similar, the first-order solution of Prandtl turbulent boundary layer equation can be obtained as [77]

$$\begin{aligned} \Delta V(x_w, r) &= V(x_2, r) - V_\infty \\ &= -\frac{V_\infty}{9} \left[C_t A_r (x_w + x_0)^{-2} \right]^{\frac{1}{3}} \left[r^{\frac{3}{2}} (3c_1^2) C_t A_r (x_w + x_0)^{-\frac{1}{2}} - \left(\frac{35}{2\pi} \right)^{\frac{3}{10}} (3c_1^2)^{-\frac{1}{5}} \right]^2 \end{aligned} \quad (3.3)$$

where $\Delta V(x_w, r)$ is the velocity deficit at distance x_w from the upstream rotor plane and radius r from the wake centerline, A_r is the rotor-disc area, C_t is the thrust coefficient, and the wake radius R_w is

$$R_w(x_w) = \left(\frac{35}{2\pi} \right)^{\frac{1}{5}} (3c_1^2)^{\frac{1}{5}} [C_t A_r (x_w + x_0)]^{\frac{1}{3}} \quad (3.4)$$

The parameters c_1 and x_0 are given by

$$c_1 = \left(\frac{D_{eff}}{2} \right)^{\frac{5}{2}} \left(\frac{105}{2\pi} \right)^{\frac{1}{2}} (C_t A_r x_0)^{-\frac{5}{6}} \quad (3.5)$$

$$x_0 = \frac{9.5 D_r}{\left(\frac{2R_{9.5}}{D_{eff}} \right)^3 - 1} \quad (3.6)$$

where D_r is the rotor diameter. In Eq. (3.6), the effective rotor diameter D_{eff} is given by

$$D_{eff} = D_r \sqrt{\frac{1 + \sqrt{1 - C_t}}{2\sqrt{1 - C_t}}} \quad (3.7a)$$

where C_t is again the thrust coefficient of the upstream turbine, and $R_{9.5}$, the wake radius at a distance of 9.5 times of the rotor diameter downstream of the turbine, is given by

$$R_{9.5} = 0.5 [R_{nb} + \min(H, R_{nb})] \quad (3.7b)$$

where H is the hub height of the upstream wind turbine and R_{nb} is given by

$$R_{nb} = \max[1.08D_r, 1.08D_r + 21.7D_r(I_a - 0.05)] \quad (3.7c)$$

where I_a is the ambient turbulence intensity. Although the first-order Larsen wake model is implemented, the second-order solution could be found in [76]. Besides, at rotor center, the first-order solution is equivalent to the second-order solution.

The Larsen Model includes the radial variation of the wind field across the rotor disc, which is important for load reduction control. Also, the turbulence intensity and ground effect are included in the Larsen Model. Therefore, the Larsen Model has been chosen in this study over the Jensen Model for the farm-operated wind turbine control. A common limitation of the Jensen and Larsen wake models is that the wake profile is axisymmetric, while the actual wake profile for the turbines in wind farm operation is typically asymmetric, mainly due to wind shear. To amend for this deficiency, in this study, the Larsen Wake Model in Eq. (3.3) is used only to calculate the hub-height wind speed obtained by setting r to zero, while the wind-shear effect and the cross profile of the wake are included by additional modification described in the following subsections, which can generate asymmetric wind profile after calculation of hub-height wind speed.

3.3. Wind Shear

In the atmospheric boundary layer, the wind speed increases with height due to the viscosity of air flow, which is known as the wind shear. Among the wind shear models developed, the most often considered is the logarithmic vertical wind shear model [174]

$$V(z) = V_{hub} \frac{\ln(z / z_0)}{\ln(H / z_0)} \quad (3.8)$$

where z is the vertical coordinate with the origin located on the ground surface, H is the hub height, V_{hub} is the hub-height wind speed, $V(z)$ is the horizontal wind speed along the z direction, and z_0 is the surface roughness which is chosen to be 0.3 (corresponding to the case of open farm land with few trees and buildings in [174]).

3.4. Wind Profile of Downstream Turbine Rotor Disc with Wake

Interaction included

For actual wind farm operation, the downstream wind turbine may reside fully or partially in the wake of the associated upstream turbines. The case of partial wake is more complicated and bears more impact on the load reduction control of the downstream turbine. Fig. 3.3 illustrates such a case of wake interaction at the downstream wind turbine. The smaller disk refers to the rotor of the downstream turbine, while the larger disk refers to the wake of the upstream turbine developed at the downwind rotor plane.

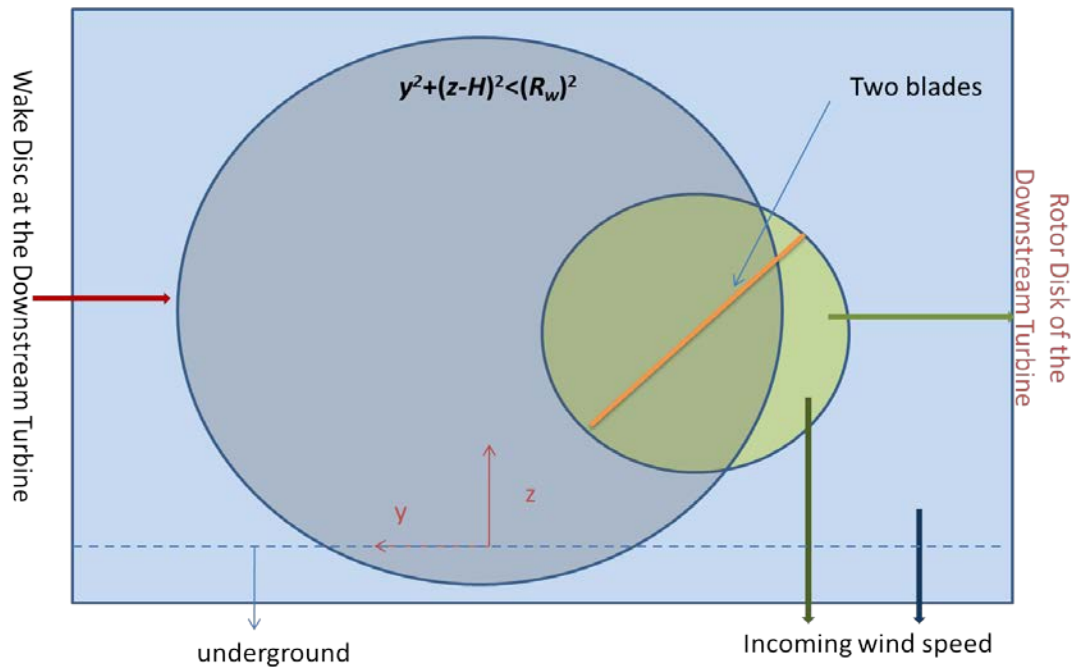


Fig. 3.3: Illustration of Wake Interaction at the Downstream Turbine

In the rotor disk at the downstream turbine, the wind profile consists of the incoming wind region and the wake region. In Fig. 3.3, the larger disk refers to the wake region while the remaining region belongs to incoming wind region. The wind profile in the incoming wind region is determined via Eq. (3.8), while the hub-height wind speed in the

wake region is calculated with the Larsen wake model in Eq. (3.3). However, neither the Jensen nor the Larsen model includes the vertical asymmetry due to the vertical shear. Therefore, such models are enhanced in this study to address vertical shear in order to generate more realistic wind profile in the cross section of the wake.

Existing wind-turbine wake studies [74, 175] have shown that the velocity deficit profile for axisymmetric wakes can be described by a Gaussian-type function in Cartesian type of coordinates. In particular, based on the characteristic of Gaussian velocity deficit distribution, van Leuven [78] proposed the so-called corrected 2-D Gaussian function for the wind deficit in the cross section of the wake, i.e.

$$\Delta V(y, z) = \Delta V_{hub} e^{-\left[\frac{y}{R_y}\right]^2} e^{-\left[\frac{z-H}{R_z}\right]^2} \frac{\ln(z/z_0)}{\ln(H/z_0)} \quad (3.9)$$

where ΔV_{hub} is the hub-height velocity deficit, R_y and R_z are the wake radii in the y and z directions, respectively. Equation (3.9) indicates an elliptical bell shape for the wake profile. In this dissertation study, the wake shape is still assumed to be circular, similar to the Jensen and Larsen wake model.

Then the wake profile at the downstream turbine is given by

$$V(x_2, y, z) = \left[V_\infty - (V_{wcenter} - V_\infty) e^{-\left(\frac{y}{R_w}\right)^2} e^{-\left(\frac{z-H}{R_w}\right)^2} \right] \frac{\ln(z/z_0)}{\ln(H/z_0)} \quad (3.10)$$

where $V_{wcenter} = V(x_2, 0, H)$ is the wind speed at the wake center, following the notations in Fig. 3.2. As shown in Fig. 3.3, the wind profile in the incoming wind region is calculated with Eq. (3.8) and that in the wake region with Eq. (3.10). In Eq. (3.10), the hub-height velocity deficit $\Delta V_{hub} = V_{wcenter} - V_\infty$ is calculated with the Larsen Model (3.3).

3.5. Wake Meandering

To facilitate the modeling and control design for more realistic operation of farm turbines, the wake meandering phenomenon is modeled. Wake meandering is illustrated with the schematic in Fig. 3.4. The coordinates are defined the same as in Fig. 3.1. Again, the upstream and downstream turbines are located at x_1 and x_2 , respectively, with spacing $x_w = x_2 - x_1$. The incoming wind speed is V_∞ , and D_w is the wake diameter at the downstream turbine. The wind profile at the downstream wind turbine can be predicted based on the incoming wind speed, ambient turbulent intensity, size of wind turbine and relative position of wind turbines by use of Larsen wake model. The major distinction of wake meandering modeling is that the wake center moves in transversal direction. The wind profile at the downstream wind turbine is composed in the following fashion. First, the transversal speed of the wake at the upstream wind turbine is calculated, then the wake center at the downstream wind turbine is predicted, finally the wind profile is composed using the Jensen or Larsen wake model with the wake-center position.

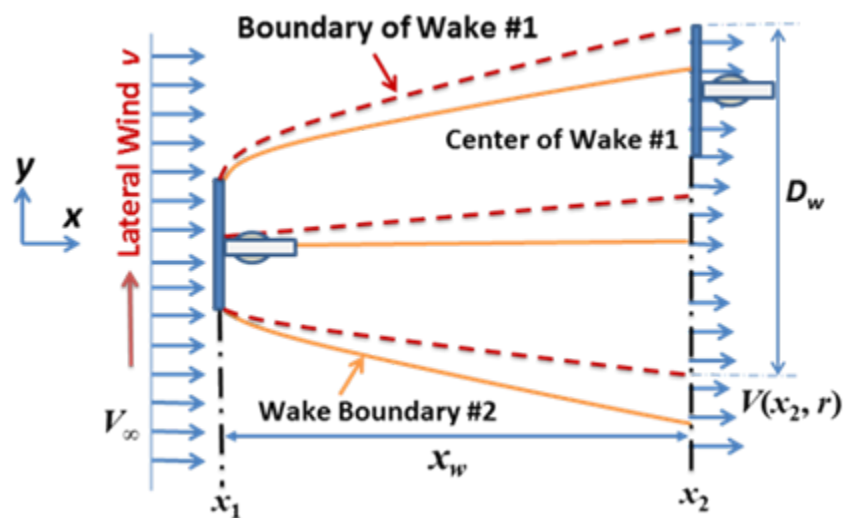


Fig. 3.4: Illustration for Wind Turbine Wake Meandering

The procedure for wake meandering simulation is proposed as follows. First, the spectral method is used to generate wind profile including wake meandering characteristic at the upstream turbine by choosing appropriate spectral model and coherence functions, as shown in Fig. 3.5. Second, SWMM (Simplified Wake Meandering Model) [82] is used to predict the wake motion at the downstream turbine based on the wind profile at the upstream turbine.

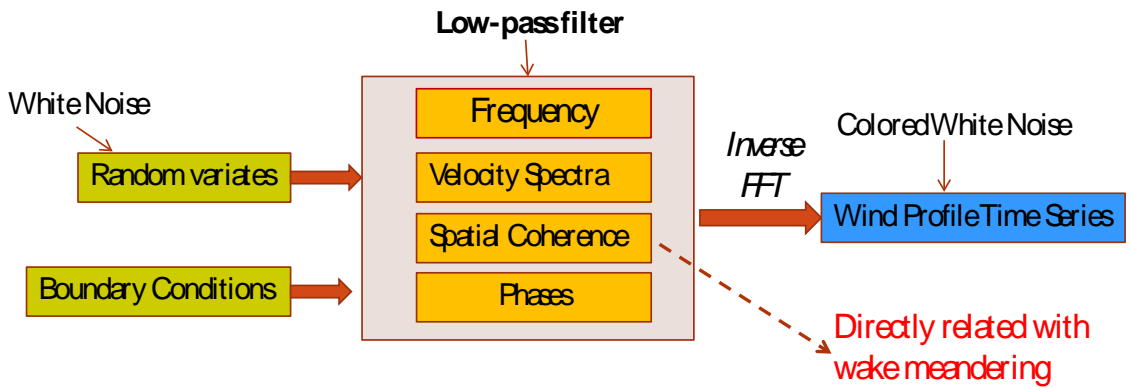


Fig. 3.5: Spectral Method to Generate Turbulent Wind [176]

According to the IEC 61400-1 standard [91], the Kaimal spectrum is given as

$$S_k(f) = \sigma_k^2 \frac{4L_k/U}{(1 + 6fL_k/U)^{\frac{5}{3}}} \quad (3.11)$$

where L_k is velocity component integral scale parameter, f is the frequency in Hz, k ($= 1, 2$ and 3) denotes the velocity component, U is the mean wind speed at hub height H , and σ_k is the variance determined by the turbulence intensity.

According to the IEC spectral models, the coherence functions of the three wind velocity components are different. For the v_1 component (i.e. the x direction in Fig. 3.4), the coherence function between points i and j on the grid is defined as [91]

$$Coh_{i,j} = \exp\left[-a\sqrt{(fl/v_1)^2 + (0.12l/L_c)^2}\right] \quad (3.12a)$$

where l is the distance between the two points, a is the coherence decrement, and L_c is a coherence scale parameter. According to [91], $a = 12$ and $L_c = 5.67 \cdot \min(60, H)$ m. The coherence function for the v_2 component (i.e. the y direction in Fig. 3.4) is defined as

$$Coh_{i,j} = \exp(-cfl/v_2) \quad (3.12b)$$

where $c = 4.2$ [88]. The coherence function for the v_3 component (i.e. the z direction in Fig. 3.4) is defined as

$$Coh_{i,j} = \begin{cases} 1 & i = j \\ 0 & i \neq j \end{cases} \quad (3.12c)$$

where w is the velocity in the vertical direction.

Based on Thomsen's theory [82], the low-pass filtered wind speed in the transversal direction at the hub height is approximated as the spatially averaged cross-component wind speed, which is deemed as the wake-center moving speed. Under Taylor's hypothesis, the wake-center moving speed for every wake "release" does not change when the wake transports from upstream wind turbine to downstream wind turbine. Thus, the wake-center position at the downstream wind turbine is determined by

$$\Delta_y = T_d \cdot V_{filt}(t) \quad (3.13a)$$

$$\Delta_z = T_d \cdot W_{filt}(t) \quad (3.13b)$$

where V_{filt} and W_{filt} are the filtered velocity along the transversal and vertical direction, respectively, at the hub center of the upstream wind turbine. The "Wind Profile Time Series" in Fig. 3.5 are used as input to the low-pass filter. T_d is the downstream traveling

time, equal to downwind distance divided by mean wind speed at the upstream wind turbine. The filtering is accomplished with the following first-order low-pass filter

$$F_{WM}(s) = 1 / (T_f s + 1) \quad (3.14)$$

where time constant T_f corresponds to a characteristic size of the rotor (in the range of radius to diameter) relative to the mean wind speed at the upstream wind turbine.

For field wind, due to the turbulent nature of wind, the hub-center wind speed components along transversal and vertical direction are generally not equal to the wake-center moving speed. The characteristic wind speed for wake meandering along the transversal and the vertical directions via the mass-density analogy [18] may be a better choice than the hub-center wind speed, especially when LIDAR measurement [177] is available. The characteristic wind speed across the rotor plane along transversal and vertical direction, i.e. V_c and W_c , can be calculated by

$$V_c = \frac{1}{A} \iint_A v dy dz \quad (3.15a)$$

$$W_c = \frac{1}{A} \iint_A w dy dz \quad (3.15b)$$

where A is the rotor disc area.

For simplicity, only the wake motion in the transversal direction is considered in this study. With such simplification, the procedure for calculating the trajectory of the wake center is summarized as follows.

- 1) Equations (3.11) and (3.12) are used to generate the turbulent wind speed at every point across the rotor plane.
- 2) Based on turbulent wind speed obtained in the first step, Eq. (3.14) is used to calculate the filtered transversal velocity at every point across rotor plane.

- 3) Use Eq. (3.15a) to calculate the wake-center moving speed based on the filtered wind speed at every point across rotor plane.
- 4) Equation (3.13a) is used to predict the wake center position based on wake center moving speed.

When the wake center at downstream wind turbine is known by use of simplified wake meandering model, the wind profile at downstream wind turbine is composed by use of the method in Section 4.

3.6. Algorithms for Wake Interaction and Wake Meandering in TurbSim

TurbSim [176] , a stochastic, full-field, turbulent-wind simulator developed by NREL, is used to generate wind profile including wake interaction and wake meandering.

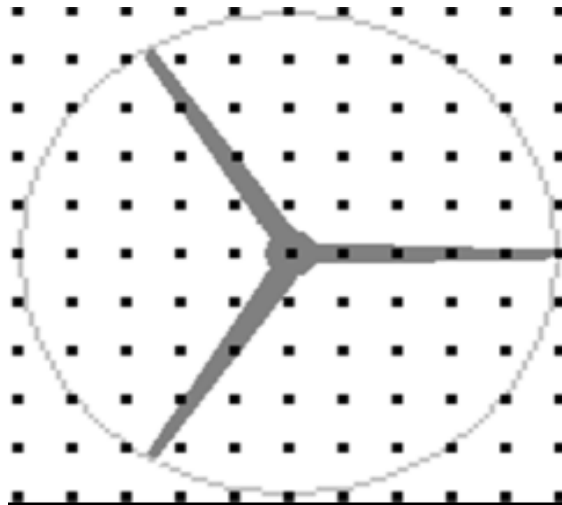


Fig. 3.6 Grid Points for Wind Profile in TurbSim [176]

Based on a statistical modeling scheme, TurbSim provides numerical simulation modeling of 3-D wind speed time series at points in Fig. 3.6. The output of TurbSim can then be used as input into AeroDyn or other relevant codes like FAST (Fatigue,

Aerodynamics, Structures, and Turbulence) [140]. “AeroDyn uses Taylor’s frozen turbulence hypothesis to obtain the local wind speeds, interpolating the TurbSim-generated fields in both time and space” [176].

In this dissertation study, the TurbSim is modified to generate wind speed at points in the 2-D vertical rectangular grids in Fig. 3.6. The wind speeds at these points include wake interaction and wake meandering characteristics described in the previous sections. The coordinates adopted in TurbSim is shown in Fig. 3.7.

The procedure for generating wind profiles including wake interaction consist of the following steps.

- 1) Calculate wake radius D_w by using Eq. (3.1) or (3.4);
- 2) For every point (x, y) in Fig. 3.6, determine if it belongs to the wake region or the incoming wind region. If $(x - L_{hub})^2 + (y - H)^2 < (D_w / 2)^2$, it belongs to the wake region, otherwise to the incoming region;
- 3) For every point in the rotor plane: if it belongs to the wake region, the wind speed at x direction is calculated by Eq. (3.10); otherwise by Eq. (3.8);

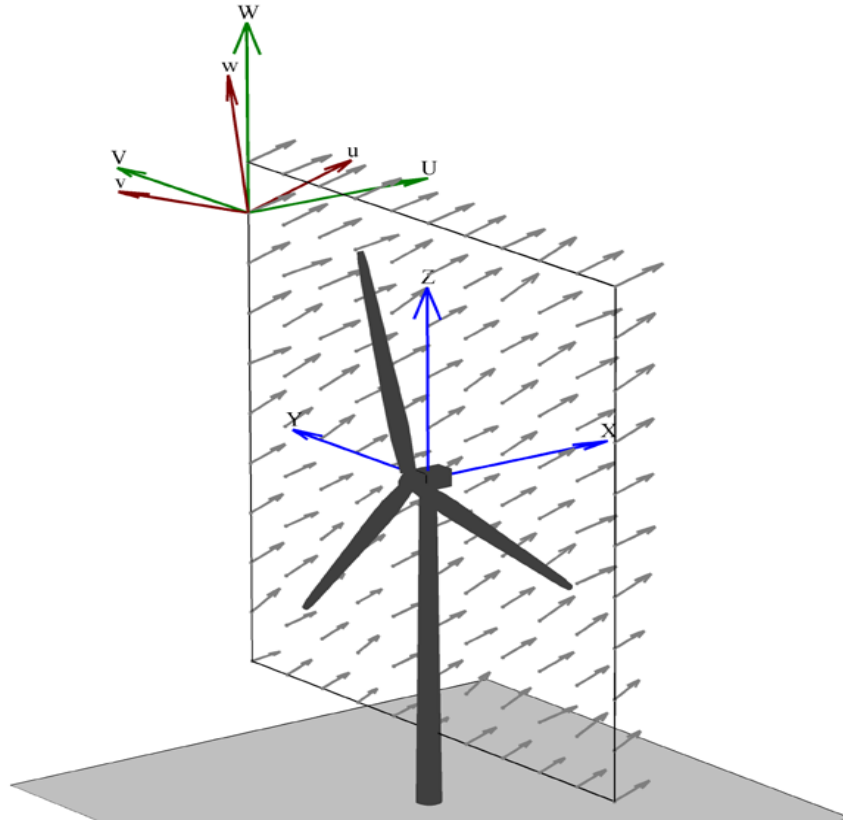


Fig. 3.7: Coordinates in TurbSim [176]

The procedures for generating the wind profiles including wake interaction and wake meandering consist of the following steps.

- 1) Set time step ΔT , the incoming wind speed V_∞ , the initial moving speed for the wake center, simulation time T_{max} ;
- 2) Calculate wake radius D_w by use Eq. (3.1) or (3.4);
- 3) The turbulent wind speed along y direction at every point with time series are generated by TurbSim's original subroutines using the special coherence function (3.12b);
- 4) Set $T_f = D_r/V_\infty$ [82], and $a = \Delta T/(T_f + \Delta T)$;

- 5) At time t , the turbulent speed along y direction at all grid points across the rotor plane were added together, and then the sum is divided by the total number of grid points so as to obtain the average of turbulent speed part $V_c(t)$, following Eq. (3.15a);
- 6) For $t \geq \Delta T$, $V_{filt}(t) = (1 - a) \times V_{filt}(t - \Delta T) + a \times V_c(t)$ which is derived based on the low-pass filter Eq. (3.14) as suggested by [178] ;
- 7) Calculate the wake center position at the downstream wind turbine $\Delta_y(t)$ by Eq. (3.13a);
- 8) $t = t + \Delta T$;
- 9) If $t \leq T_{max}$, return to step 5; otherwise, proceed to step 10.
- 10) Reset t to 0;
- 11) Define L_{hub} as the distance between wake center and hub center of downstream wind turbine and update L_{hub} based on $\Delta_y(t)$ and relative position of downstream and upstream wind turbines;
- 12) Calculate wake radius D_w by using Eq. (3.1) or (3.4);
- 13) For every point (x, y) in Fig. 3.6, determine if it belongs to the wake region or the incoming wind region. If $(x - L_{hub})^2 + (y - H)^2 < (D_w / 2)^2$, it belongs to the wake region, otherwise to the incoming region;
- 14) For every point in the rotor plane: if it belongs to the wake region, the wind speed at x direction is calculated by Eq. (3.10); otherwise by Eq. (3.8);

15) $t = t + \Delta T$;

16) If $t < T_{max}$, go to step 11;

Simulated wind profiles along with corresponding controllers could be found in Chapter 4 and Chapter 5.

Chapter 4. Individual Pitch Control of Wind Turbine Including Wake Interaction

In this chapter, the individual pitch control for load reduction of a downstream wind turbine is designed based on static wake of upstream turbine. The asymmetric wake model described in Chapter 3 is adopted to predict the wind profile across the rotor of the downstream wind turbine without considering the time-varying phenomenon of wake meandering. According to the composite wind profile within the rotor disc, the LQ control design is performed for segments along azimuth. In order to obtain more accurate model for IPC design, an artificial wind pattern, named as *equivalent circular wind profile*, is generated. As benchmark, the DAC control scheme is also implemented based on the vertical wind shear only.

The remainder of this chapter is organized as follows. When wake interaction is considered, the controller switching strategy adopted is described in the Section 4.1. Section 4.2 presents how to obtain more accurate linearized state-space models by use of equivalent circular wind profile and different pitch reference in terms of the azimuth angle. The DAC and periodic control design are reviewed in Sections 4.3 and 4.4, respectively. Simulation results are shown in Section 4.5. This part of work is concluded in Section 4.6.

4.1. Controller Switching Strategy

A relatively general situation of wake interaction is illustrated in Figure 3.3, which is used for idea-proof simulation study in this chapter. The upstream and downstream

turbines are assumed to be at the same height. The wake interaction is mixed with the vertical wind shear, which makes the case more complicated than what has been dealt with in the previous DAC design, e.g. by Wright [52, 53]. To deal with this situation, we have resorted to the periodic control scheme by Stol [179], where the rotor disc is divided into a number of circular sectors in terms of the azimuth angle, and the LQ controller is designed for every sector, similar to the illustration in Fig. 4.1. The overall control is realized by switching between these segmental controllers. Instead of the scheme of equal-azimuth segmentation of 24 sectors in [179], in this study, we have considered the change in the H_∞ norm of the wind turbine models between individual sectors and then reduce the number of sectors for controller design.

4.2. Determination of Local Pitch Reference along Azimuth

For IPC, due to the asymmetry nature of the wind across the rotor disc, the reference for the blade pitch angle varies with the azimuth angle. In this study, as in many other similar studies on wind turbine controls, NREL's FAST software [140] is used to obtain the piecewise linear models. If the linearized state-space models along the azimuth are obtained by use of "FAST linearization" module [140], the blade pitch angle is the same for different azimuth angles. Such approximation would result in more inaccuracy when wake induced asymmetry is included. In order to obtain more accurate linearized state-space models of wind turbine along the azimuth, it is preferred to obtain the pitch reference for different azimuthal angles for any specific wind profile.

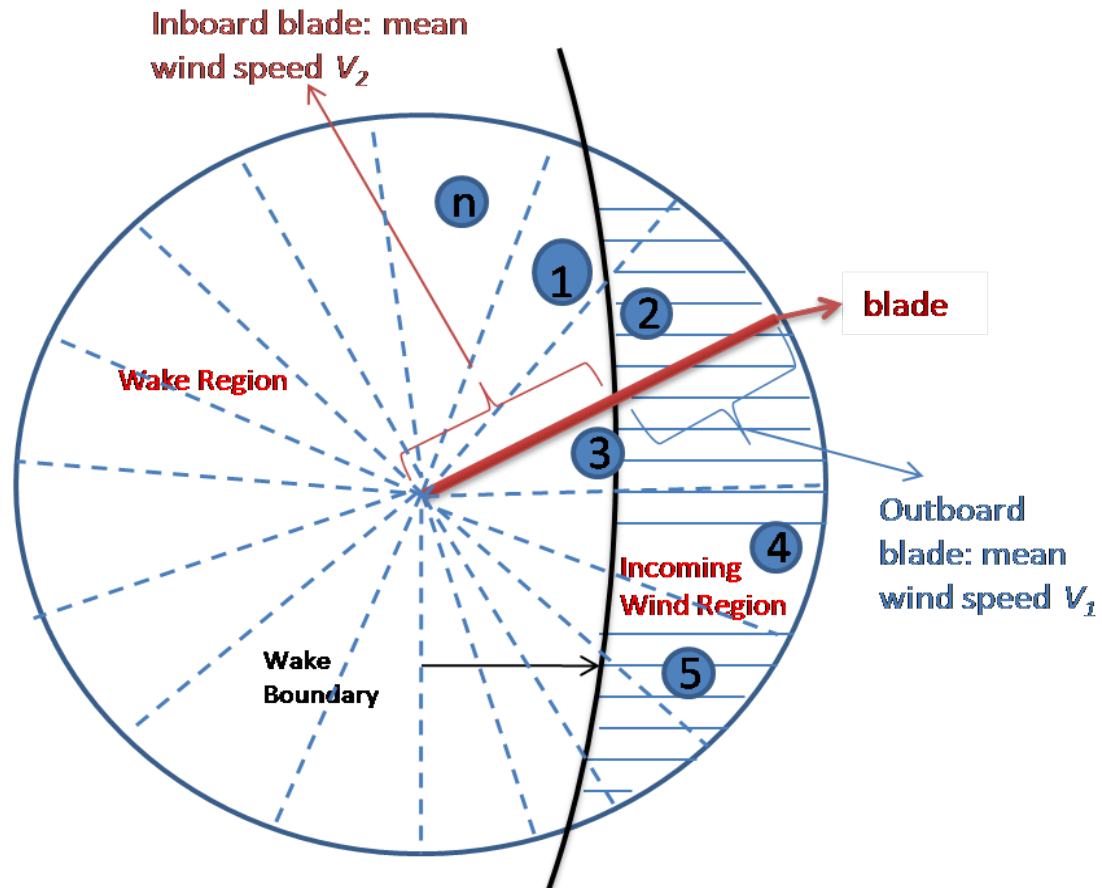


Fig. 4.1 Switching IPC Controller Strategy

As for linearization of the wind turbine model, an operating point is usually defined by the combination of the blade pitch angle, the rotor speed and the wind speed. The detailed linearization theory and procedure that is followed are described in detailed in [52]. Typically, there are two approaches to obtaining linearized state-space models of wind turbine by use of “FAST linearization” module. One method is that a steady-state solution is computed to obtain the linearized state-space models, and the other is that an unsteady solution is computed with the initial condition. For the former method, the pitch angle and the rotor speed converge to the operating point when the wind profile is provided. In order to obtain such steady-state solution, the pitch reference is obtained for a specific azimuth angle with the help from a so-called *equivalent circular wind profile*

(ECWP). For a specific radial profile of wind speed along the blade length at certain azimuth angle, an ECWP is created by duplicating this profile for all different azimuth angles, as shown in Fig. 4.2. Such a fictitious wind profile is generated for obtaining steady-state solution which can help derive the local pitch reference.

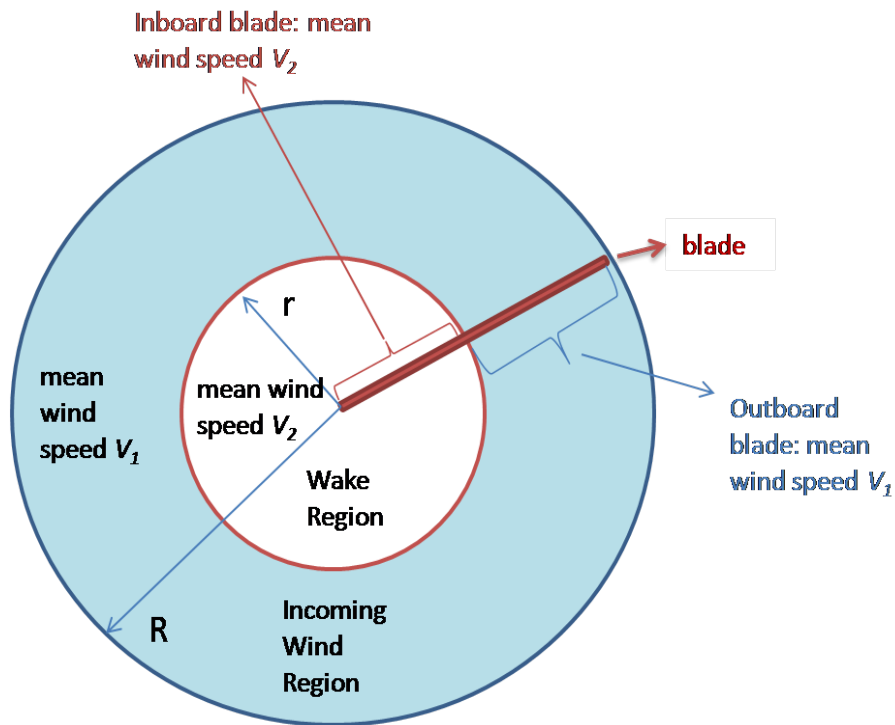


Fig. 4.2 Equivalent Circular Wind Profile (ECWP)

When all pitch references are obtained along azimuth by use of ECWP, the corresponding linearized state-space model along azimuth are obtained by use of unsteady state solution and original wind profile. In this situation, the initial pitch angle of different blades should be set as the corresponding pitch reference at the corresponding azimuth angle, the initial rotor speed should be set as rated rotor speed in Region 3 and the running time should be less than one period in order to make sure that rotor speed does not change very much.

4.3. Disturbance Accommodating Control

The DAC control design procedure [49] is briefly presented in this section. More details are available in Wright [52]. The state-space model of wind turbine dynamics can be described as

$$\dot{x} = Ax + Bu + \Gamma u_d \quad (4.1a)$$

$$y = Cx \quad (4.1b)$$

where x is the state vector, u is the control input vector, y is the measurement vector, u_d is the disturbance vector, A is state matrix, B is the input matrix, C relates the measurement vector with the state vector, and Γ is the disturbance gain matrix. A critical step in DAC design is to model the periodic change of wind load due to vertical wind shear with the so-called “disturbance generator”, whose dynamics is described with

$$u_d(t) = \theta z_d(t) \quad (4.2a)$$

$$\dot{z}_d(t) = F_d z_d(t); \quad z_d(0) = z_d^0 \quad (4.2b)$$

where z_d is the state vector for the disturbance generator. For wind shear disturbance related with 2-blade wind turbine and step wind disturbance,

$$\theta = \begin{bmatrix} 1 & 0 & 0 \\ 0 & 0 & 1 \end{bmatrix} \quad (4.3a)$$

$$F_d = \begin{bmatrix} 0 & 1 & 0 \\ -\Omega^2 & 0 & 0 \\ 0 & 0 & 0 \end{bmatrix} \quad (4.3b)$$

where Ω is the rotor speed.

In order to include the disturbance dynamics into the control design, the state vector is augmented by including the disturbance vector. The feedback control law can be expressed as

$$u = G\hat{x} + G_d\hat{z}_d = \bar{G} \begin{bmatrix} \hat{x} \\ \hat{z}_d \end{bmatrix}^T \quad (4.4)$$

where $\bar{G} = [G \quad G_d]$.

The state observer is designed as

$$\dot{\hat{x}} = A\hat{x} + Bu + K(y - \hat{y}) + \Gamma\hat{u}_d \quad (4.5a)$$

$$\hat{y} = C\hat{x} \quad (4.5b)$$

The disturbance state estimator is designed as

$$\dot{\hat{z}}_d(t) = F\hat{z}_d(t) + K_d(y - \hat{y}) \quad (4.6)$$

Finally augmented state space model can be expressed as

$$\begin{bmatrix} \dot{\hat{x}} \\ \dot{\hat{z}}_d \end{bmatrix}^T = \bar{L} \begin{bmatrix} \hat{x} \\ \hat{z}_d \end{bmatrix}^T + \bar{K}y \quad (4.7)$$

where

$$\bar{L} = \begin{bmatrix} A + BG - KC & \Gamma\theta + BG_d \\ -K_dC & F \end{bmatrix} \quad (4.8a)$$

$$\bar{K} = [K \quad K_d]^T \quad (4.8b)$$

Then the transfer matrix of the feedback controller can be calculated as

$$T(s) = \bar{G}(sI - \bar{L})^{-1}\bar{K} \quad (4.9)$$

The DAC provides an elegant solution to analytically incorporating the vertical shear into an LTI system framework. However, the disturbance generator is based on a simplification of the vertical shear, and such simplification may limit its application to actual wind turbine operation.

4.4. Periodic Control

Stol [179] adopted the periodic control strategy to implement DAC. At first, the state-space models along azimuth were obtained. In this method, the wind shear was not modeled as the disturbance in the state-space models. Only the hub-height wind disturbance was chosen. The change of state-space models along azimuth showed the wind shear characteristics. Then the MIMO controllers were designed based on these models. Finally, for closed-loop realization, the controllers were switched along azimuth. Stol [179] divided the rotor disc into 24 segments along azimuth which means each segment includes 15° . Recently, the LQR and periodic control schemes were used for IPC of offshore wind turbines without disturbance terms in the state-space model [151]. In this study, the LQR and periodic control methods are used for the segmented plant models.

The LQR method is simply described in the following, for which the details can be found in any standard optimal control text. The disturbance term is not considered in the state-space model. The system described by

$$\dot{x} = Ax + Bu \quad (4.10a)$$

$$y = Cx \quad (4.10b)$$

with the cost function defined as

$$J = \int_0^{\infty} (x^T Qx + u^T Ru) dt \quad (4.11)$$

For minimizing the above cost, the state feedback control law is

$$u = Gx \quad (4.12a)$$

where G is given by

$$G = -R^{-1}B^T P \quad (4.12b)$$

and P is found by solving the Algebraic Riccati Equation

$$A^T P + PA - PBR^{-1}B^T P + Q = 0 \quad (4.13)$$

The weightings in Q and R matrices need to be adjusted to improve the performance of the controller.

Similarly, the state observer can be designed

$$\dot{\hat{x}} = A\hat{x} + Bu + K(y - \hat{y}) \quad (4.14a)$$

Using the feedback control law $u = G\hat{x}$, we have

$$\dot{\hat{x}} = L\hat{x} + Ky \quad (4.14b)$$

where $L = A + BG - KC$. Thus, the equivalent transfer function of the closed loop system is

$$T(s) = G(sI - L)^{-1}K \quad (4.15)$$

4.5. Simulation Results

4.5.1. Simulation Platform

To evaluate the effectiveness of the proposed IPC scheme, simulation study has been conducted with FAST [140], Aerodyn [138] and TurbSim [176] developed by NREL, along with Matlab® Simulink. TurbSim is modified to generate wind profiles, as described in Chapter 3. Wind profile files generated by TurbSim are the input files of Aerodyn and FAST. Aerodyn is a preprocessor of FAST for calculating the aerodynamic loads on the turbine blades, which can be used in FAST. FAST can be used to model the dynamics for both two- and three-blade, horizontal-axis wind turbines. Control simulation with FAST has been facilitated by the Simulink interface. In this study,

TurbSim is modified to generate the wind profile including wake interaction and the ECWP. Both the upstream and downstream wind turbines used for this study adopt the model of NREL's CART (Controls Advanced Research Turbine) facility [180], which is a two-blade 600 kW variable-speed-variable-pitch turbine.

4.5.2. Wind Profile with Wind Shear and Wake Effect

The allocation of the upstream and downstream turbines is shown in Fig. 3.2. As mentioned in Chapter 3, the Larsen wake model was chosen. The incoming wind speed V_∞ is assumed to be 18m/s, the ambient turbulence intensity is 18%, the diameter of the upstream turbine D_r for CART [180] is 46m. For modern wind farms, x_w/D_r is usually designed as 8 to 10. In this study, this ratio is assumed to be 8. Typical values of thrust coefficient C_t range from 0 to about 1. When the power coefficient reaches its maximum, thrust coefficient C_t is about 0.728. This study adopts 0.7 for C_t . Application of the Larsen wake model gives that the diameter of the wake at the downwind turbine grows to 204.22 m, and the wind speed at the wake center becomes 16.76 m/s.

The wind profile was then generated through TurbSim [176] by modifying the relevant program codes to incorporate the wake related wind velocity superposition. Usually the typical wind speed consists of the mean and the turbulent components. In TurbSim, the turbulent portion of wind is generated first following the spectral density function specified, and then the mean wind speed is added to form the final wind profile. As a simplified treatment, this study does not consider the turbulent portion of wind. It is worthwhile to point out that turbulent generally increases in the wake, which implies increased fatigue load for the downstream turbines.

In the TurbSim codes provided by NREL, the rotor disc is regarded as a whole to calculate the mean wind speed. Since this study includes the wake interaction as well, the mean wind speed profile across the disc has to be calculated within two areas: the area without wake effect and that with velocity overlap due to wake effect. The TurbSim codes have been modified accordingly to generate the wind profile including wake effect. Figure 4.3 shows the 2D wind speed distribution within the rotor disc of the downwind turbine due to the wind shear only, while Figure 4.4 shows the profile reflecting the wind velocity overlap based on the Larsen wake model and the wind shear model with L_{hub} equal to $0.9R_w$.

4.5.3. ECWP and Different Pitch Reference along Azimuth

Recall in Section 2, the ECWP refers to the scenario that the wind speed along the azimuth direction is the same but is different along the radial direction (i.e. along the blade length). For the simulation example, the ECWP is obtained through modifying TurbSim with the following procedure. The wind information is first extracted at some azimuth and then copied to all azimuths. For example, if we want to generate an equivalent circular wind profile at 45° azimuth as shown in Figure 4.4, we need to copy the wind distribution at 45° azimuth to all azimuths, as shown in Figure 4.5. For different azimuth angles, the corresponding ECWP needs to be generated respectively to obtain the corresponding pitch reference. All the pitch references obtained along azimuth for the special wind profile in Figure 4.4 are plotted in Figure 4.6.

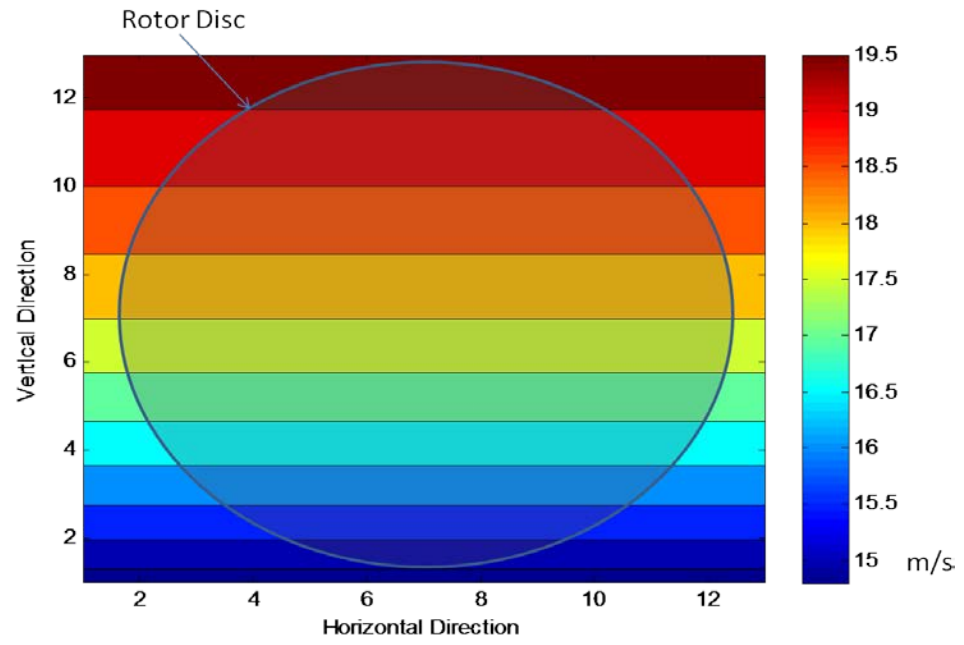


Fig. 4.3 Wind Speed Distributions within Rotor Disc due to Wind Shear

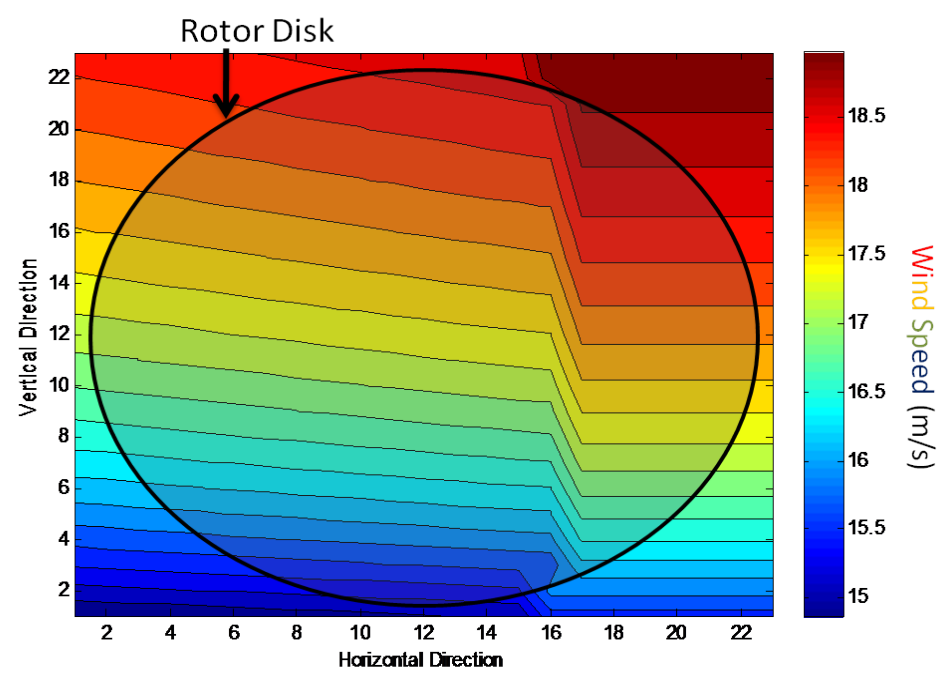


Fig. 4.4 Wind Profile with Wind Shear and General Wake Interaction

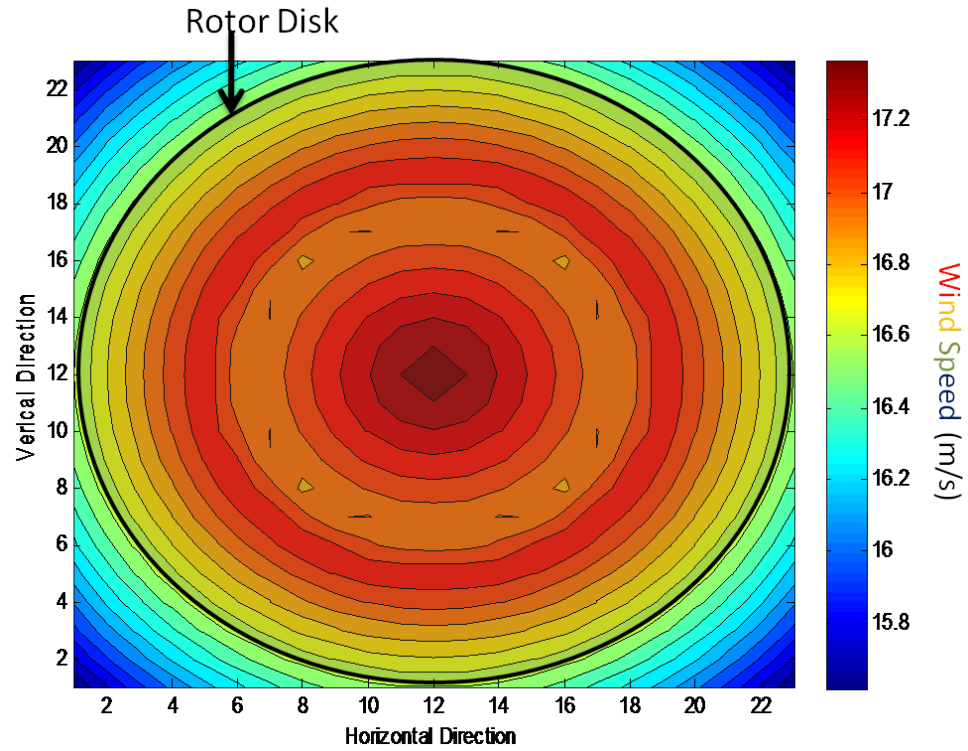


Fig. 4.5 Equivalent Circular Wind Profile for The Simulation Example

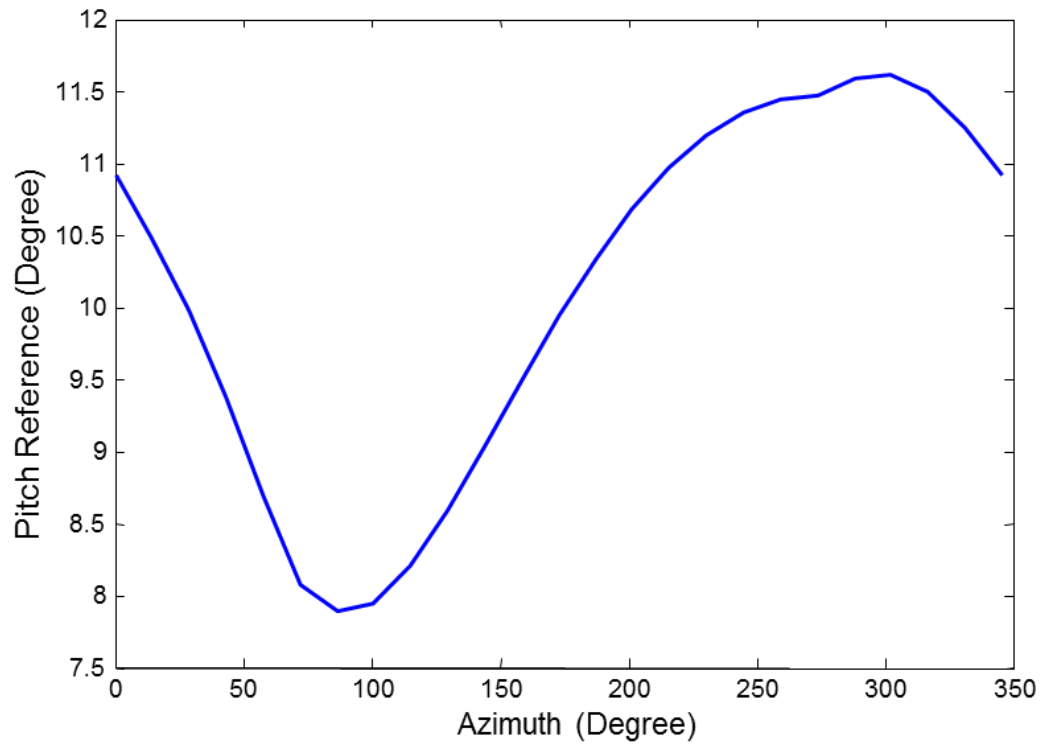


Fig. 4.6 Pitch Reference along Azimuth Obtained with ECWP

4.5.4. Model Linearization for Individual Pitch Control

The 9-state space models for IPC Design were obtained by use of “FAST linearization” module, with the descriptions of the states listed in Table 4.1. Three measurement outputs were used for state estimation: the generator speed, the tip deflection of the first asymmetric flap mode, i.e. $(\Delta x_1 - \Delta x_2)/2$, and the fore-aft moment on the tower base. The disturbance inputs include wind shear and hub-height wind disturbances and the averaged state-space models were used across the rotor plane when DAC approach was used. When the periodic control and LQR methods were used, our treatment does not include disturbance input, and the circular wind profile needs to be used to generate the corresponding state-space models.

Table 4-1: State Description for a 9-state Wind Turbine Model (CART)

States	Description
Δx_1	1 st tower fore-aft bending moment
Δx_2	Drivetrain rotational-flexibility
Δx_3	Perturbed blade-1 1 st flap deflection
Δx_4	Perturbed blade-2 1 st flap deflection
Δx_5	Derivative of state 1
Δx_6	Perturbed rotor rotational speed
Δx_7	Derivative of state 2
Δx_8	Perturbed blade-1 1 st flap velocity
Δx_9	Perturbed blade-2 1 st flap velocity

4.5.5. Rotor Disc Segmentation

Initially the rotor disc is divided into 24 sectors (similar to Stol [179]), each covering 15° azimuth angle. Accordingly, 24 state-space models are obtained along the azimuth angle. As the variation of wind turbine dynamics is considered non-uniform in azimuth angle, such simple segmentation may be too conservative for some sectors. Therefore, we use

the variation of the H_∞ norm of the plants between neighbored sectors to justify the segmentation scheme. Instead of considering the infinite bandwidth, the difference of maximum singular value ranging from DC to 100 rad/second between state-space models of neighboring sectors along azimuth is plotted, showed in Figure 4.7.

The 100 rad/second is considered the 40 dB below the DC magnitude response. Segmentation along azimuth is based on the following two rules.

- 1) If the difference in the maximum singular value for neighboring state-space models is below 4 dB, it is merged into the neighboring segment.
- 2) The difference in the maximum singular value between neighboring state-space models should not be greater than 6 dB.

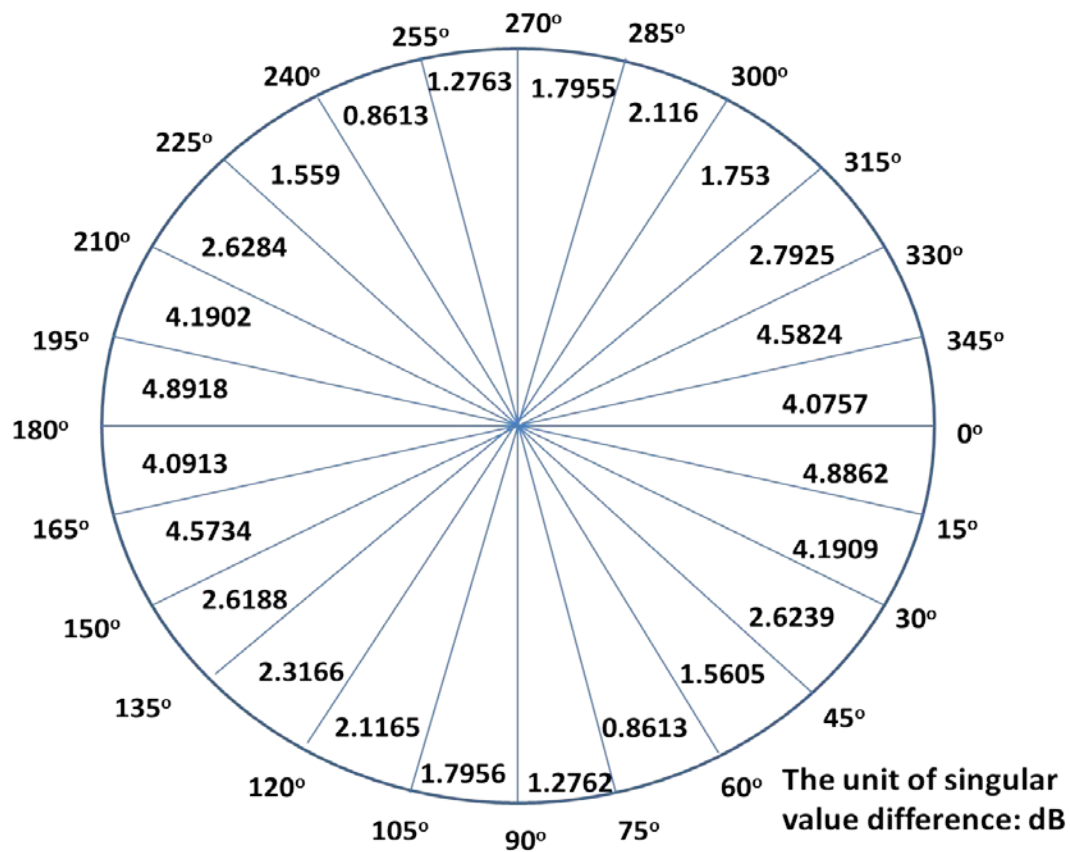


Fig. 4.7 Maximum Singular Value Difference within Rotor Disc

Notice that these two rules can be adjusted by controller designer, based on different robustness need. In other words, if lower robustness is required, the norm difference can be increased.

Based on these rules, the number of the controllers is reduced from 24 to 16. The sectors centered at azimuth angle 45° , 75° , 105° , 135° , 225° , 255° , 285° and 315° were merged to their respective neighbor sectors, as shown in Figure 4.8.

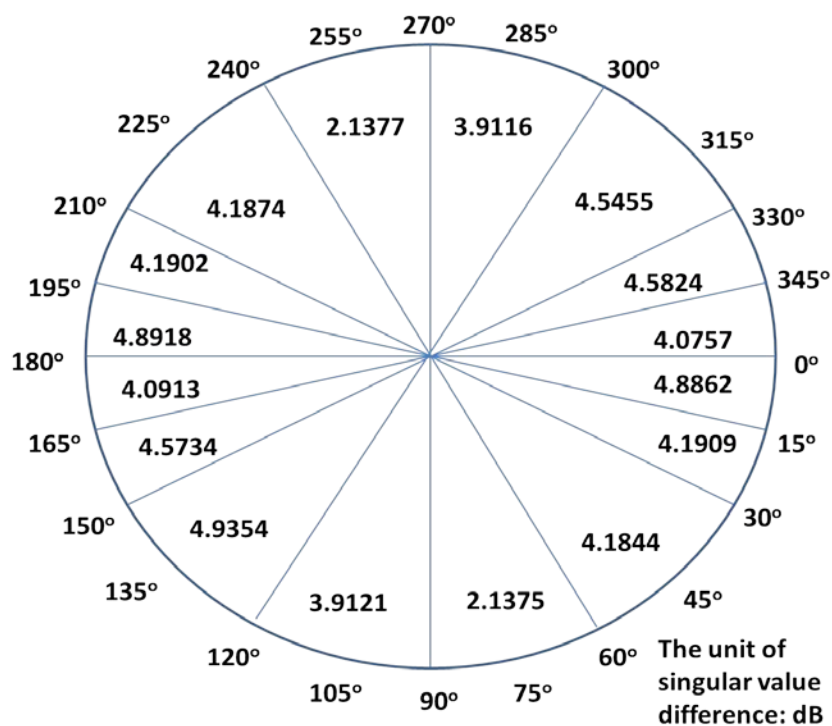
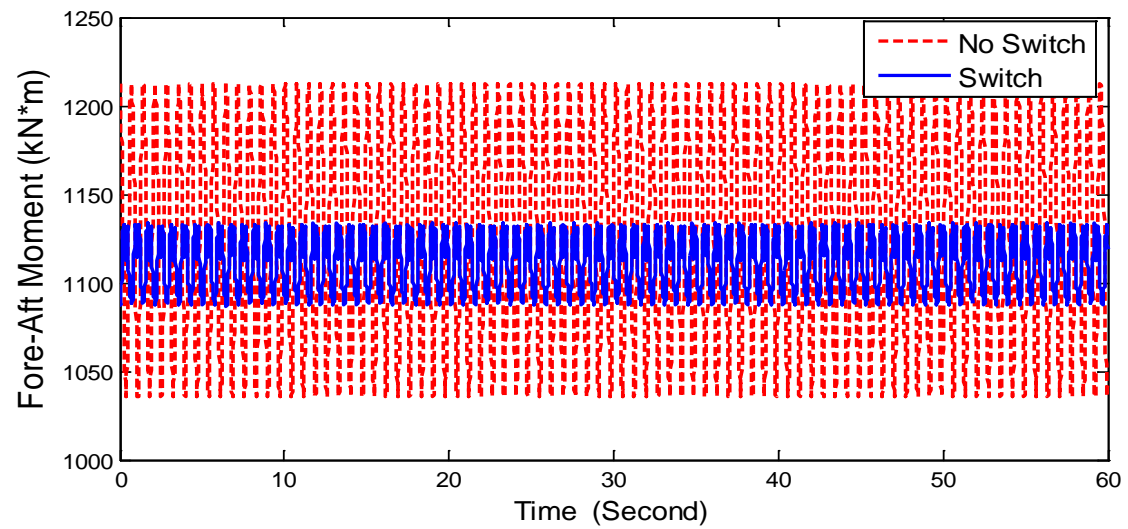


Fig. 4.8 Sixteen Segments of Rotor Disc after Segment Merge

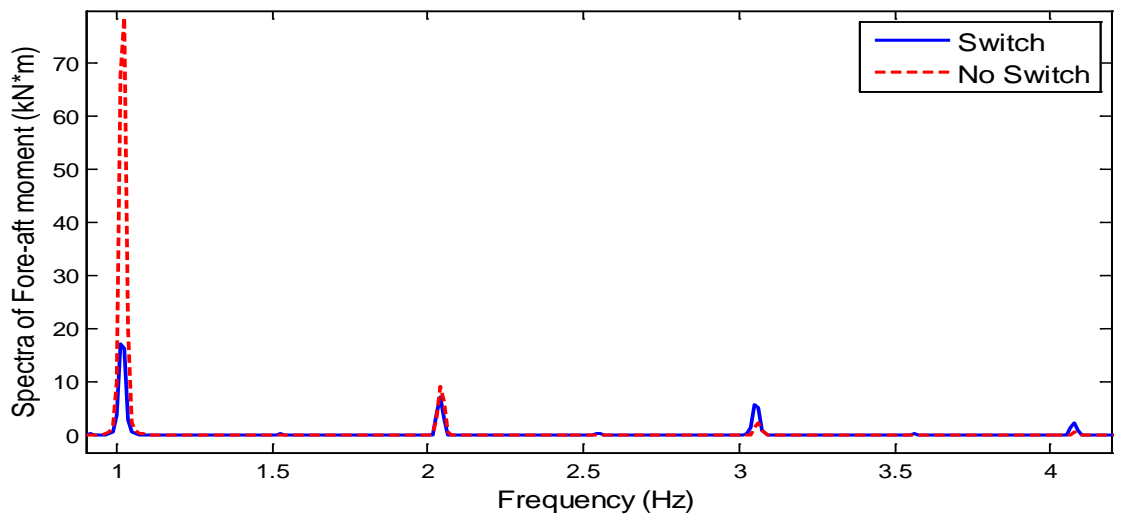
4.5.6. Comparison of Switching and Non-switching Controller

The wake induced wind profile in Figure 3.2 is then used to test the switching control schemes. The DAC based controller was designed based on the averaged state-space model obtained under 16.8 m/s hub-height wind speed including wind shear. Sixteen switching controllers are designed to reduce the load based on state-space models with different pitch reference along azimuth. Figure 4.9(a) shows the temporal profile of the

tower-base fore-aft moment using the switching controller designed based upon the wake model versus the standard DAC control with only the wind shear considered. The corresponding spectra in Figure 4.9(b) show that the primary mode at 1 Hz is significantly suppressed, while some higher harmonics are slightly increased.



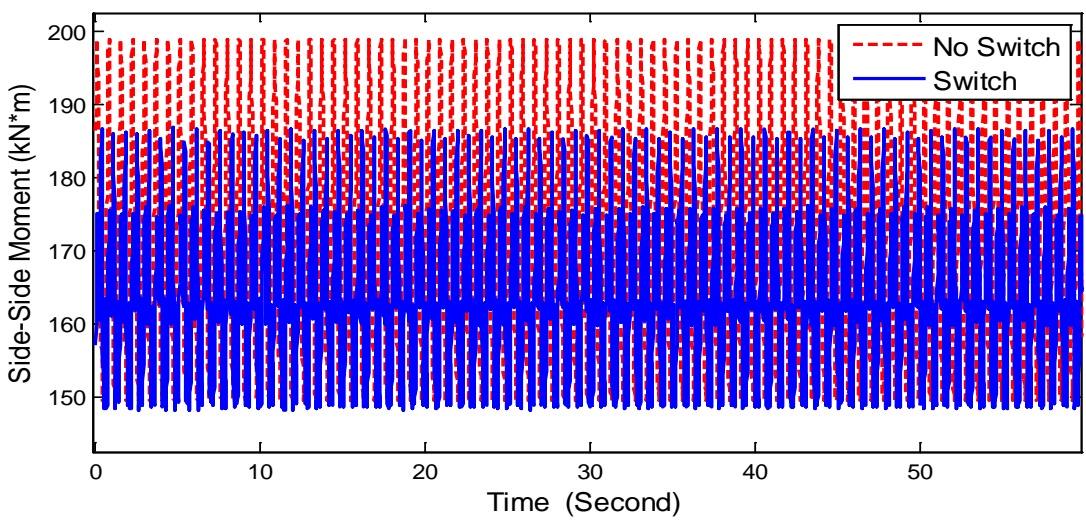
a) Steady-state Temporal profile



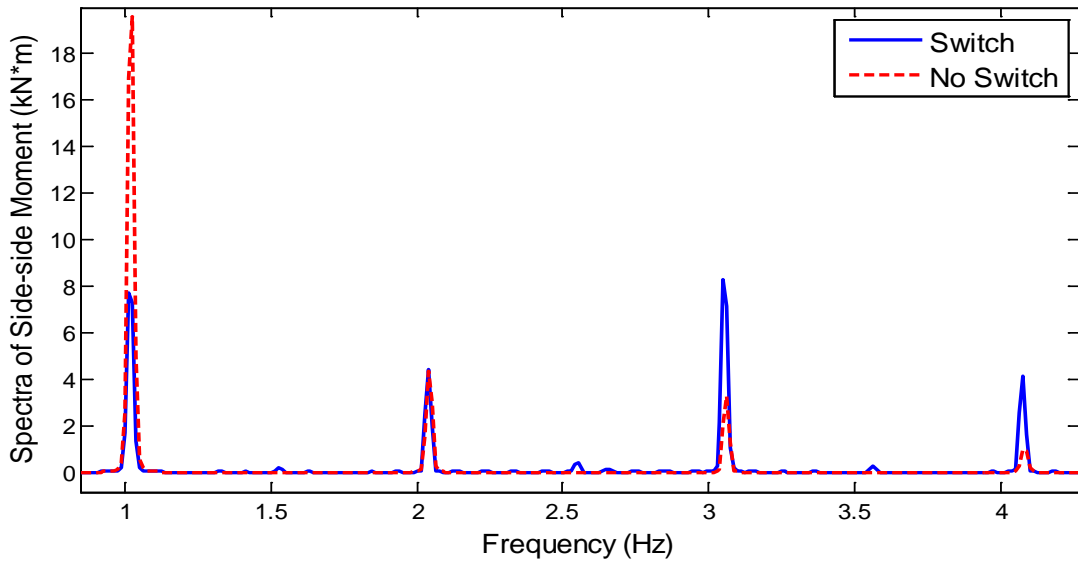
b) Spectra

Fig. 4.9 Tower-base Fore-aft Bending Moment using the Proposed Method (Switch) and DAC (No Switch)

Similar load control performance is demonstrated for the tower-base side-to-side moment, as shown in Figure 4.10. Significant reduction is observed for 1 Hz while load increased for higher harmonics (close to 3 Hz and 4 Hz) modes.



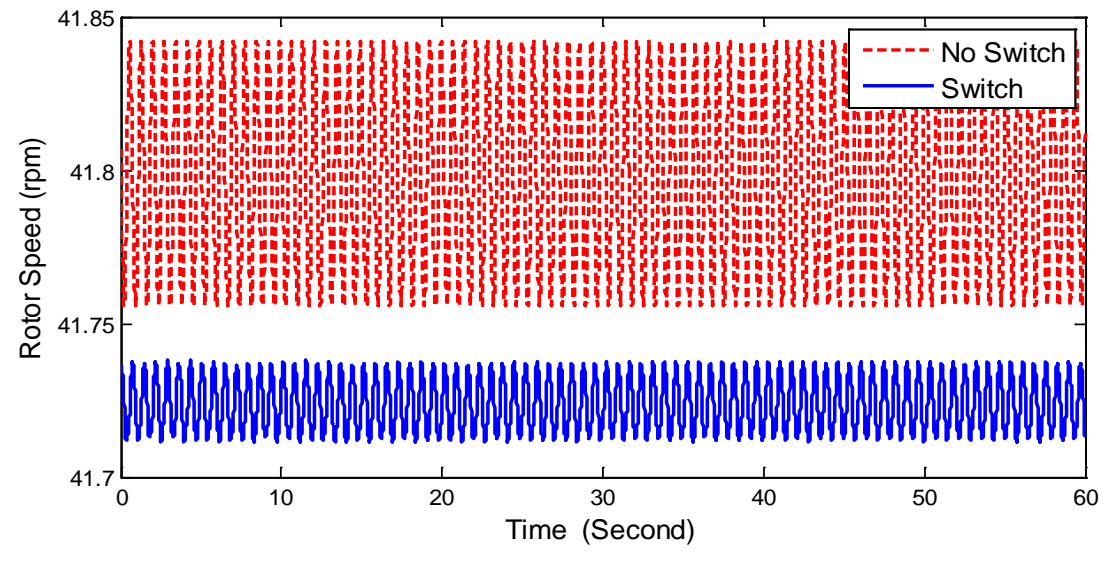
a) Steady-state Temporal Profile



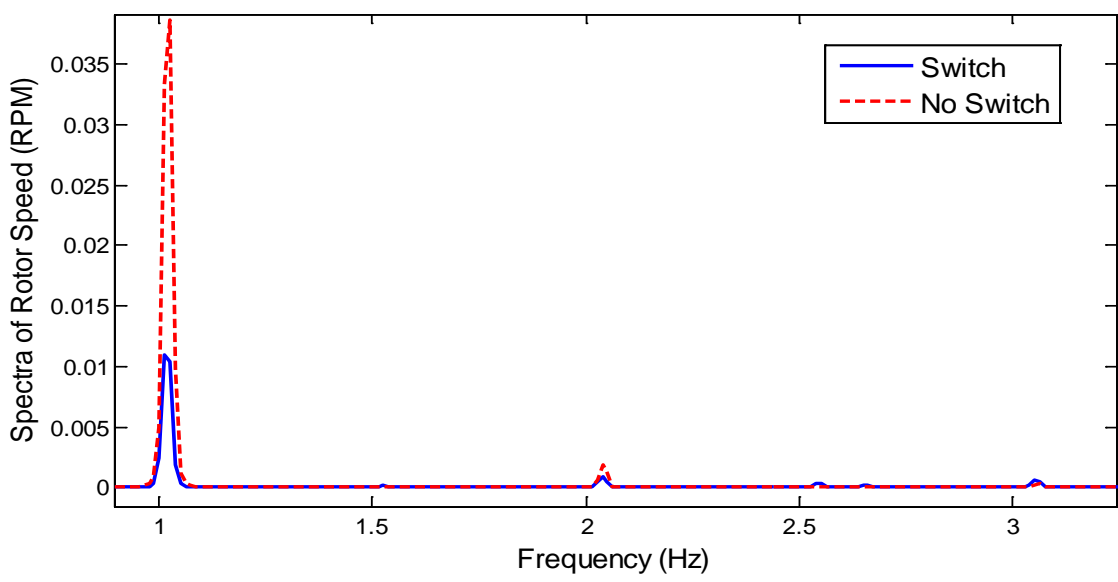
b) Spectra

Fig. 4.10 Tower-base Side-to-side Bending Moment using the Proposed Method (Switch) and DAC (No Switch)

Figure 4.11 shows that the mean and variation of rotor speed were both reduced regarding the rated speed of 41.7 rpm, by use of the switching controllers compared with the traditional DAC. Therefore, the proposed strategy can indeed improve load reduction and speed regulation for turbines subject to wake interaction.



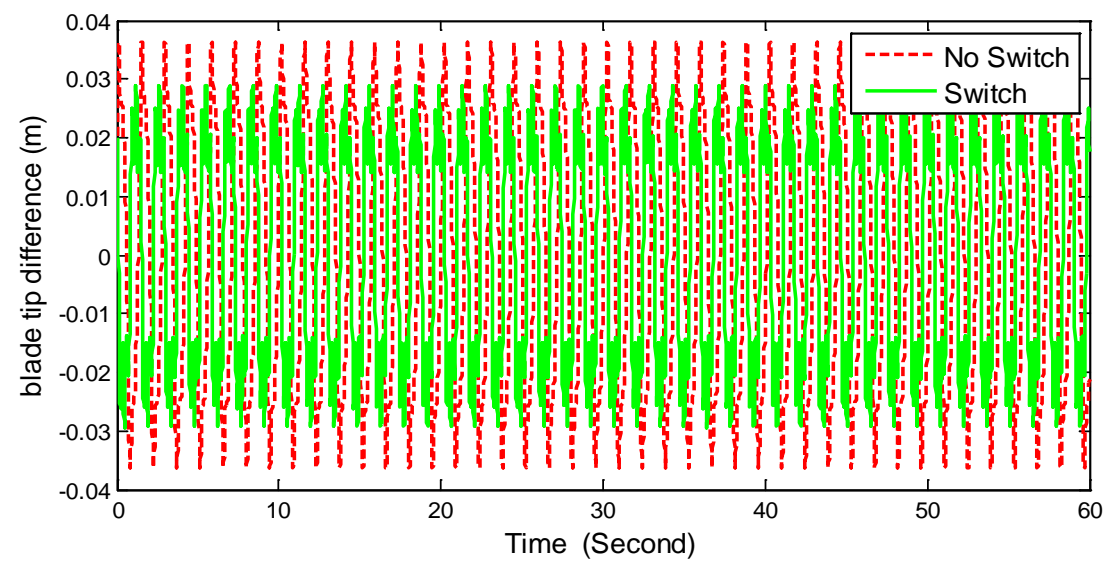
a) Steady-state Temporal Profile



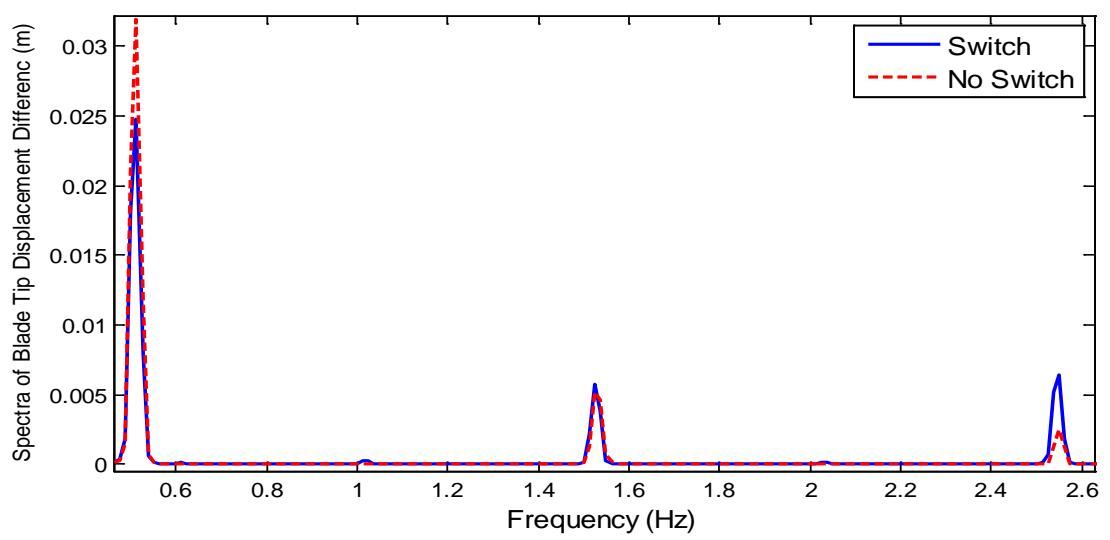
b) Spectra

Fig. 4.11 Rotor Speed using the Proposed Method (switch) and DAC (no switch)

Figure 4.12 shows blade tip displacement difference using the switching controllers and the standard DAC. Plot (b) shows that the 1.6 Hz and 2.6 Hz modes are slightly increased with the proposed method, while the 0.5 Hz mode is suppressed. The overall change is insignificant.



a) Steady-state Temporal Profile



b) Spectra

Fig. 4.12 Blade-tip Displacement Difference using the Proposed Method (Switch) and DAC (No Switch)

4.6. Summary

This chapter presents an improvement on the IPC scheme for load reduction by including the wake interaction. The Larsen wake model is applied for composing the rotor wind profile for downstream turbines under wake interaction, and a switched control strategy is thus developed based on the composite wind profile. The wind profile was generated by modifying the TurbSim codes. The idea of equivalent circular wind profile was proposed to obtain different pitch references along azimuth. When different pitch references along azimuth are used, more accurate state-space models of wind turbine can thus be generated via FAST linearization. Based on such models, the IPC are designed following both the DAC and the periodic control frameworks. Simulation results showed that the tower-base fore-aft bending moment, the tower-base side-to-side bending moment, the rotor speed fluctuation and the blade-tip displacement difference are significantly suppressed.

Chapter 5. Model Predictive Control of Wind Turbine Including Wake Meandering

As described in Chapter 1, the meandering phenomenon of upstream turbine leads to time-varying nature of wind loads on the downstream turbines. This implies additional time-varying asymmetry of the effective turbine model. Therefore, the wind turbine load reduction control is further complicated. To deal with such odd, a practical solution is to design (model predictive) controllers based on a number of linearized wind turbine models under the predicted patterns of superposed wind profile. Then, a relevant issue arises: – how to handle the “intermediate region” between any two selected patterns. Instead of using the controller interpolation idea, this dissertation study adopts a Multiple-Model Predictive Control framework, which is built upon a consecutive process of plant updating via the recursive Bayesian estimation. In other words, the plant for each step of controller (MPC) design is obtained from weighting a number of pre-defined plant models.

Section 5.1 describes multi-blade coordinate (MBC) transformation which is used to convert the azimuth-periodic wind turbine models/variables into a time-invariant counterpart under static wind profile. A practical approach with enhanced stability robustness and relatively low computational burden, the Dual Mode MPC, is described in Section 5.2. The multiple-model predictive control algorithm is presented in Section 5.3. Finally, simulation study is given in Section 5.4, which validates the effectiveness of the proposed control strategies.

5.1. Multi-Blade Coordinate Transformation

Typical multi-body analysis of wind turbine dynamics is built upon several sets of coordinates: the earth coordinates, the blade coordinates (Fig. 5.1), the coordinates on the nacelle (Fig. 5.2) and the coordinates on the tower base (Fig. 5.3) [140].

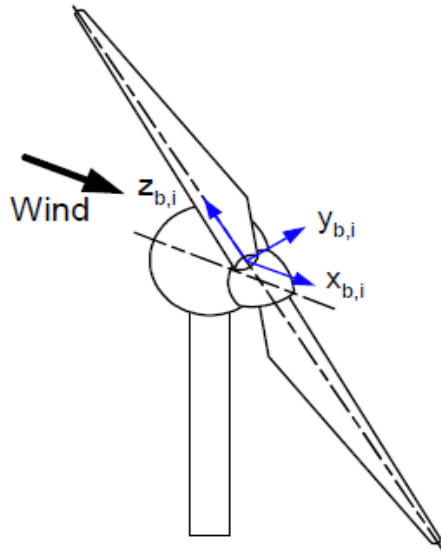


Fig. 5.1 Blade Coordinate System [140]

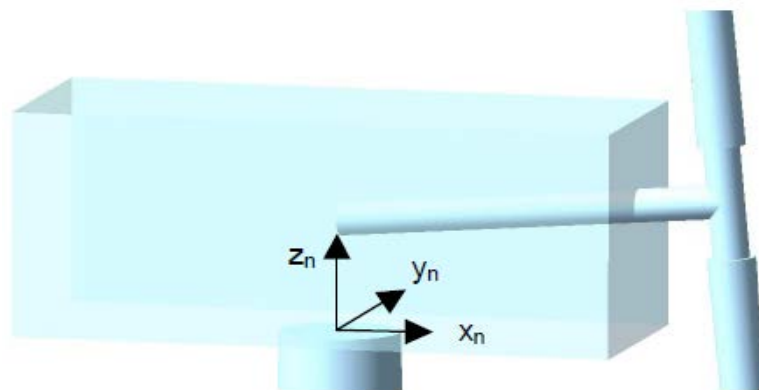


Fig. 5.2 Nacelle Coordinate System [140]



Fig. 5.3 Tower-base Coordinate System [140]

The Blade Coordinates in Fig. 5.1 rotate with wind turbine blades. Under this set of coordinates, the wind turbine dynamics is periodic in azimuth under steady wind, as well as the corresponding state-space models. As consequence, the dynamic loads of wind turbine (e.g. blades and tower) are periodic. Such temporal/spatial change of plant model presents significant difficulty for controller design. Considering the maturity and convenience of controller design in linear time-invariant (LTI) models, the Multi-blade Coordinate (MBC) transformation has been developed to convert the time/azimuth periodic plant models/variables into their time-invariant counterparts [181, 182]. The MBC transformation is a widely used technique in the helicopter field [183]. In the remainder of this section, the MBC transformation is reviewed by following the description by Bir [2].

According to MBC, for a 3-blade turbine, three nonrotating degrees of freedom (DOF), q_o^j , q_c^j and q_s^j , can be converted into three rotating DOF's, q_1^j , q_2^j and q_3^j , by the following transformation:

$$\begin{bmatrix} q_1^j \\ q_2^j \\ q_3^j \end{bmatrix} = T \begin{bmatrix} q_o^j \\ q_c^j \\ q_s^j \end{bmatrix} \quad (5.1)$$

where q_b^j is the j^{th} rotating DOF for the b^{th} blade with $b = 1, 2, 3$. In the non-rotating frame, q_o^j , q_c^j , q_s^j are the average mode, the cosine-cyclic mode and the sine-cyclic mode, respectively. The transformation matrix T and its inverse are defined as

$$T = \begin{bmatrix} 1 & \cos \psi_1 & \sin \psi_1 \\ 1 & \cos \psi_2 & \sin \psi_2 \\ 1 & \cos \psi_3 & \sin \psi_3 \end{bmatrix} \quad (5.2)$$

$$T^{-1} = \frac{1}{3} \begin{bmatrix} 1 & 1 & 1 \\ 2 \cos \psi_1 & 2 \cos \psi_2 & 2 \cos \psi_3 \\ 2 \sin \psi_1 & 2 \sin \psi_2 & 2 \sin \psi_3 \end{bmatrix} \quad (5.3)$$

where ψ_1 , ψ_2 and ψ_3 are azimuthal angles of blades 1, 2 and 3, respectively. It is trivial to justify that $\psi_1 + \psi_2 + \psi_3 = 2\pi$ at any time. Notice that the inverse of matrix T is needed in order to convert a rotating DOF to its nonrotating counterpart, while the nonsingularity of T is guaranteed by the geometrical relationship among ψ_1 , ψ_2 and ψ_3 .

Based on Eqs. (5.1), (5.2) and (5.3), the wind turbine dynamics of the 3-blade horizontal-axis wind turbine can be converted from the rotating frame to the non-rotating frame as follows, based on the procedure developed by Bir [181]. In general, the aeroelastic analysis of wind turbine dynamics deals with lumped-element equations of motion (EOM) and its output equations in the following form:

$$M\ddot{X} + C\dot{X} + KX = Fu + F_d w \quad (5.4)$$

$$Y = C_v \dot{X} + C_d X + Du + D_d w \quad (5.5)$$

where X is the coordinate vector, u is the control input vector, and w is the disturbance vector. M denotes the mass matrix that contains direct blade inertias and blade-tower coupling inertias, C contains both structural damping and gyroscopic terms, and K contains structural and aerodynamic stiffness terms as well as the centrifugal effect. F and F_d denote the control input, and disturbance input matrices, respectively. Y is the output vector. C_v and C_d are output matrices for velocity and displacement, respectively. D and D_d are the feedthrough matrices for the control input and the disturbance input, respectively.

For wind turbine control problem, the motion vector is defined as

$$X = \left[X_F^T \quad q_1^1 \quad q_2^1 \quad q_3^1 \quad \cdots \quad q_1^j \quad q_2^j \quad q_3^j \quad \cdots \quad q_1^m \quad q_2^m \quad q_3^m \right]^T \quad (5.6)$$

where X_F is an $nF \times 1$ column vector representing the nF fixed-frame-referenced DOF, q_b^j is the j^{th} rotating DOF for the b^{th} blade, and m is the total number of rotating DOFs for each blade. The length of vector X is $nF + 3m$.

As the aeroelastic codes (for example, FAST) generate equations of motion in a numerical form, the substitutional method is typically used to convert the EOM (5.3) into the non-rotating form [181]. Based on Eq. (5.1), vector X in the rotating-frame is related to its counterpart in the nonrotating-frame vector, X_{NR} , via the foregoing MBC transformation,

$$X = T_1 X_{NR} \quad (5.7)$$

where

$$B_{dNR} = \begin{bmatrix} T_1^{-1} & 0 \\ 0 & T_1^{-1} \end{bmatrix} B_d \quad (5.18)$$

$$C_{NR} = T_{10}^{-1} [C_1 T_1 + \Omega C_2 T_2 \quad C_2 T_1] \quad (5.19)$$

$$C = [C_1 \quad C_2] \quad (5.20)$$

$$D_{NR} = T_{10}^{-1} D T_{1c} \quad (5.21)$$

$$D_{dNR} = T_{10}^{-1} D_d \quad (5.22)$$

$$T_2 = \begin{bmatrix} \mathbf{0}_{nF \times nF} & & & & & \\ & \tilde{t}_2 & & & & \\ & & \tilde{t}_2 & & & \\ & & & \ddots & & \\ & & & & \tilde{t}_2 & \\ & & & & & \tilde{t}_2 \end{bmatrix}_{(nF+3m) \times (nF+3m)} \quad (5.23)$$

$$\tilde{t}_2 = \begin{bmatrix} 0 & -\sin \psi_1 & \cos \psi_1 \\ 0 & -\sin \psi_2 & \cos \psi_2 \\ 0 & -\sin \psi_3 & \cos \psi_3 \end{bmatrix} \quad (5.24)$$

$$T_3 = \begin{bmatrix} \mathbf{0}_{nF \times nF} & & & & & \\ & \tilde{t}_3 & & & & \\ & & \tilde{t}_3 & & & \\ & & & \ddots & & \\ & & & & \tilde{t}_3 & \\ & & & & & \tilde{t}_3 \end{bmatrix}_{(nF+3m) \times (nF+3m)} \quad (5.25)$$

$$\tilde{t}_3 = \begin{bmatrix} 0 & -\cos \psi_1 & -\sin \psi_1 \\ 0 & -\cos \psi_2 & -\sin \psi_2 \\ 0 & -\cos \psi_3 & -\sin \psi_3 \end{bmatrix} \quad (5.26)$$

$$T_{1c} = \begin{bmatrix} I_{n_{uF} \times n_{uF}} & & & & & \\ & T & & & & \\ & & T & & & \\ & & & \ddots & & \\ & & & & T & \\ & & & & & T \end{bmatrix}_{(n_{uF}+3n_{uR}) \times (n_{uF}+3n_{uR})} \quad (5.27)$$

$$T_{10} = \begin{bmatrix} I_{F_o \times F_o} & & & & & \\ & T & & & & \\ & & T & & & \\ & & & \ddots & & \\ & & & & T & \\ & & & & & T \end{bmatrix}_{(F_o+3m_o) \times (F_o+3m_o)} \quad (5.28)$$

In the above equations, n_{uF} and n_{uR} are the number of control inputs in the fixed and rotating frames, respectively; F_o and m_o are the number of outputs in the fixed and rotating frames, respectively. More details on MBC transformation for 3-blade wind turbine are available in [181].

When time-invariant models Eqs. (5.13) and (5.14) are used for controller design, measurements at rotating frame, such as the blade-root flapwise moment, need to be converted into the non-rotating frame by use of the inverse of matrix T , and then corresponding variables at fixed frame are used for controller design with MBC. Similarly, the control inputs (pitch angles) in the fixed frame need to be converted back to the rotating frame again by use of matrix T . See the controller configure when MBC is used in Fig. 5.4.

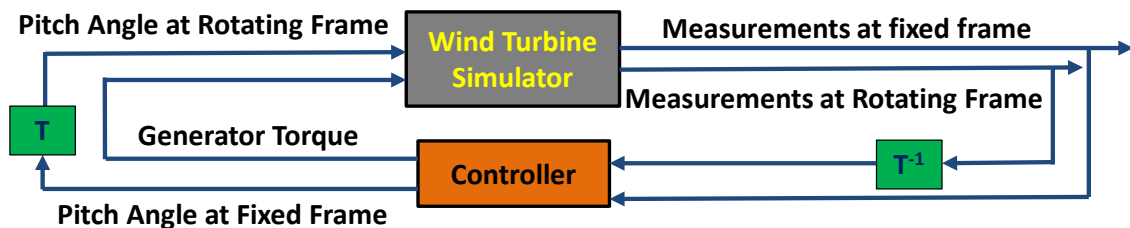


Fig. 5.4 Multi-Blade Coordinates for Controller Design

5.2. Dual-Mode Model Predictive Control

The terminology *dual mode control* is originally from nonlinear control [5]. This control strategy covers two modes: one mode is used when the system is far from the operating

point; the other mode is used when the system is close to the operating point. Then, the control strategy automatically switches into different modes when the system is operating at different desired states.

In MPC, the “dual mode” notation is different from that in nonlinear control. The Dual Mode in MPC indicates how the predictions are set up. The main motivation of dual mode prediction is to handle the predictions over an infinite horizon which implies nominal stability [92]. Usually, the first mode refers to the period within the prediction horizon, i.e. the estimation of $x_{k+i|k}$ where $i = 0, 1, 2, \dots, H_p - 1$; while the second mode is the state prediction beyond the prediction horizon, i.e. the estimation of $x_{k+i|k}$ for $i = H_p, H_p + 1, \dots$. The controller for the first mode is designed by use of classical MPC algorithms. The controller for the second mode is designed by use of special algorithms, such as LQR, for ensuring stability. The Closed-loop Paradigm (CLP) is considered as a good framework for dual-mode MPC [92]. In this study, the CLP MPC by Rossiter [92] is adopted, which is simply described in the following.

The discrete-time state-space model of the given plant is

$$\begin{aligned} x_{k+1} &= Ax_k + Bu_k \\ y_{k+1} &= Cx_k \end{aligned} \tag{5.29}$$

The control input has the following dual-mode form

$$\underline{u}_{CLP} = \begin{bmatrix} -Kx_k + c_k \\ -Kx_{k+1|k} + c_{k+1} \\ \vdots \\ -Kx_{k+n_c|k} + c_{k+n_c-1} \\ -Kx_{k+n_c|k} \\ \vdots \\ -K\Phi^{n_y-n_c}x_{k+n_c|k} \end{bmatrix} \quad (5.30)$$

and matrix Φ is the closed-loop state matrix with the use of state feedback gain K

$$\Phi = A - BK \quad (5.31)$$

The cost function for CLP is defined as

$$J = \underline{c}^T S_c \underline{c} + 2\underline{c}^T S_{cx} x \quad (5.32)$$

where

$$\underline{c} = \begin{bmatrix} c_k^T & c_{k+1}^T & \cdots & c_{k+n_c-1}^T \end{bmatrix} \quad (5.33)$$

$$S_c = H_c^T \text{diag}(Q)H_c + H_{cu}^T \text{diag}(R)H_{cu} + H_{c2}^T P H_{c2} \quad (5.34)$$

$$S_{cx} = H_c^T \text{diag}(Q)P_{cl} + H_{cu}^T \text{diag}(R)P_{clu} + H_{c2}^T P P_{cl2} \quad (5.35)$$

$$P = \begin{bmatrix} -K \\ -K\Phi \\ -K\Phi^2 \\ \vdots \\ \vdots \end{bmatrix} \quad (5.36)$$

$$H_{cu} = \begin{bmatrix} B & 0 & 0 & \cdots \\ -KB & B & 0 & \cdots \\ -K\Phi B & -KB & B & \cdots \\ \vdots & \vdots & \vdots & \vdots \end{bmatrix} \quad (5.37)$$

The detailed derivation could be found in the Chapter 7 in the book [92].

By use of CLP, the dual-mode MPC algorithms [92] include Dead Beat Terminal Conditions (SGPC), No Terminal Control (NTC), Terminal Mode by Elimination of Unstable Modes (EUM), and Linear Quadratic Optimal MPC (LQMPC). Rossiter [92] considers that the LQMPC is the best algorithm in general and provides a well-structured objective function with unconstrained optimum on the origin. Therefore, in this study, the LQMPC described by Rossiter [92] is adopted, and presented briefly as follows.

The structure of the dual-mode MPC is shown in Fig. 5.5. An LQ regulator is designed for the inner loop with state estimation based on the Luenberger observer. K is the state feedback control gain based on the LQR design, with Q and R being the weighting matrices. The inner-loop LQ regulator can stabilize an open-loop unstable plant, and also enhance the robustness of the overall system operation. Then, $S_{cx} = 0$ for (5.32), and the cost function becomes

$$J = \sum_{i=0}^{H_p-1} (c_{k+i|k})^T \tilde{Q} c_{k+i|k} \quad (5.38)$$

where H_p is the prediction horizon, $c_{k+i|k}$ is the control perturbation and \tilde{Q} is a weighting matrix defined as

$$\tilde{Q} = B^T \Sigma B + R \quad (5.39)$$

with matrix Σ obtained by

$$\Sigma - \Phi^T \Sigma \Phi = Q + K^T R K \quad (5.40)$$

At step k , the estimation of state x_k (\hat{x}_k), is obtained via a Luenberger observer, based on which the feedback control law is the superposition of the state feedback and control perturbation, i.e.

$$u_k = -K \hat{x}_k + c_k \quad (5.41)$$

where c_k is the control perturbation based on the MPC to be designed.

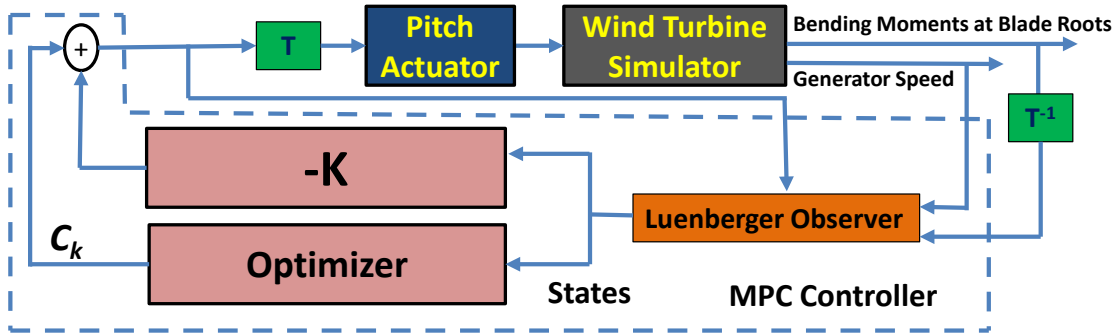


Fig. 5.5. Block Diagram of Dual-mode MPC based IPC control

The constraints for the control input are formulated as

$$M\bar{u}_k - N \leq 0 \quad (5.42)$$

where

$$\bar{u}_k = \begin{bmatrix} -K \\ -K\Phi \\ -K\Phi^2 \\ \vdots \end{bmatrix} x_k + \begin{bmatrix} I & 0 & 0 & \dots \\ -KB & I & 0 & \dots \\ -K\Phi B & -KB & I & \dots \\ \vdots & \vdots & \vdots & \vdots \end{bmatrix} \underline{c}_k \quad (5.43)$$

$$\bar{u}_k = P_{clu} x_k + H_{cu} \underline{c}_k \quad (5.44)$$

$$\bar{u}_k = \begin{bmatrix} u_k & u_{k+1} & \dots & u_{k+H_p-1} \end{bmatrix}^T \quad (5.45)$$

$$\underline{c}_k = \begin{bmatrix} c_k & c_{k+1} & \dots & c_{k+H_p-1} \end{bmatrix}^T \quad (5.46)$$

Eq. (5.44) is a compact form of Eq. (5.43) which is derived from Eqs. (5.29) and (5.41).

Substituting Eq. (5.44) into (5.42), the constraints for the control perturbation becomes

$$MH_{cu} \underline{c}_k \leq N - MP_{clu} x_k \quad (5.47)$$

When the observer is used, constraints condition is

$$MH_{cu} \underline{c}_k \leq N - MP_{clu} \hat{x}_k \quad (5.48)$$

The control perturbation c_k is calculated by solving the quadratic programming problem associated with cost function (5.38) under inequality (5.48). In the beginning, the author attempted to use the Matlab function *quadprog* in order to solve the quadratic programming optimization problem, but *quadprog* could not handle the number of constraints involved in this problem. Finally the qpOASES solver [127] was used as it performed better for the large-dimension optimization problem involved.

The foregoing scenario is for the dual-mode MPC design based on a single state-space model of wind turbine. However, when the wake center moves, the aerodynamic loads on the downstream wind turbine will change, which in turn changes the wind turbine dynamics significantly. A practical solution to such situation is to obtain linearized state-space model for different wake-center positions, based on which the MPC controller can be designed. This can be illustrated in Fig. 5.6, the solid horizontal line stands for wake center range which is equally divided by n points for controller switching. For the n points, based on the corresponding wake-center positions, different steady wind profiles without wake meandering but including wake interaction are generated in order to obtain the linearized state-space models. As shown in Fig. 5.7, the IPC controllers are switched based on wake center position, and each controller is designed with the aforementioned dual-mode MPC controller design procedure.

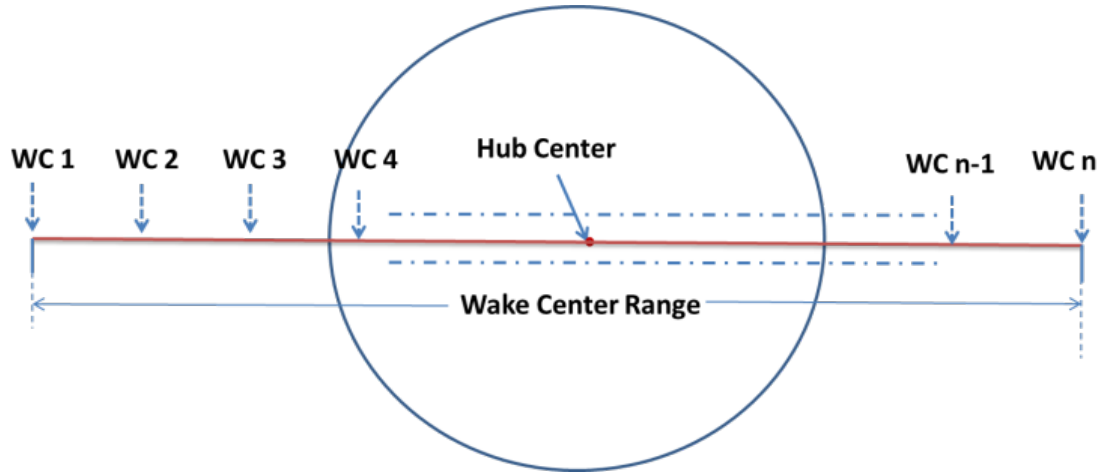


Fig. 5.6. Illustration for Wake Center Positions for Controller Switching

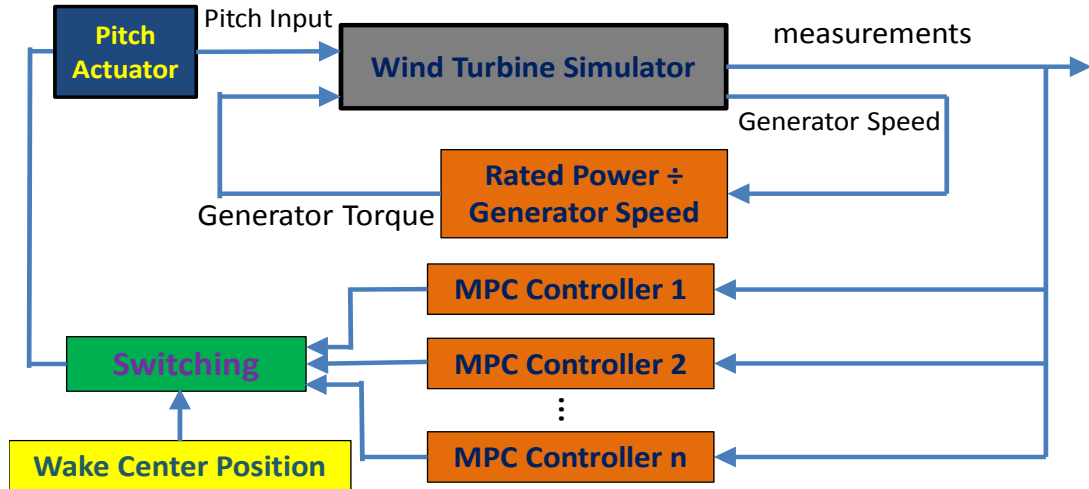


Fig. 5.7 Controller Switching for Dual-mode MPC based IPC Control under Wake Meandering

5.3. Multiple-Model Predictive Control

In previous section, the dual-model MPC controllers were simply switched to deal with wake meandering. In order to deal with time-varying operating conditions due to wake meandering and ensure smooth controller transition, a multiple-model predictive control (MMPC) algorithm [20, 122, 184] is used in this section.

The concept of MMPC design is shown in Fig. 5.8. Assume the system behavior can be approximated as some weighted average of the N linear discrete-time state-space

models

$${}^i x_{k|k-1} = {}^i A^i x_{k-1} + {}^i B \tilde{u}_{k-1} \quad (5.49)$$

$${}^i y_{k|k} = {}^i C^i x_{k|k} \quad (5.50)$$

where $i = 1, \dots, N$ is the model index and \tilde{u}_{k-1} is the control input perturbation.

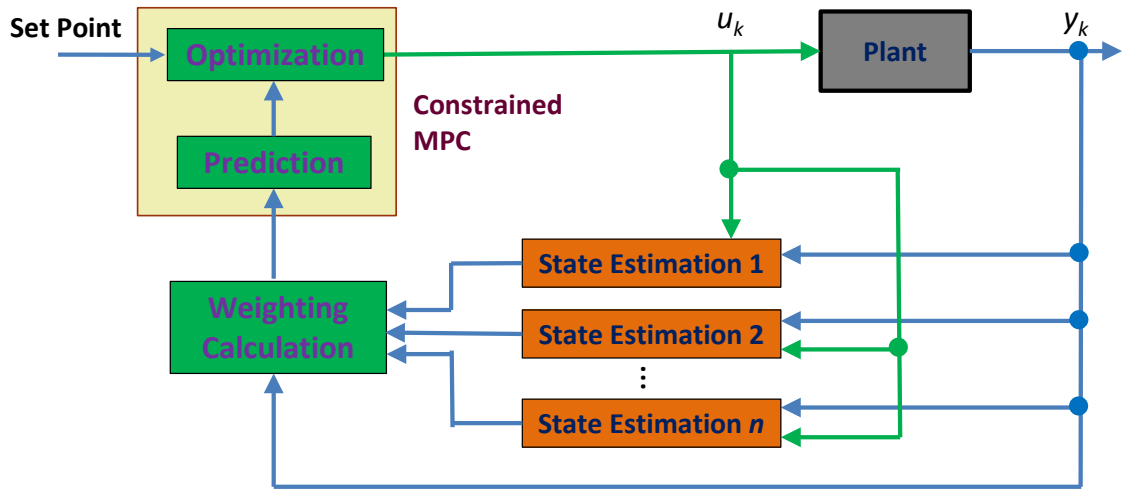


Fig. 5.8 Algorithm for Multiple-Model Predictive Control

This study follows the framework in [8], but in a simplified fashion, with the random noise and plant perturbation ignored. With such simplification, state estimation is based on the Luenberger observer, i.e.

$${}^i \hat{x}_{k|k} = {}^i \hat{x}_{k|k-1} + {}^i L(y_k - {}^i C^i \hat{x}_{k|k-1}) \quad (5.51)$$

The weighting for different models are calculated by use of Bayesian probability

$${}^i w_k = \begin{cases} \frac{{}^i p_k}{\sum_{j=1}^N {}^j p_k} & {}^i p_k > \mu \\ 0 & {}^i p_k \leq \mu \end{cases} \quad (5.52)$$

where μ is an artificial limit on the probability, and is effectively the threshold for determining the set of “active” models. Recursively, the probability of the system behavior belonging to the i -th model is

$${}^i p_k = \frac{\exp\left(-0.5 {}^i \varepsilon_k^T \Lambda {}^i \varepsilon_k\right) {}^i p_{k-1}}{\sum_{s=1}^n \exp\left(-0.5 {}^s \varepsilon_k^T \Lambda {}^s \varepsilon_k\right) {}^s p_{k-1}} \quad (5.53)$$

where

$${}^i \varepsilon_k = y_k - {}^i \hat{y}_{k|k} = y_k - {}^i C {}^i \hat{x}_{k|k} \quad (5.54)$$

Λ is a diagonal scaling matrix for the residuals and determined based on the covariance of each model. Λ needs to be tuned for plant performance adjustment.

The cost function in terms of the incremental control is defined as

$$f(\Delta U) = \frac{1}{2} \Delta U^T H \Delta U + g^T \Delta U \quad (5.55)$$

where

$$\Delta U = [\Delta \tilde{u}_k \quad \Delta \tilde{u}_{k+1} \quad \dots \quad \Delta \tilde{u}_{k+m-1}]^T \quad (5.56)$$

$$H = 2W_u + 2(S_c^a S_e)^T W_y S_c^a S_e \quad (5.57)$$

$$g = -2(S_c^a S_e)^T W_y (Y_{sp} - S_x^a - S_c^a U_0) \quad (5.58)$$

$$S_x^a = \sum_{i=1}^N {}^i W_k \begin{bmatrix} {}^i C {}^i A \\ {}^i C {}^i A^2 \\ \vdots \\ {}^i C {}^i A^p \end{bmatrix}_{(p \times n_y) \times (n_x)} {}^i \hat{x}_k \quad (5.59)$$

$$S_e = \begin{bmatrix} I_{(n_u \times n_u)} & & 0 \\ \vdots & \ddots & \\ I_{(n_u \times n_u)} & \dots & I_{(n_u \times n_u)} \end{bmatrix}_{(p \times n_y) \times ((m-1) \times n_u)} \quad (5.60)$$

$$S_c^a = \sum_{i=1}^N {}^i W_k \begin{bmatrix} {}^i C^i B & & 0 \\ \vdots & \ddots & \\ {}^i C^i A^{p-1} B & \cdots & {}^i C^i B \end{bmatrix}_{(p \times n_y) \times (p \times n_u)} \quad (5.61)$$

n_u is the number of control inputs, n_y is the number of measurements, p is the prediction horizon for the states, m is the control horizon.

For wind turbine IPC, the control inputs need to first observe to the following range constraints:

$$\begin{aligned} u_{\min} &< u_{k+j} < u_{\max} \\ u_{\min} &= \left[(0 - u_r) \pi / 180 \quad (0 - u_r) \pi / 180 \quad (0 - u_r) \pi / 180 \right]^T \\ u_{\max} &= \left[(90 - u_r) \pi / 180 \quad (90 - u_r) \pi / 180 \quad (90 - u_r) \pi / 180 \right]^T \end{aligned} \quad (5.62)$$

where u_r is the pitch reference in degree while the unit of u_{k+j} is radian. In this study, pitch references were obtained through the FAST linearization module [140] when rated rotor speed and wind profiles were known. Also, the constraints for pitch rate (radian/sec) are

$$\bar{u}_{\min} < \frac{u_{k+j} - u_{k+j-1}}{T_s} < \bar{u}_{\max} \quad (5.63)$$

where T_s is the sampling period, and

$$\bar{u}_{\min} = \left[-10\pi / 180 \quad -10\pi / 180 \quad -10\pi / 180 \right]^T \quad (5.64)$$

$$\bar{u}_{\max} = \left[10\pi / 180 \quad 10\pi / 180 \quad 10\pi / 180 \right]^T \quad (5.65)$$

As the MMPC design is applied to the time-invariant models in the non-rotating frame, the constraints (5.62) in the rotating frame need to be converted into the non-rotating frame via the MBC transformation Eq. (5.3). Besides, the cost function is valued with the incremental control input rather than control input. The MMPC for wind turbine control incorporating MBC transformation is shown in Fig. 5.9.

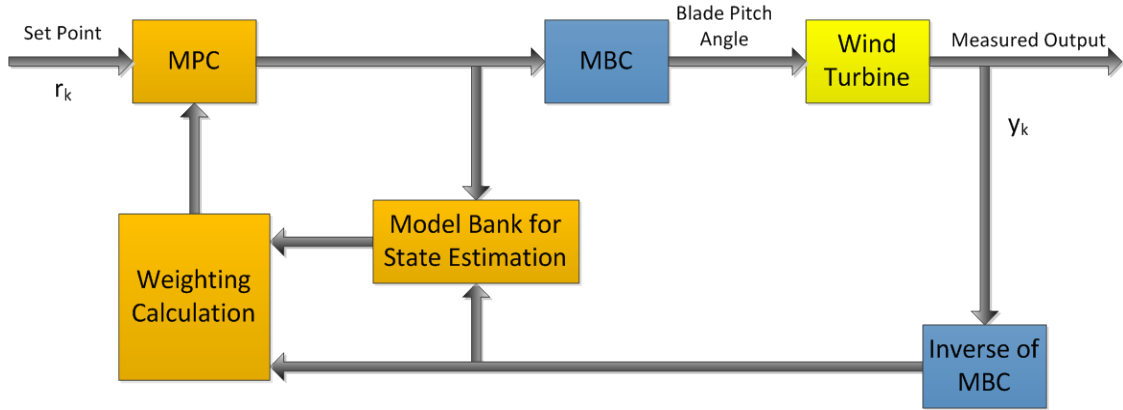


Fig. 5.9 Illustration of MMPC based Wind Turbine Control Incorporating MBC Transformation

The (blade pitch) control input sequence in the rotating frame is denoted as

$$\underline{u}_k = [u_k \quad u_{k+1} \quad u_{k+2} \quad \dots \quad u_{k+m-1}]^T \quad (5.66)$$

and its counterpart in the non-rotating frame is denoted as

$$\tilde{\underline{u}}_k = [\tilde{u}_k \quad \tilde{u}_{k+1} \quad \tilde{u}_{k+2} \quad \dots \quad \tilde{u}_{k+m-1}]^T \quad (5.67)$$

By use of MBC transformation, we have

$$\begin{Bmatrix} \underline{u}_{k-1} \\ \underline{u}_k \end{Bmatrix} = \begin{bmatrix} T & & & \\ & T & & \\ & & \ddots & \\ & & & T \end{bmatrix}_{[n_u \times (m+1)] \times [n_u \times (m+1)]} \begin{Bmatrix} \tilde{\underline{u}}_{k-1} \\ \tilde{\underline{u}}_k \end{Bmatrix} \quad (5.68)$$

The relationship between blade pitch control input and its increment is

$$\Delta U = \begin{Bmatrix} \tilde{u}_k - \tilde{u}_{k-1} \\ \tilde{u}_{k+1} - \tilde{u}_k \\ \vdots \\ \tilde{u}_{k+m-1} - \tilde{u}_{k+m-2} \end{Bmatrix} = M \begin{Bmatrix} \tilde{u}_{k-1} \\ \tilde{u}_k \end{Bmatrix} \quad (5.69)$$

where

Finally, the quadratic programming problem is to minimize cost function Eq. (5.55) with constraints Eqs. (5.72) and (5.73), and it is solved again by qpOASES [127].

5.4. Simulation Study

5.4.1. Simulation Platform

To evaluate the effectiveness of the foregoing two MPC schemes, similar to Chapter 4, simulation study has been conducted with the NREL 5MW Wind Turbine Model [185] using the FAST [186], Aerodyn [138] and TurbSim [176] software packages and Matlab® Simulink.

A particular effort in this study is that the author modified the TurbSim codes from NREL in order to generate the wind profile including wake interaction and wake meandering. The NREL 5MW [185] onshore turbine model is used, which is a three-blade variable-speed variable-pitch turbine, with rotor diameter of 126 m, blade length of 61.5 m and hub height of 87.6 m.

5.4.2. Simulated Wake Meandering Model

Allocation of upstream and downstream turbines follows Fig. 5.10. Both turbines are assumed to be the NREL 5MW turbine, as described in Appendix B. The distance between upstream and downstream wind turbines are $8D_r$. The incoming wind speed V_∞ is assumed to be 18 m/s, and the ambient turbulence intensity is 18%. Based on the spectral method and simplified wake meandering implemented in TurbSim, the wake-center trajectory along the transversal direction at the downstream wind turbine is obtained as shown in Fig. 5.11, which shows that the wake-center position falls within the range of $[-144, 173]$ m in the transversal direction and the coordinate of the averaged

wake center position is -14.5 m. The wake-center moving speed in the transversal direction falls within the range of $[-2.5, 3.0]$ m/s. Based on the Larsen wake model, the wake diameter at the downwind turbine grows to 281 m, the mean wind speed across the wake plane becomes 16.7 m/s and the time constant T_f is 7 for wake meandering in this simulation case.

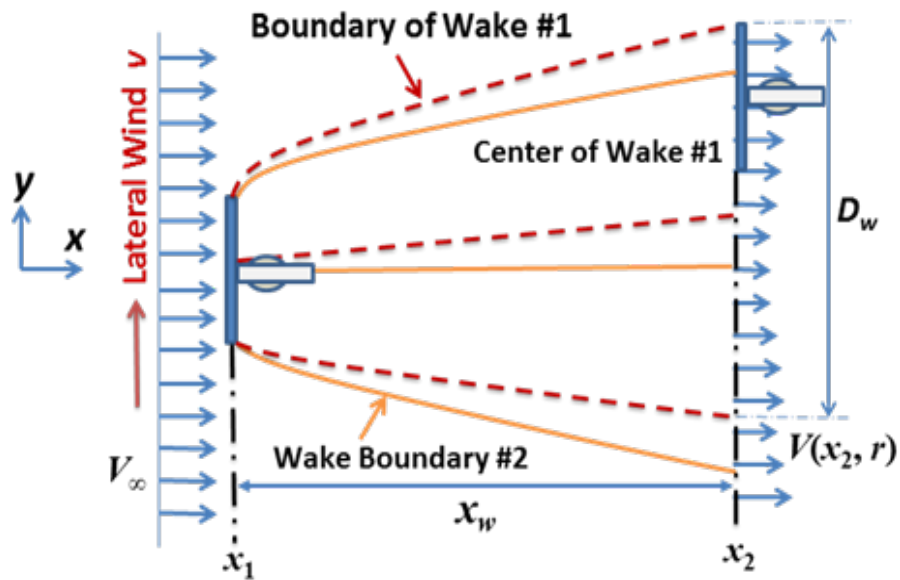


Fig. 5.10 Illustration of wake meandering for two turbines in a wind farm

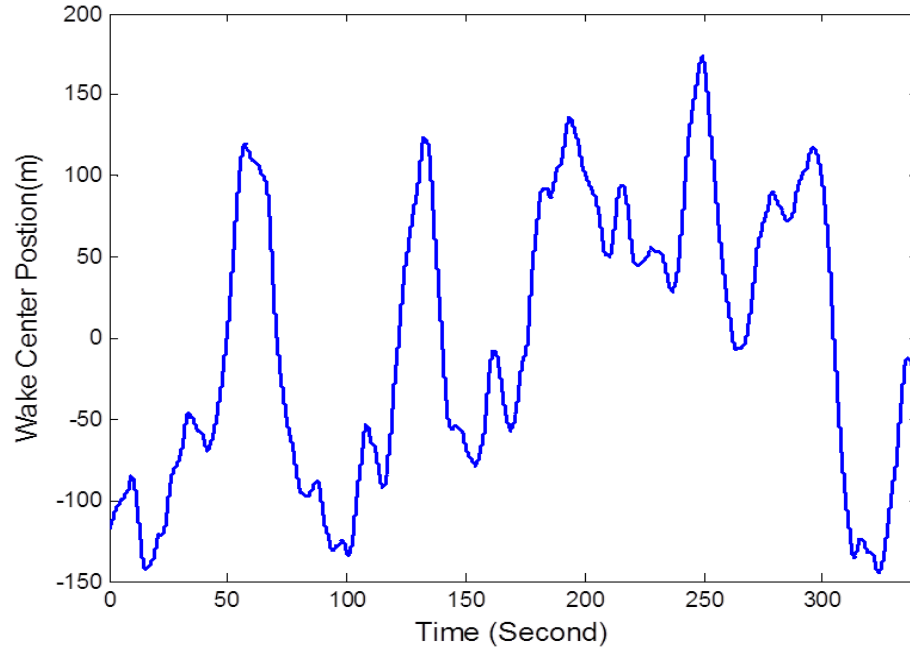
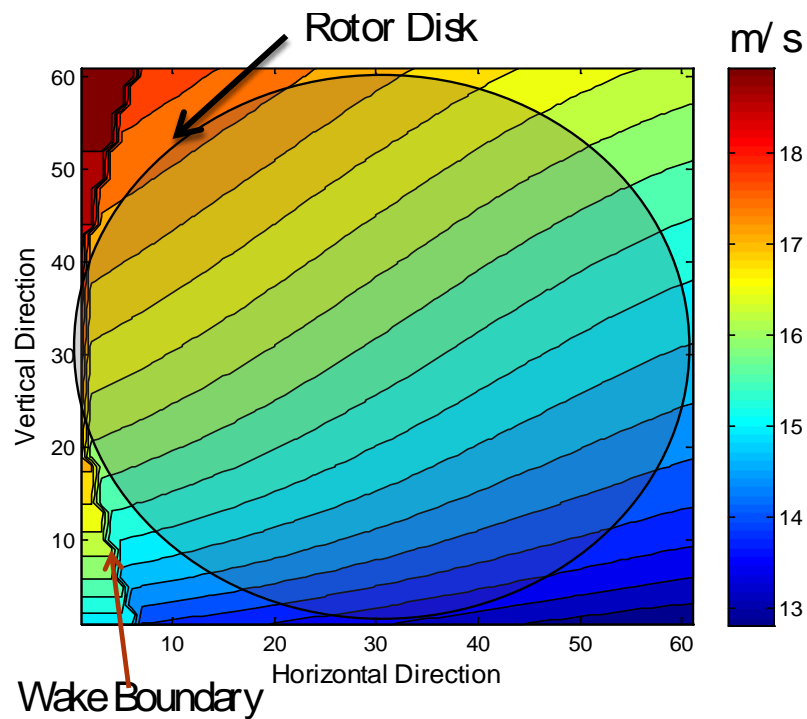
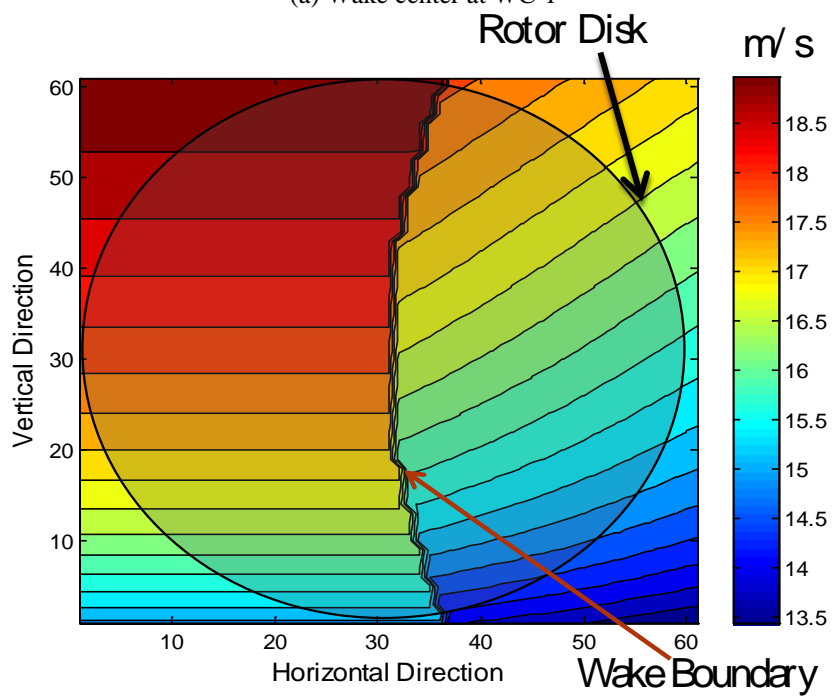


Fig. 5.11. Wake Center Trajectory at the Downstream Wind Turbine

The range is divided by 11 nodal points in equal distance. Based on the wake-center positions corresponding to the 11 nodal points, steady wind profile is generated without considering wake meandering but including wake interaction and used to obtain linearized state-space models. When the wake center position is known, Eq. (3.10) is used to compose the wind profile including wake interaction. Fig. 5.12 shows wind profiles for two positions of the wake center: one is located at the left most position and the other is when the rotor center is near the wake boundary. The difference in the wind profile is clearly observed.



(a) Wake center at WC-1



(b) Wake center at WC-11

Fig. 5.12 Wind Profiles at the Downstream Wind Turbine for Different Wake-Center Positions

5.4.3. Model Linearization and MBC Transformation

For each section in Fig. 5.6, the wind profile is assumed steady, and the corresponding linearized state-space turbine model was obtained from FAST. As shown in Table 5.1, a 9-state dynamic model is considered for the dual-mode MPC, in which the state vector includes the rotor speed, the shaft rotational strain and the flapwise bending moment for each blade. For MMPC, a 7-state model is considered by neglecting the drivetrain rotational-flexibility and its derivative in Table 5.1. The measurements for dual mode MPC include the generator speed and the flapwise bending moment at the root of each blade (Table 5.2).

For the illustrative example, and for each wind profile considered, the rotor disc is divided into 36 sectors, each covering 10° azimuth angle. Accordingly, 36 state-space models are obtained along the azimuth angle for each wind profile. The MBC [181] is used to convert the state-space models in the rotating frame to those in the fixed frame. Then the average system of the 36 linearized state space models in the fixed frame is obtained by averaging the according A, B, C, D matrices [181].

Table 5-1: STATE DESCRIPTION FOR A 9-STATE WIND TURBINE MODEL (NREL 5MW TURBINE)

Symbol	States
Δx_1	Perturbed Drivetrain Rotational-flexibility
Δx_2	Perturbed 1 st Flapwise Bending Mode of Blade 1
Δx_3	Perturbed 1 st Flapwise Bending Mode of Blade 2
Δx_4	Perturbed 1 st Flapwise Bending Mode of Blade 3
Δx_5	Perturbed Rotor Rotational Speed
Δx_6	Derivative of State Δx_1
Δx_7	Derivative of State Δx_2
Δx_8	Derivative of State Δx_3
Δx_9	Derivative of State Δx_4

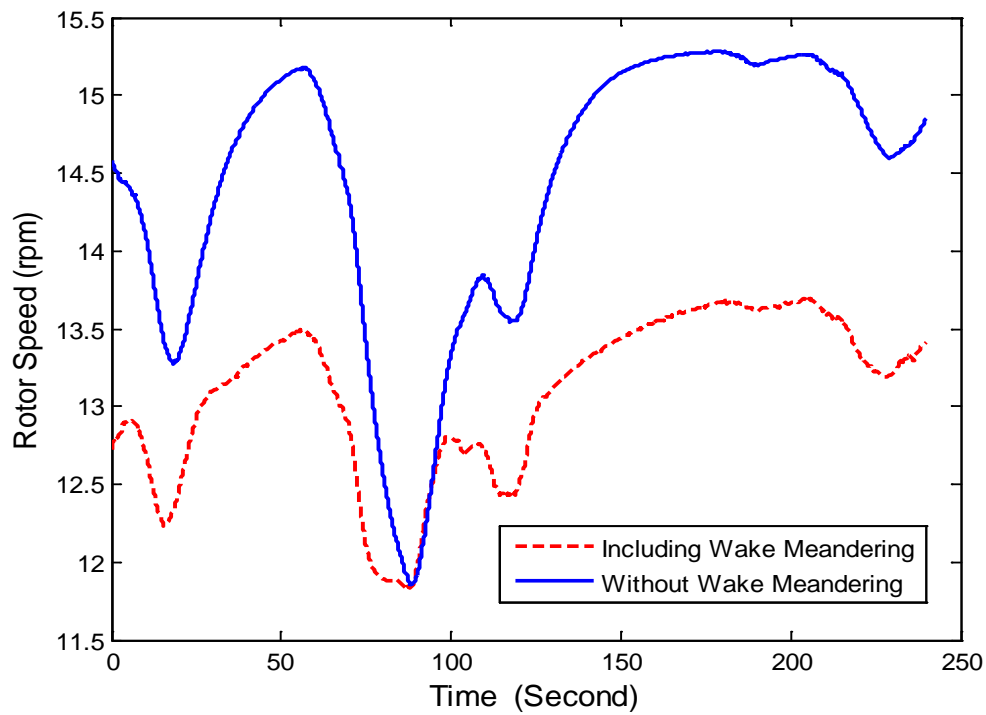
Table 5-2: MEASUREMENTS FOR NREL 5MW

Symbol	Measurements
y_1	Generator Speed or Rotor Speed
y_2	Flapwise Bending Moment at the Root of Blade 1
y_3	Flapwise Bending Moment at the Root of Blade 2
y_4	Flapwise Bending Moment at the Root of Blade 3

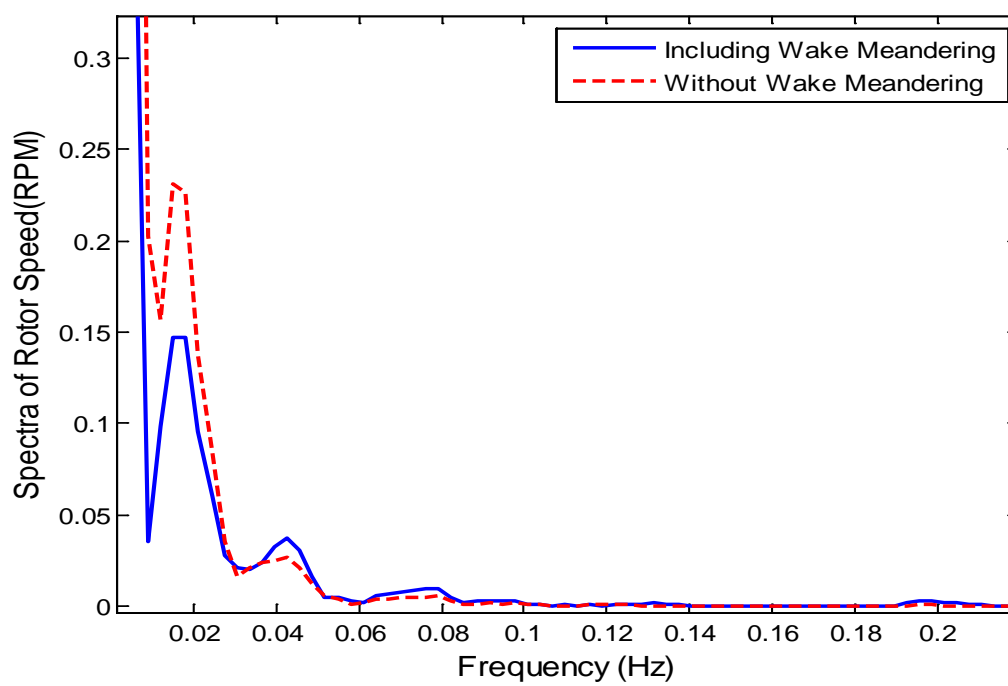
5.4.4. Simulation Results for Dual-Mode MPC Based IPC

The wind profile including wake meandering is then used to test the switching control schemes. Based on averaged state-space model generated by use of steady wind profile with averaged wake center position, the baseline MPC controller is designed first. Then, eleven switching controllers are designed to reduce the load based on state-space models generated by use of different steady wind profile with different wake center position at downstream wind turbine. The sampling period is 0.1 seconds and the prediction horizon is 20. Fig. 5.13(a) shows the temporal profile of the rotor speed using the switching controller designed based upon wake meandering model and single MPC controller. The rated rotor speed for NREL 5MW is 12.1 rpm. The corresponding spectra in Fig. 5.13(b) show that the rotor-speed fluctuation below 0.025 Hz is significantly suppressed.

Fig. 5.14 (a) shows the temporal profiles of the flapwise bending moment at the root of Blade #1 before and after the wake meandering is considered during controller design. The corresponding spectra in Fig. 5.14 (b) show that the mode at frequency about 0.13 Hz is suppressed significantly. The flapwise bending moments at other blade roots are similarly suppressed by 39% at the 1P frequency.

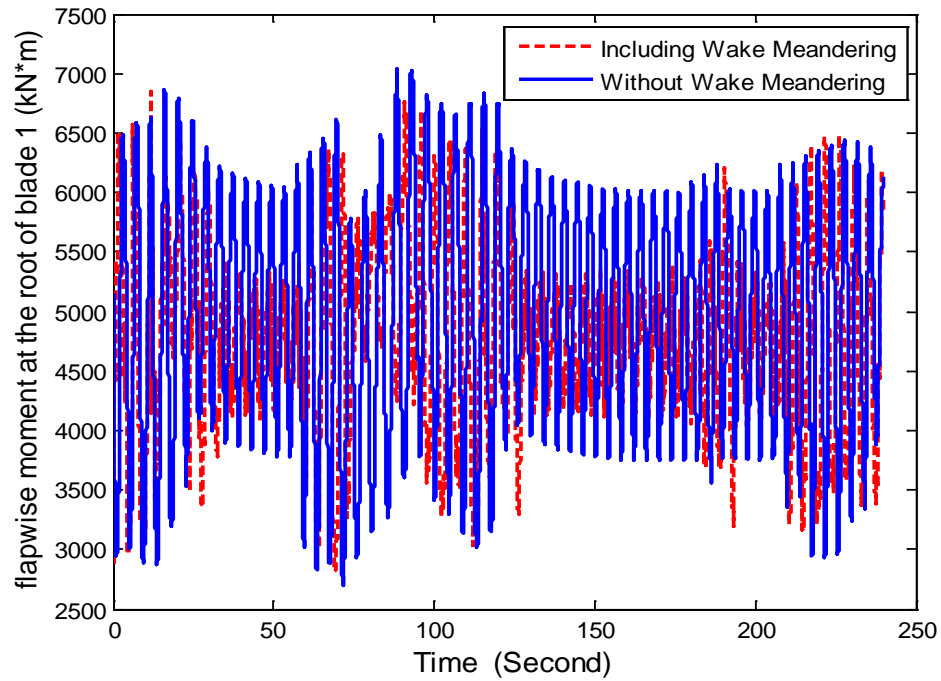


a) Steady-state Temporal Profile

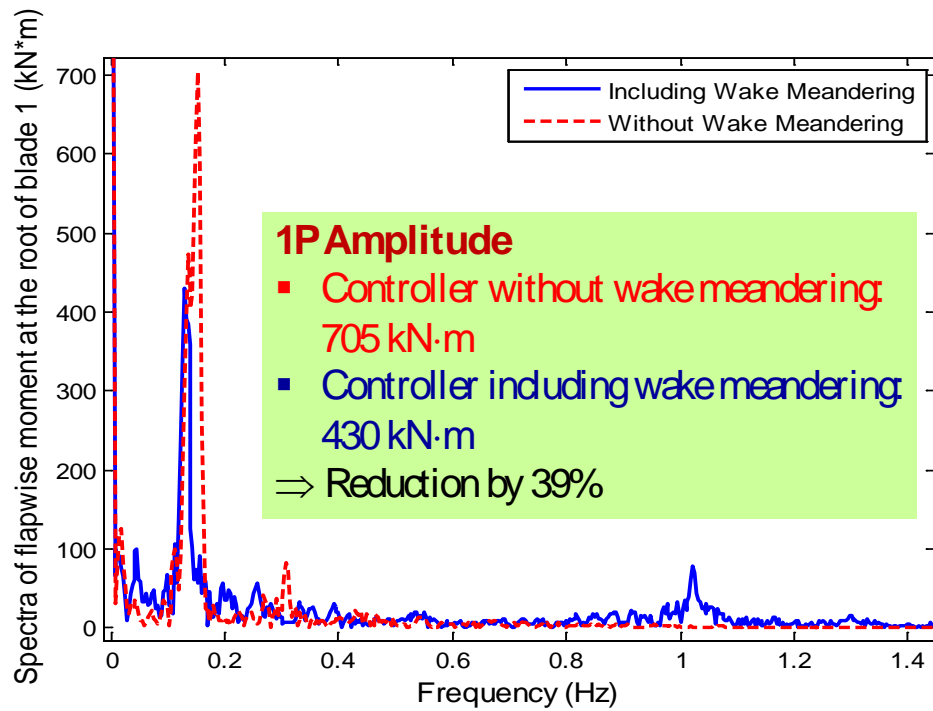


b) Spectra

Fig. 5.13. MPC Controlled Rotor Speed with and without Considering Wake Meandering



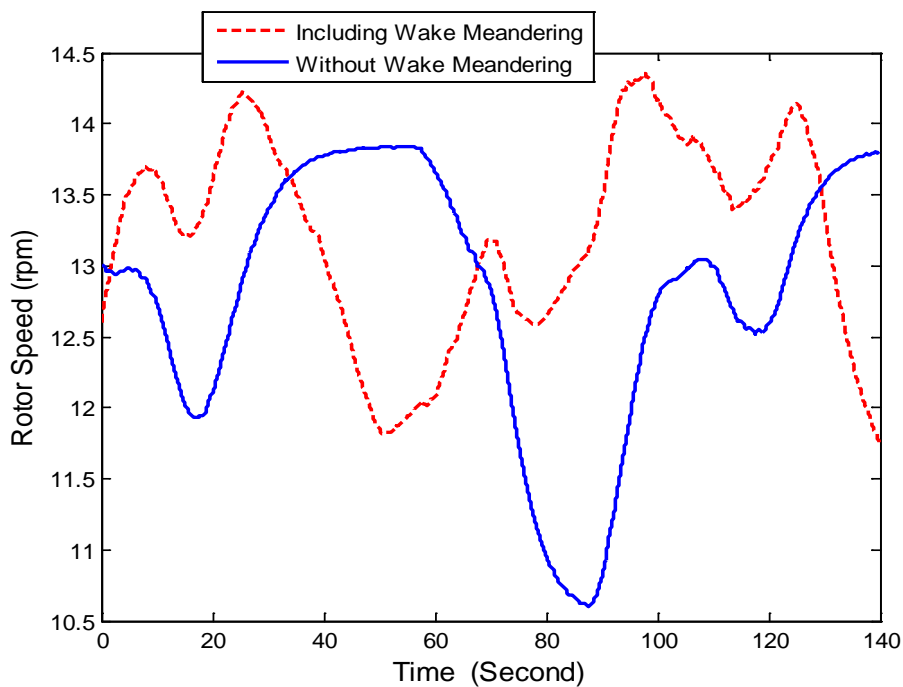
a) Steady-state Temporal Profile



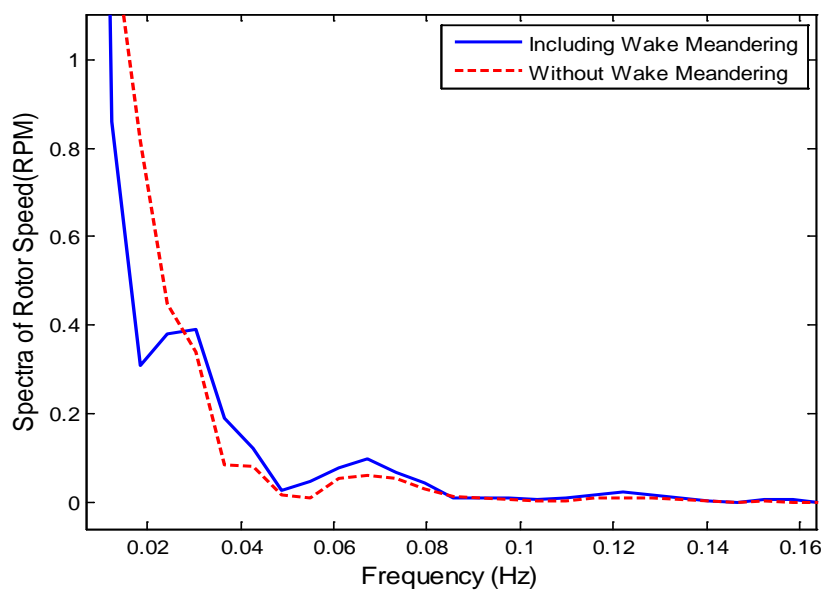
b) Spectra

Fig. 5.14: MPC Controlled Flapwise Moment at the Root of Blade-1 with and without Considering Wake Meandering

based upon wake meandering model and single MPC controller. The corresponding spectra in plot (b) show that the amplitude below 0.03 Hz is significantly suppressed.



a) Steady-state temporal profile

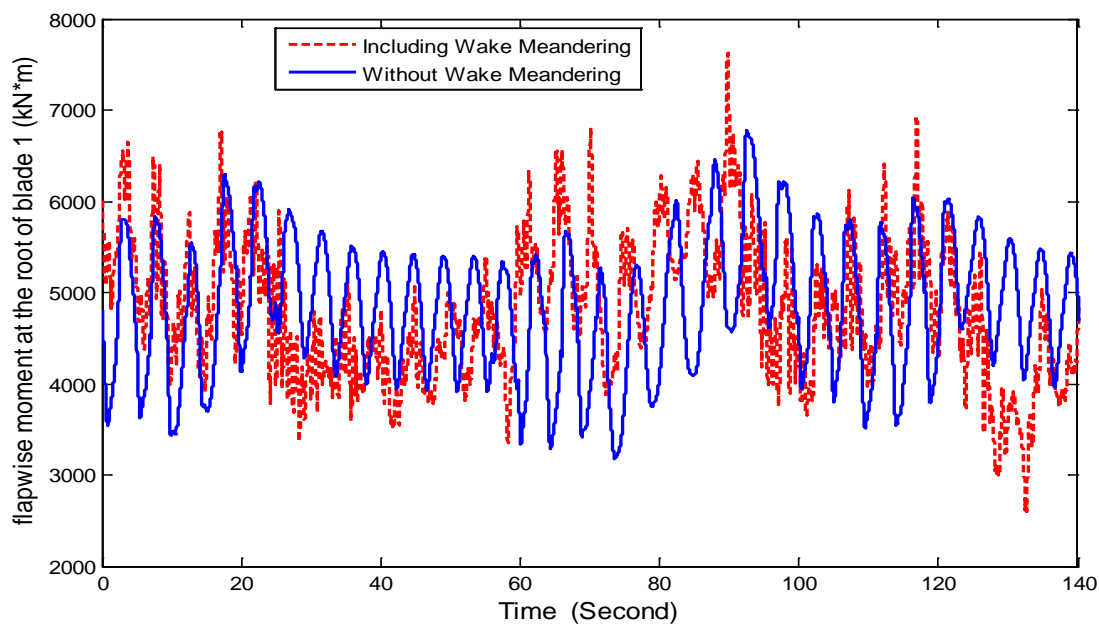


b) Spectra

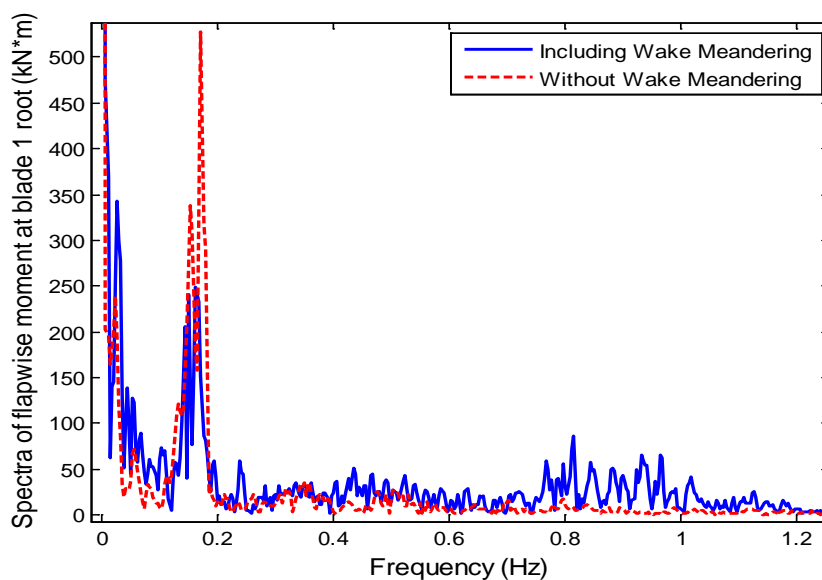
Fig. 5.15. Rotor Speed with and without Considering Wake Meandering.

Fig. 5.16 (a) shows the temporal profile of flapwise bending moment at the root of

Blade #1 before and after the wake meandering is considered during controller design. The corresponding spectra in plot (b) show that the mode at frequency near 0.2 Hz is significantly suppressed. The flapwise bending moments at other blade roots are suppressed similarly.



a) Steady-state temporal profile



b) Spectra

Fig. 5.16. Flapwise Bending Moment at the Root of Blade-1.

Fig. 5.17 shows that the rate constraints of blade pitching are basically satisfied. Fig. 5.18 shows that pitch angle remains within 0° to 90° . Fig. 5.19 shows the weighting profile between two models at a given instant, where model mode number i means that models i and $i+1$ are being used.

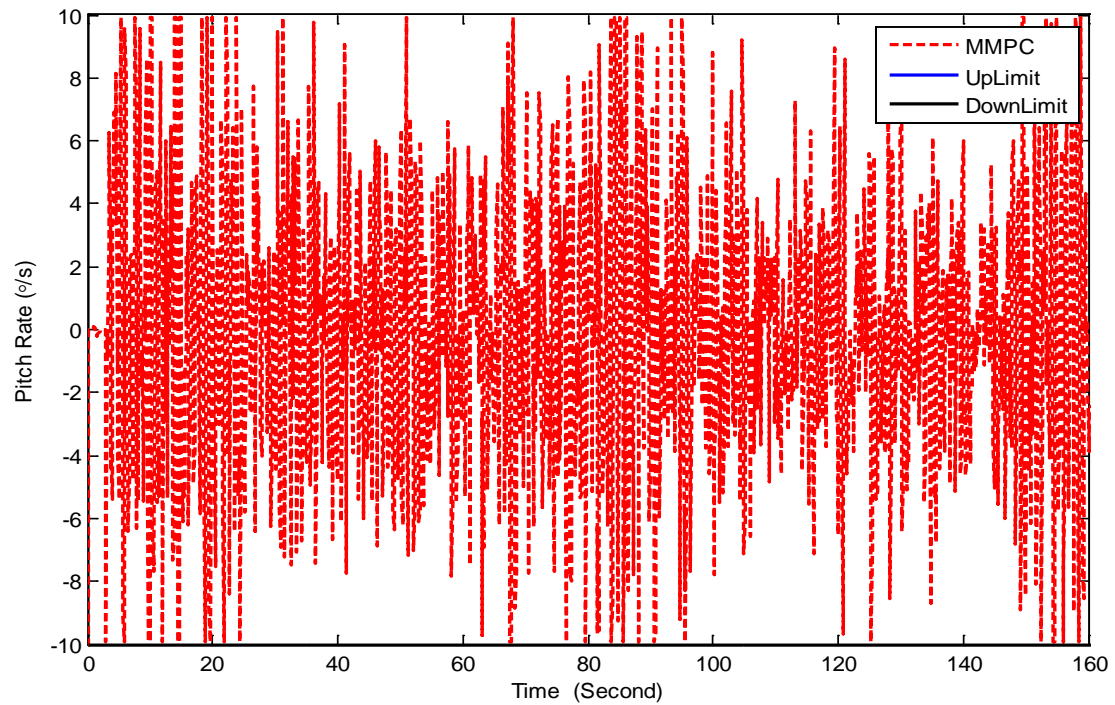


Fig. 5.17: Temporal Profile for the Pitch Angle Rate for the MMPC IPC

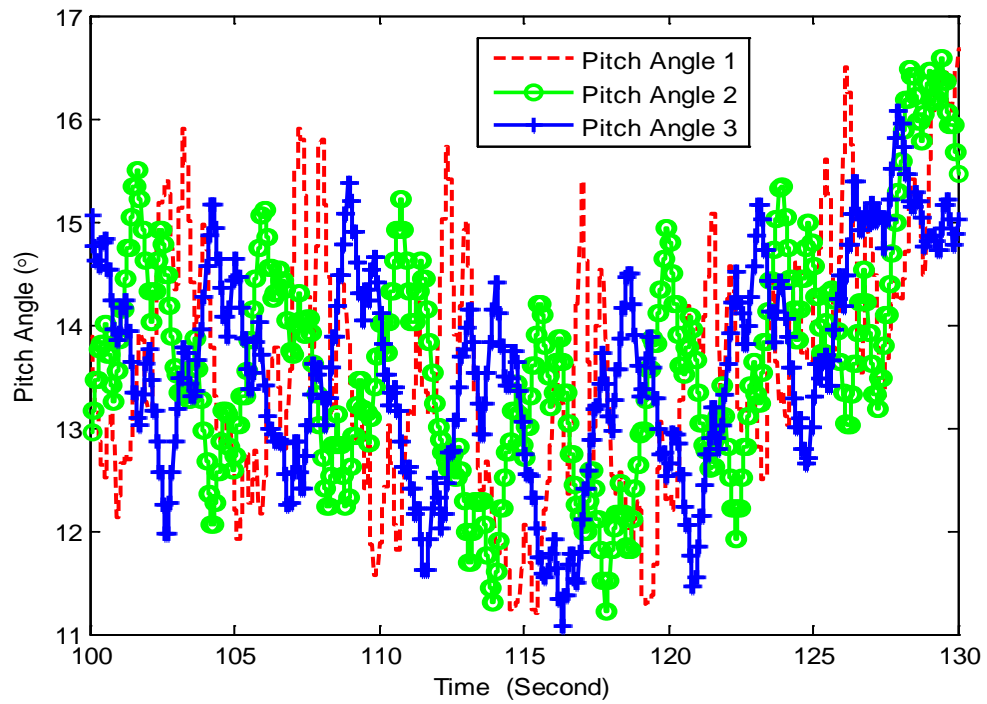


Fig. 5.18: Temporal Profile of Pitch Angle for the MMPC IPC

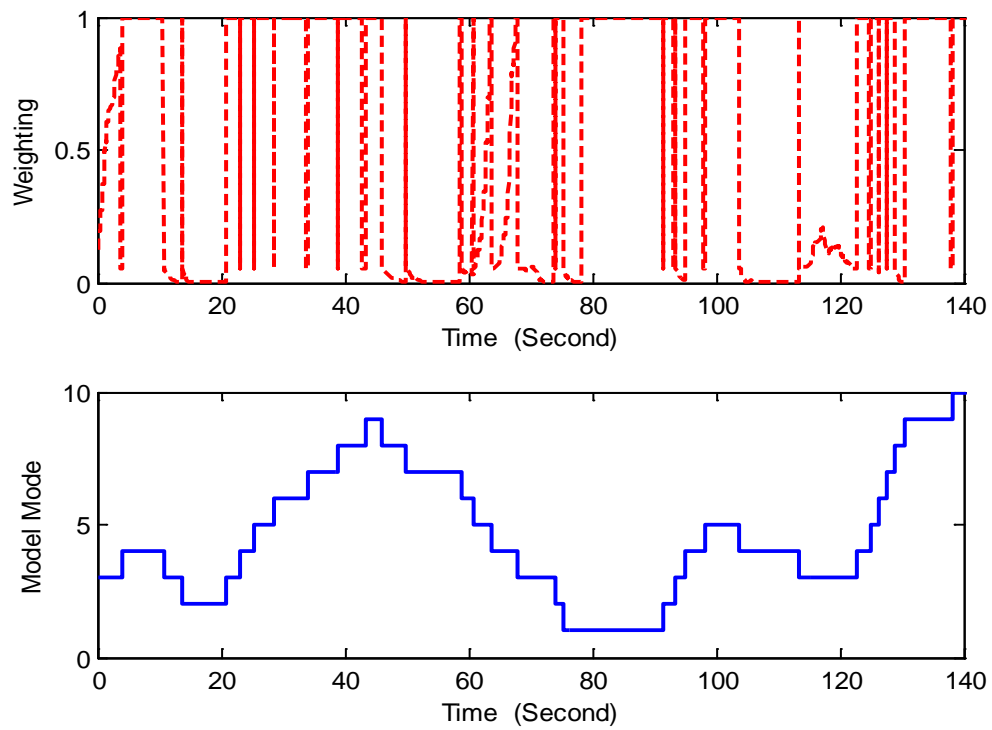


Fig. 5.19: Weighting and Model Mode in MMPC

5.5. Summary

This chapter presents two MPC based IPC schemes for load reduction of wind turbine under a wake meandering scenario, i.e. the dual-mode MPC and the MMPC. After obtaining the linearized state-space models via MBC, switched dual mode MPC are used to deal with wake meandering and MMPC are designed in order to ensure smooth controller transition. Compared to the baseline dual-mode MPC with single state-space model, the variations in the rotor speed and the blade-root flapwise moment are significantly suppressed by use of switched dual-mode MPC. While compared to the baseline MPC controller, the variations in the rotor speed and the blade-root flapwise moment are significantly suppressed by use of MMPC that incorporates wake meandering in its design.

Chapter 6. Maximizing Wind Energy Capture via Nested-loop Extremum Seeking Control

This Chapter proposes a novel control approach for optimizing wind farm energy capture with the scheme of nested-loop extremum seeking control (NLESC). Similar to Bellman's Principle of Optimality, it has been shown in earlier work that, for cascaded wind turbines, the axial induction factors of individual wind turbines can be optimized from downstream to upstream units in a sequential manner, i.e. the turbine operation can be optimized based on the power of the immediate turbine and its downstream units. In this study, this scheme is illustrated for wind turbine array with variable-speed turbines for which torque gain is controlled to vary axial induction factors.

The proposed NLESC scheme is demonstrated with a 3-turbine wind turbine array using the SimWindFarm simulation platform. Simulation results under smooth and turbulent winds show the effectiveness of the proposed scheme. Analysis shows that the optimal torque gain of each turbine in a cascade of turbines is invariant with wind speed if the wind direction does not change, which is supported by simulation results for smooth wind inputs. As changes of upstream turbine operation affects the downstream turbines with significant delays due to wind propagation, a cross-covariance based delay estimate is proposed as adaptive phase compensation between the dither and demodulation signals.

The remainder of this chapter is organized as follows. Section 6.1 presents the idea of nested optimization of cascade wind turbine array based on which the NLESC wind farm control strategy [22] is proposed. The NLESC framework for wind farm control is described in Section 6.2. For the extremum seeking control involved, an adaptive phased

compensation scheme is also presented to handle the significant delay between upstream turbine control and downstream power measurement. The simulation study is presented in Section 6.3, with conclusion in Section 6.4.

6.1. Nested Optimization of Cascaded Wind Turbine Array

For cascaded wind turbine array, the relationships on optimal axial induction factors have been recently studied by Corten and Schaak [21] based on the 1-D simplified wind turbine model. Based on this result, the NLESC has recently been proposed in a patent by Seem and Li [22]. Justification of nested-loop optimization for maximizing energy capture of a cascade of wind turbines is provided by Dr. Yaoyu Li in Appendix A. Based on the work [22] and Appendix A, the NLESC for maximizing energy capture of a cascade of wind turbines is proposed in this section. In this study, the dither extremum seeking control is adopted as the core of the NLESC although other ESC schemes may work as well. The key idea of NLESC is: the ESC (or any other appropriate self-optimizing controller) for an upstream turbine should be designed to maximize the combined total power output of this upstream turbine and downstream turbines in the wake of this upstream turbine. A better choice for self-optimizing controller is ESC.

A special case of a wind farm is that there are a cascade of turbines and wind speed blows from turbine 1 to turbine n . Turbine $i+1$ to n are in the wake of turbine i , which is shown in Fig. 6.1. This figure also shows supervisory control loop of turbines. The control objective is to maximize the total power of turbine i to n through control of turbine i . The measurement for turbine i is the sum of power of turbines i through n . The control input is generator torque. In Fig. 6.1, P_i is power of turbine i , k_i is generator torque gain for turbine i , ω_i is generator speed of turbine i .

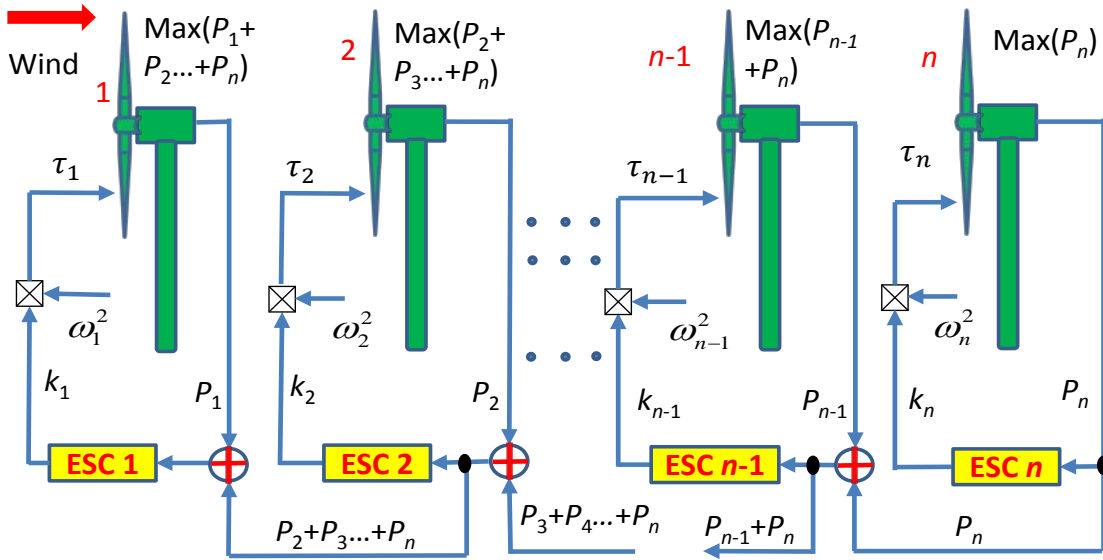


Fig. 6.1 NLESC Control for A Cascaded Array of Wind Turbines

6.2. NLESC Based Wind Farm Control Design

Extremum seeking control is used to online search an optimal input $u_{opt}(t)$ which leads to the maximum or minimum of a generally unknown time-varying cost function $l(t, u)$, where $u(t) \in \mathbb{R}^m$ is the input vector

$$u_{opt}(t) = \arg \min_{u \in \mathfrak{U}^m} l(t, u) \quad (6.1)$$

A typical ESC structure to minimum seeking [187] is shown in Fig. 6.2. $y(t)$ is the measurement of the cost function $l(t, u)$, $n(t)$ is the noise, $F_I(s)$ is the input dynamics, $F_O(s)$ is the output dynamics, d_1 is the demodulating signal, and d_2 is the dither signal;

$$d_1^T(t) = [\sin(\omega_1 t) \dots \sin(\omega_m t)] \quad (6.2)$$

$$d_2^T(t) = [a_1 \sin(\omega_1 t + \alpha_1) \dots a_m \sin(\omega_m t + \alpha_m)] \quad (6.3)$$

where ω_i are the dithering frequencies for each input channel and α_i are phase difference between the dithering and demodulating signals. The dither signal d_2 is used to generate control input perturbation which leads to cost function variance. Then High Pass Filter

$F_{HP}(s)$ is used to remove the DC value of cost function. The demodulation signals d_1 works with Low Pass Filter $F_{LP}(s)$ together to extract the signal proportional to the gradient $\partial l/\partial u$. The integral is used to ensure the stability of controller. The compensator $K(s)$ is used to accelerate the convergence.

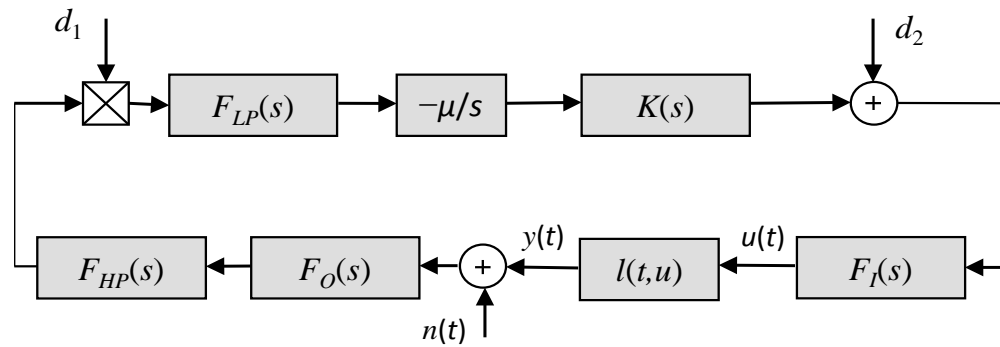


Fig. 6.2 Block Diagram of Dither ESC Algorithms

In the field of wind turbine control, ESC has been studied for maximizing energy capture of individual wind turbines [8, 188-190]. Creaby *et al.* [8] proposed multivariable ESC based on the measurement of the rotor power. Munteanu *et al.* [188] proposed wind turbulence as search disturbance instead of sinusoidal search signals for ESC design to reach maximum wind power. Pan *et al.* [189] proposed sliding mode ESC for energy capture improvement of wind turbines. Hawkins *et al.* [190] used Lyapunov-based ESC to increase energy capture of wind turbines. The ESC design in this study follows the guidelines in [187].

In the following, it will be shown how to properly choose output measurement of ESC to maximize energy capture of wind farm in steady wind and turbulent wind. A wind farm with three turbines is used as an illustrative example. Turbines 2 and 3 are in the wake of turbine 1, while turbine 3 is in the wake of turbine 2.

6.2.1. Steady Wind

The generator torque gains are used as designed control input of ESC for both steady and turbulent wind. The sum of mechanical power of all turbines in the wake of a turbine is selected as the output measurement of ESC for this turbine.

The control algorithm of three turbines under steady wind is shown in Fig. 6.3, where k_i is the generator torque gain of turbine i and ω_i is the generator speed of turbine i . The output measurement for ESC of turbine 1 is the sum of all three turbines' aerodynamic power; that for ESC of turbine 2 is the combined aerodynamic power of turbines 2 and 3.

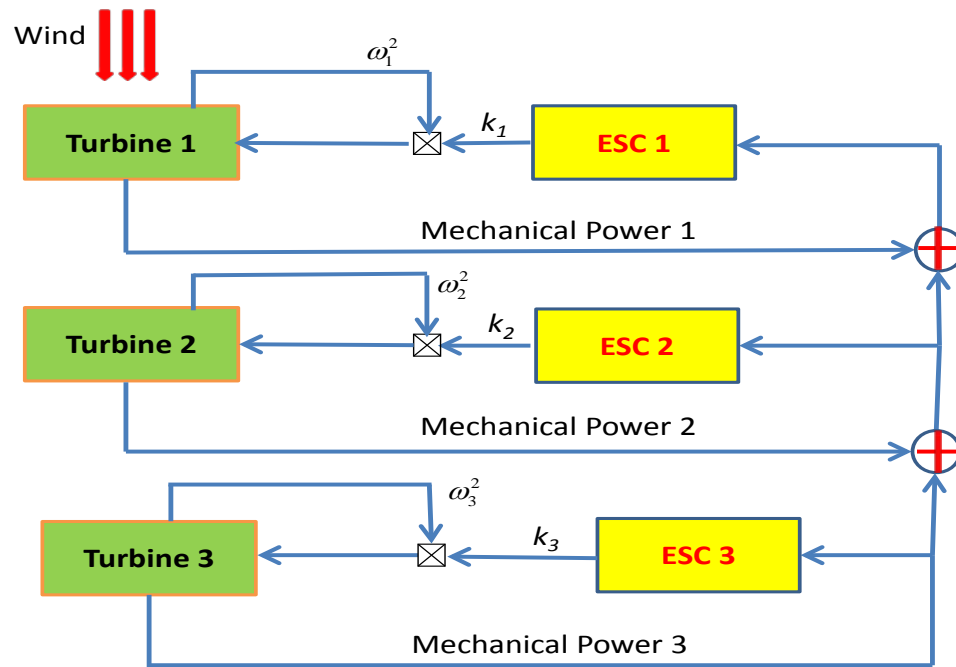


Fig. 6.3 ESC of Three Turbines under Steady Wind

6.2.2. Turbulent Wind

For turbulent wind, the power coefficient is used as the output measurement of ESC. The traditional power coefficient for individual turbines is defined as

$$C_p = \frac{P}{0.5\rho AV_\infty^3} \quad (6.4)$$

For turbines in wind farm, we need to extend the concept of power coefficient. The general power coefficient of turbine i is defined as:

$$K_i = \frac{P_i + \sum_{j=1}^m P_j}{\rho V_i^3 A / 2} \quad (6.5)$$

where P_i is the power of turbine i , P_j is the power of those turbines in the wake of turbine i , m is turbine number in the wake of turbine i , V_i is the wind speed at wind turbine i , A is the rotor area of turbine i . Similar concept is defined in [21] for a cascaded array of turbines. The generalized power coefficient concept is useful for any kind of wind farms.

Under turbulent wind, it takes time to travel to downstream turbines for air flow when wind speed at upstream turbines change. For example, for a wind farm consisting of turbines with rotor diameter $D = 126$ m (i.e. the NREL's 5 MW turbine adopted in this study), a row spacing of $5D$ leads to about 1 minute delay for wake transportation from the upstream to its downstream unit under wind speed of 8 m/s. The larger a wind turbine array is, the longer delay time of wake transportation for the whole wind farm is. In this situation, we have to redefine optimization objective general power coefficient including wake transportation delay time.

$$K_i(t) = \frac{P_i(t-T_i) + \sum P_j(t-T_j) + P_k(t)}{\rho(V_i(t-T_i))^3 A / 2} \quad (6.6)$$

where all turbine j and k are in the wake of turbine i . We assume that it takes the longest time to arrive turbine k for air flow from turbine i , which is compared with the transportation time from turbine i to other turbines j . T_i is the transportation time of air

flow from turbine i to turbine k . T_j is the difference between transportation time of air flow from turbine i to k and that from turbine j to k .

The discrete-time general power coefficient is

$$K_i(m) = \frac{P_i(t-l_i) + \sum P_j(m-l_j) + P_k(m)}{\rho(V_i(m-l_i))^3 A / 2} \quad (6.7)$$

where m is the current time, l_i and l_j are the indices of T_i and T_j , respectively.

6.2.3. Cross-Covariance Based Adaptive Delay Compensation

When wind speed at upstream changes, wake transportation delay time between upstream and downstream turbines also changes. The time delay in Eq. (6.7) can be estimated based on the cross covariance between two wind speed signals, i.e.

$$\hat{R}_{DC} = \frac{1}{N} \sum_{k=1}^N [V_1(kT) - \bar{V}_1][V_2(kT + \tau) - \bar{V}_2] \quad (6.8)$$

where T is the sampling interval, \bar{V}_1 and \bar{V}_2 are the average value, and N is the number of samples used for estimation. The delay can be determined by

$$\hat{D}_{DC} = \arg \left[\max_{\tau} (\hat{R}_{DC}(\tau)) \right] \quad (6.9)$$

6.3. Simulation Study

To evaluate the effectiveness of the proposed NLESC scheme, simulation study has been conducted with SimWindFarm [191]. The SimWindFarm platform an open source toolbox based on Matlab/Simulink, which is suitable for wind farm control design. It includes the capability of layout planning for a given wind farm, and simulation can be performed under different wind conditions. In particular, wake effects are simulated by

including the dynamic wake meandering as described in [18]. Simplified NREL 5MW model [191] is used in SimWindFarm through modification of NREL 5MW model [192] for the wind turbine array. In this study, in order to implement NLESC, the default controller for NREL 5MW in SimWindFarm was modified so that the torque gain, instead of the power reference, is used as the control input for each turbine.

Throughout this study, the wind turbine array simulated consists of a cascade of three turbines with 5D (i.e. 630 m) spacing. Simulations are performed for both steady and turbulent winds.

6.3.1. Simulation for Steady Wind

For steady wind, two free-stream (i.e. at the first turbine) wind speeds are simulated, 6m/s and 10 m/s, respectively.

First, the static map between the total power output and the torque gains is obtained. For 6 m/s, the maximum total power is 1.7246 MW with the corresponding optimal torque gains for turbines 1, 2, and 3 being 2.9, 2.85 and 2.3, respectively. The optimal torque gain for the third turbine is the same with that in individual turbine control level because there is no other turbine in its wake. Fig. 6.4 shows the power coefficient map in terms of the tip speed ratio (TSR) for the stand-alone NREL 5MW turbine, in which the optimal TSR is achieved at torque gain of 2.3. A power map in terms of the torque gains of Turbine #1 and Turbine #2 is shown in Fig. 6.5, with torque gain of Turbine #3 at its optimum of 2.3.

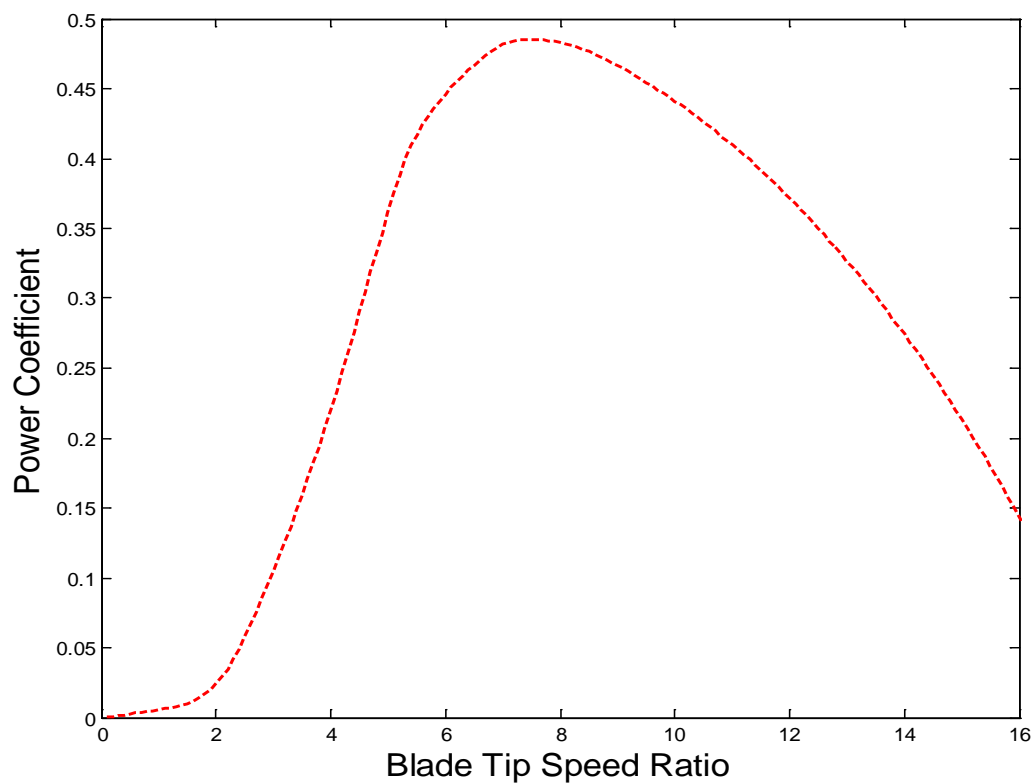


Fig. 6.4 Power Coefficient of NREL 5MW with Pitch Angle 0°

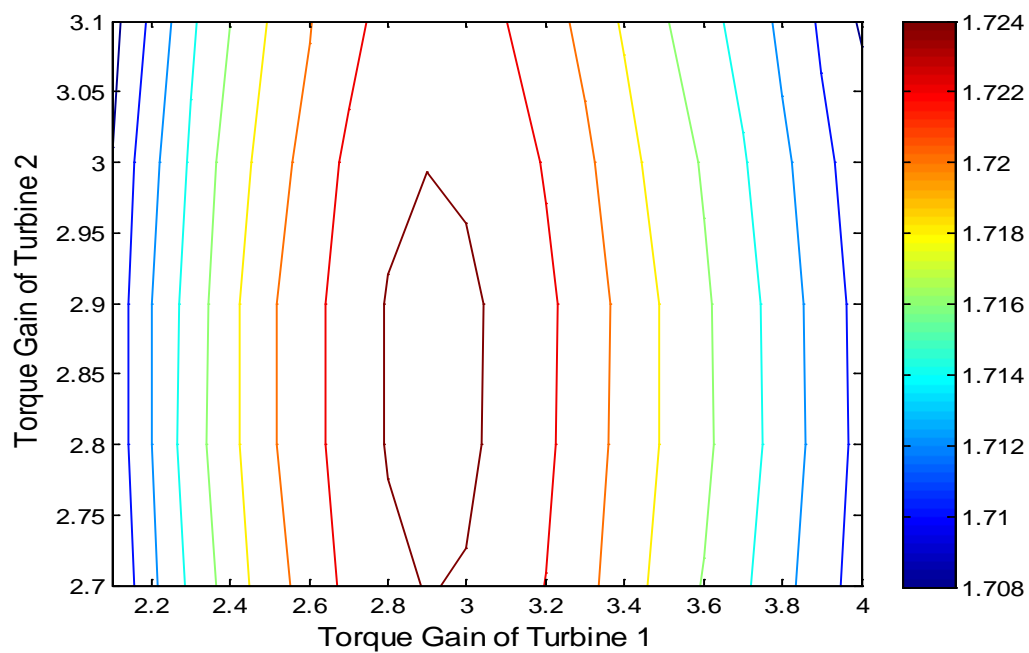


Fig. 6.5 Static Map of Power Capture for Two Cascaded Turbines at 6m/s

For the dither ESC algorithm shown in Fig. 6.2, the dither period is usually chosen 8 to 10 times of the period corresponding to the cut-off frequency of the input dynamics. The input dynamics for the third turbine (i.e. the stand-alone operated turbine) is determined by step response test in SimWindFarm simulation, with the torque gain as input and the power as output. As to be seen later, the input dynamics of power regulation is a first-order system, without delay for the immediate turbine, while with delay for downstream turbines. The time constant for the input dynamics without delay is estimated by linear regression after log transformation of the step response data [8, 193], which is briefly described below.

For an individual turbine or last one in an array of turbines, a first-order dynamics is used to approximate its input dynamics between torque gain and power. Its transfer function could be described as

$$F_{IP}(s) = \frac{1}{\tau s + 1} \quad (6.10)$$

Its step response could be described as

$$X_{out}(t) = KA_{in}(1 - e^{-t/\tau}) \quad (6.11)$$

If a logarithmic transformation is applied to the system output, we obtained a linear relation between the transformed output and the time

$$Z = \ln\left(1 - \frac{X_{out}}{KA_{in}}\right) = -\frac{t}{\tau} \quad (6.12)$$

where the slope is

$$\frac{dZ}{dt} = -\frac{1}{\tau} \quad (6.13)$$

With the recorded data points, the time constant τ can be estimated by linear regression:

$$\tau = -\frac{\Delta t}{\Delta Z} \quad (6.14)$$

For the NREL 5MW turbine, the step response of power output under torque-gain input is shown could be found in Fig. 6.6. Then Z could be calculated by Eq. (6.12), as shown in Fig. 6.7. By Eq.(6.14), the time constant of input dynamics is 8 second.

Then dither period in ESC for the third turbines is chosen as 80s, which are about 10 times of their respectively period of input dynamics.

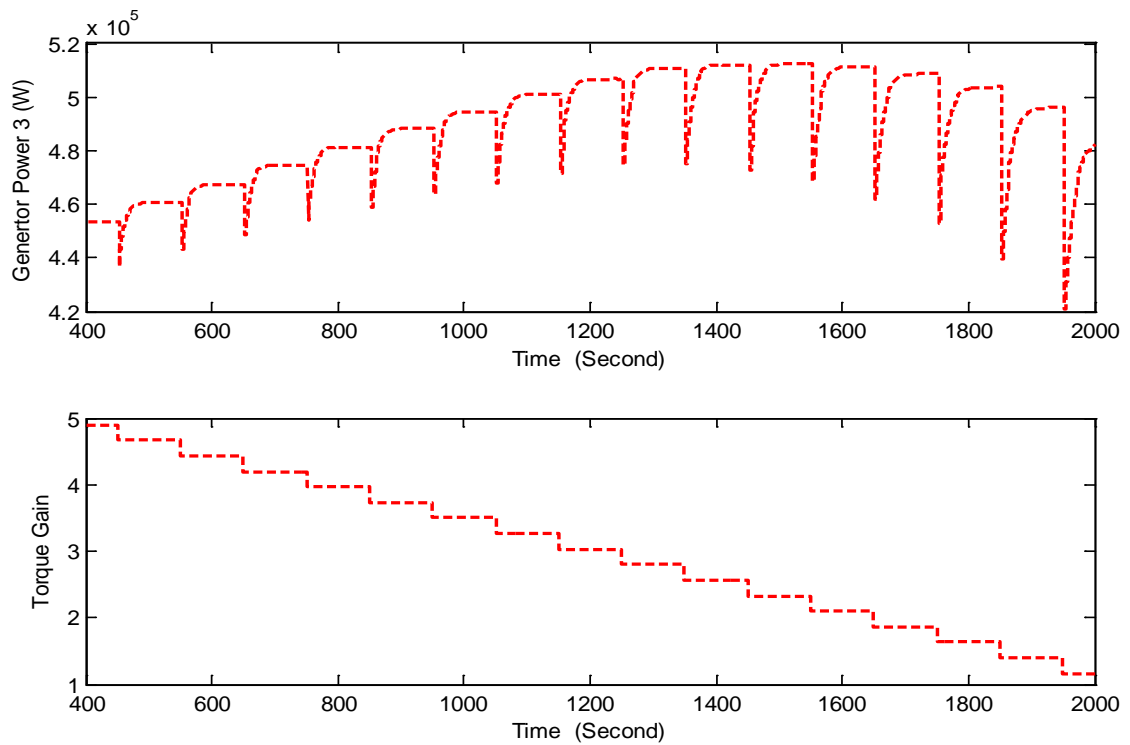


Fig. 6.6 Step Response of NREL 5MW Power

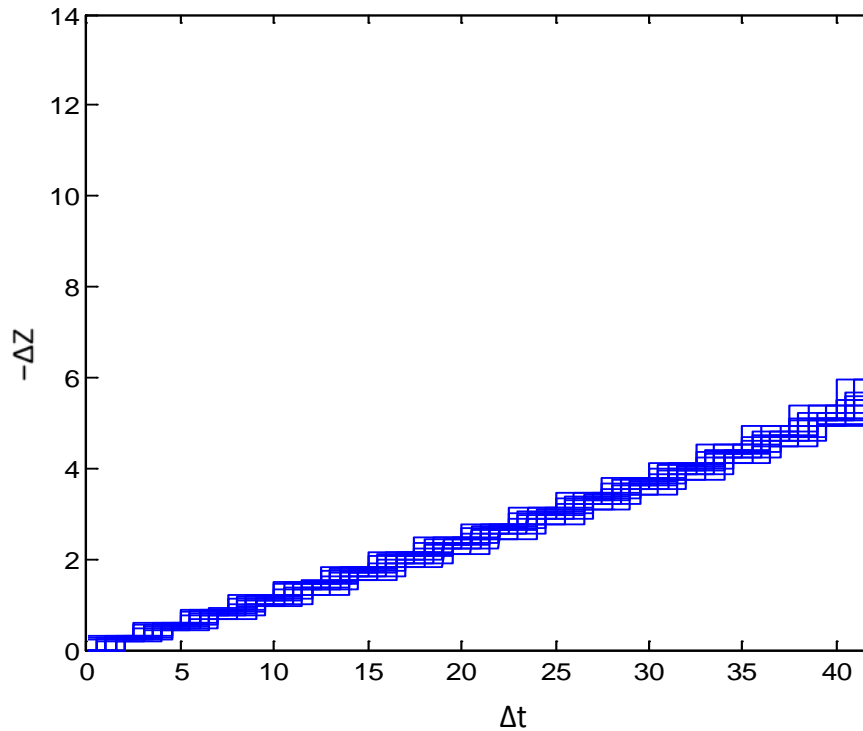


Fig. 6.7 Estimation of Time Constant of for Torque Based Power Regulation

For the third turbine, the high-pass filter in ESC is

$$\frac{s^2}{s^2 + 0.1111s + 0.0062} \quad (6.15)$$

while the low-pass filter in ESC is

$$\frac{0.0062}{s^2 + 0.1111s + 0.0062} \quad (6.16)$$

The Bode diagrams of input dynamics, low-pass filter and high-pass filter for the 3rd turbine is shown in Fig. 6.8. The dither frequency for the 3rd turbine is 0.0785 rad/s. The phase angle in dither signal for 3rd turbine is chosen as $\alpha_p = -57.8581^\circ$, which results in $\theta_p = \alpha_p + \angle F_{IP}(j\omega_p) + \angle F_{HP}(j\omega_p) \approx 0^\circ$ at this dither frequency.

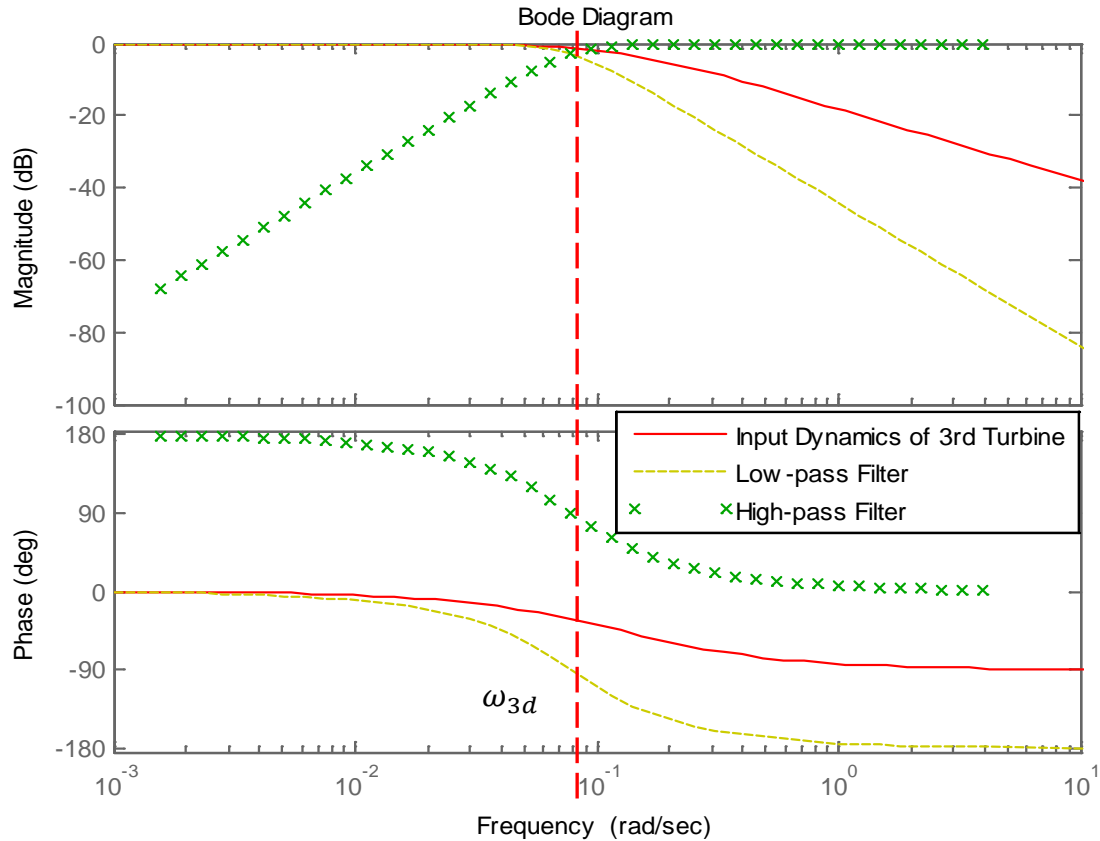


Fig. 6.8 Illustration of ESC Dither Frequency and Phase Compensation for Turbine #3

The input dynamics between torque gain of the second turbine and the power summation of the 2nd and 3rd turbine could be estimated by first-order dynamics (6.10) with time delay due to wake transportation, i.e.

$$F_{IPd}(s) = e^{-sT_2} F_{IPd}(s) = \frac{e^{-sT_2}}{\tau s + 1} \quad (6.17)$$

where T_2 is the delay time due to wake transportation.

Similarly, the input dynamics between torque gain of the 1st turbine and the power summation of the 1st, 2nd and 3rd turbine could also be estimated by Eq. (6.17). The only difference is that T_2 is replaced with T_1 the wake transportation time from the 1st turbine to 3rd turbine.

For the case with wind speed 6m/s at the 1st turbine, wake transportation time from the second turbine to the third turbine is about 105 second ($= 5 \times 126 \text{m} \div 6 \text{m/s}$), which is lower than actual wake transportation time due to wind deficit after turbines. Similarly, wake transportation time from 1st turbine to 3rd turbine is 226 ($= 113 \times 2$) seconds.

Then, the dither periods in ESC for the first and second turbines are chosen as 2800s and 1400s, which are about 10 times of their respectively period of input dynamics.

For the first turbine, the high-pass filter in ESC is designed as

$$\frac{s^2}{s^2 + 0.0032s + 5.0355 \times 10^{-6}} \quad (6.18)$$

while the low-pass filter is designed as

$$\frac{5.0355 \times 10^{-6}}{s^2 + 0.0032s + 5.0355 \times 10^{-6}} \quad (6.19)$$

The Bode diagram of input dynamics, low-pass filter and high-pass filter for 1st turbine is shown in Fig. 6.9. Dither frequency for 1st turbine is 0.0022 rad/s. For better extraction of gradient information, the phase angle is chosen as $\alpha_p = -59.9144^\circ$, which results in $\theta_p = \alpha_p + \angle F_{IP}(j\omega_p) + \angle F_{HP}(j\omega_p) \approx 0^\circ$ at this dither frequency.

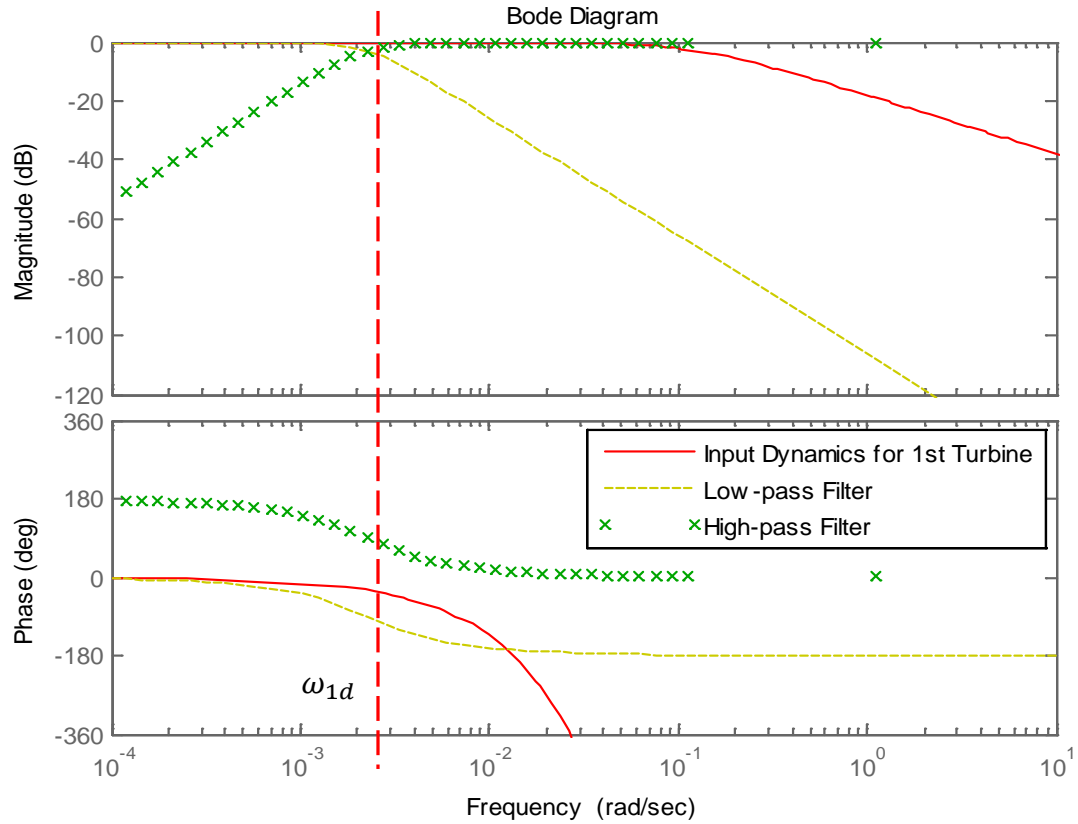


Fig. 6.9 Illustration of ESC Dither Frequency and Phase Compensation for Turbine #1

For the second turbine, the high-pass filter in ESC is designed as

$$\frac{s^2}{s^2 + 0.0063s + 2.0142 \times 10^{-5}} \quad (6.20)$$

while the low-pass filter in ESC is

$$\frac{2.0142 \times 10^{-5}}{s^2 + 0.0063s + 2.0142 \times 10^{-5}} \quad (6.21)$$

Similarly, the Bode diagrams of input dynamics, low-pass filter and high-pass filter for the 2nd turbine is shown in Fig. 6.10. The dither frequency for the 2nd turbine is 0.0045 rad/s. For better tracking, the phase angle is chosen as $\alpha_p = -60.9437^\circ$, which results in

$$\theta_p = \alpha_p + \angle F_{IP}(j\omega_p) + \angle F_{HP}(j\omega_p) \approx 0^\circ \text{ at this dither frequency.}$$

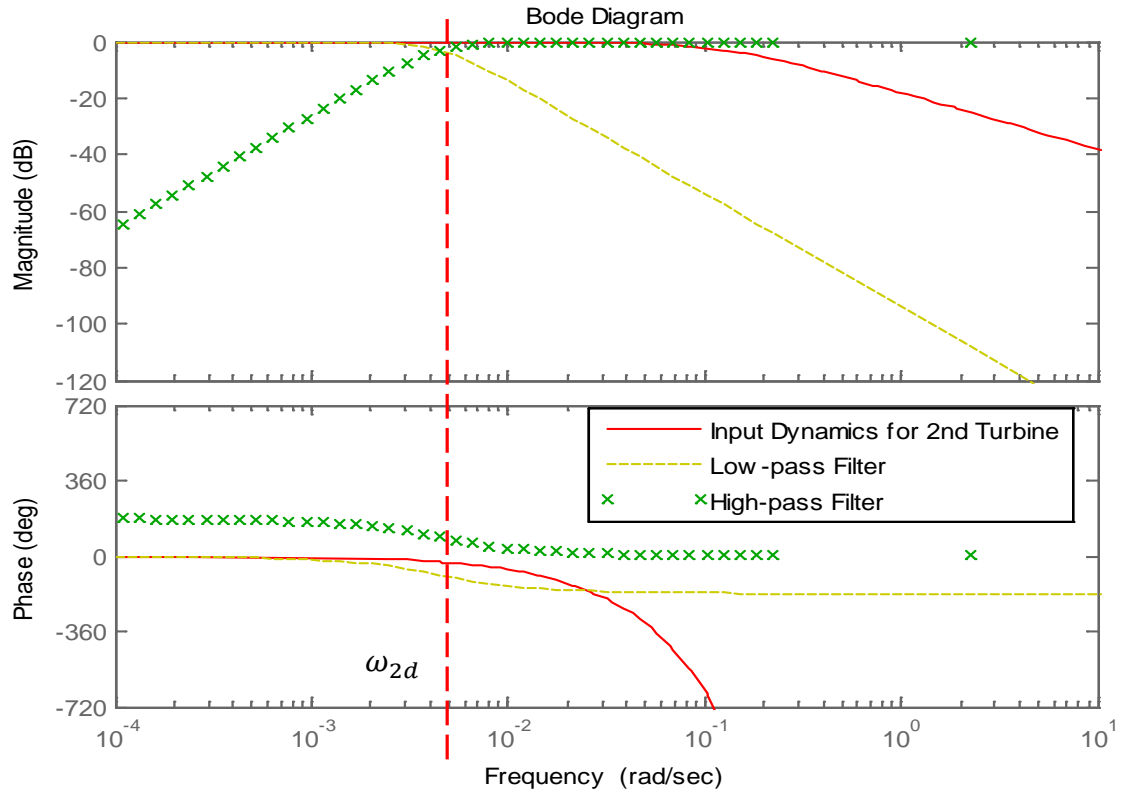


Fig. 6.10 Illustration of ESC Dither Frequency and Phase Compensation for Turbine #2

For the smooth 6 m/s wind, the forward loop gains for the 1st, 2nd and 3rd turbine are set at 8×10^{-8} , 1.5×10^{-7} and 1.2×10^{-5} , respectively. For the 10 m/s case, the forward loop gains for the 1st, 2nd and 3rd turbines are set as 1×10^{-8} , 2.5×10^{-8} and 1.2×10^{-6} , respectively. For steady wind cases, the dither amplitudes are 0.01, 0.01 and 0.05 for 1st, 2nd and 3rd turbine, respectively.

The torque gains for three turbines are plotted in Fig. 6.11, which shows torque-based ESC for three turbines are turned on at 400s, 1500s and 3500s, respectively. In current simulation, the ESC controllers of three turbines are turned on in sequence in order to better distinguish the associated searching transients. The wind speed profiles at the three turbines are shown in Fig. 6.12, which reveals that the wind speeds at the second and

third turbines both increase when the ESC's for the first and second turbines were turned on.

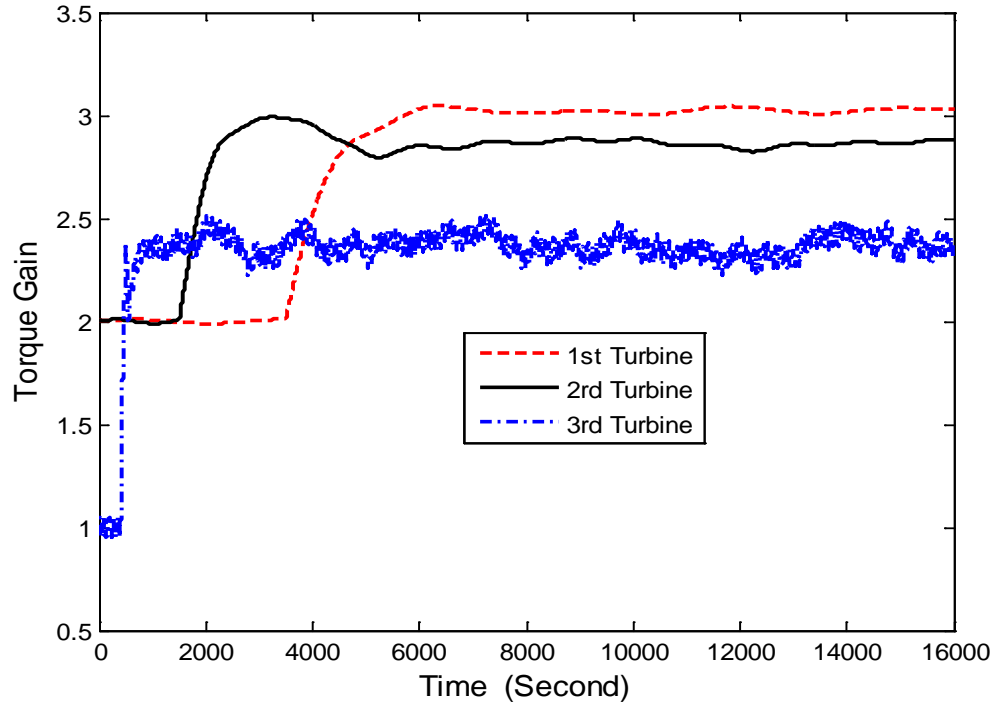


Fig. 6.11 Torque Gain Profiles for NLESC Search under 6m/s Smooth Wind

The generator speeds for the three turbines are plotted in Fig. 6.13, which shows that the generator speed profiles of Turbines 1 and 2 are reduced when their ESC are turned on. Fig. 6.12 and Fig. 6.13 show that the rotor speeds of upstream turbines are reduced so that the wind speeds at the downstream turbines increase, and in consequence, the total power output of the wind farm increases. Fig. 6.14 compares the total power output of the ESC control with that by use of SimWindFarm's default controller, which is described in Appendix G. During the period [10000s, 16000s], the total energy captured increases by 8.7%. During the same period, the average torque gains for the 1st, 2nd and 3rd turbines are 3.02, 2.86 and 2.36, respectively, as compared to the corresponding optimum values of 2.9, 2.85 and 2.3, respectively from the static map.

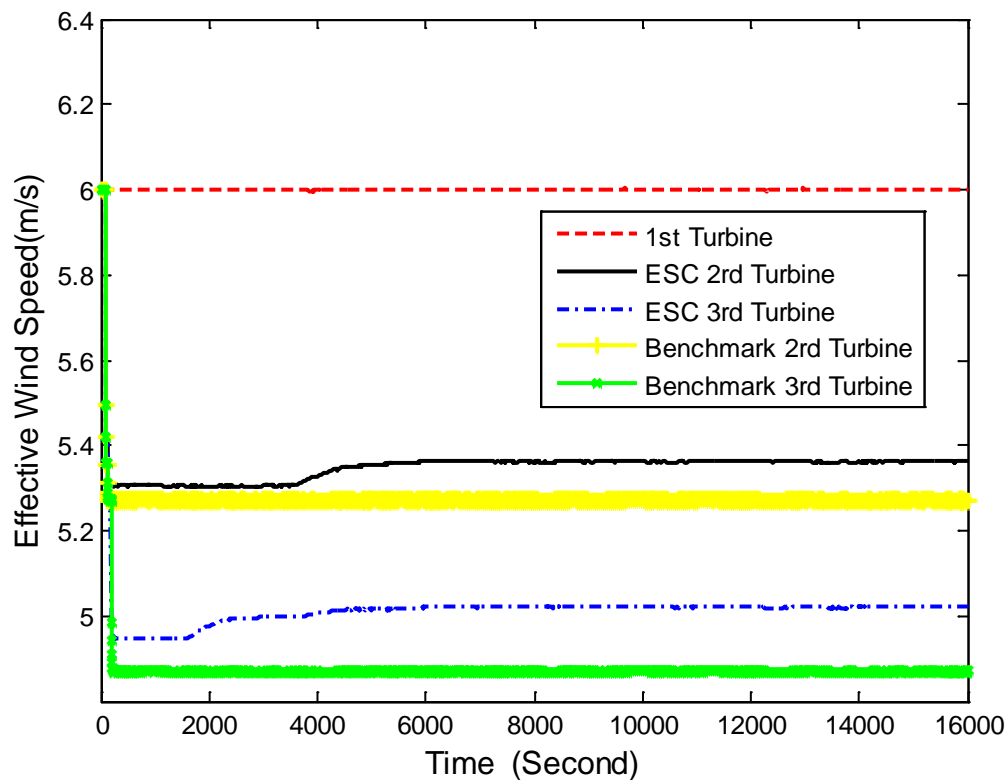


Fig. 6.12 Wind Speed at Each Turbine for NLESC Search under 6m/s Smooth Wind

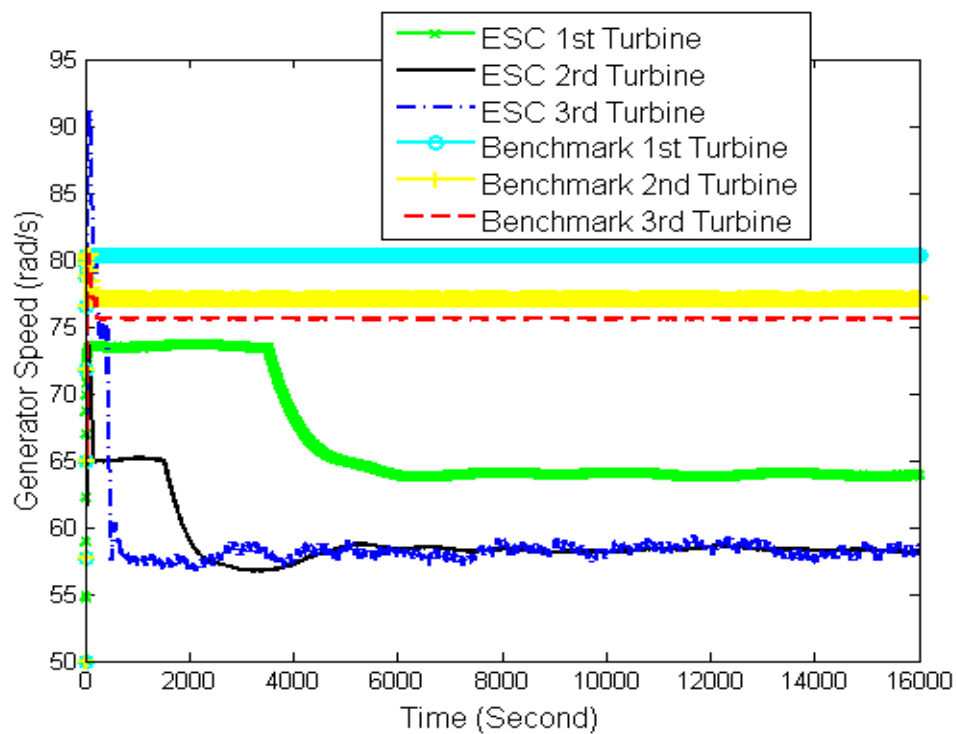


Fig. 6.13. Generator Speed Profiles for NLESC Search under 6m/s Smooth Wind

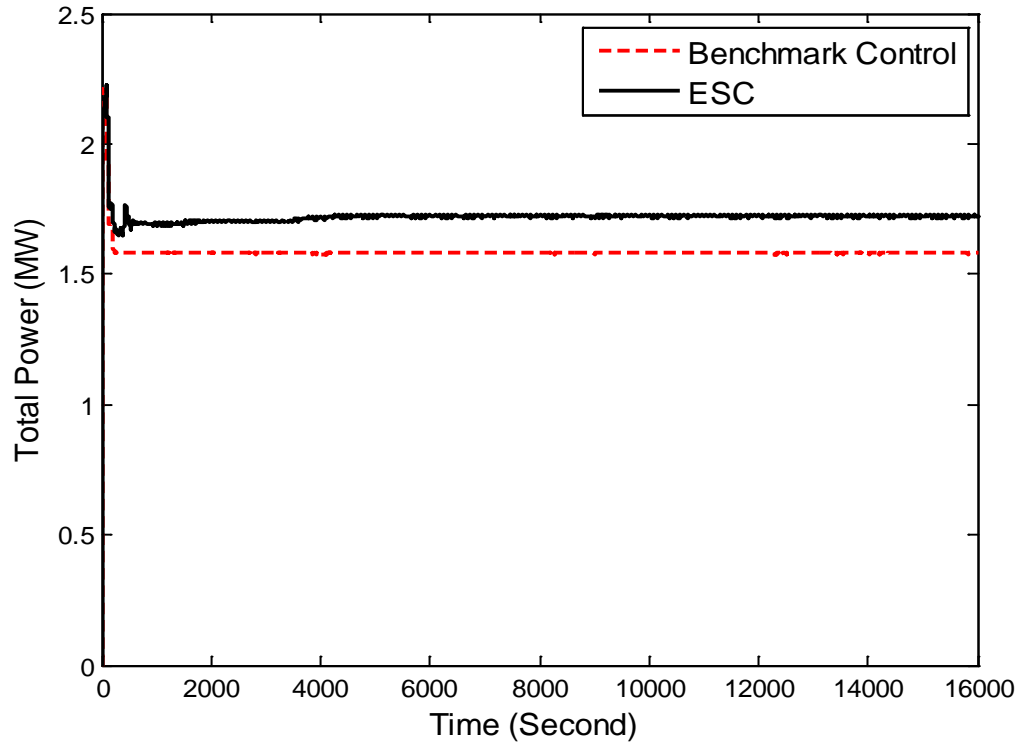


Fig. 6.14. Total Power Profiles for NLESC Search under 6m/s Smooth Wind

Next, the wind speed at the first turbine is increased to 10m/s. Through a 750-second sweeping simulation, the optimal torque gains of the static power map obtained turn out to be the same as those for the 6 m/s case, which verifies that the optimal torque gains are invariant with wind speed. For the NLESC simulation under smooth 10 m/s wind, the profiles of torque gains, effective wind speed and generator speed are shown in Fig. 6.15, Fig. 6.16 and Fig. 6.17, respectively.

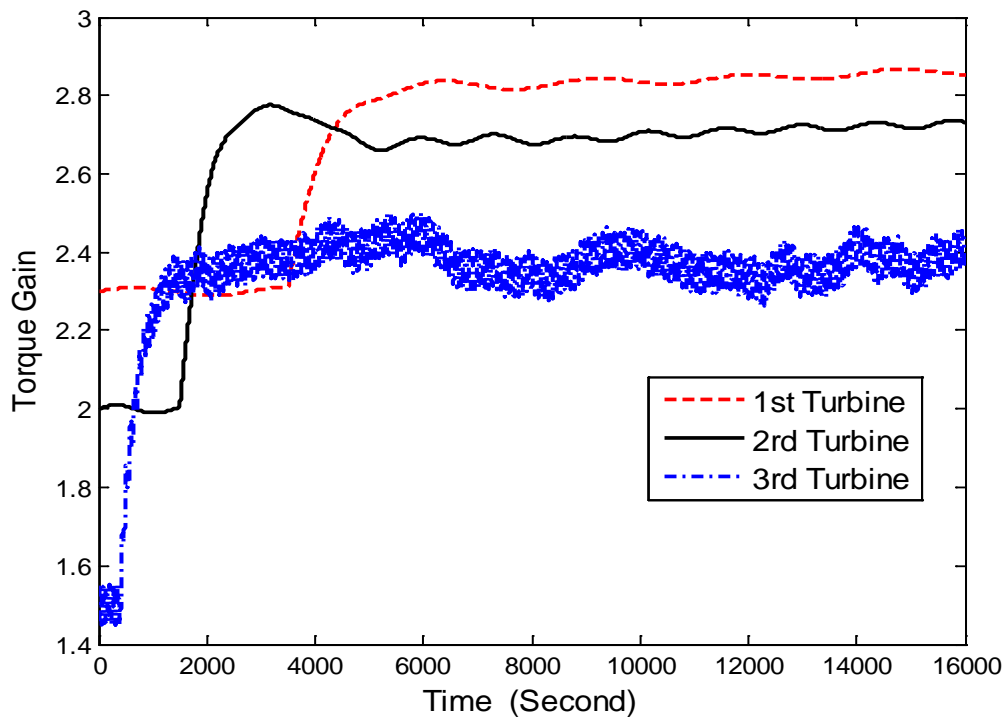


Fig. 6.15. Torque Gain Profiles for NLESC Search under 10 m/s Smooth Wind

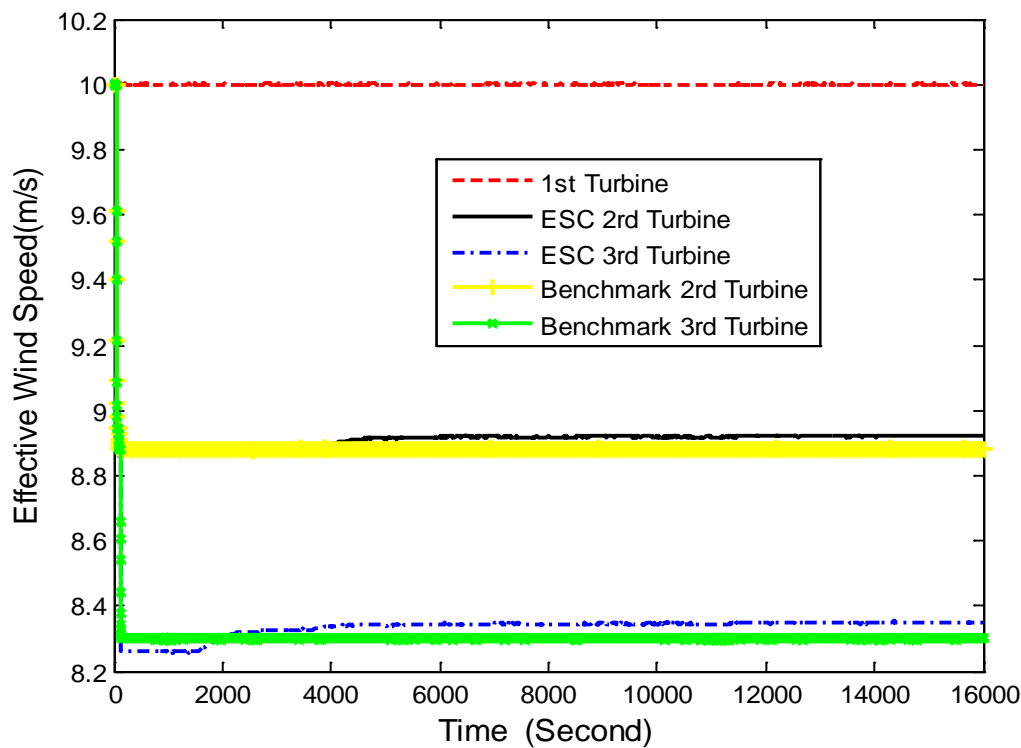


Fig. 6.16. Effective Wind Speed at Each Turbine for NLESC Search under 10 m/s Smooth Wind

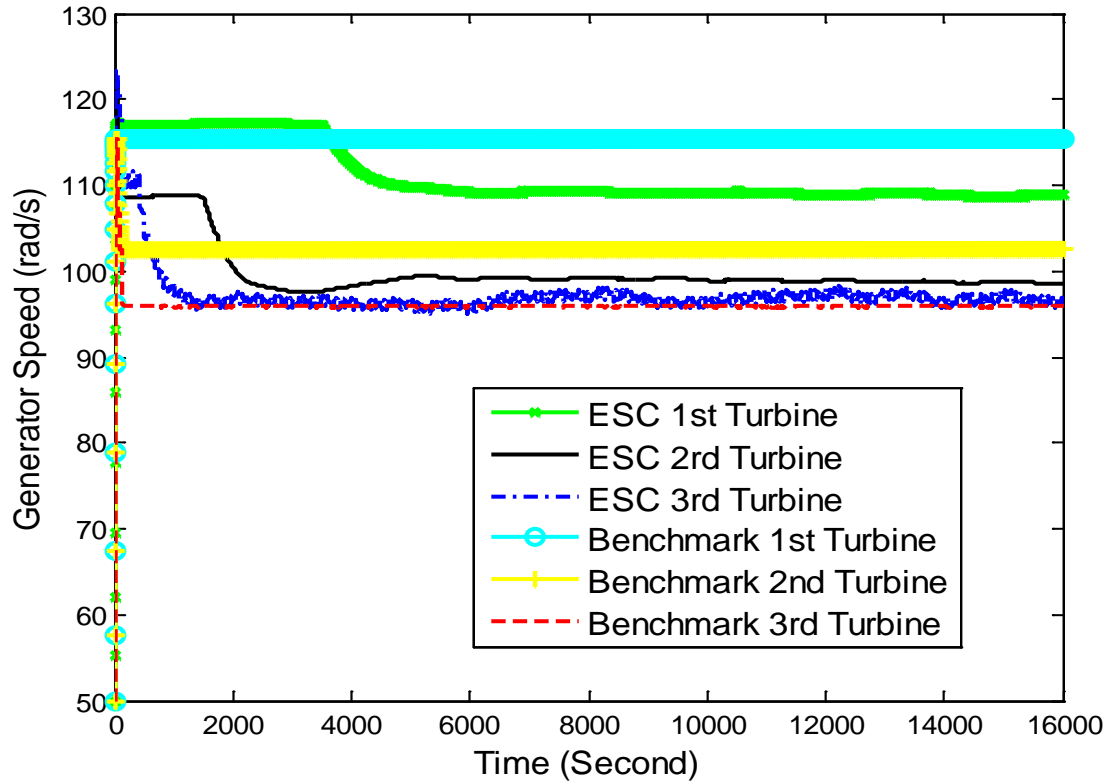


Fig. 6.17 Generator Speed Profiles for NLESC Search under 10 m/s Smooth Wind

Compared to the benchmark controller, the total power captured was increased by 0.34% during the period [10000s, 16000s], as shown in Fig. 6.18. It seems that the NLESC yields more benefit in power capture under lower wind speed than high wind speed (i.e. near the rated wind speed), which is consistent with simulation results in [194].

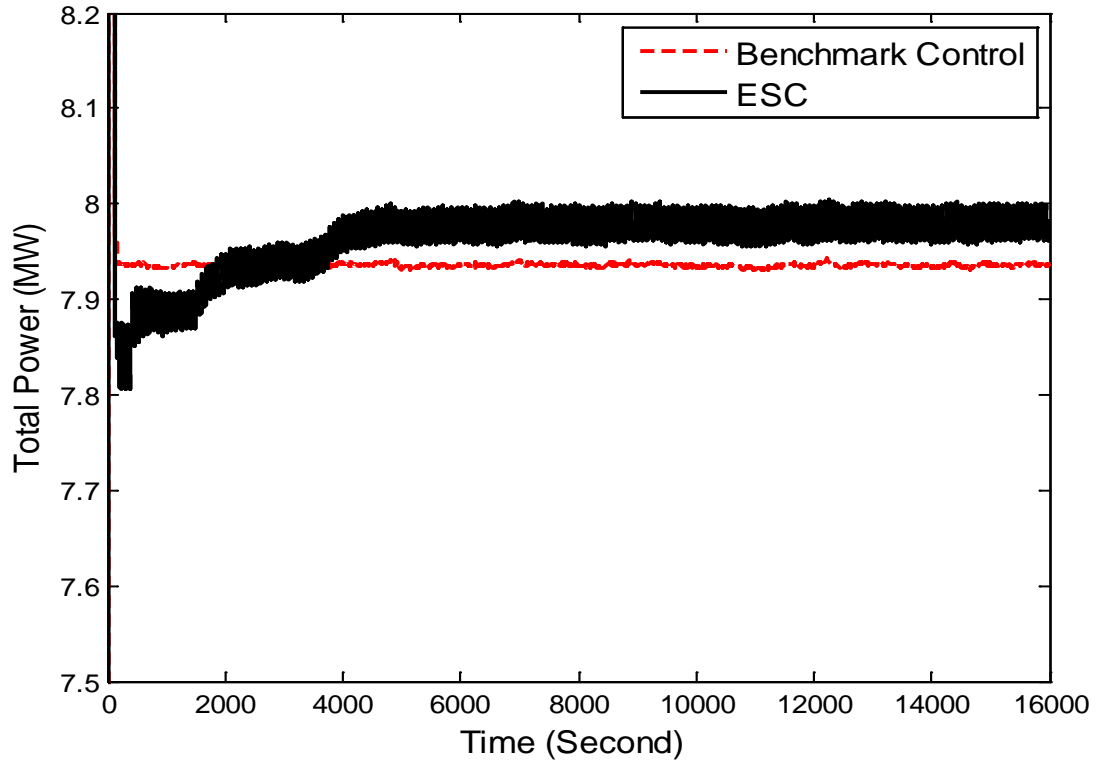


Fig. 6.18 Total Power Profiles for ESC Search for Smooth 10 m/s Wind

6.3.2. Turbulent Wind

Simulation was then performed for a turbulent wind case, with the mean wind speed of 8m/s and the turbulent intensity to be 5%. The effective wind speed at the 1st turbine is the same for both the NLESC and benchmark controllers, as shown in Fig. 6.19. For the 2nd and 3rd turbines, Fig. 6.20 and Fig. 6.21 show that the effective wind speeds with the NLESC controllers are higher than that with the benchmark controller. The dither frequencies remain the same as those used in steady wind. The dither amplitudes are 0.05, 0.03 and 0.1 for 1st, 2nd and 3rd turbine, respectively, which are larger than those for the smooth wind case. The forward-loop gains for the 1st, 2nd and 3rd turbines are 0.1, 0.23 and 1, respectively. The forward-loop gains in turbulent wind cases are much bigger than those for steady wind cases because power coefficients rather than power are used as

output for the turbulent wind case. The torque gains are plotted in Fig. 6.22. Generator speeds for 1st, 2nd and 3rd turbine are plotted in Fig. 6.23, Fig. 6.24 and Fig. 6.25, respectively. Compared to the default controller in SimWindFarm, the energy capture is increased by 1.3% during the period [10000s, 30000s], as shown in Fig. 6.26.

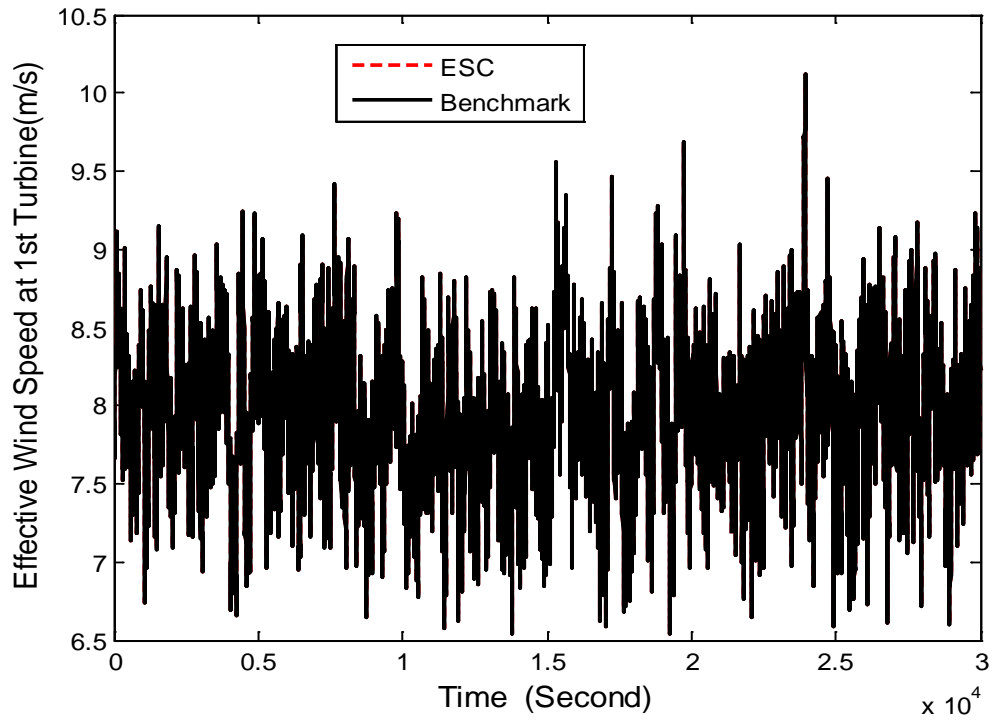


Fig. 6.19. Effective Wind Speed Profile at Turbine #1 under 8 m/s 5% Turbulent Wind

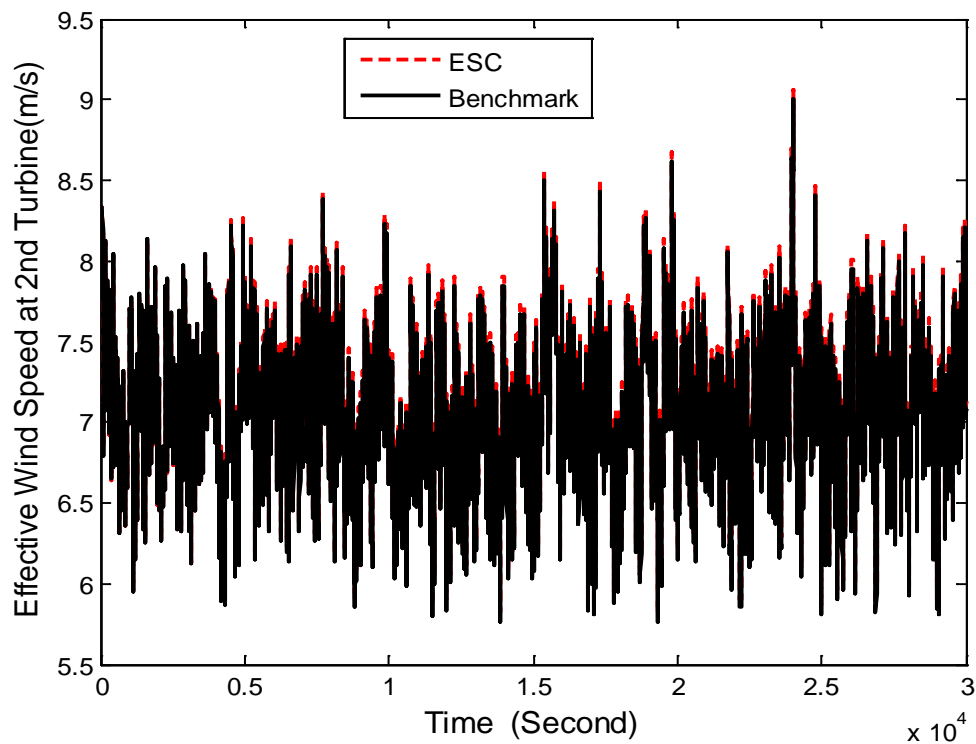


Fig. 6.20 Effective Wind Speed Profile at Turbine #2 under 8 m/s 5% Turbulent Wind

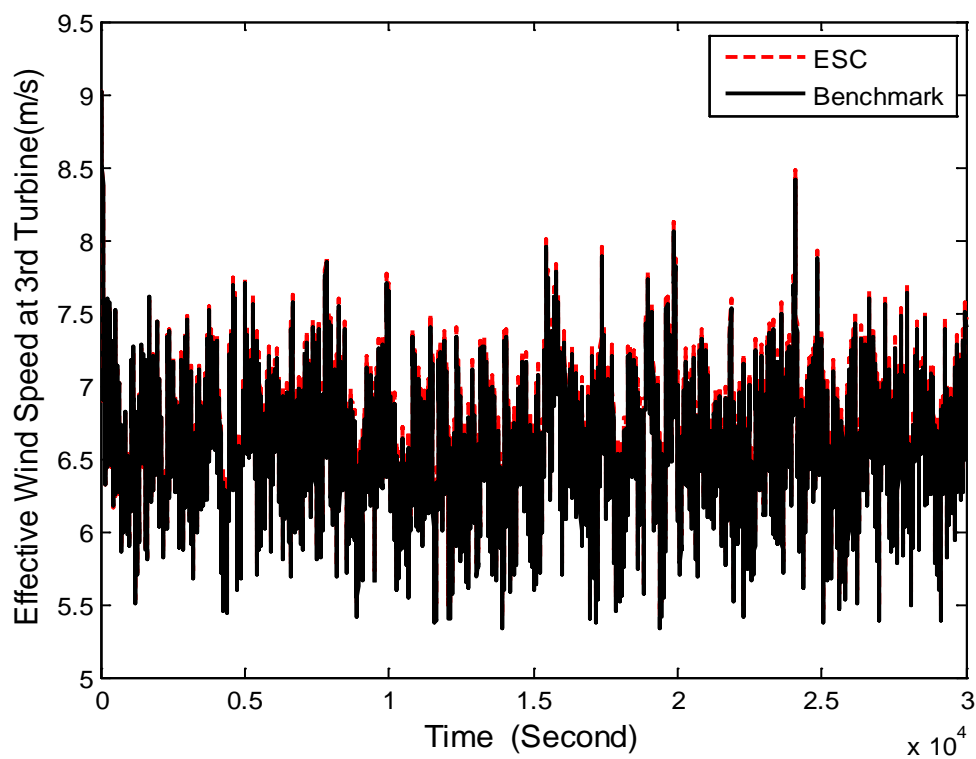


Fig. 6.21. Effective Wind Speed Profile at Turbine #3 under 8 m/s 5% Turbulent Wind

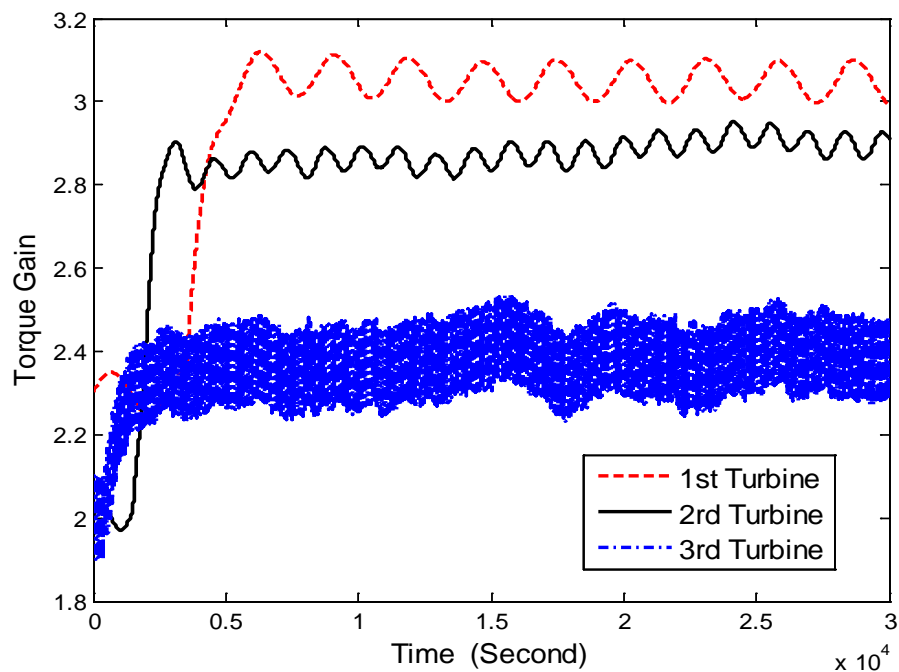


Fig. 6.22. Torque Gains under 8 m/s 5% Turbulent Wind

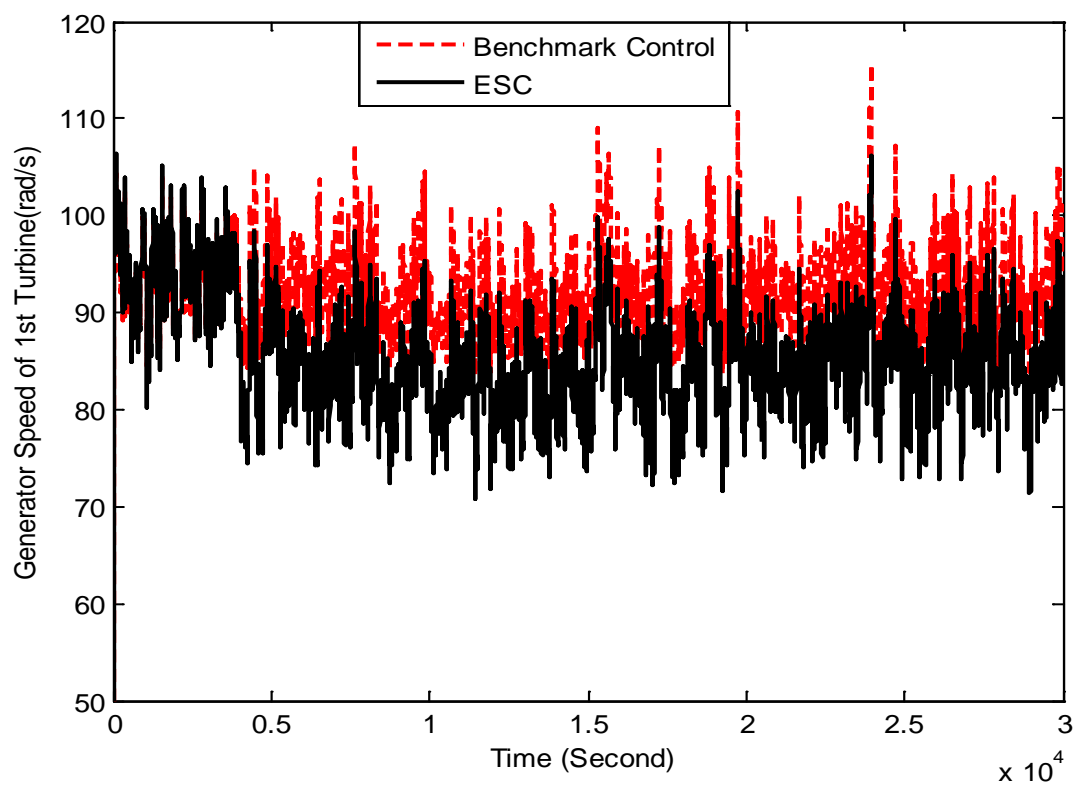


Fig. 6.23 Generator Speed at Turbine 1 under 8 m/s 5% Turbulent Wind

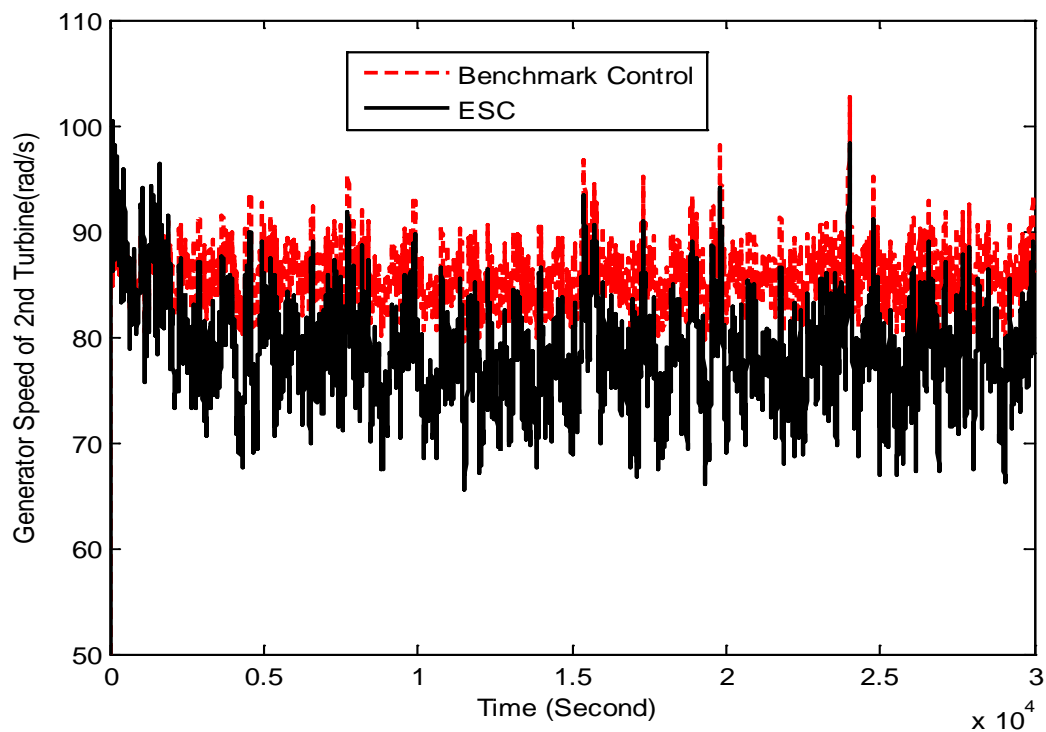


Fig. 6.24 Generator Speed at Turbine 2 under 8 m/s 5% Turbulent Wind

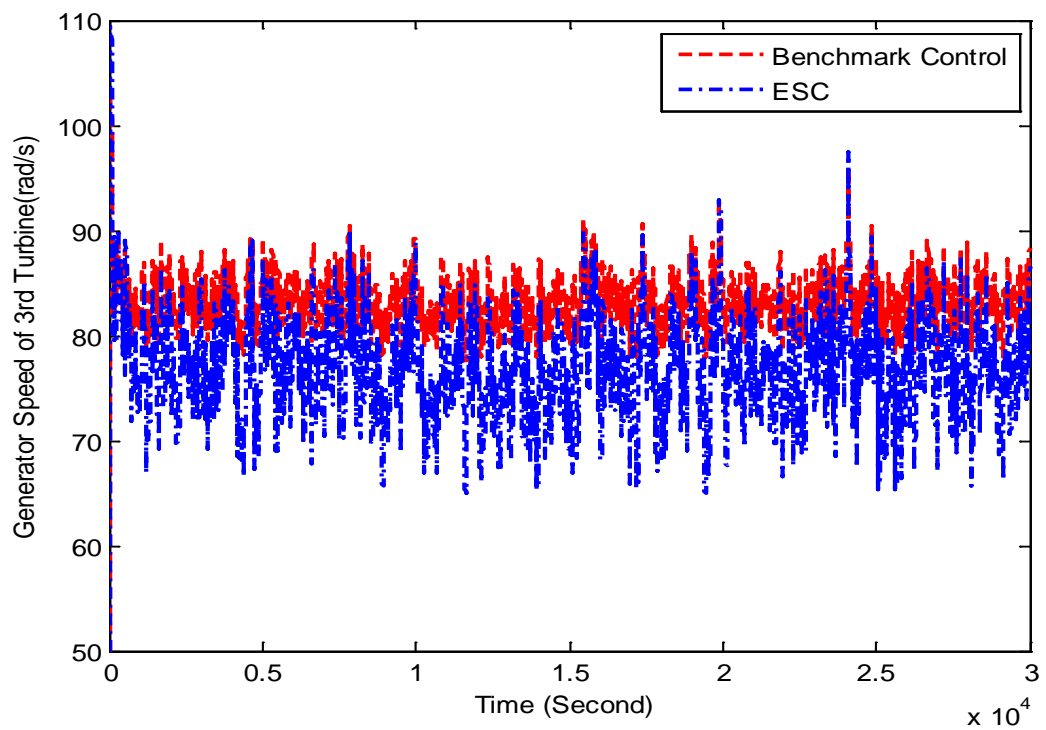


Fig. 6.25 Generator Speed at Turbine 3 under 8 m/s 5% Turbulent Wind

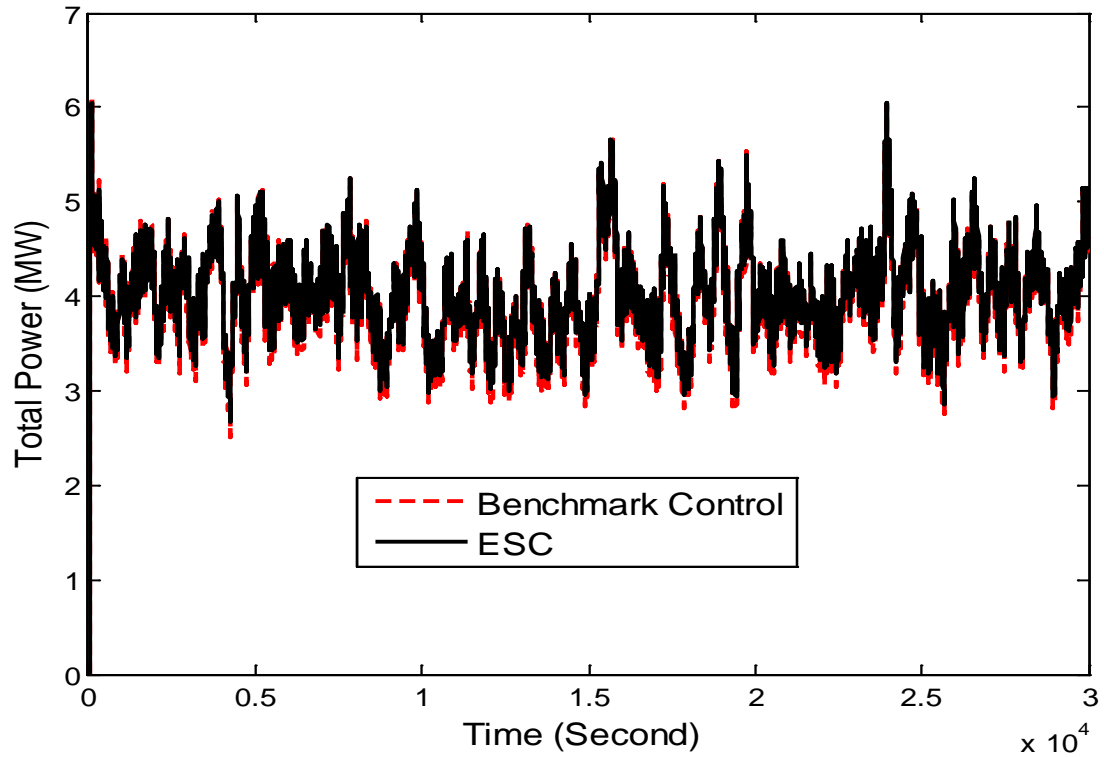


Fig. 6.26. Total Power under 8 m/s 5% Turbulent Wind

6.4. Conclusion

This part of dissertation study evaluates an NLESC wind farm controller which aims to maximize the farm-level energy capture. Static mapping under different wind speed validates the analytical result that the optimal torque gains are invariant with the wind speed in terms of maximizing the whole-farm power capture. Compared with the default controller available in SimWindFarm, the effectiveness of the NLESC was verified by simulation results under both steady and turbulent winds.

Chapter 7. Active Vane Control for Stabilization of Floating Offshore Wind Turbine

Control of offshore floating wind turbines has emerged as a much more complicated problem compared to the land based units. Stabilization and load reduction control are both important for floating turbines, while such tasks are challenged by underactuation situation. This chapter evaluates a novel idea [35] for controlling the roll and pitch motion of floating wind turbines respectively by actively controlled vertical and horizontal vanes. The structural dynamics of the floating wind turbine with the vane actuator is simulated through modifying Tail-Furling module in software FAST [140]. Proportional-integral (PI) controllers are applied to control the vane actuators based on tower pitch or roll motions. While an individual blade pitch controller is designed for other aspects of wind turbine control. The Hywind platform [195] is adopted for the simulation model of floating offshore turbine. For the active vane control, different measurement feedback schemes (including velocity and acceleration on tower top) and different vane areas are evaluated. Simulation results show that of the roll motion of the floating turbine can be effectively reduced, and the damage equivalent loads (DEL) relevant to the side-to-side bending moment at tower base is reduced from 19% to 42% under turbulent wind with mean speed 18 m/s.

The remainder of this chapter is organized as following. The vertical vane design and simulation platform is described in Section 7.1, and the horizontal vane design is described in Section 7.2. Simulation results are presented in Section 7.3.

7.1. Vertical Vane Design

7.1.1. Design Approach

Vertical vane actuators are placed at tower top in order to effectively increase damping of floating turbine tower along side-to-side direction. For wind turbines, significantly high weight at tower top due to the use of inertial forces leads to difficulty of installation and maintenance, as well as the high power requirement. The active vertical vane control is based on the use of the aerodynamic forces which would have higher force-to-weight ratio and leads to lower cost, compared to heavier TMD (Tuned Mass-Spring Damper) [33].

Besides, the active vertical vane design requires the use of downwind turbine design; otherwise the active vertical vane would reside in the near wake of the wind turbine rotor and its aerodynamic behavior would be intractable. For land based wind turbines, upwind design is typically preferred over downwind design as downwind design leads to the shadow effect that leads to significant periodic fatigue load and power fluctuation. However, for offshore wind turbines, reducing blade weight is of higher benefit, and thus downwind design has received better acceptance because lighter blades can be used when blade-tower collision is not a concern. Side view and top view of downwind wind turbines including vertical vanes are shown in Fig. 7.1.

7.1.2. Simulation Platform for Vertical Vane

Jonkman [196] developed an aeroelastic model of a small furling wind turbine by use of the Kane's method [197] and implemented it in FAST [140]. In this study, the tail-furling module in FAST is modified to simulate the vane actuator. In the furling input files, tail-

furling degree is set to False. The distance from the tail fin center of pressure to tower axis is set to half of the nacelle length such that the yaw moment generated by the vertical vane is small and the yawing action of the vertical vane is disabled. To simulate vertical vane, the degree status of tail-furling need to be set according to Table 7-1 and the configuration of tail-furling is shown in Fig. 7.2.

Table 7-1: List of Status for Tail-Fin Degrees of Freedom for Vertical Vane

Variables	Description	Status	Values
TFinSkew	The skew angle of the tail fin chordline in the nominally horizontal plane	On	The same with vane pitch angle
TFinTilt	The tilt angle of the tail fin chordline from the nominally horizontal plane	Off	0
TFinBank	The bank angle of the tail fin plane about the tail fin chordline	Off	0
TFriDOF	Tail-furl degree	Off	False

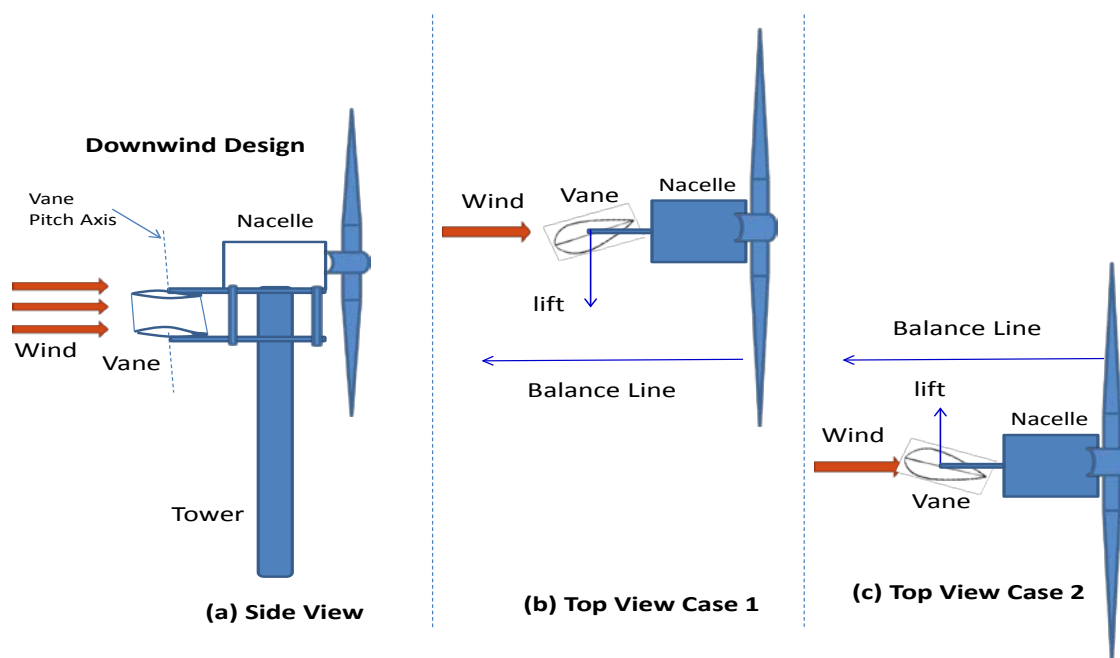


Fig. 7.1. Vertical Vane Design a) Side View; b) Top View 1; c) Top View 2.

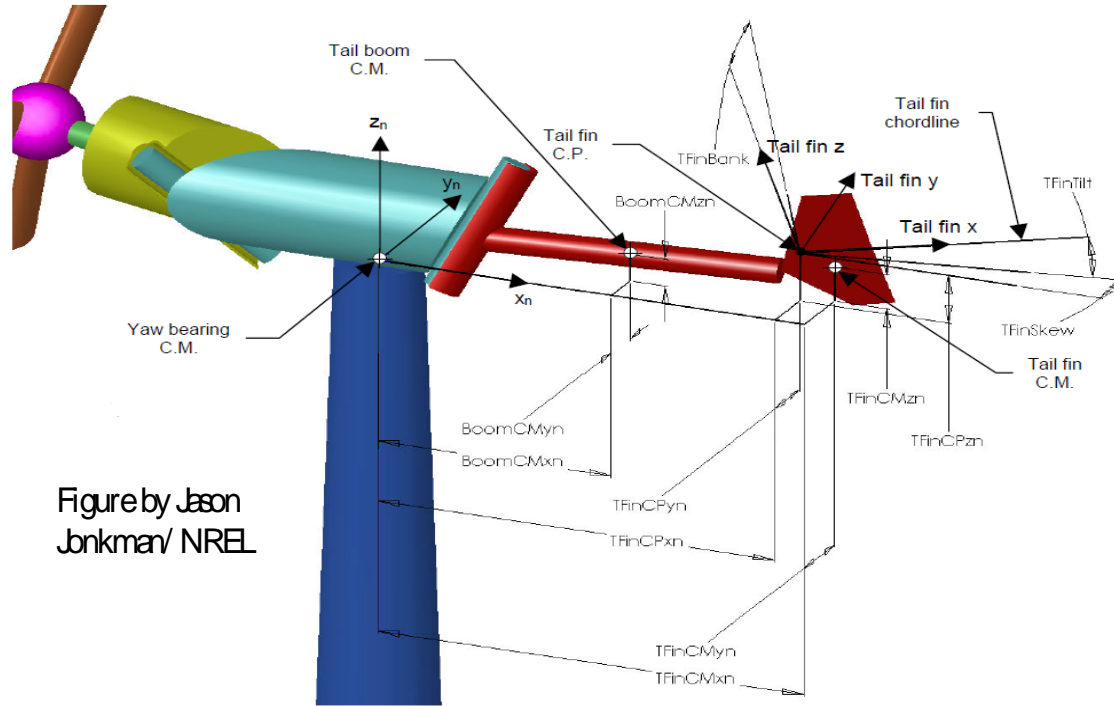


Figure by Jason
Jonkman/ NREL

Fig. 7.2. Configuration of Tail-Furling

Originally tail-furling is passively controlled in FAST. The working principle of passive-controlled tail-furling is:

- a) When wind speed is above rated wind speed, the rotor is yawed and/or tilted out of wind direction due to higher thrust loading on the rotor;
- b) When wind speed is below rated wind speed, the rotor is returned to wind direction due to lower thrust loading on the rotor;

In this study, the active control input of vertical vane is the vane pitch angle, which is defined as the angle between nominal downwind direction and the plane composed of vertical vane's airfoil chord lines. In FAST, the angle TFinSkew stands for vertical vane pitch angle. To facilitate the controller design, we modified FAST subroutines related with variable TFinSkew and rebuilt the Simulink interface of FAST including vane pitch control, shown in Fig. 7.3.



Fig. 7.3. Simulink Interface of FAST including Vertical Vane Pitch Control.

7.1.3. Airfoils for Vertical Vane

When wind turbine is located at the equilibrium point along the side-to-side direction, it is desirable not to have aerodynamic forces generated by the vertical vane. Therefore, symmetrical airfoils or symmetrical pair of airfoils should be used. In this study, symmetrical airfoil NACA0012 is used, and its aerodynamic characteristics can be found in a report by Sandia National Laboratory [198]. The lift and drag coefficients of NACA0012 are plotted in Fig. 7.4. To achieve tractable control action, stall operation is avoided. The range of angle of attack for nearly linear lift characteristics (no stall) is from -20° to 20° . In order to fully test the capability of vertical vane to stabilize floating turbine in side-to-side direction, a high-lift airfoil [199] is also used and its aerodynamic coefficients were modified to simulate a pair of high-lift airfoils for symmetry achievement.

7.1.4. Controller Design of Floating Offshore Turbine with Vertical Vane Control

In this study, blade pitch control, generator torque control and vertical vane pitch control are considered. The objective is to compare the wind turbine performance with and

without the vertical vane control so that the effectiveness of the active vane control can be evaluated.

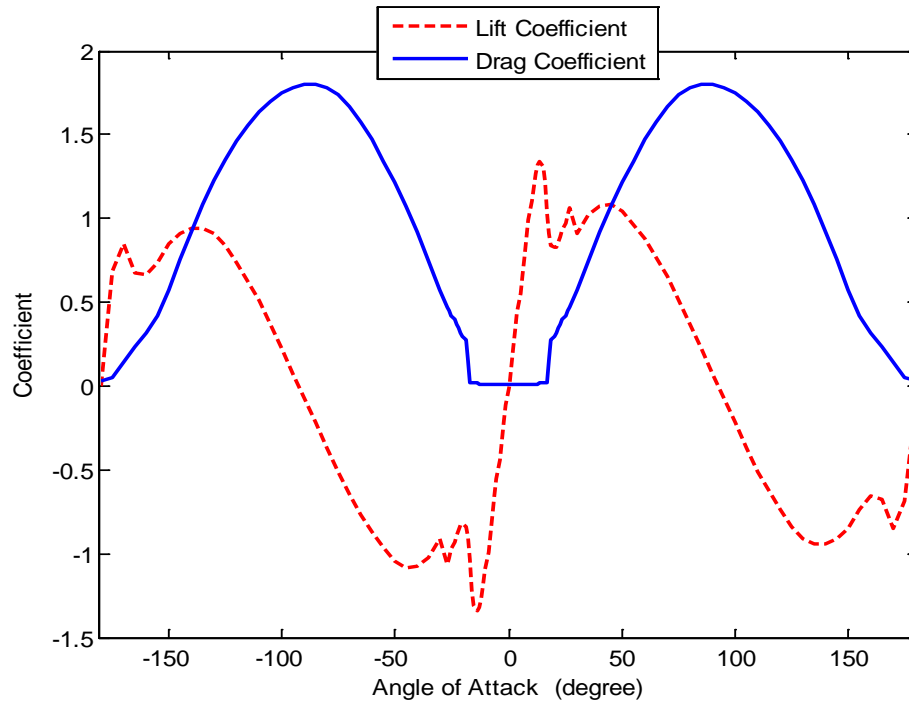


Fig. 7.4. Lift and Drag Coefficients of NACA0012

Jonkman [195] redesigned PI-based blade pitch controller for floating turbine with Hywind platform based on his previous work [192] and suggestion from Larsen and Hansen [32] about negative damping for the tower pitch motion. Such PI pitch controller [195] and PI-based Individual pitch controllers [10] are implemented together as the benchmark of collective pitch control in this chapter.

For the generator torque control, different wind turbine operation regions correspond to different control modes. Below the rated wind speed, the generator torque is designed to be proportional to the square of generator speed. Above the rated wind speed, the generator torque is equal to rated power output over the product of generator speed and generator efficiency.

The PI-based vertical vane controllers are designed based on different measurements including the side-to-side velocity and side-to-side acceleration at the tower top. The controller loop including vertical vane control is shown in Fig. 7.5.

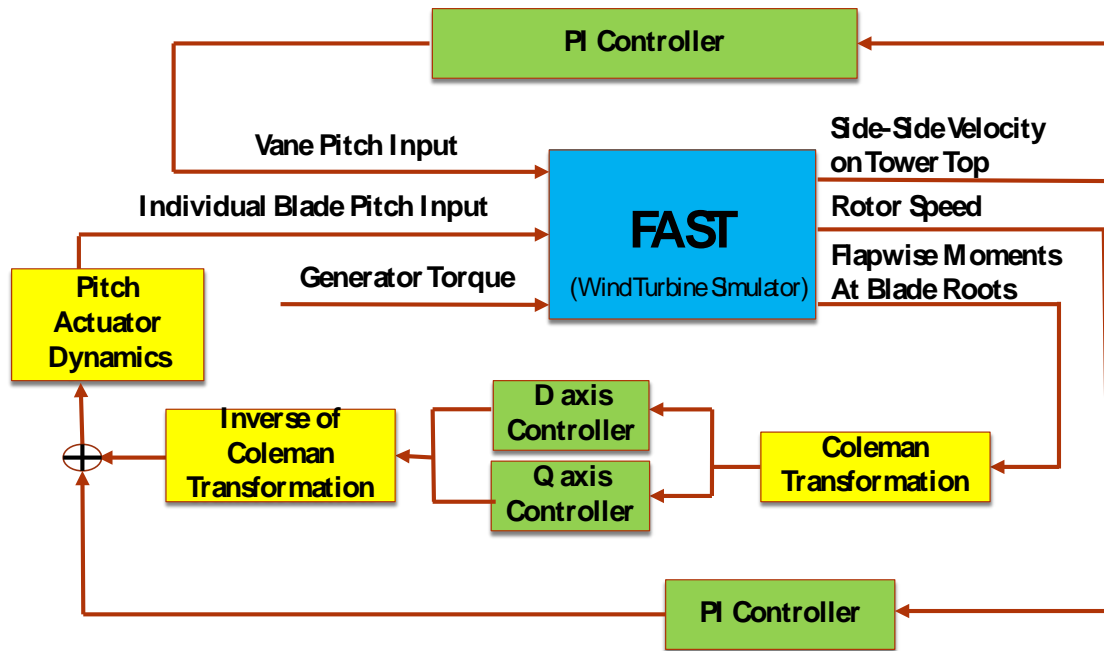


Fig. 7.5. Vertical Vane Control Loop

7.2. Horizontal Vane Design

In order to stabilize the pitch motion of floating turbine, a horizontal vane is proposed in [35] to increase tower damping of pitch motion. A simple treatment is to put the horizontal vane under the nacelle bedplate as the way of installing the vertical vane, but the moment arm length thus resulted would be insufficient. Based on this situation, a horizontal vane is placed at tower base, which is shown in Fig. 7.6.

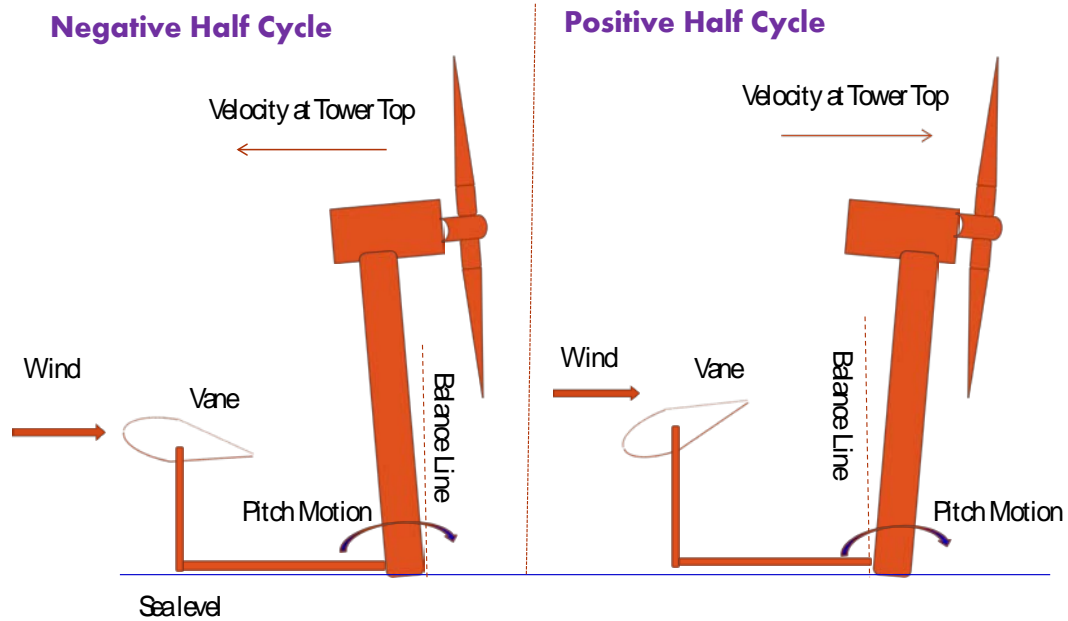


Fig. 7.6. Configuration of Horizontal Vane

Horizontal vane is also simulated through modifying Tail-Furling module of FAST software. Settings of FAST input for tail fin are listed in Table 7-2. For horizontal vane control, a new FAST Simulink interface is also built for controller design.

Table 7-2: FAST Setting for Horizontal Vane

Variables	Description	On/Off	Values
TFinSkew	The skew angle of the tail fin chordline in the nominally horizontal plane	On	0
TFinTilt	The tilt angle of the tail fin chordline from the nominally horizontal plane	Off	The same with horizontal vane pitch angle
TFinBank	The bank angle of the tail fin plane about the tail fin chordline	Off	90 degree
TFrIDOF	Tail-furl degree	Off	False

PI-based horizontal vane controllers are designed based on the measurement of fore-aft velocity and acceleration on tower top. The whole controller loop including horizontal

vane control is nearly the same to that in Fig. 7.5 except that the measurement for vane controller is fore-aft velocity or acceleration on tower top.

7.3. Simulation Results

7.3.1. Simulation Results for Vertical Vane

NREL FAST [140] is used to simulate floating turbine including vertical vane. To facilitate controller design in Simulink, FAST Simulink interface including vane control is rebuilt. The floating turbine model with Hywind platform defined by Jonkman [195] is used. In the following, both vertical vane with NACA0012 airfoil and that with high lift airfoil are tested under turbulent wind based on different measurements and different vane areas. The mean wind speed of turbulent wind is set as 18m/s and turbulence intensity is set as Class A according to IEC standard. Turbulent wind files are generated by use of TurbSim [176]. Stochastic wave is generated from the JONSWAP spectrum with a significant wave height 3.7 m and a peak spectral period 14 seconds suggested by Jonkman [149].

7.3.1.1. Vertical Vane and NACA 0012 with Different Measurements and Upwind

Design as Benchmark

In this subsection, upwind floating turbine with Hywind platform is used as benchmark when PI-based individual blade pitch control and variable torque control are used. Vane pitch controllers with airfoil NACA0012 are tested on downwind floating turbine with the Hywind platform when both the side-to-side acceleration and the side-to-side velocity at the tower top are used as feedback measurements and the same blade pitch controller and torque controller with benchmark are used. Fig. 7.7, Fig. 7.8, Fig. 7.8 and Fig. 7.10 show that the generator power and the rotor speed do not change much when the vertical

vane control is used. Fig. 7.11 and Fig. 7.12 show that the side-to-side velocity at the tower top is significantly alleviated when the vertical vane control is used. Compared with the case when the side-to-side acceleration at the tower top is used as feedback, the side-to-side velocity at the tower top is further reduced when the side-to-side velocity at the tower top is used as feedback.

Fig. 7.13 and Fig. 7.14 show that the vane pitch angle has more activity at high frequency when the side-to-side acceleration is used as measurement. Fig. 7.15, Fig. 7.16, Fig. 7.17, Fig. 7.18, Fig. 7.19 and Fig. 7.20 show that the platform translational sway displacement, the roll displacement and the side-to-side moment are reduced when both side-to-side velocity and acceleration at tower top are used as measurement. Compared with the case when acceleration feedback is used, displacement and loads are further reduced when velocity is used as measurement.

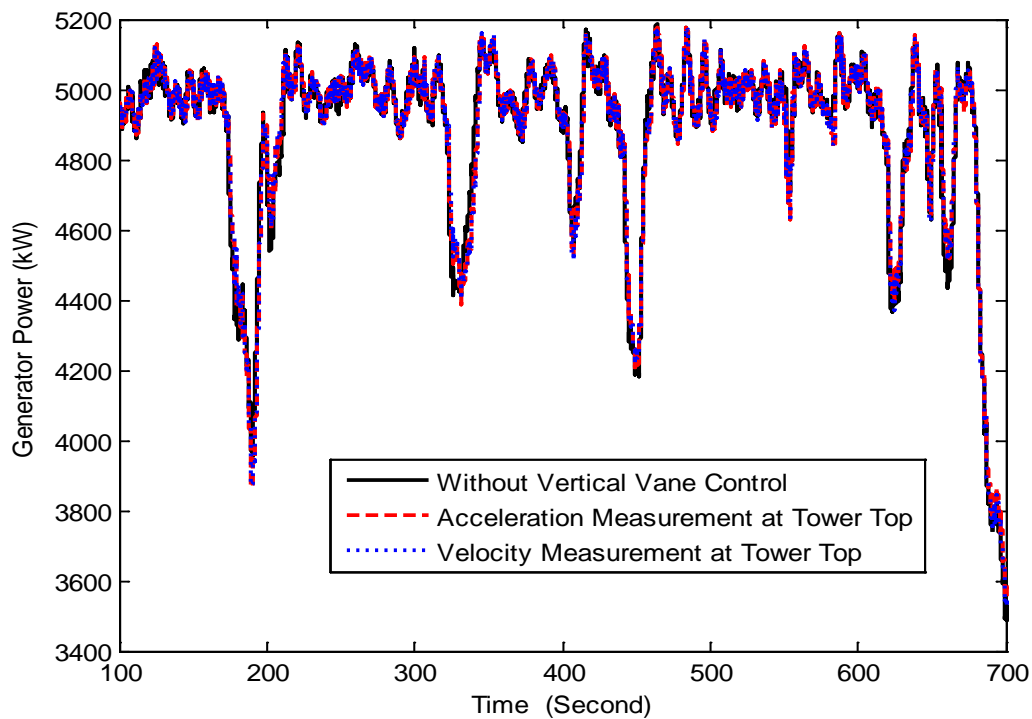


Fig. 7.7. Generator Power (Vertical Vane, NACA0012, Upwind as Benchmark)

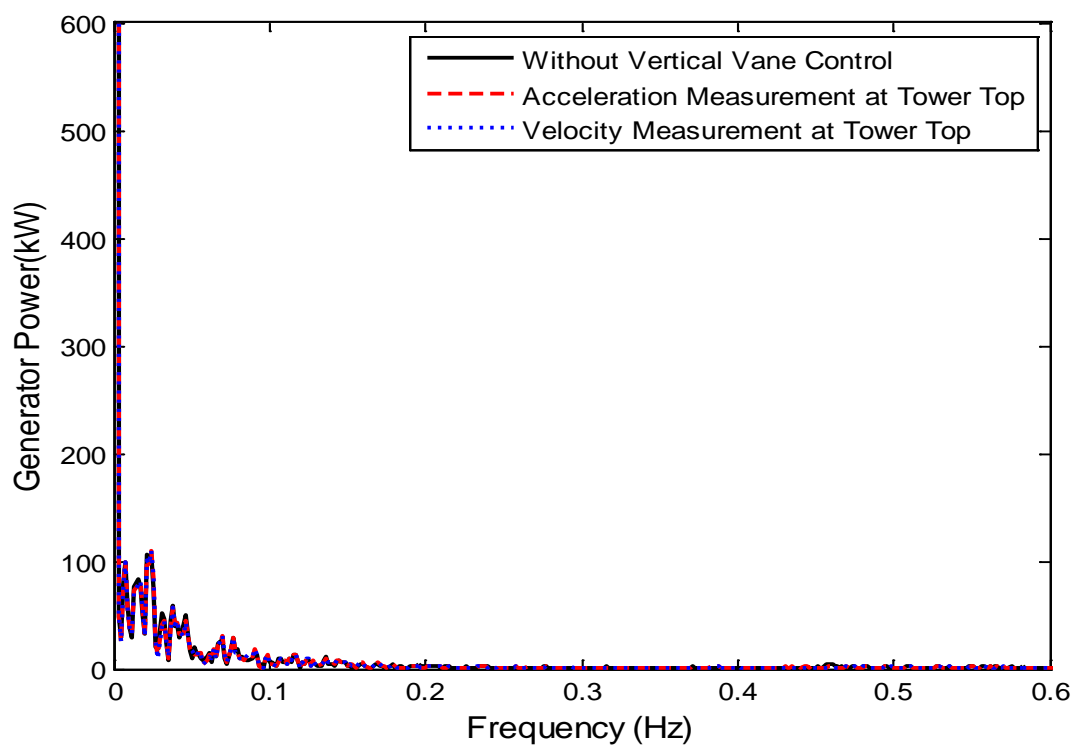


Fig. 7.8 Spectra of Generator Power (Vertical Vane, NACA0012, Upwind as Benchmark)

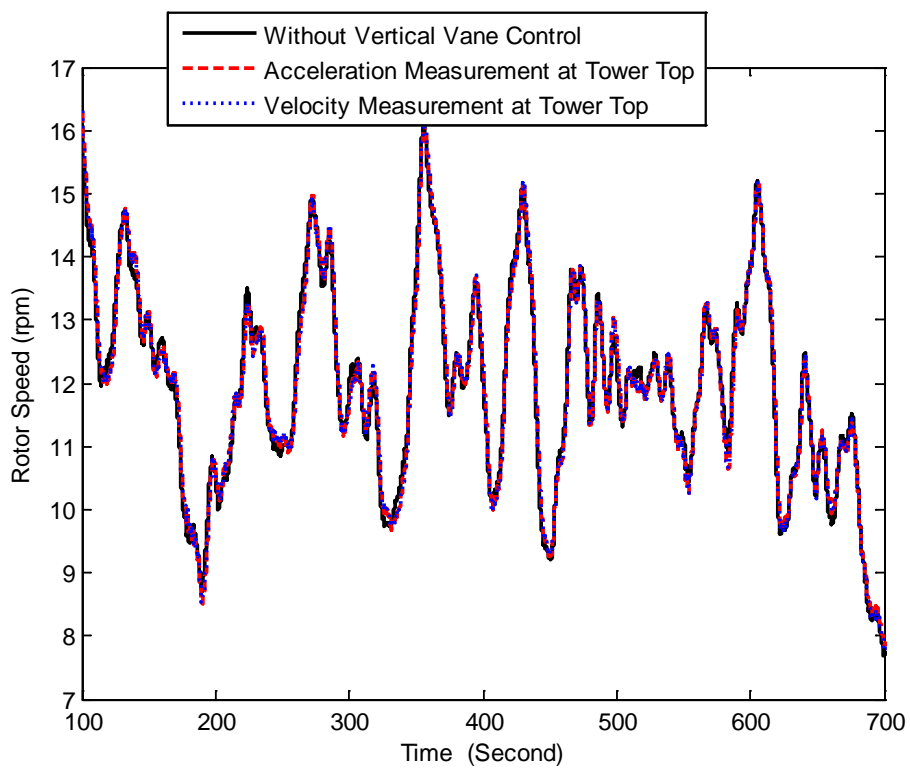


Fig. 7.9. Rotor Speed (Vertical Vane, NACA0012, Upwind as Benchmark)

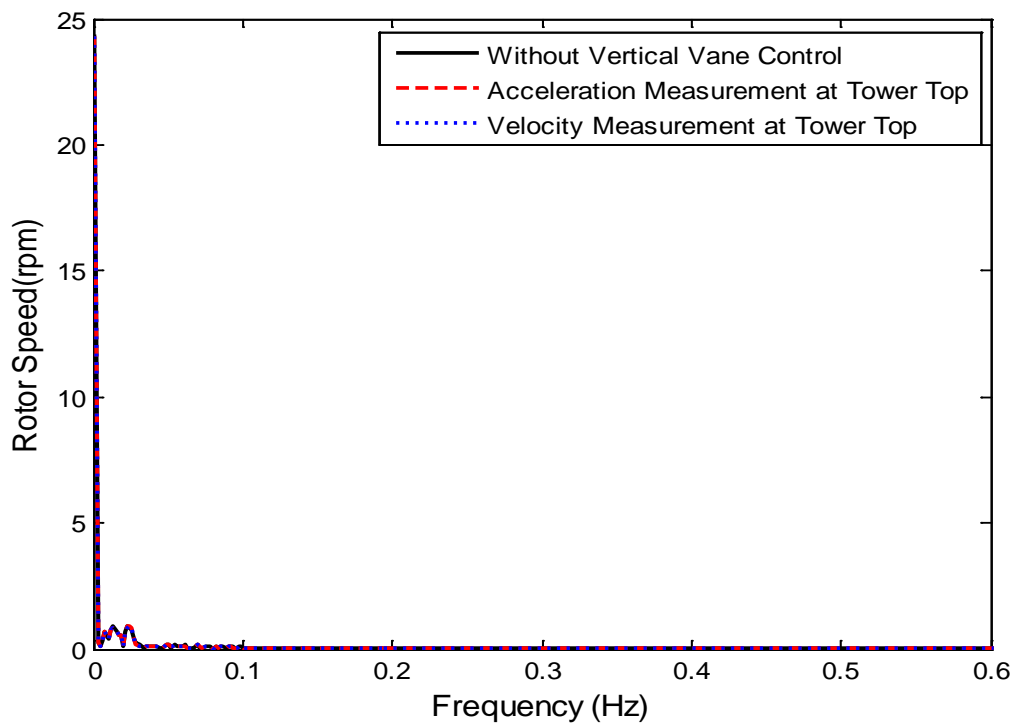


Fig. 7.10. Spectra of Rotor Speed (Vertical Vane, NACA0012, Upwind as Benchmark)

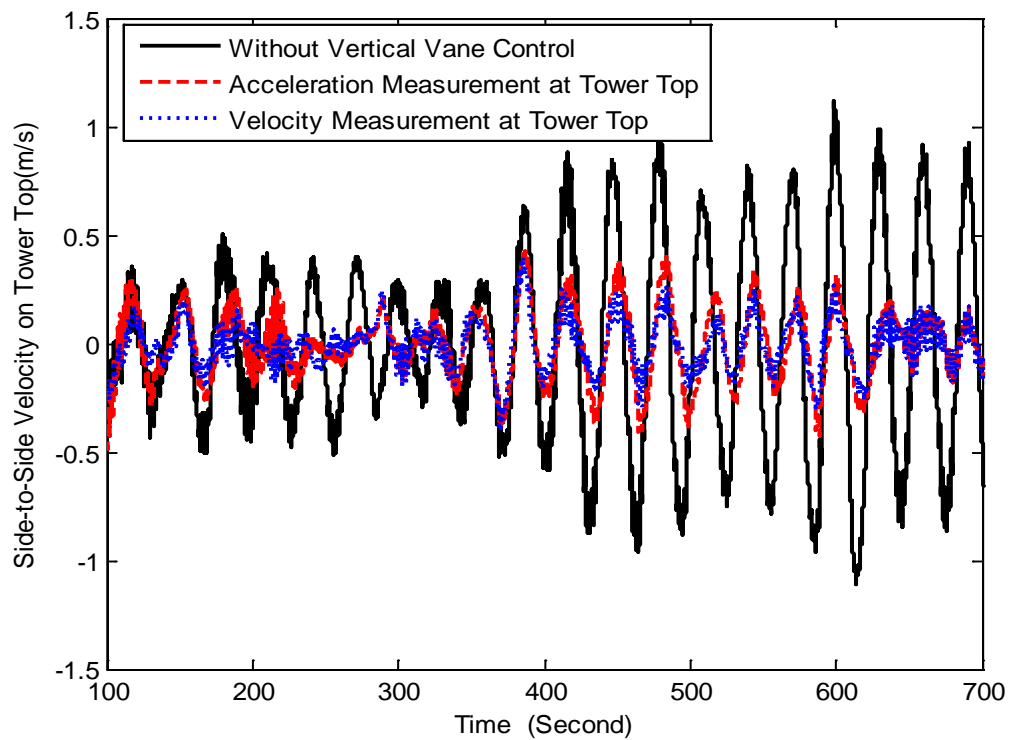


Fig. 7.11. Side-to-Side Velocity (Vertical Vane, NACA0012, Upwind as Benchmark)

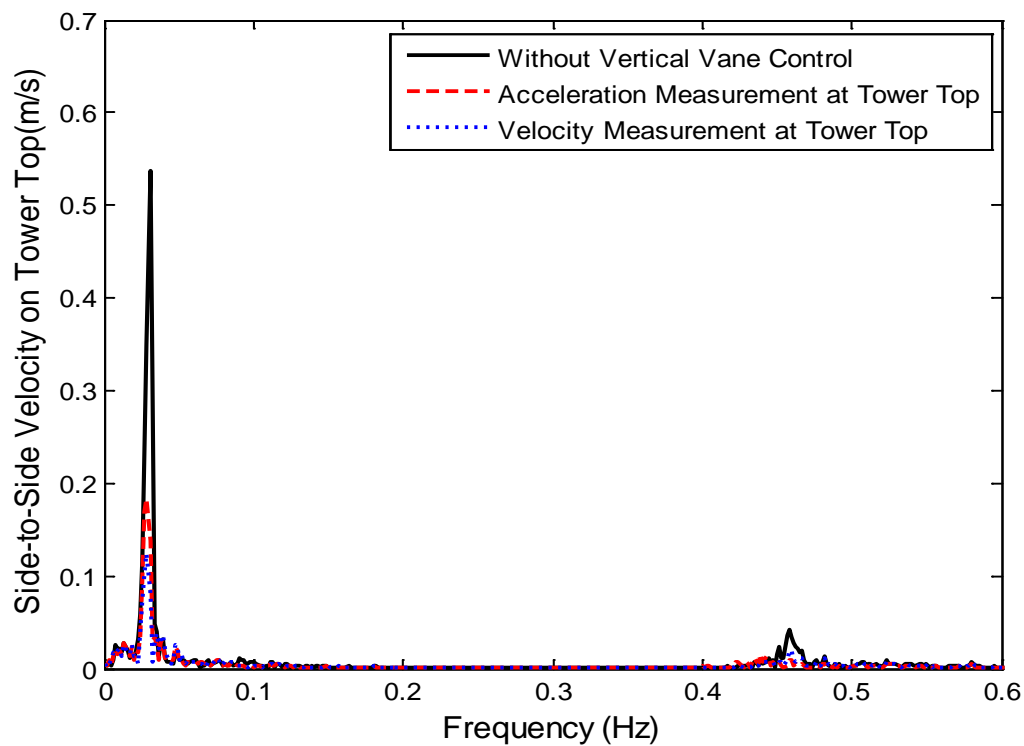


Fig. 7.12. Spectra of Side-to-Side Velocity (Vertical Vane, NACA0012, Upwind as Benchmark)

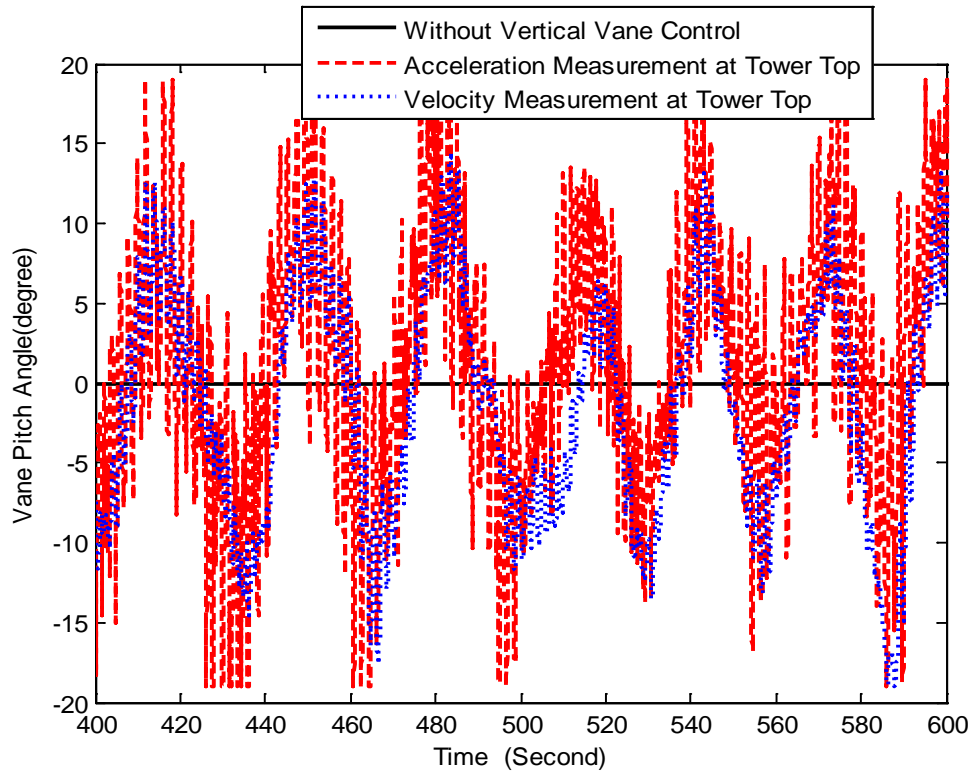


Fig. 7.13. Vane Pitch Angle (Vertical Vane, NACA0012, Upwind as Benchmark)

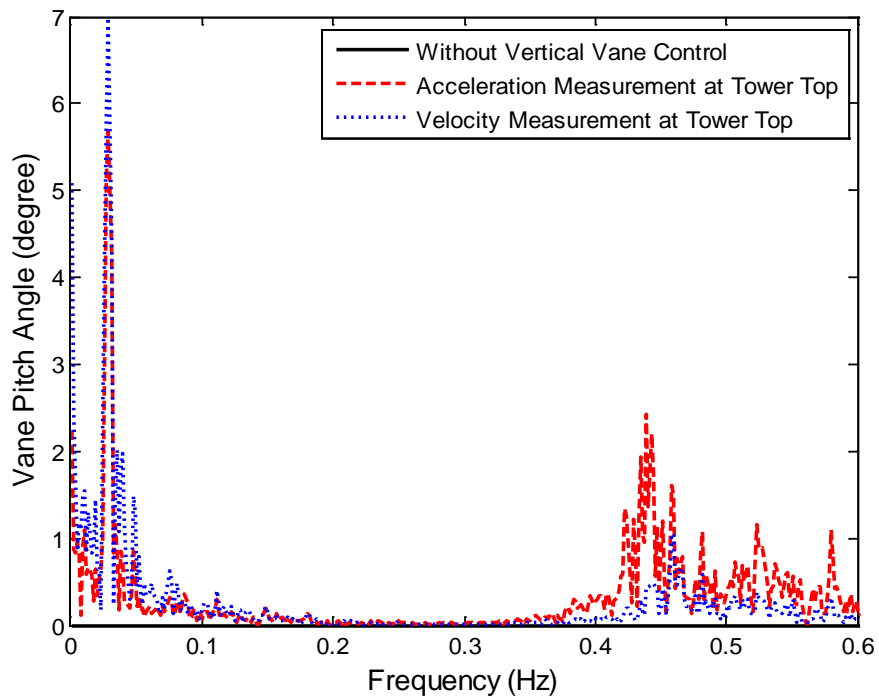


Fig. 7.14. Spectra of Vane Pitch Angle (Vertical Vane, NACA0012, Upwind as Benchmark)

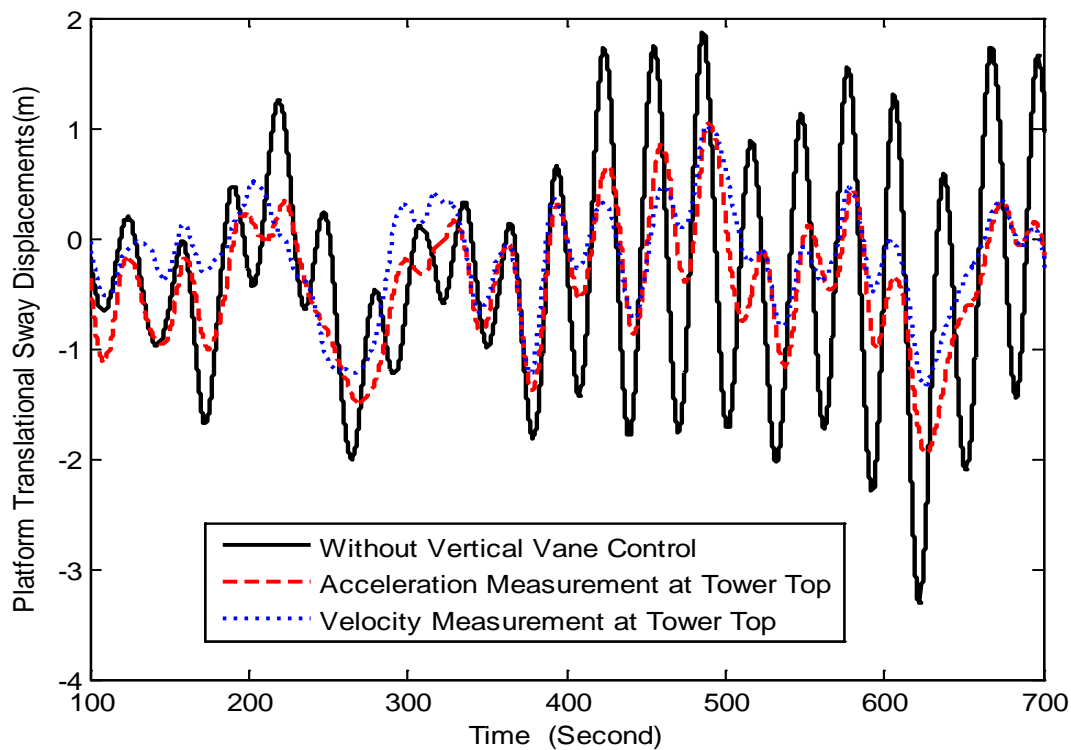


Fig. 7.15. Platform Sway Displacement (Vertical Vane, NACA0012, Upwind as Benchmark)

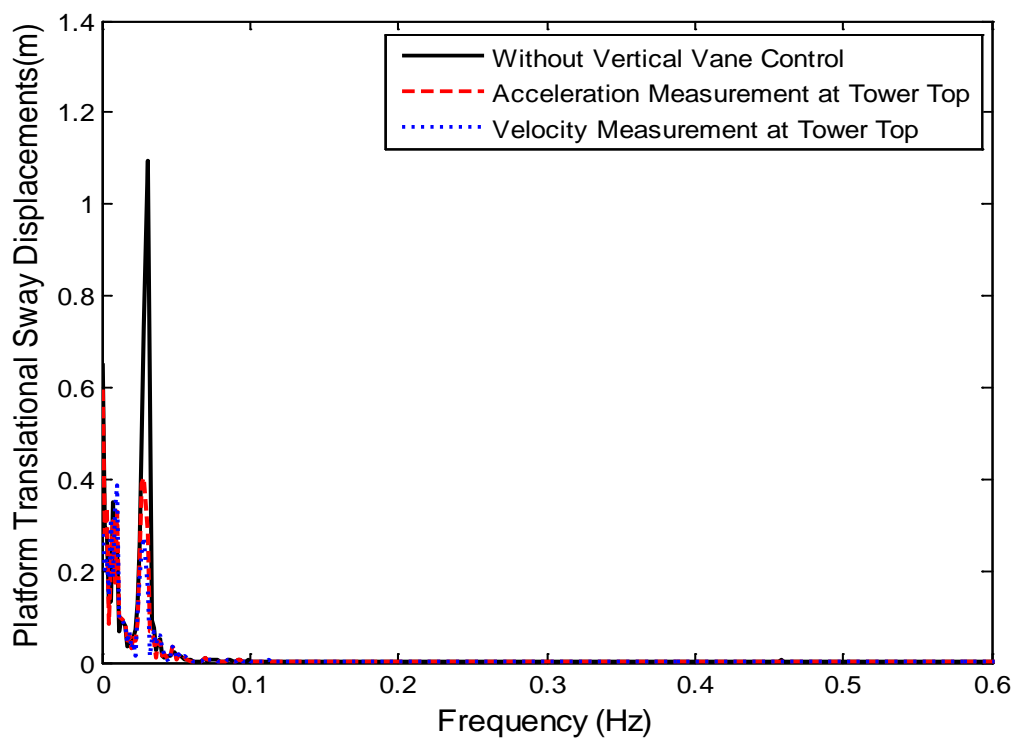


Fig. 7.16. Platform Sway Displacement Spectra (Vertical, NACA0012, Upwind as Benchmark)

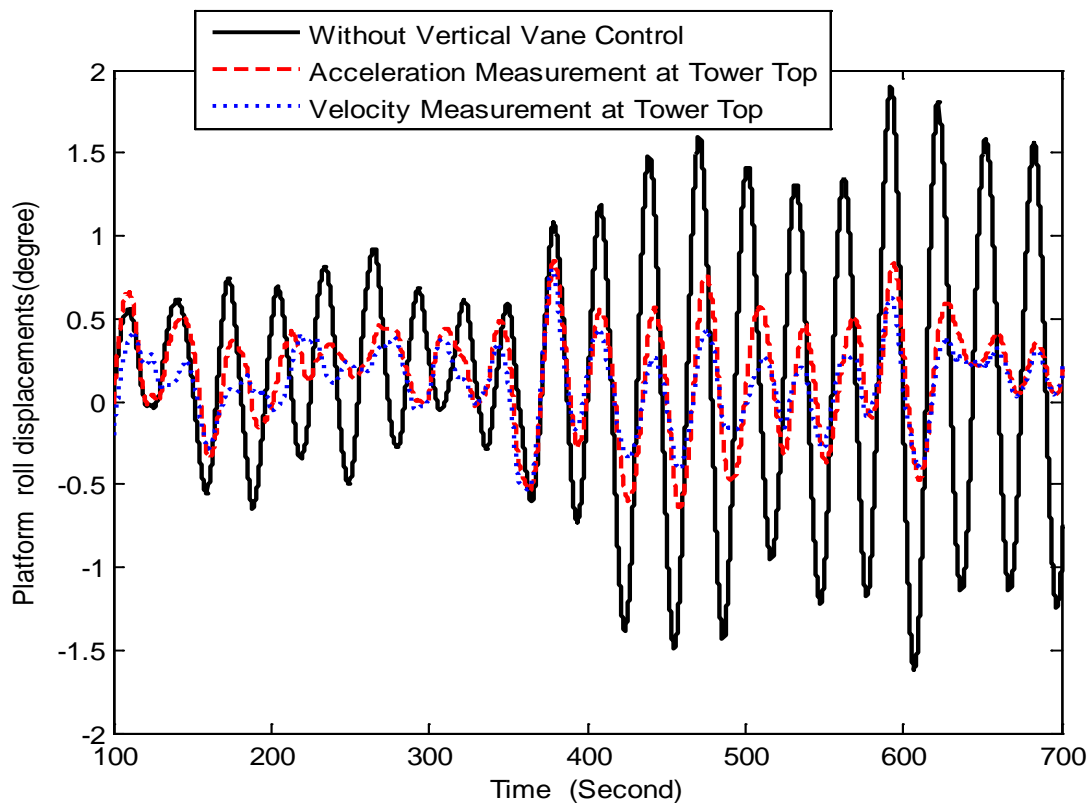


Fig. 7.17. Platform Roll Displacement (Vertical Vane, NACA0012, Upwind as Benchmark)

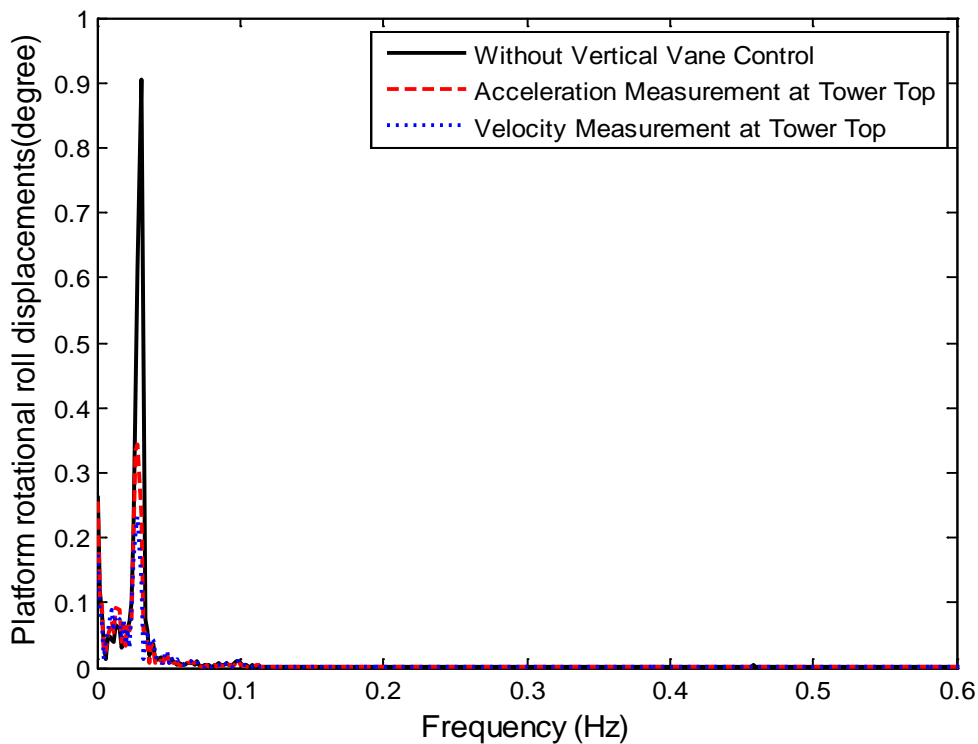


Fig. 7.18. Platform Roll Displacement Spectra (Vertical, NACA0012, Upwind as Benchmark)

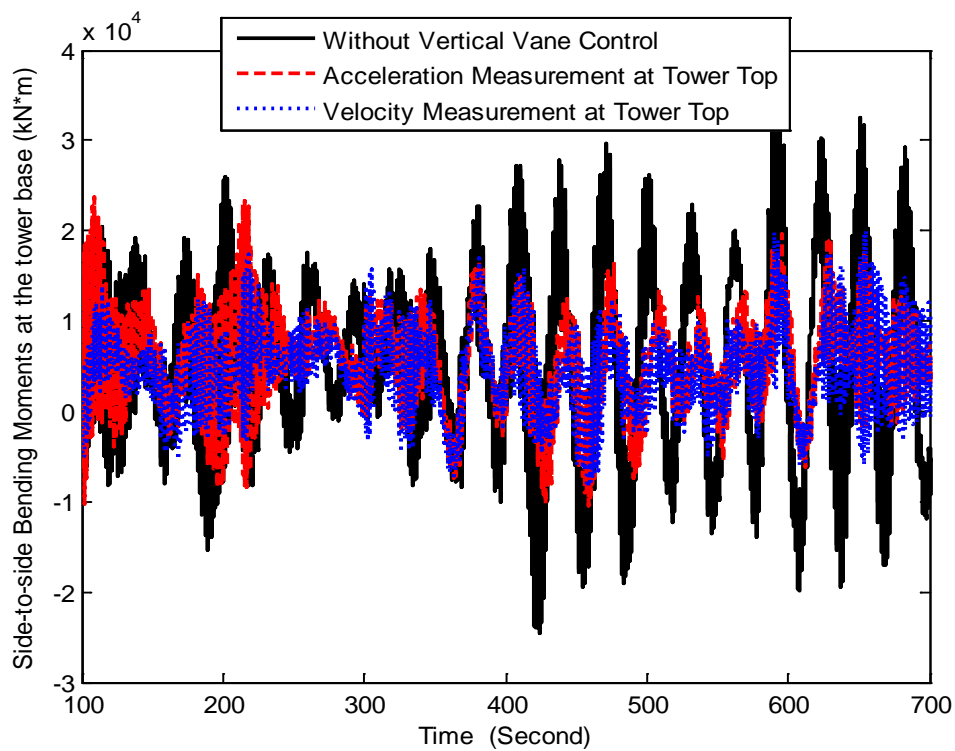


Fig. 7.19. Side-to-Side Bending Moment (Vertical Vane, NACA0012, Upwind as Benchmark)

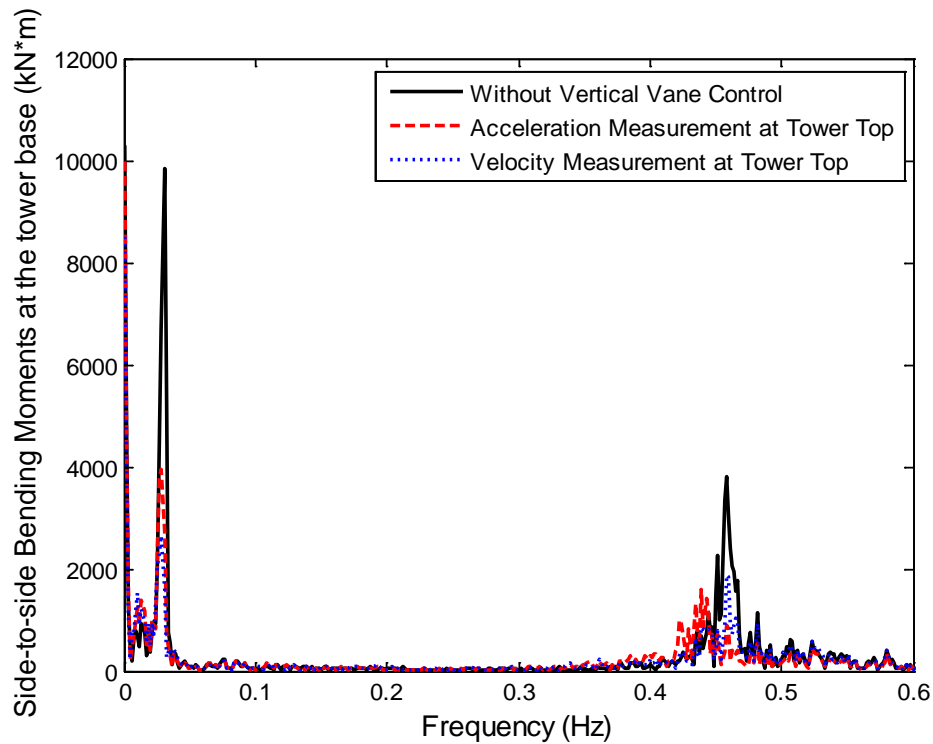


Fig. 7.20. Side-to-Side Bending Moment Spectra (Vertical, NACA0012, Upwind as Benchmark)

7.3.1.2. Vertical Vane and NACA 0012 with Different Measurements and Downwind Design as Benchmark

Similar to the previous section, downwind floating turbine with Hywind platform is used as benchmark when PI-based individual blade pitch control and variable torque control are used. Vane pitch controllers with airfoil NACA0012 are tested on downwind floating turbine with Hywind platform when both the side-to-side acceleration and the side-to-side velocity at tower top are used as measurements and the same blade pitch controller and torque controller with benchmark are used. Fig. 7.21 through Fig. 7.24 show that generator power and rotor speed do not change a lot when vertical vane control is used.

Fig. 7.25 and Fig. 7.26 show that the vane pitch angle has more activity at high frequency when side-to-side acceleration is used as measurement. Fig. 7.27 and Fig. 7.28 show that side-to-side velocity at tower top is significantly alleviated when vertical vane control is used. Compared with that when side-to-side acceleration at tower top is used as measurement, side-to-side velocity at tower top is further reduced when side-to-side velocity at tower top is used as measurement. Similarly, Fig. 7.29 through Fig. 7.34 show that the platform sway displacement, the roll displacement and the side-to-side moment are reduced when both velocity and acceleration are used as measurement. Compared with that when acceleration is used as measurement, displacement and loads are further reduced when velocity is used as measurement.

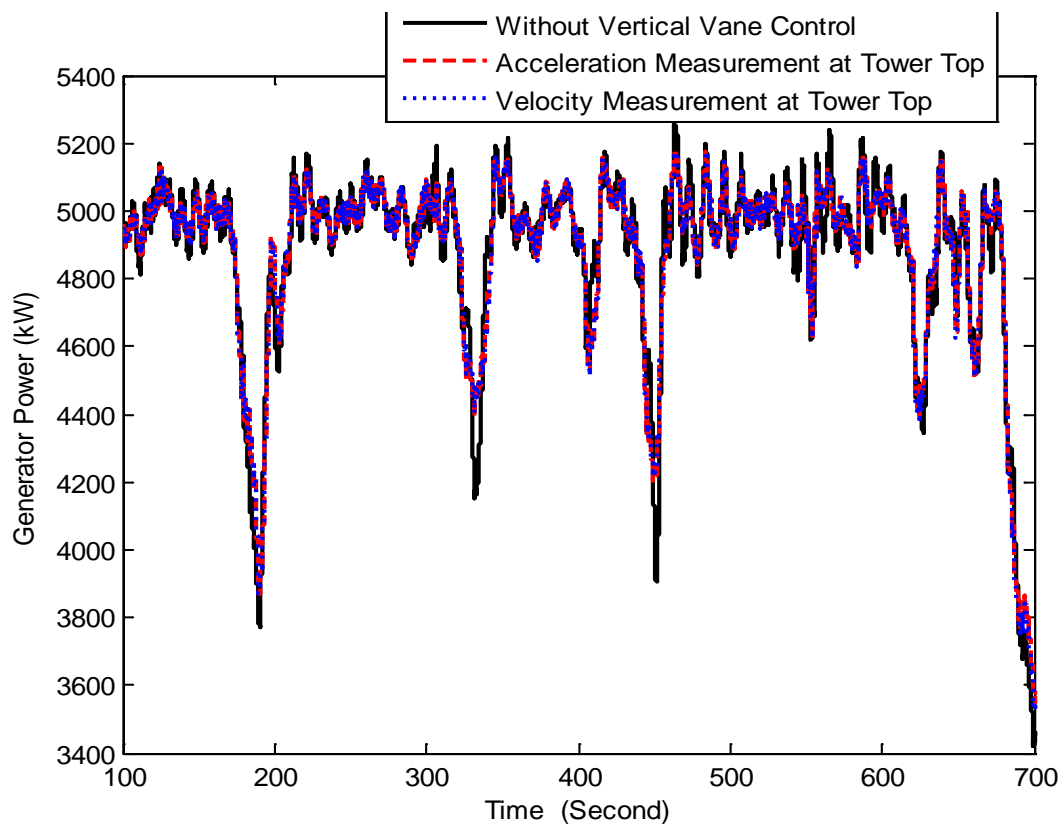


Fig. 7.21. Generator Power (Vertical Vane, NACA0012, Downwind as Benchmark)

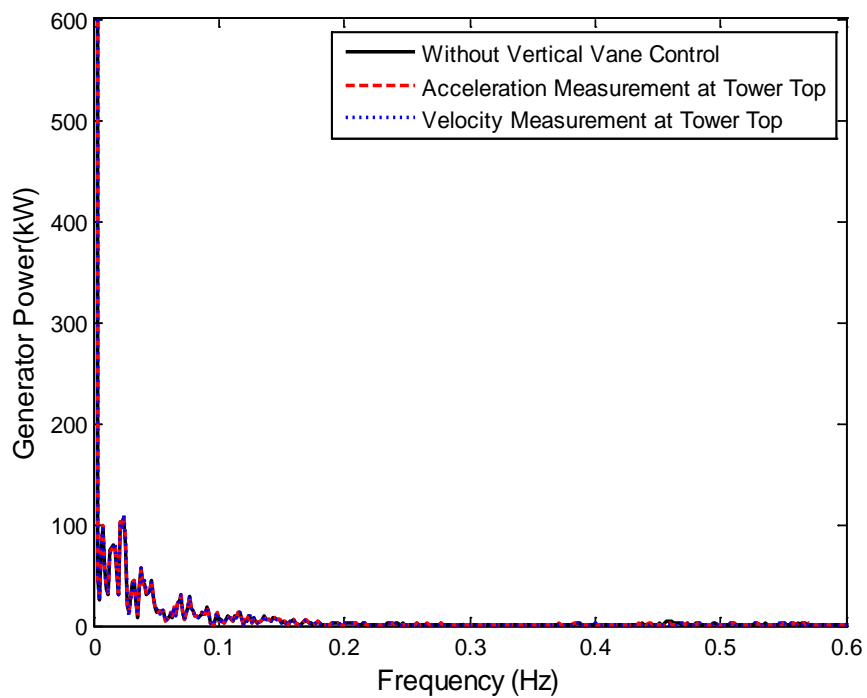


Fig. 7.22. Generator Power Spectra (Vertical Vane, NACA0012, Downwind as Benchmark)

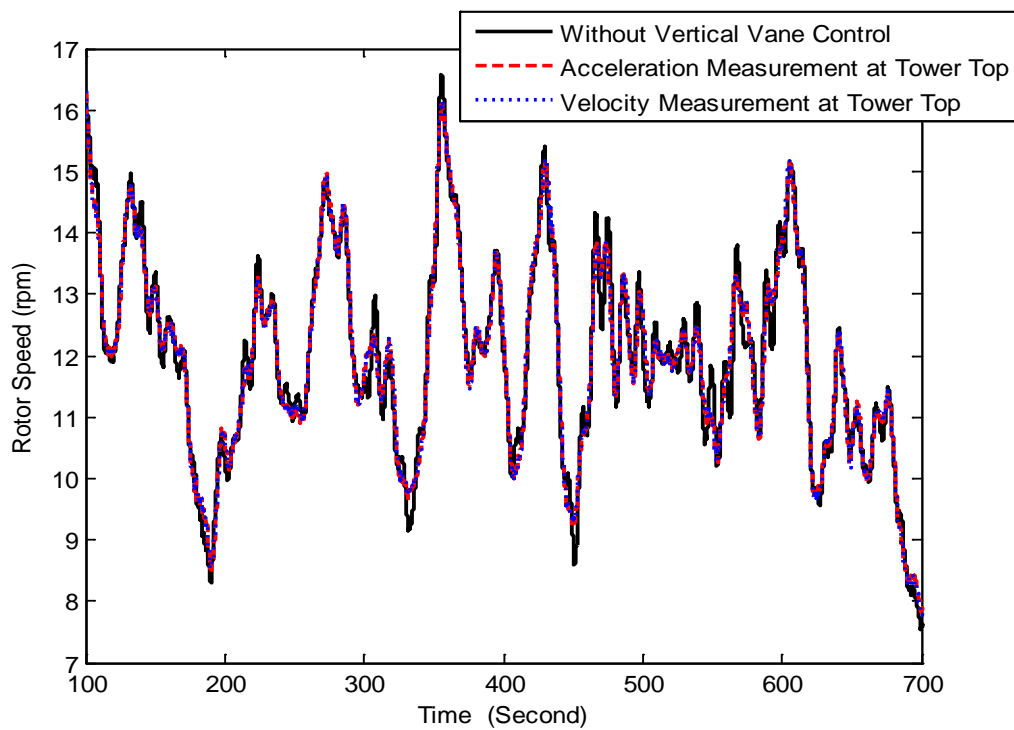


Fig. 7.23. Rotor Speed (Vertical Vane, NACA0012, Downwind as Benchmark)

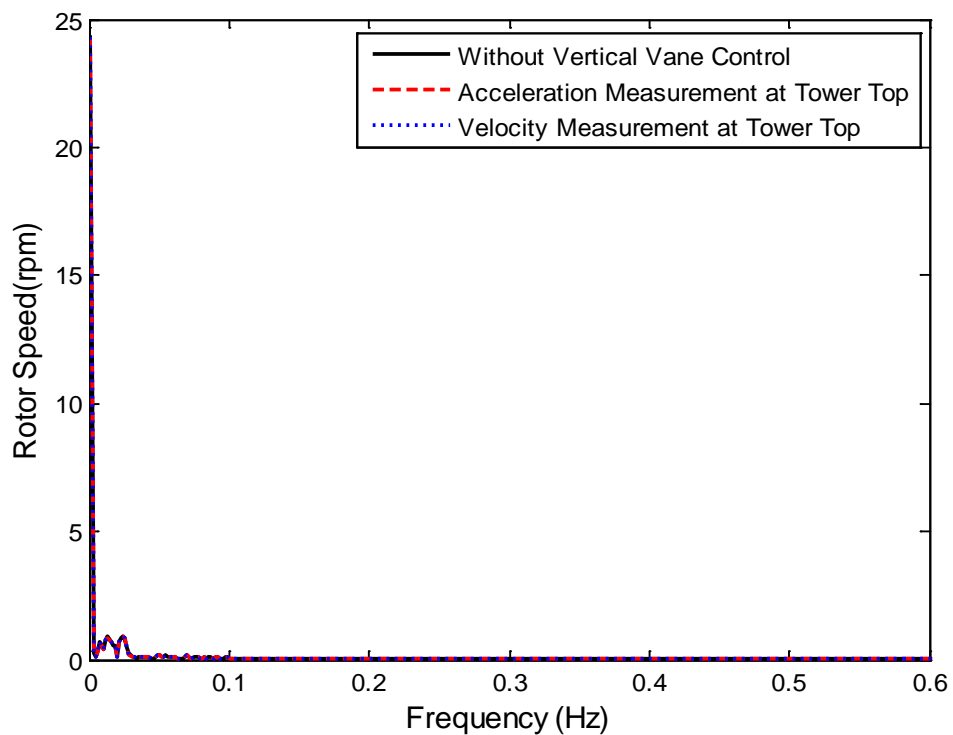


Fig. 7.24. Rotor Speed Spectra (Vertical Vane, NACA0012, Downwind as Benchmark)

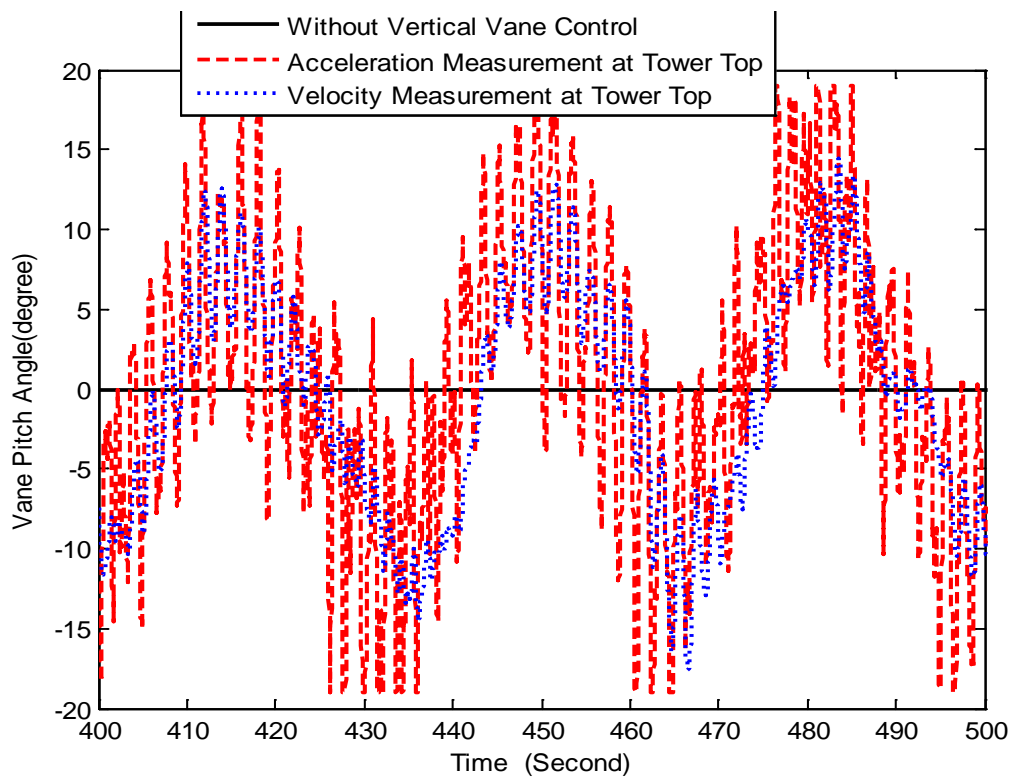


Fig. 7.25. Vane Pitch Angle (Vertical Vane, NACA0012, Downwind as Benchmark)

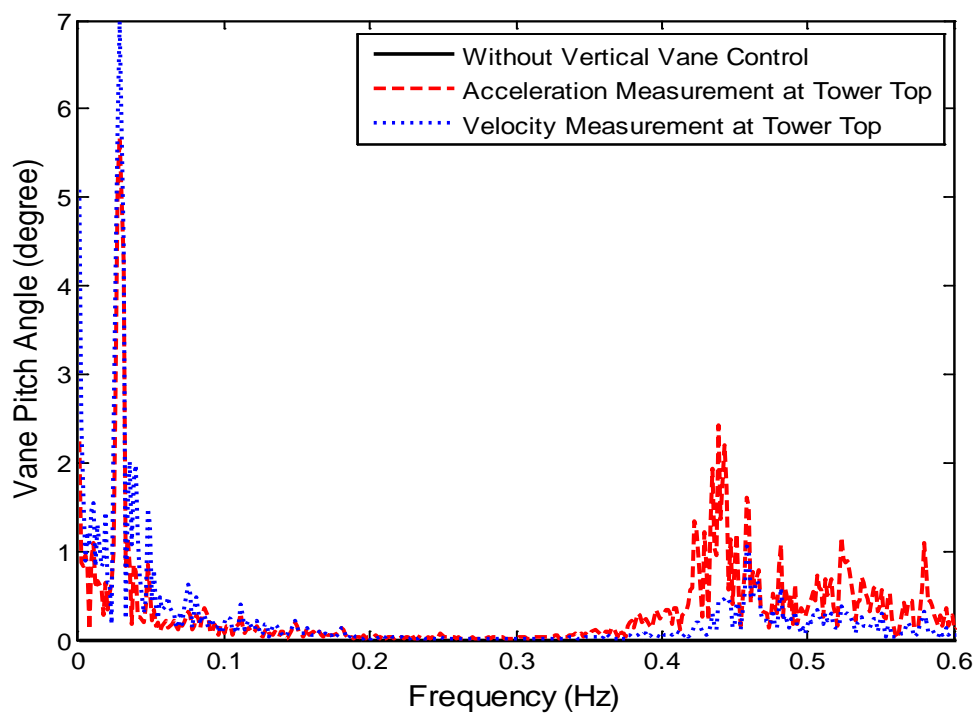


Fig. 7.26. Vane Pitch Angle Spectra (Vertical Vane, NACA0012, Downwind as Benchmark)

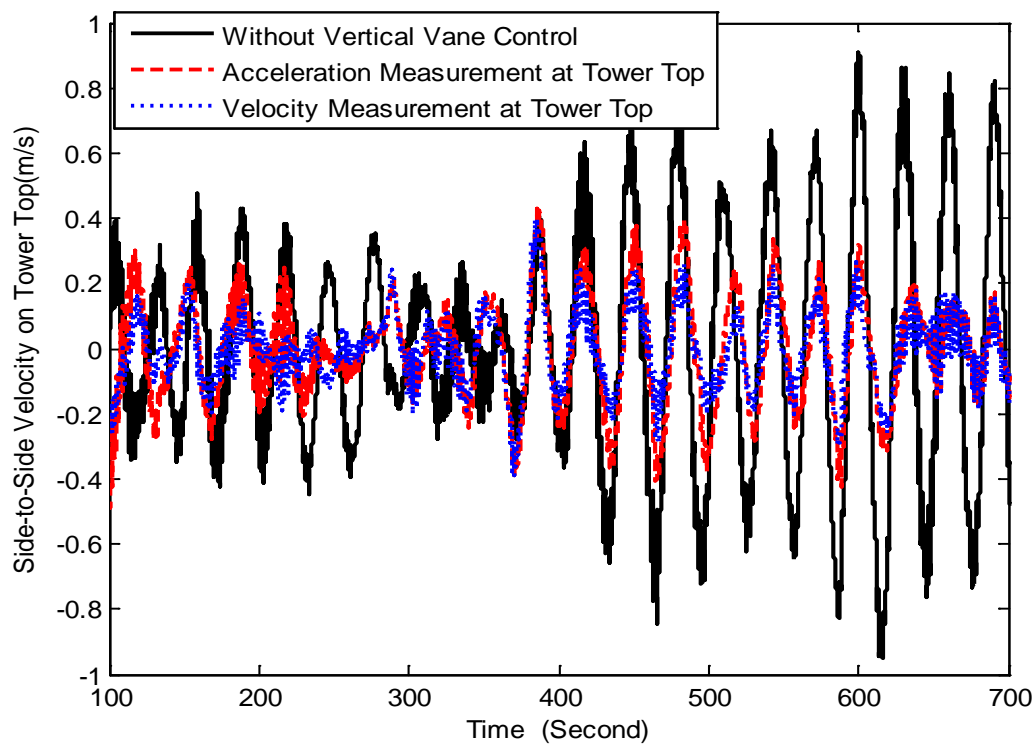


Fig. 7.27. Side-to-Side Velocity (Vertical Vane, NACA0012, Downwind as Benchmark)

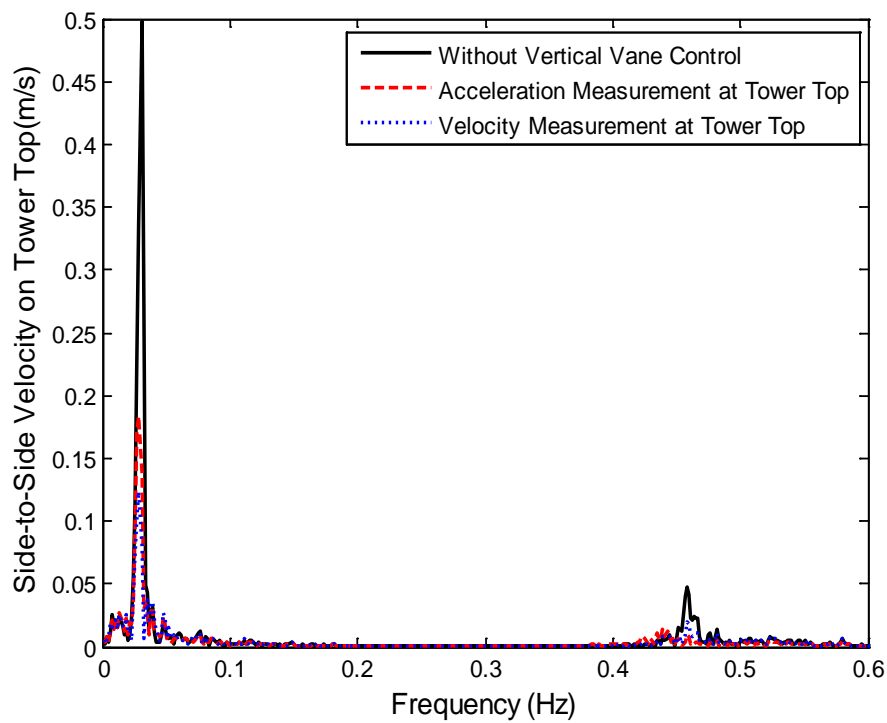


Fig. 7.28. Side-to-Side Velocity Spectra (Vertical Vane, NACA0012, Downwind as Benchmark)

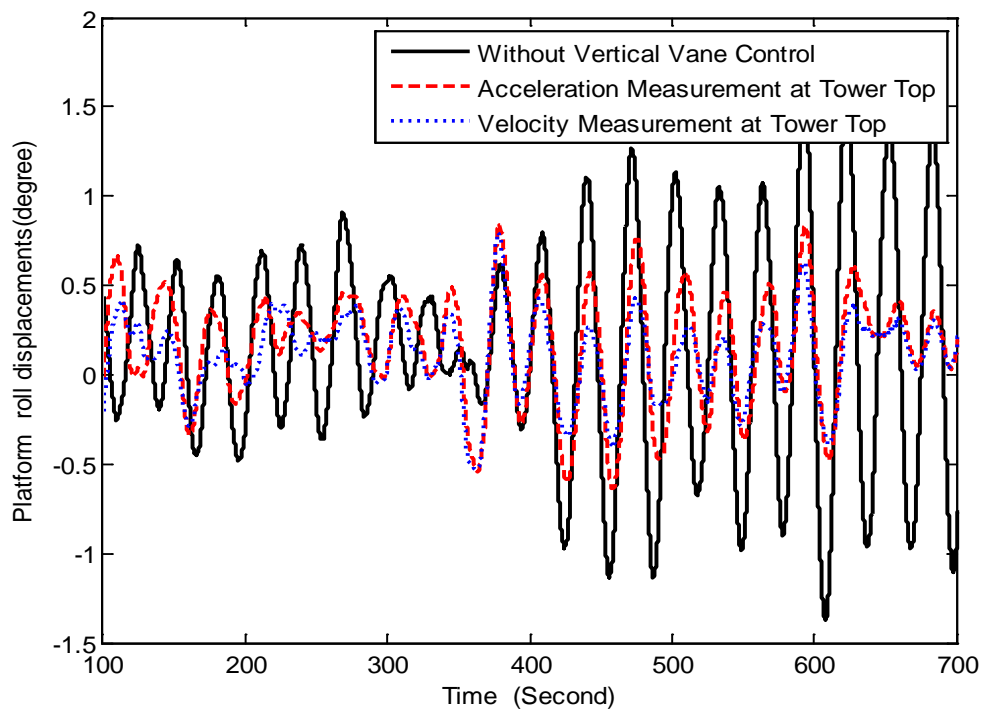


Fig. 7.29. Roll Displacement (Vertical Vane, NACA0012, Downwind as Benchmark)

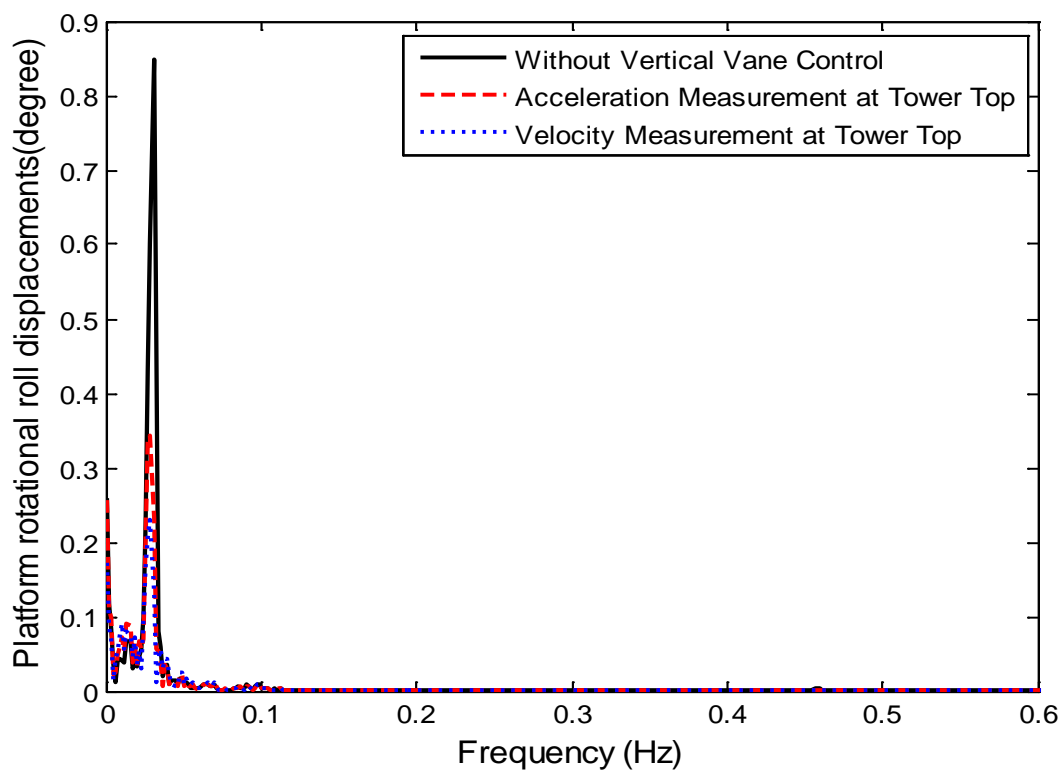


Fig. 7.30. Roll Displacement Spectra (Vertical Vane, NACA0012, Downwind as Benchmark)

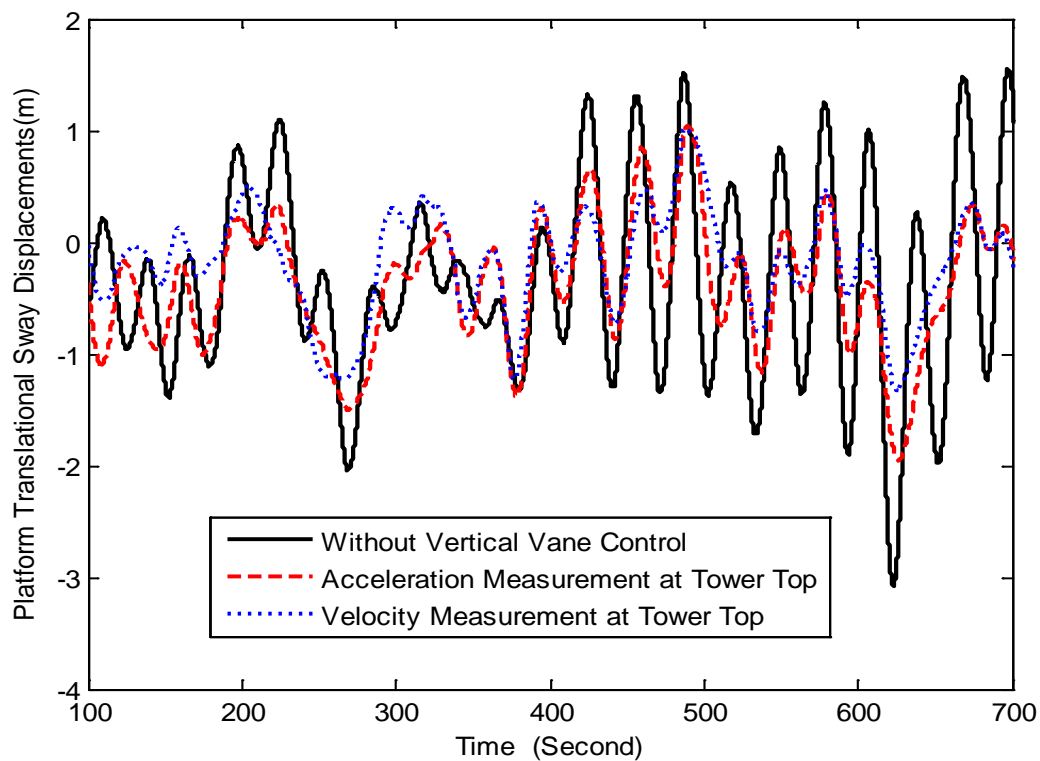


Fig. 7.31. Sway Displacement (Vertical Vane, NACA0012, Downwind as Benchmark)

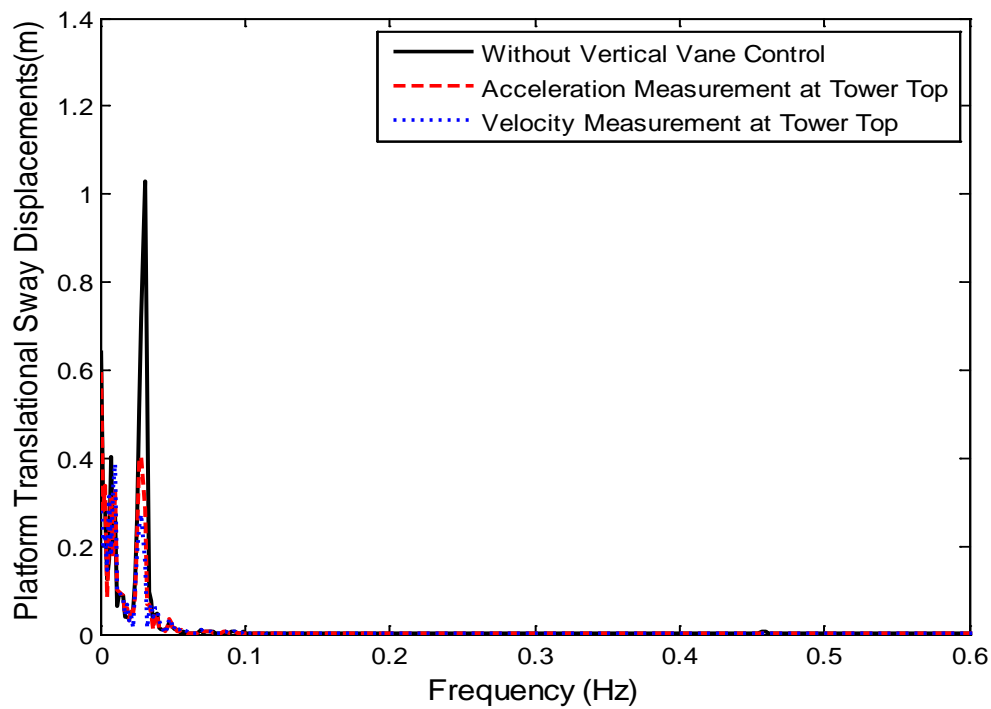


Fig. 7.32. Sway Displacement Spectra (Vertical Vane, NACA0012, Downwind as Benchmark)

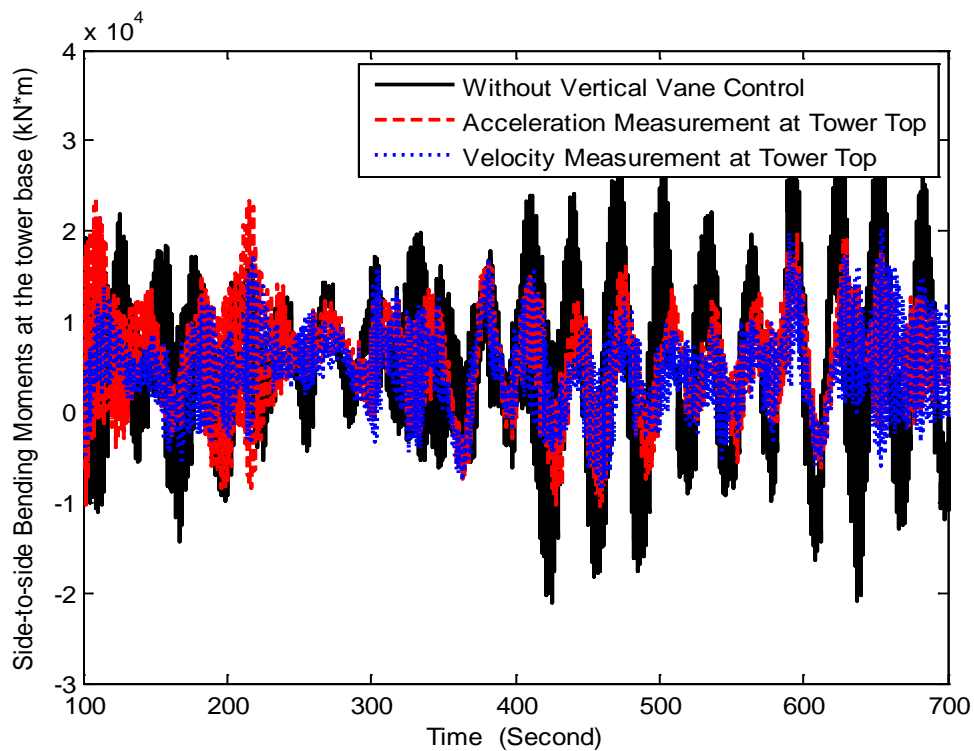


Fig. 7.33. Side-to-Side Bending Moment (Vertical, NACA0012, Downwind as Benchmark)

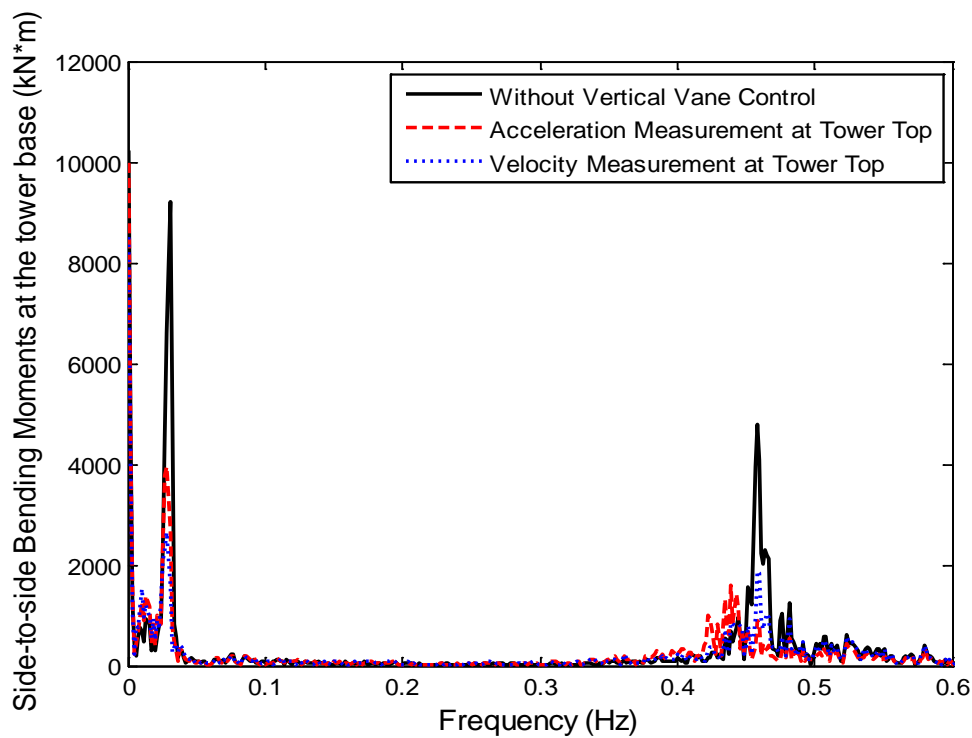


Fig. 7.34. Side-to-Side Bending Moment Spectra (Vertical, NACA0012, Downwind as Benchmark)

7.3.1.3. Vertical Vane and NACA 0012 with Different Vane Area and Downwind

Design as Benchmark

In this subsection, the vane pitch controllers with different vane areas are tested on downwind floating turbine when side-to-side velocity at tower top is used as the measurement and airfoil NACA0012 is used. A downwind floating turbine with PI-based IPC and variable torque controller is used as benchmark. Figures 7.33 through 7.36 show that the generator power and the rotor speed do not change a lot when vertical vane control is used.

Fig. 7.39 and Fig. 7.40 show that the vane pitch angle has more variation when vane area is smaller, i.e. more control actions. Fig. 7.41 and Fig. 7.42 show that the side-to-side velocity at the tower top is significantly alleviated when the vertical vane control is used. The bigger the vane area is, the more reduction of the side-to-side velocity at the tower top is. Fig. 7.43 through Fig. 7.48 show that the roll displacement, the platform sway displacement, and side-to-side moment are significantly reduced. In summary, the bigger the vane area is, the more reduction of displacement or loads in side-to-side direction is.

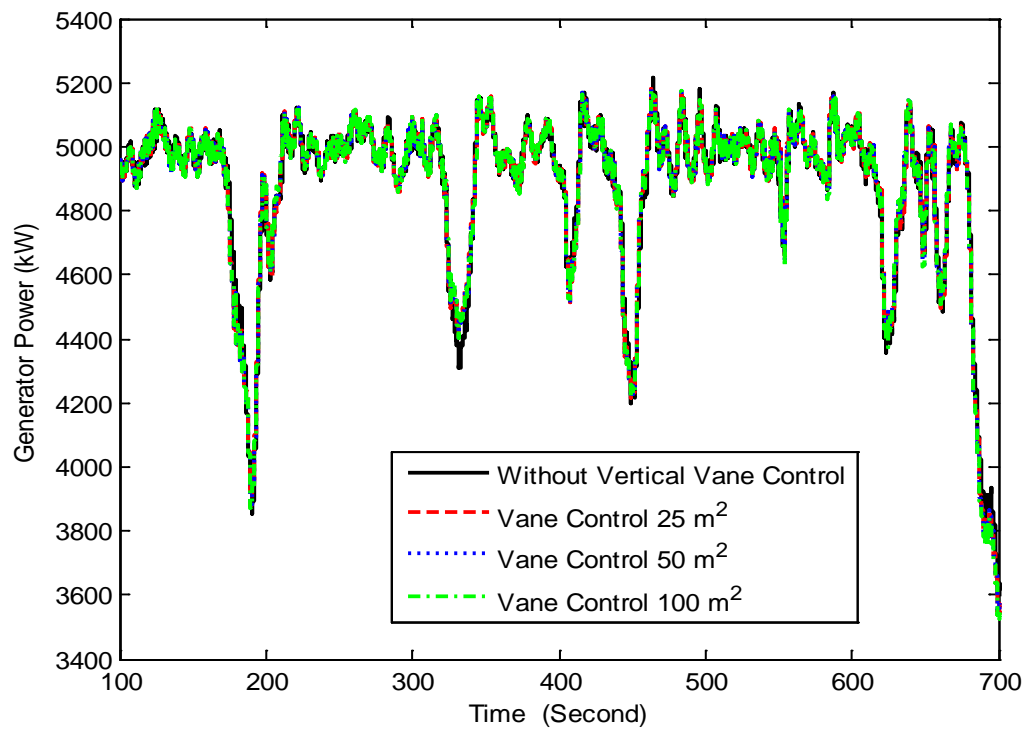


Fig. 7.35. Generator Power (Vertical Vane, NACA0012, Downwind as Benchmark)

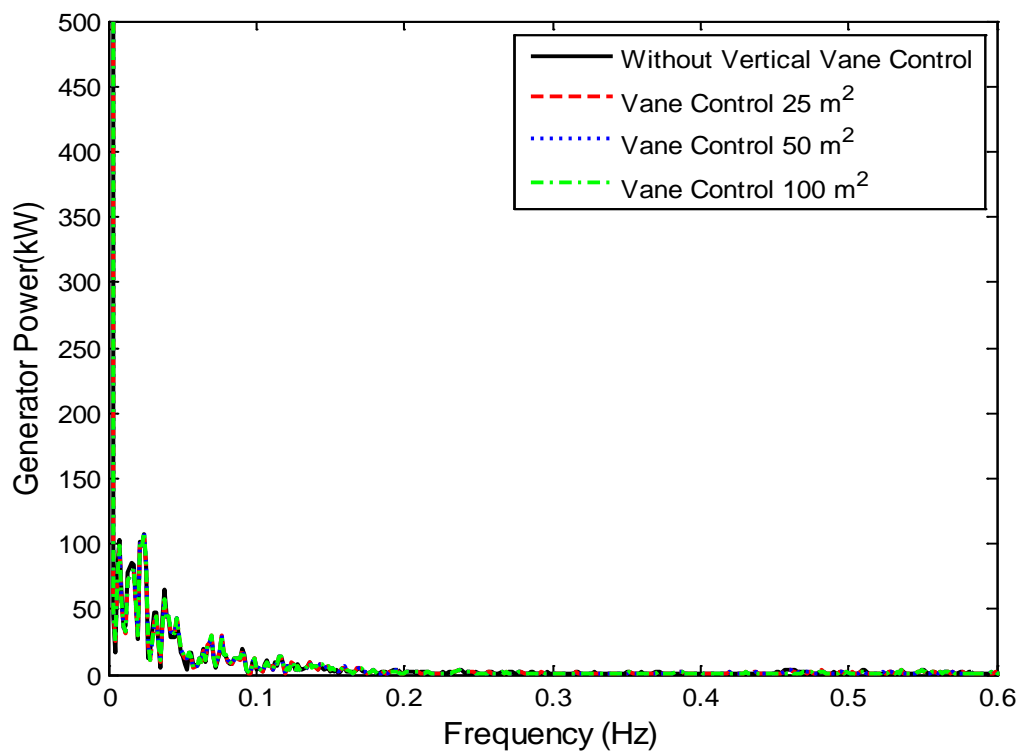


Fig. 7.36. Generator Power (Vertical Vane, NACA0012, Downwind as Benchmark)

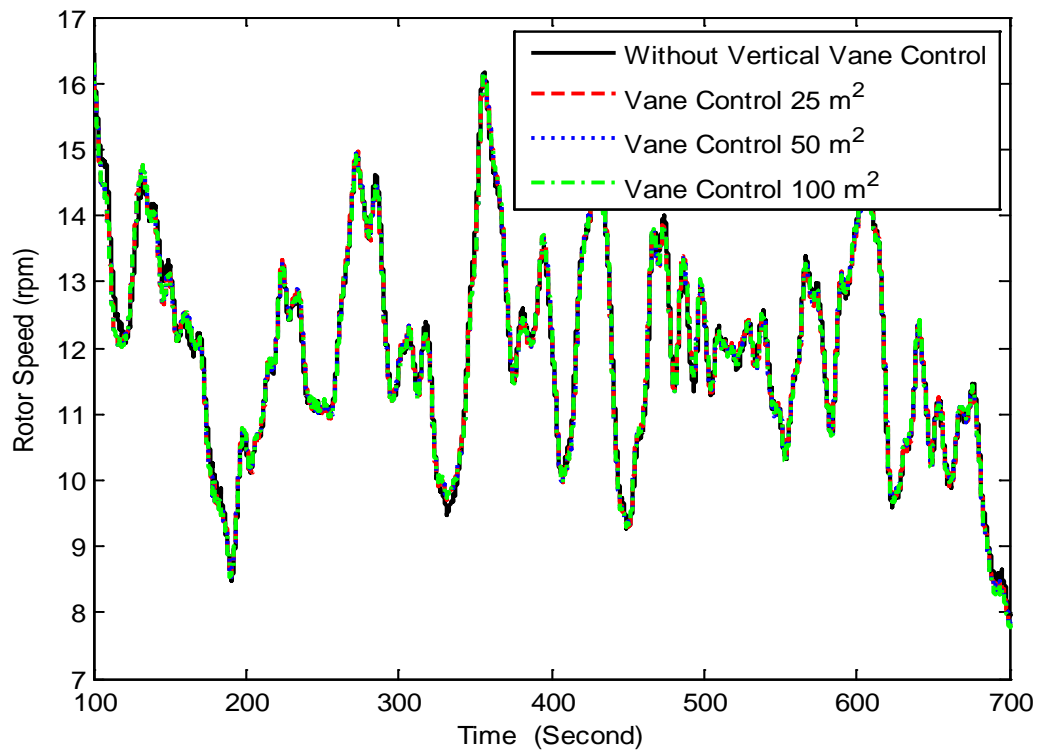


Fig. 7.37. Rotor Speed (Vertical Vane, NACA0012, Downwind as Benchmark)

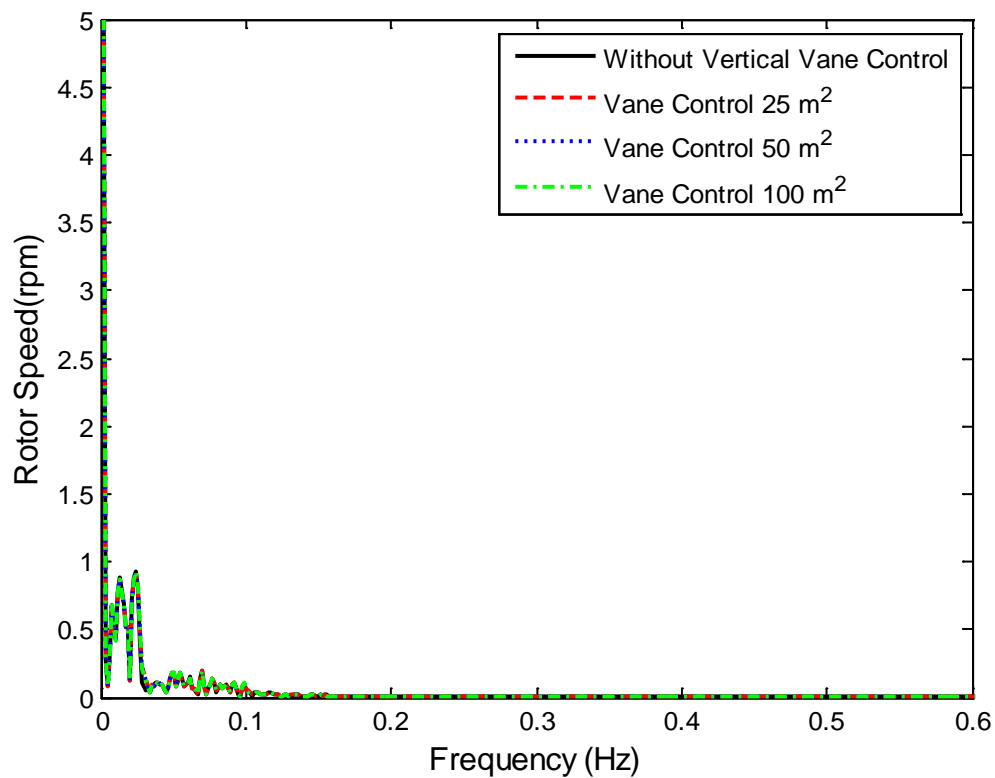


Fig. 7.38. Rotor Speed Spectra (Vertical Vane, NACA0012, Downwind as Benchmark)

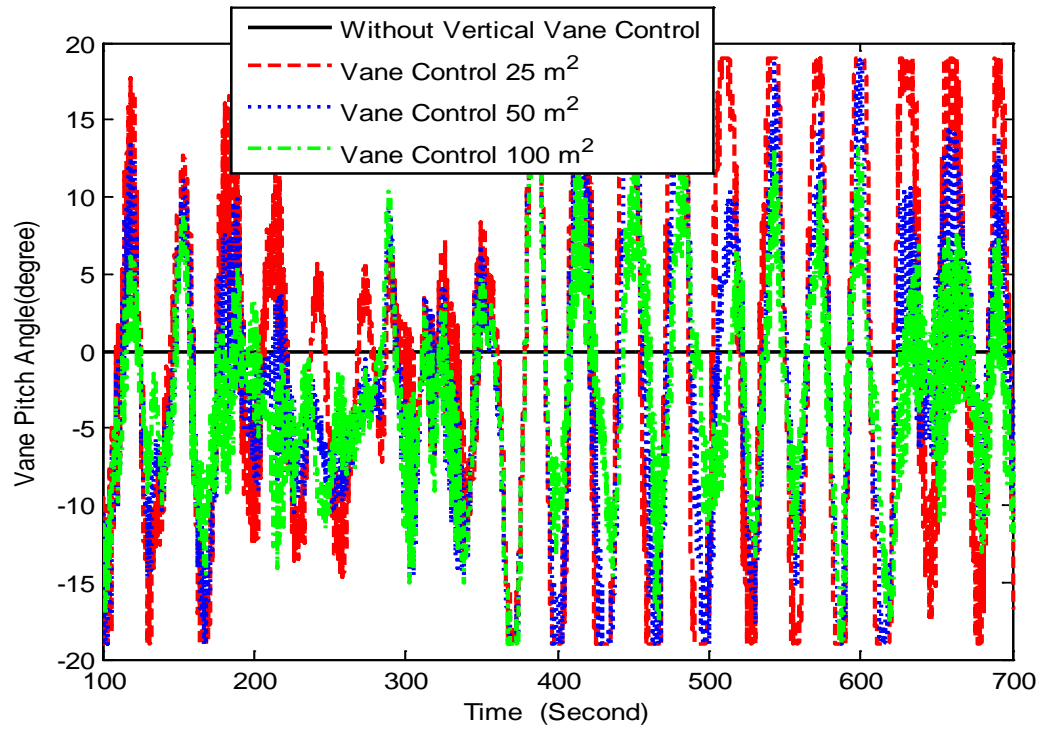


Fig. 7.39. Vane Pitch Angle (Vertical Vane, NACA0012, Downwind as Benchmark)

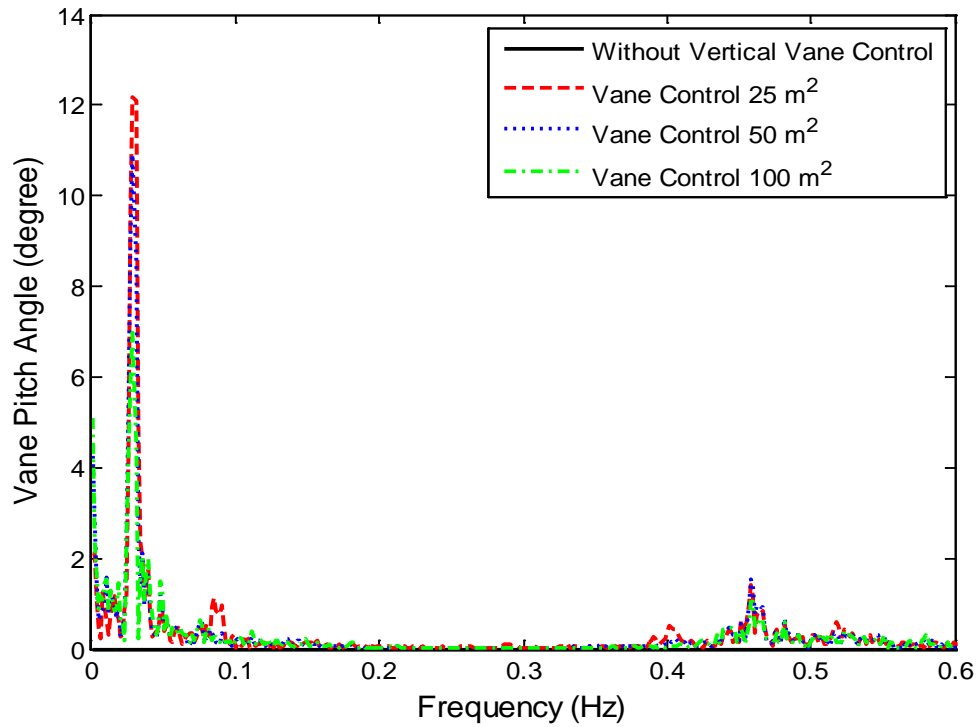


Fig. 7.40. Vane Pitch Angle Spectra (Vertical Vane, NACA0012, Downwind as Benchmark)

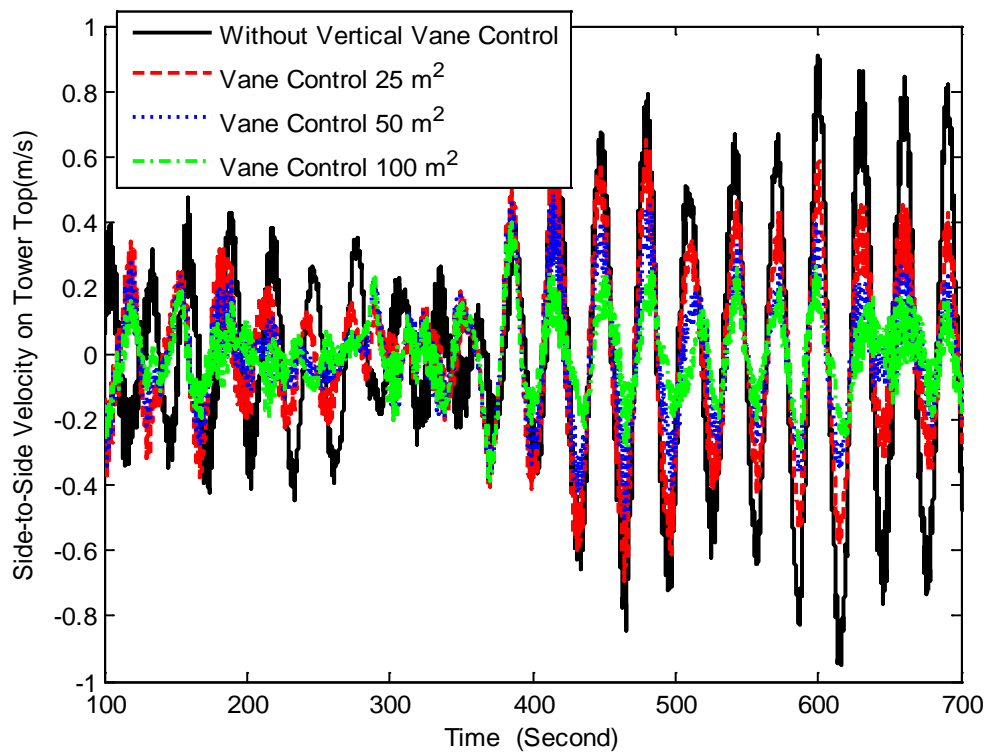


Fig. 7.41. Side-to-Side Velocity (Vertical Vane, NACA0012, Downwind as Benchmark)

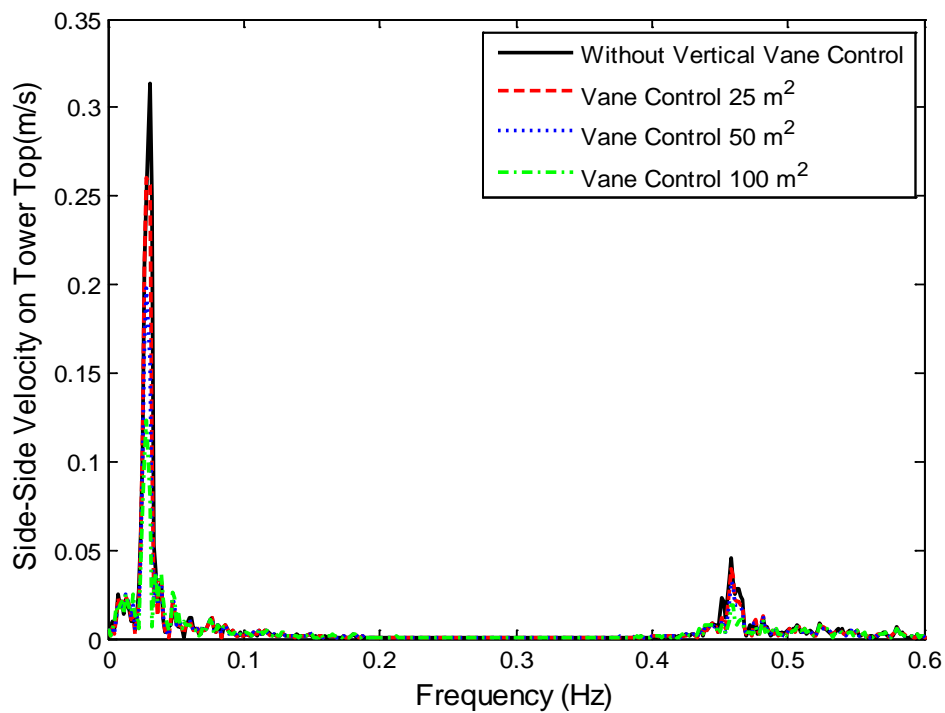


Fig. 7.42. Side-to-Side Velocity Spectra (Vertical Vane, NACA0012, Downwind as Benchmark)

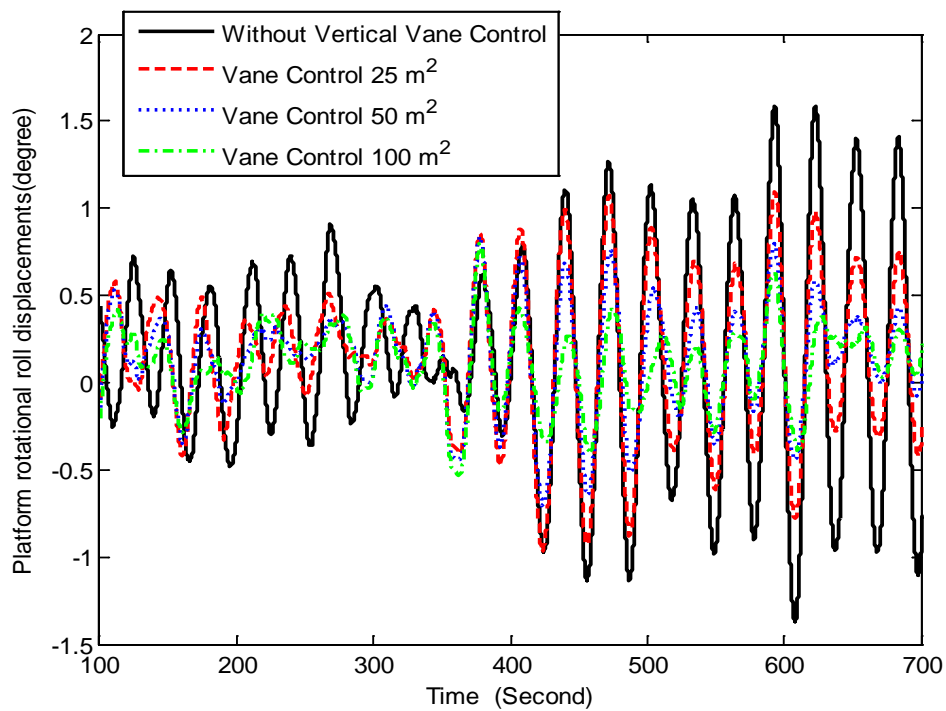


Fig. 7.43 Roll Displacement (Vertical Vane, NACA0012, Downwind as Benchmark)

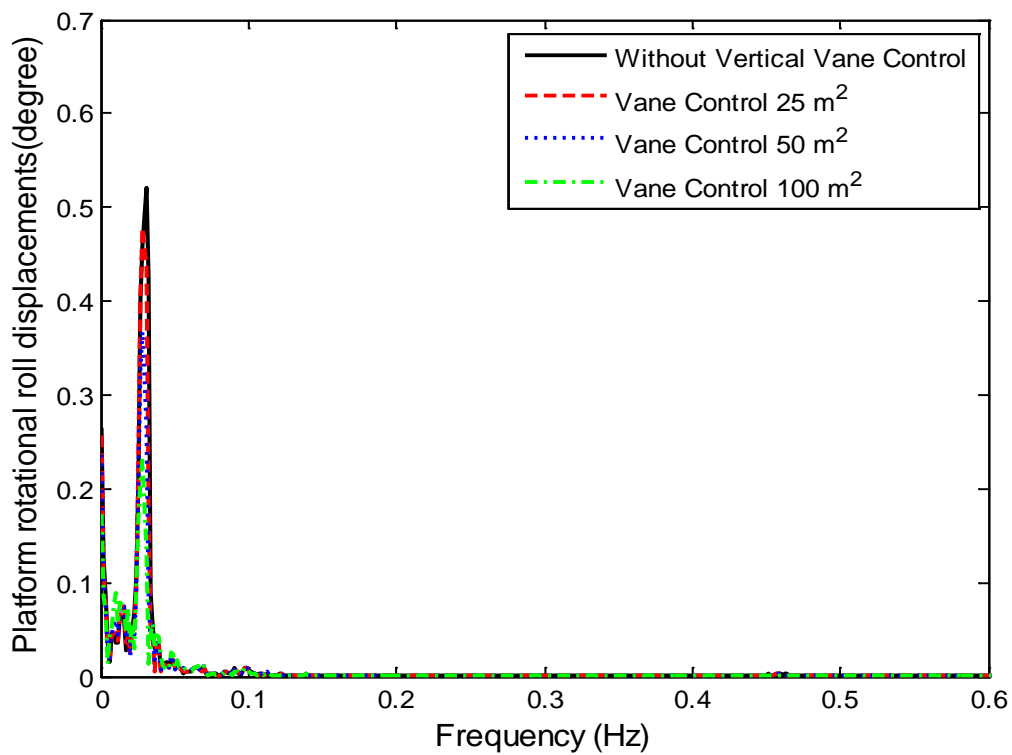


Fig. 7.44. Roll Displacement Spectra (Vertical Vane, NACA0012, Downwind as Benchmark)

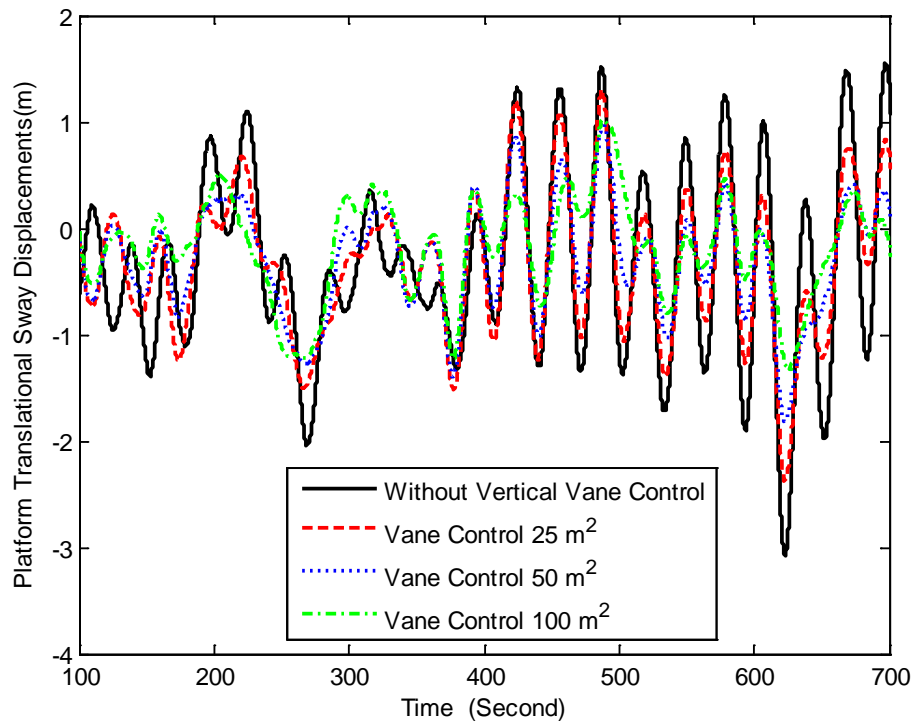


Fig. 7.45. Sway Displacement (Vertical Vane, NACA0012, Downwind as Benchmark)

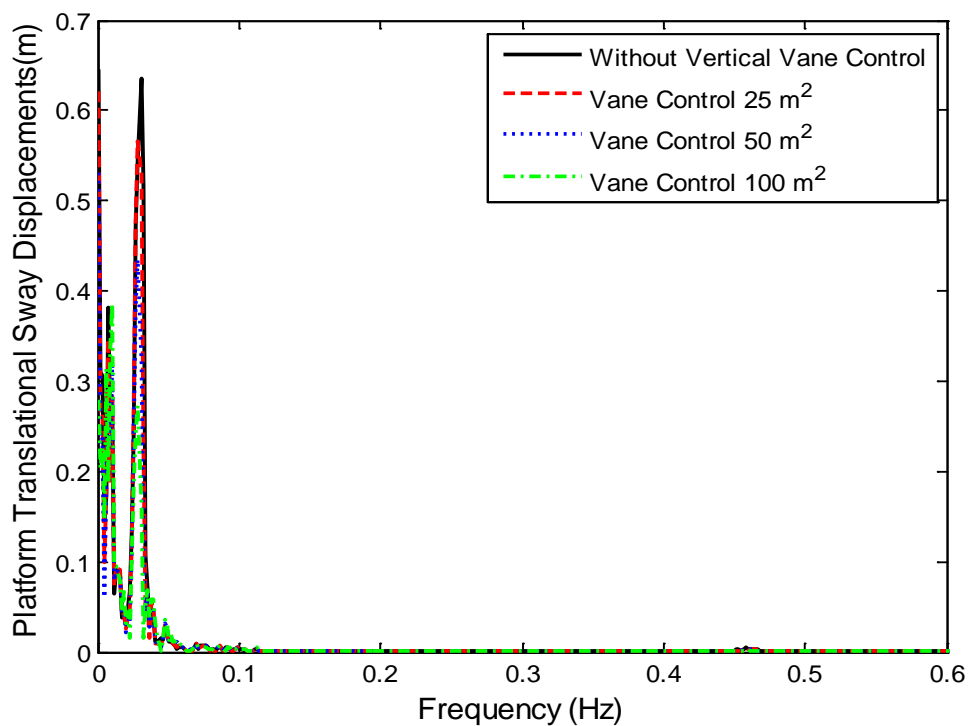


Fig. 7.46 Sway Displacement Spectra (Vertical Vane, NACA0012, Downwind as Benchmark)

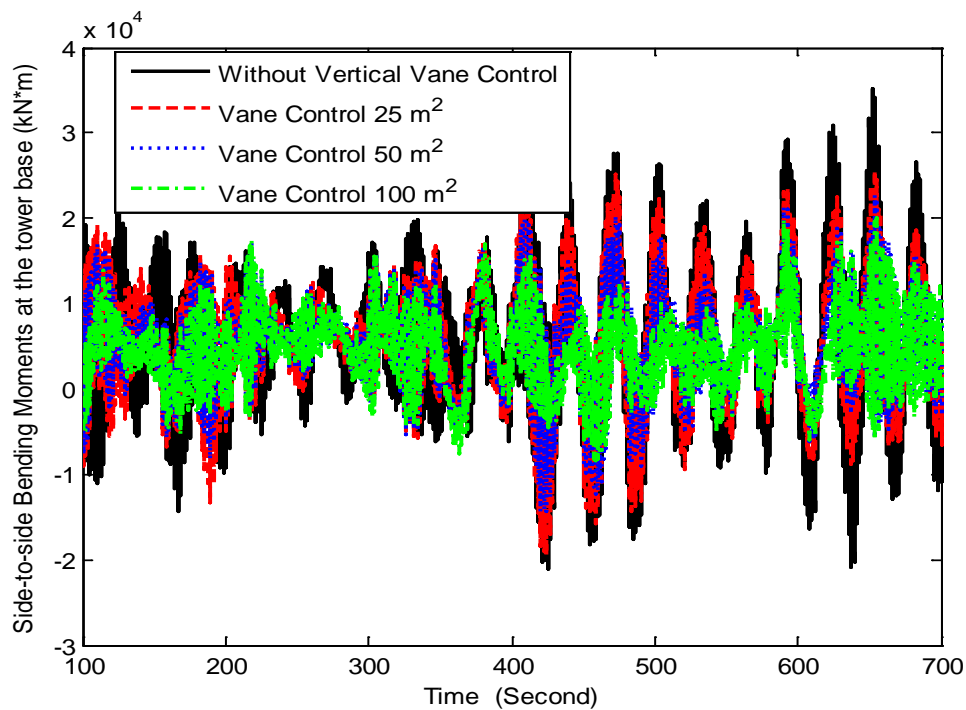


Fig. 7.47. Side-to-Side Bending Moment (Vertical Vane, NACA0012, Downwind as Benchmark)

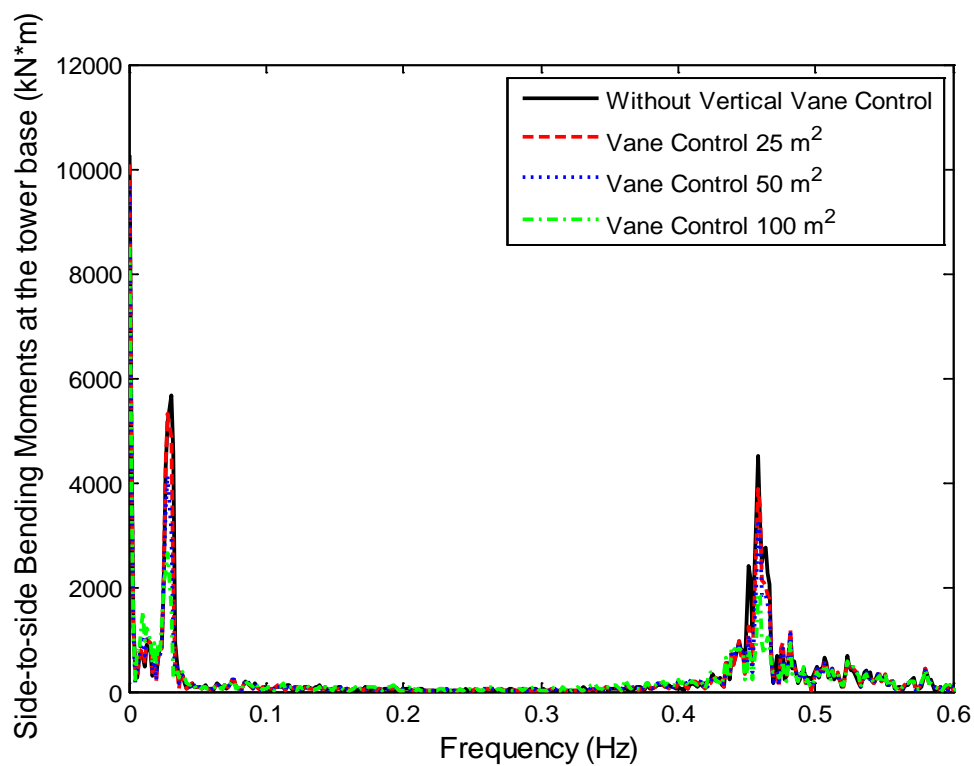


Fig. 7.48. Side-to-Side Bending Moment (Vertical Vane, NACA0012, Downwind as Benchmark)

7.3.1.4. High Lift Airfoil and Vertical Vane with Different Measurements and Downwind Design as Benchmark

In this subsection, the vane pitch controllers with a highlift airfoil are tested on downwind floating turbine with Hywind platform when both side-to-side acceleration and side-to-side velocity at tower top are used as measurements. Downwind floating turbine with Hywind platform is used as benchmark when PI-based IPC and variable torque control are used. Fig. 7.49 through Fig. 7.52 show that the generator power and rotor speed do not change a lot when vertical vane control is used. Fig. 7.53 and Fig. 7.54 show that, compared with the vane control with traditional NACA0012 airfoil, variation of side-to-side velocity at tower top is further reduced when a highlift airfoil is used. Vane pitch angle and its spectral is shown in Fig. 7.55 and Fig. 7.56.

Figures 7.55 through 7.60 show that platform translational roll displacement, sway displacement and side-to-side moment are further reduced when a high-lift airfoil is used and both the velocity and the acceleration along side-to-side direction at tower top are used as measurement. Compared with that when the acceleration is used as measurement, the sway displacement and loads are further reduced when the velocity is used as the measurement.

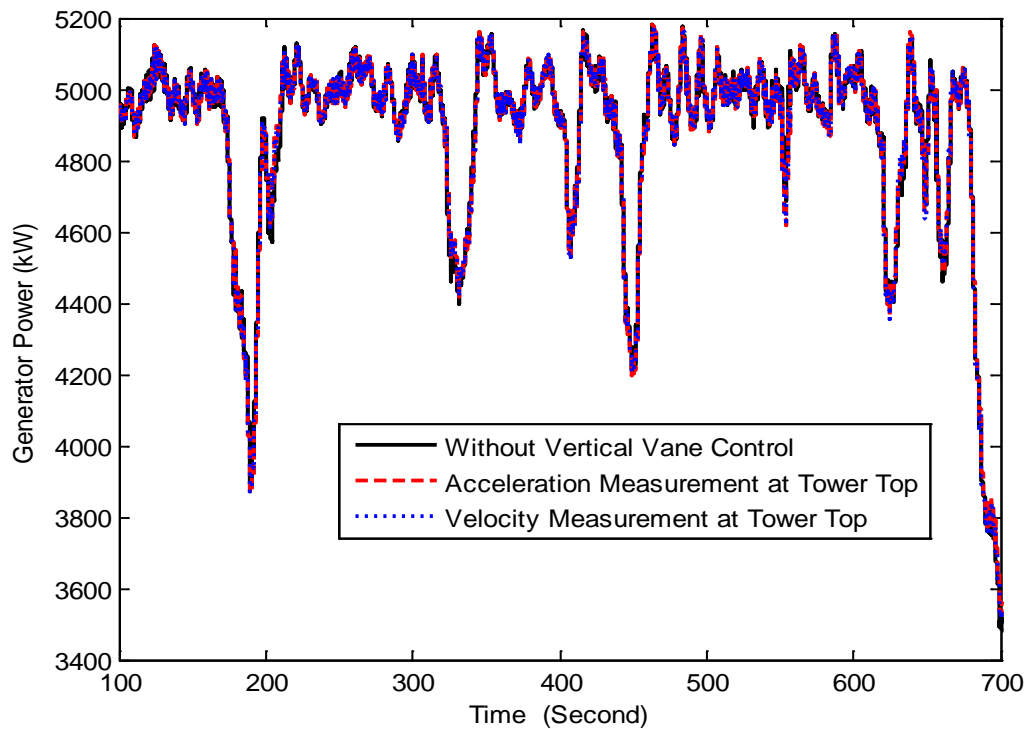


Fig. 7.49. Generator Power Comparison (Vertical Vane, Highlift Airfoil, Downwind as Benchmark)

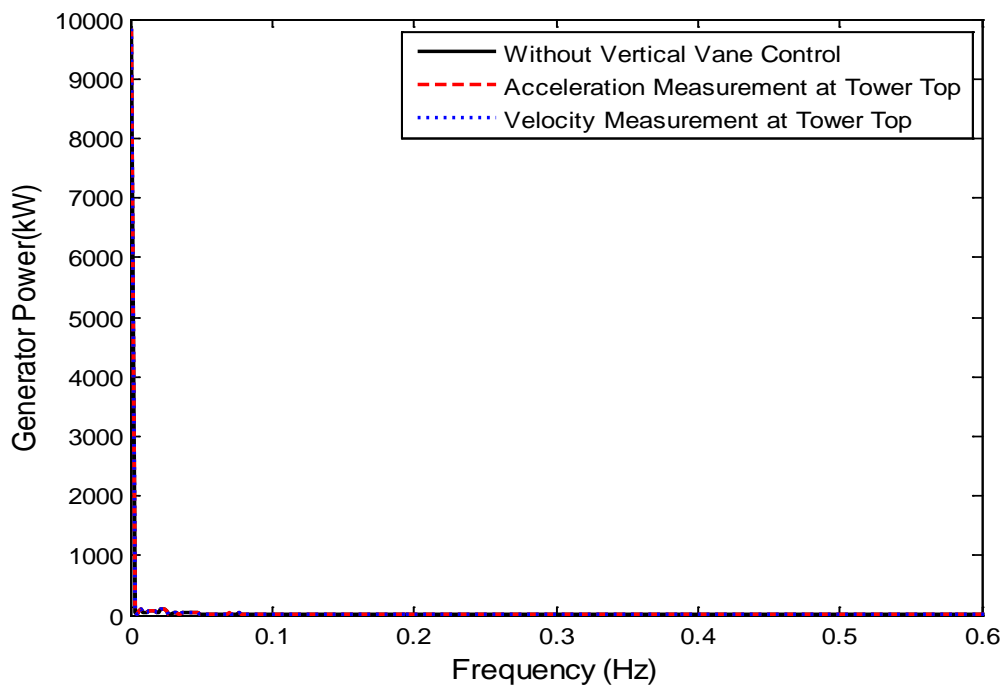


Fig. 7.50 Generator Power Spectral (Vertical Vane, Highlift Airfoil, Downwind as Benchmark)

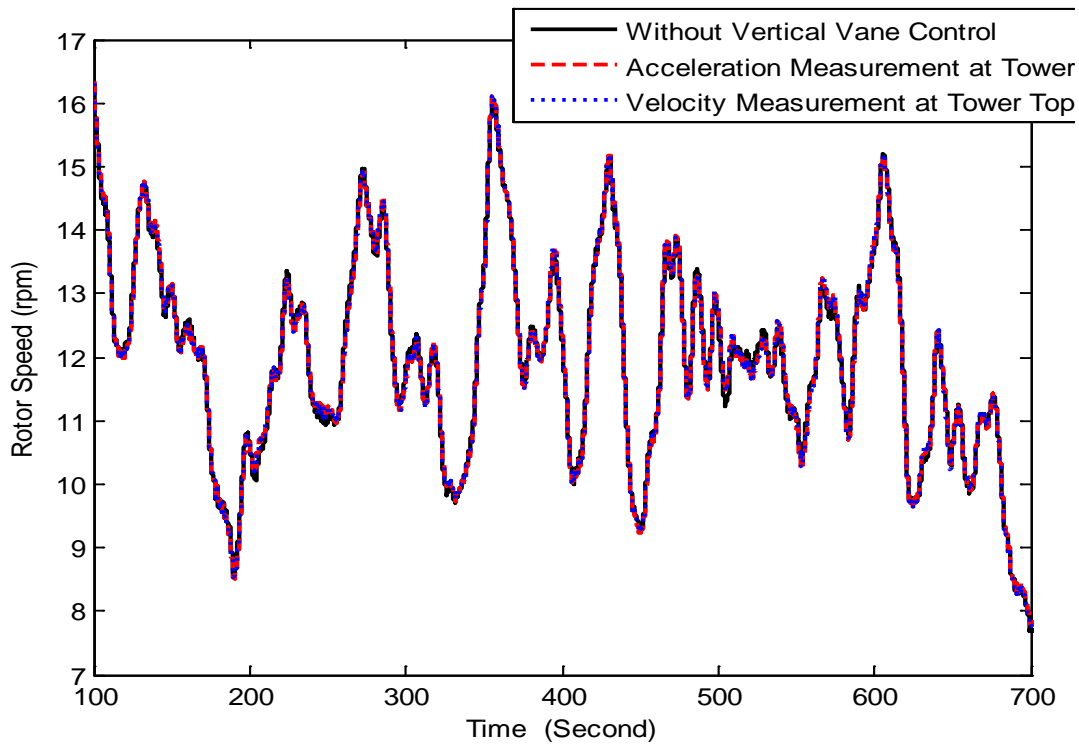


Fig. 7.51 Rotor Speed (Vertical Vane, Highlift Airfoil, Downwind as Benchmark)

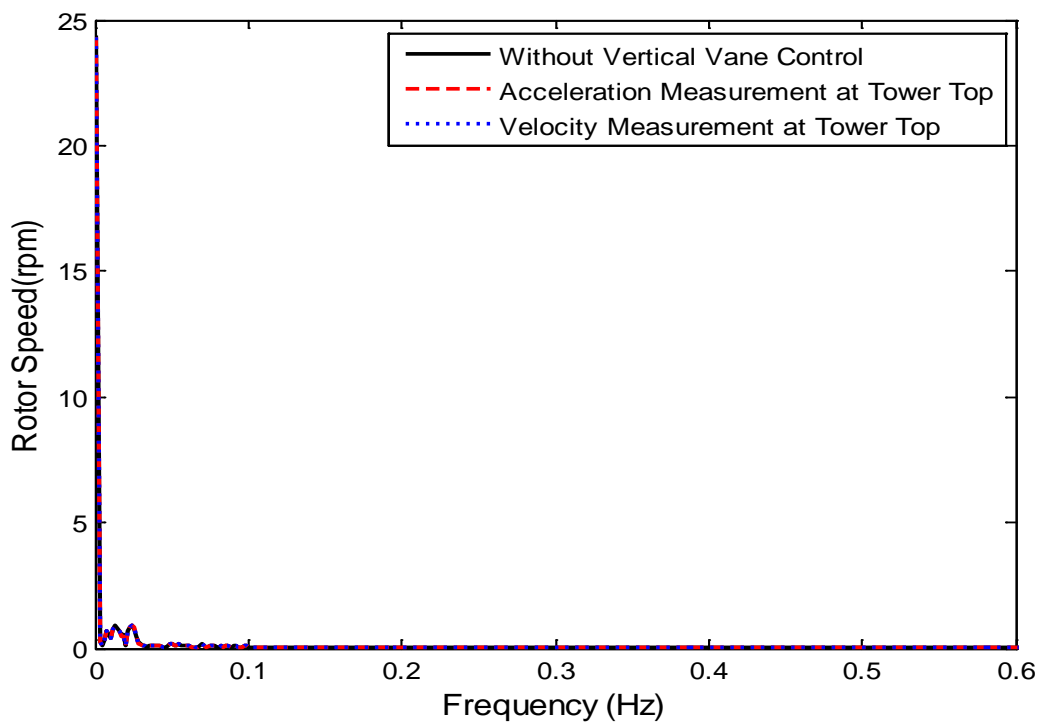


Fig. 7.52 Rotor Speed Spectra (Vertical Vane, Highlift Airfoil, Downwind as Benchmark)

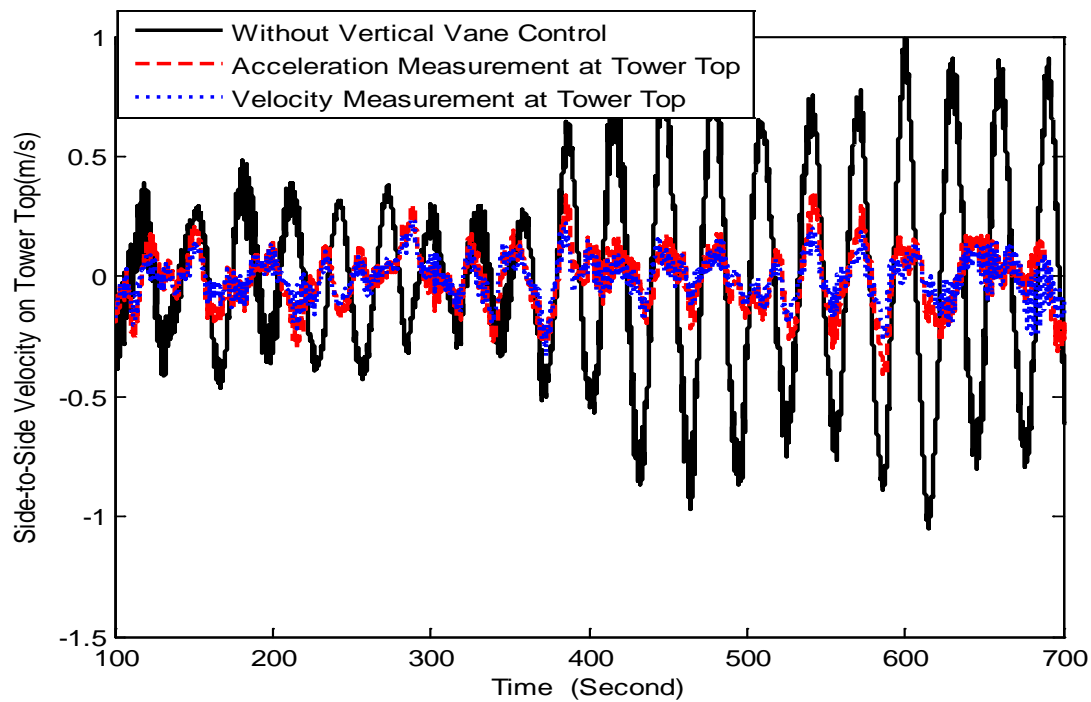


Fig. 7.53 Side-to-side Velocity on Tower Top (Vertical Vane, Highlift Airfoil, Downwind as Benchmark)

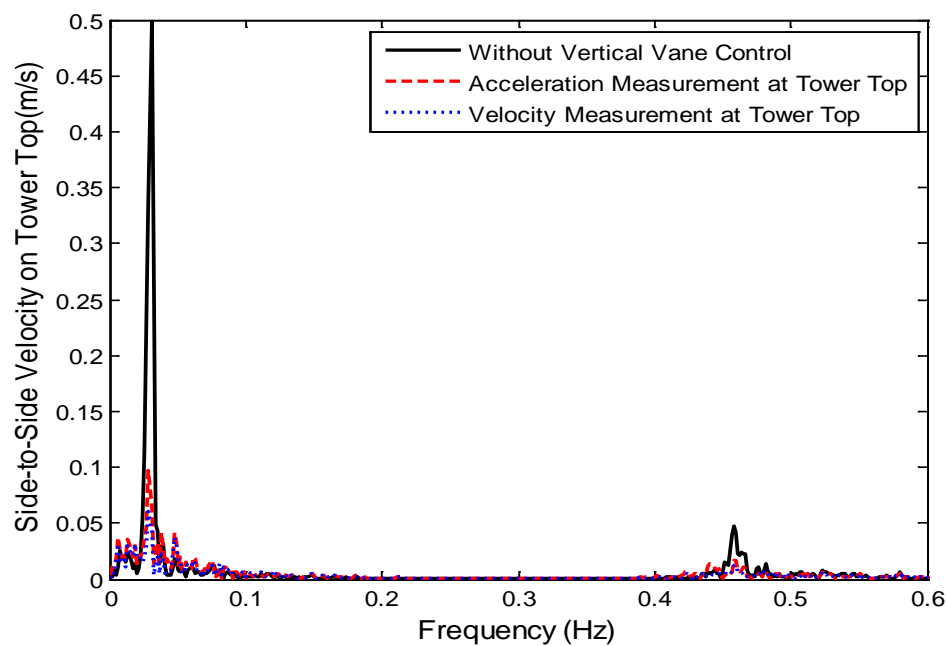


Fig. 7.54 Spectra of Side-to-side Velocity on Tower Top (Vertical Vane, Highlift Airfoil, Downwind as Benchmark)

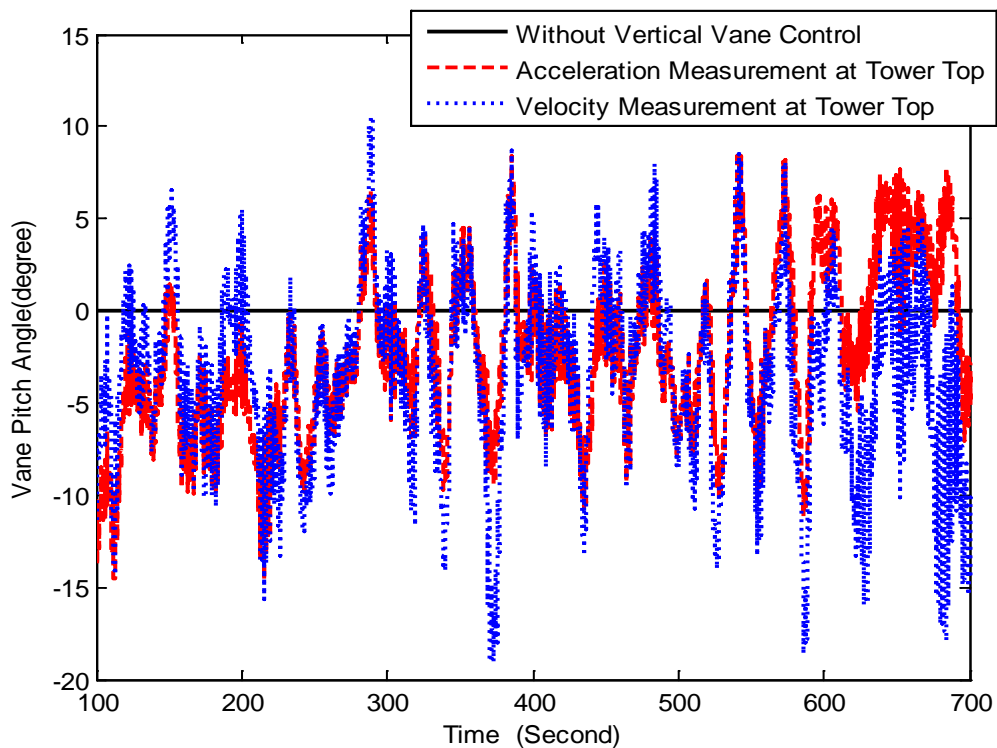


Fig. 7.55 Vane Pitch Angle (Vertical Vane, Highlift Airfoil, Downwind as Benchmark)

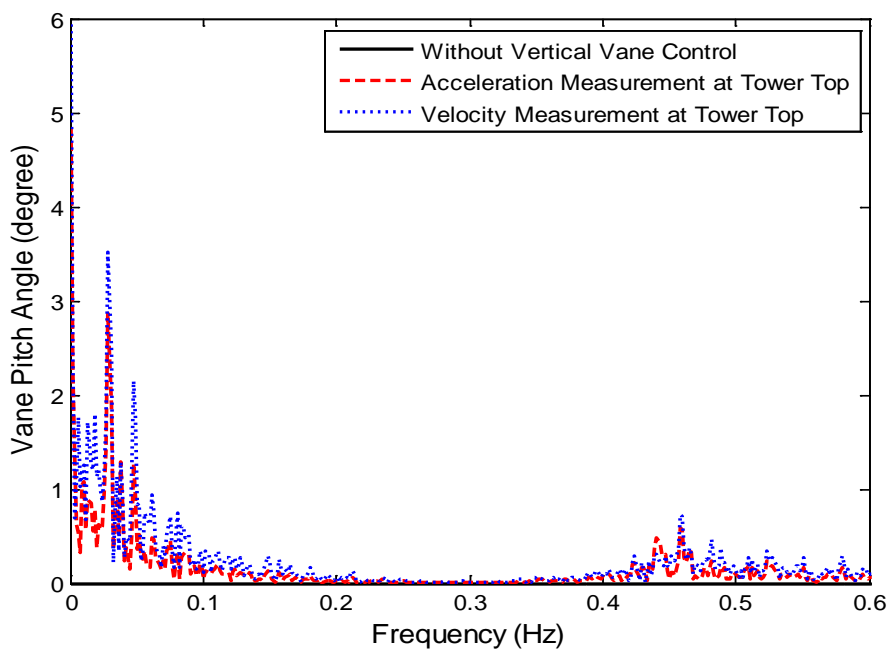


Fig. 7.56 Vane Pitch Angle Spectra (Vertical Vane, Highlift Airfoil, Downwind as Benchmark)

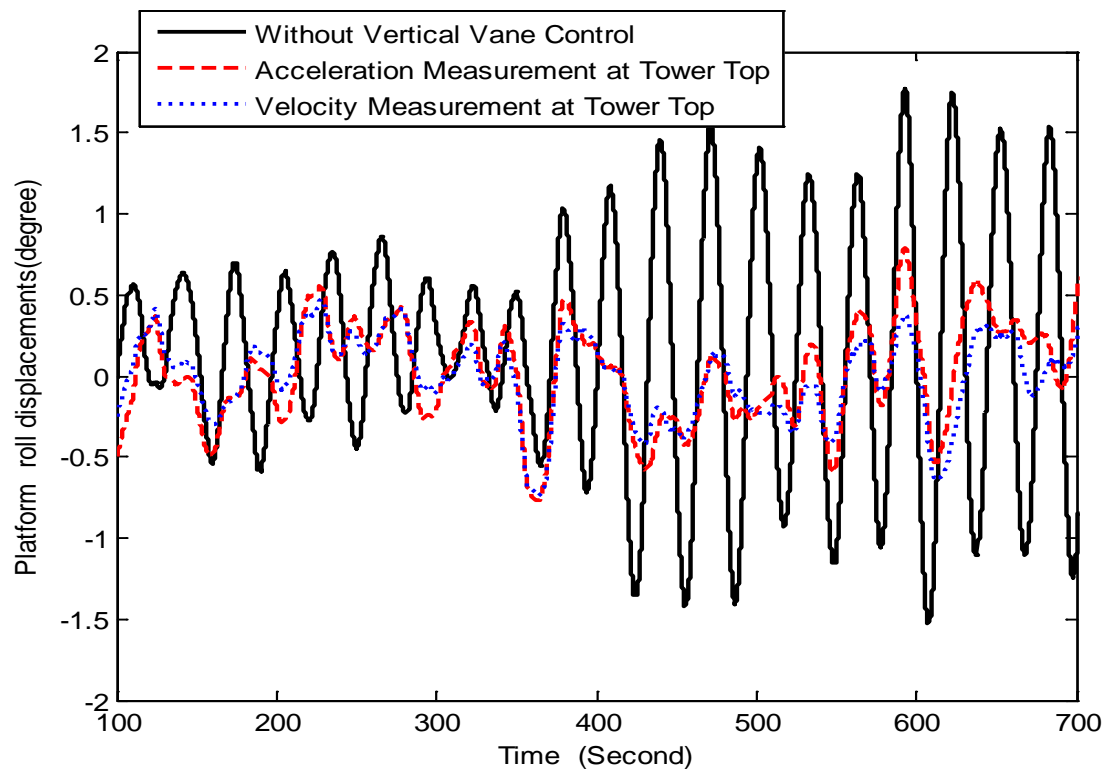


Fig. 7.57 Platform Roll Displacement (Vertical Vane, Highlift Airfoil, Downwind as Benchmark)

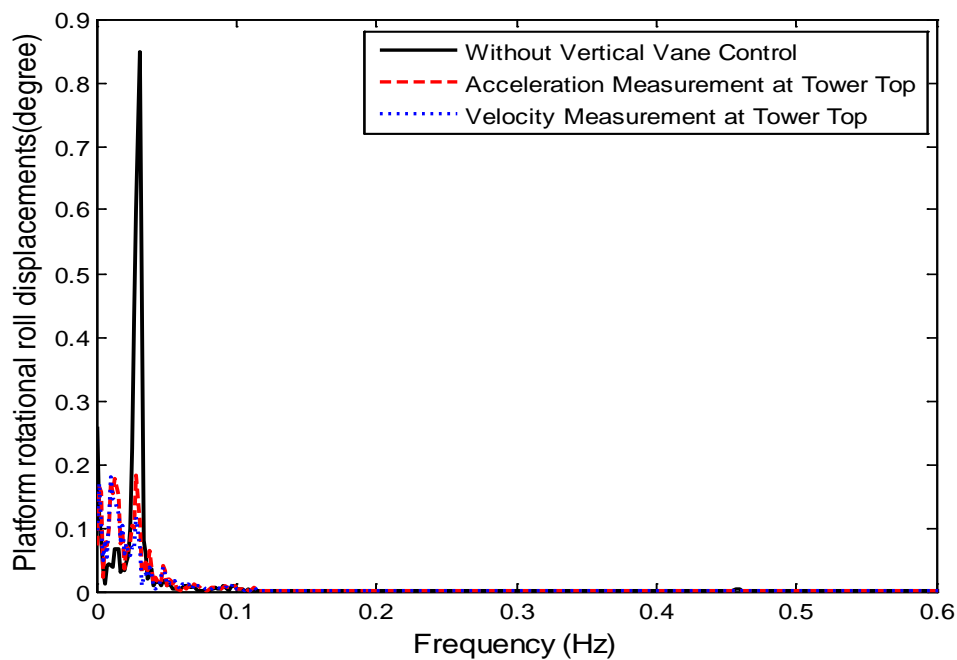


Fig. 7.58 Platform Roll Displacement Spectra (Vertical Vane, Highlift Airfoil, Downwind as Benchmark)

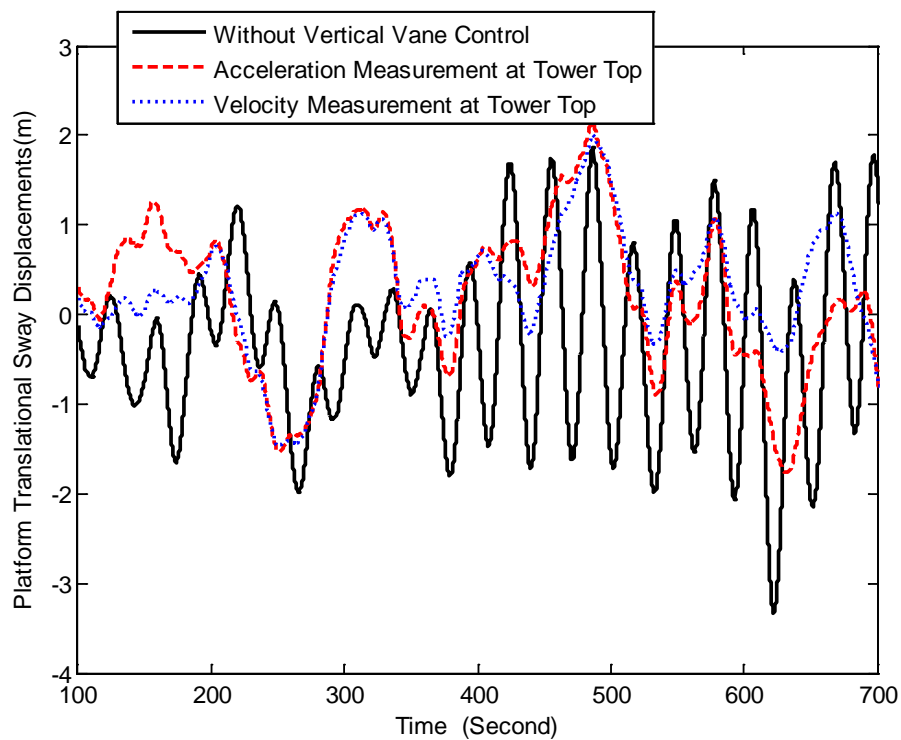


Fig. 7.59 Platform Sway Displacement (Vertical Vane, Highlift Airfoil, Downwind as Benchmark)

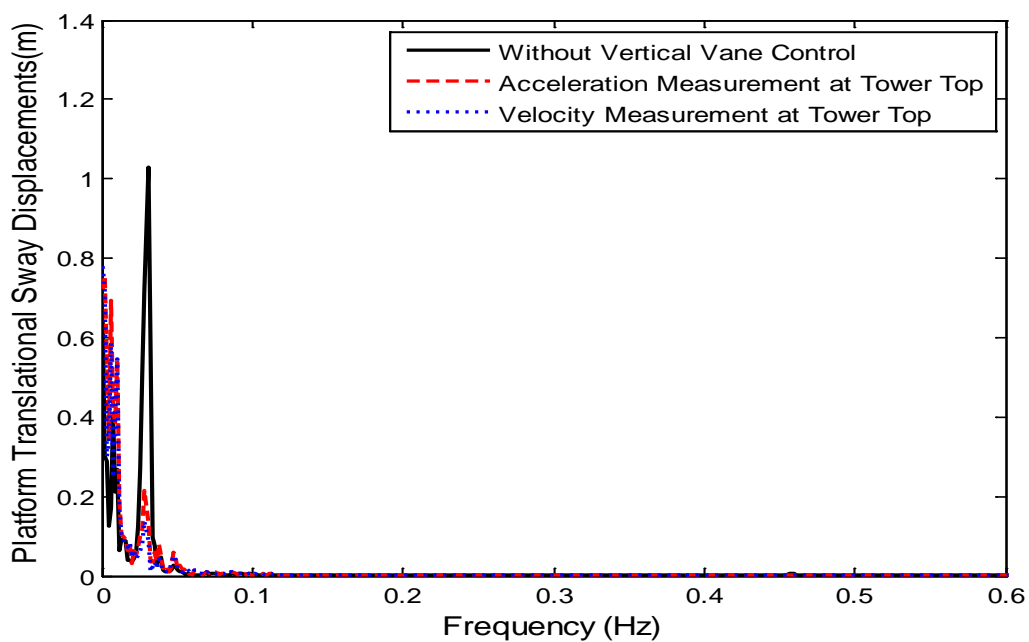


Fig. 7.60 Platform Sway Displacement Spectra (Vertical Vane, Highlift Airfoil, Downwind as Benchmark)

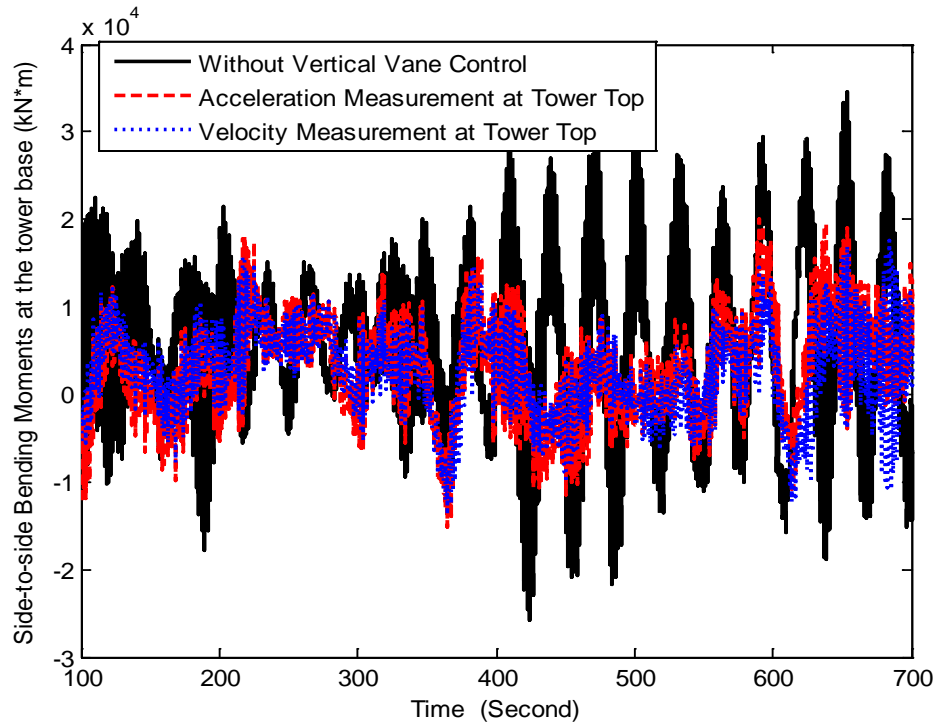


Fig. 7.61 Side-to-side Bending Moment (Vertical Vane, Highlift Airfoil, Downwind as Benchmark)

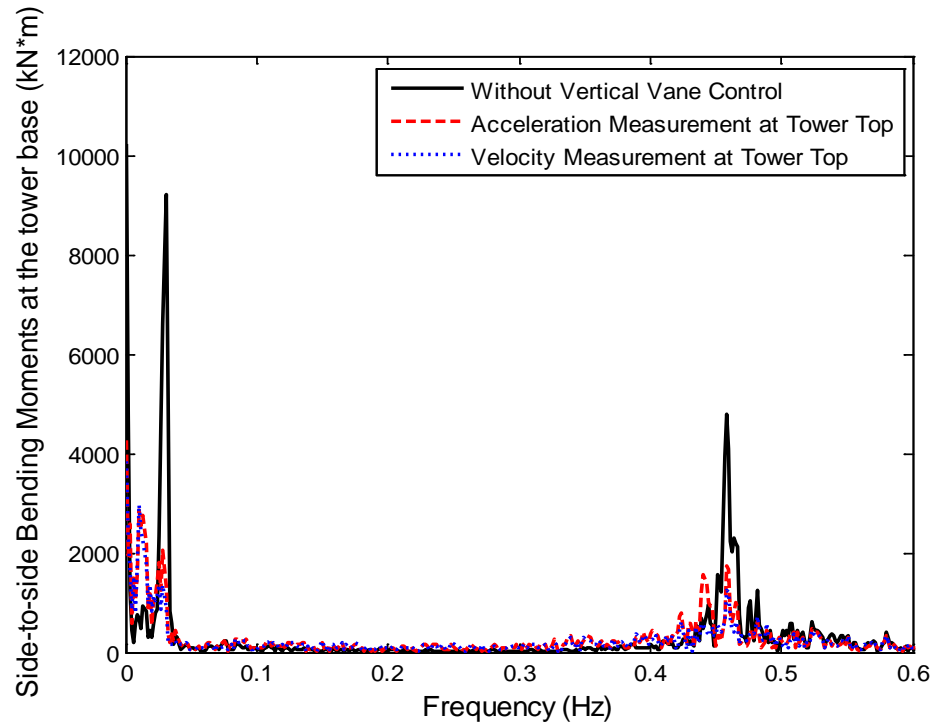


Fig. 7.62 Side-to-side Bending Moment Spectra (Vertical Vane, Highlift Airfoil, Downwind as Benchmark)

7.3.1.5. High Lift Airfoil and Vertical Vane with Different Vane Area and Downwind Design as Benchmark

In this section, vertical vane pitch controllers with different vane areas are tested on downwind floating turbine when side-to-side velocity at tower top is used as the measurement and highlift airfoil is used. Downwind floating turbine with PI-based individual pitch controller and variable torque controller is used as benchmark. Fig. 7.63, Fig. 7.64, Fig. 7.65 and Fig. 7.66 show that the generator power and the rotor speed do not change very much when vertical vane control is used. Fig. 7.67 and Fig. 7.68 show that the vane pitch angle has more activity when vane area is smaller. Fig. 7.69 and Fig. 7.70 show that the side-to-side velocity at the tower top is significantly alleviated when the vertical vane control is used. The bigger vane area is, the more reduction in the side-to-side velocity at the tower top is. Fig. 7.71, Fig. 7.72, Fig. 7.73, Fig. 7.74, Fig. 7.75 and Fig. 7.76 show that the platform sway displacement, the roll displacement and the side-to-side moment are significantly reduced. In summary, the bigger vane area is, the more reduction of displacement or loads in the side-to-side direction is.

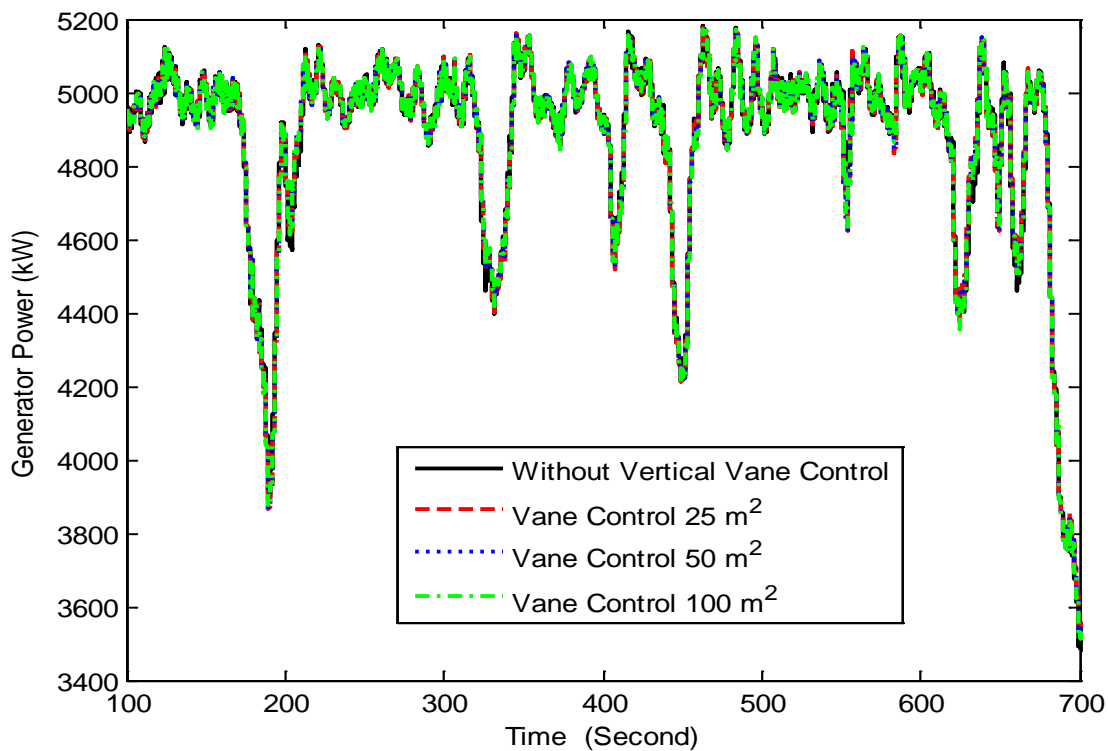


Fig. 7.63 Generator Power (Vertical Vane, Highlift Airfoil, Downwind as Benchmark)

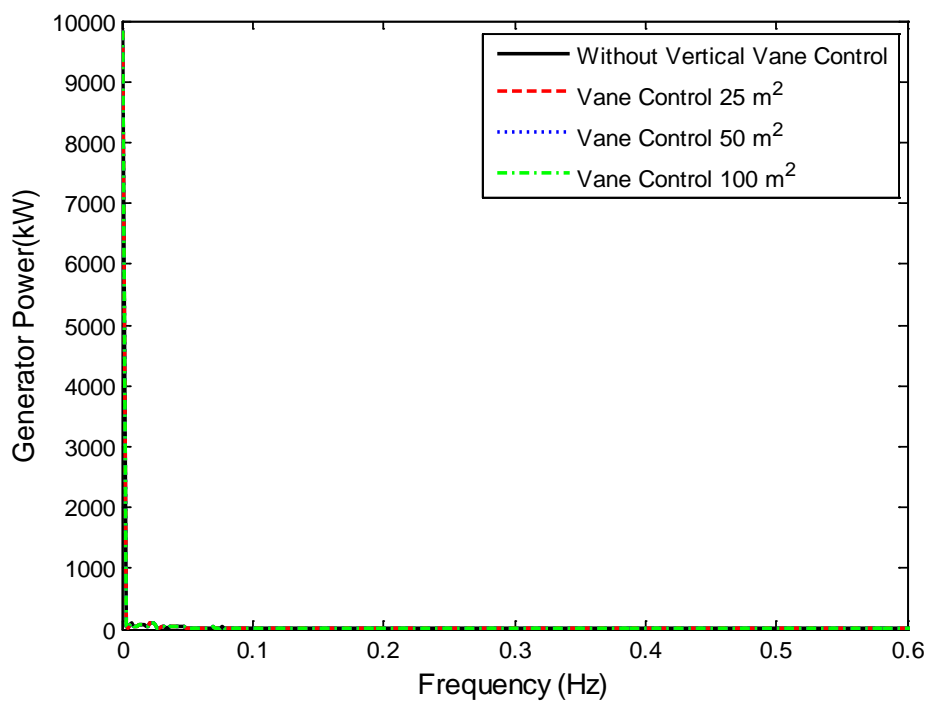


Fig. 7.64 Generator Power Spectra (Vertical Vane, Highlift Airfoil, Downwind as Benchmark)

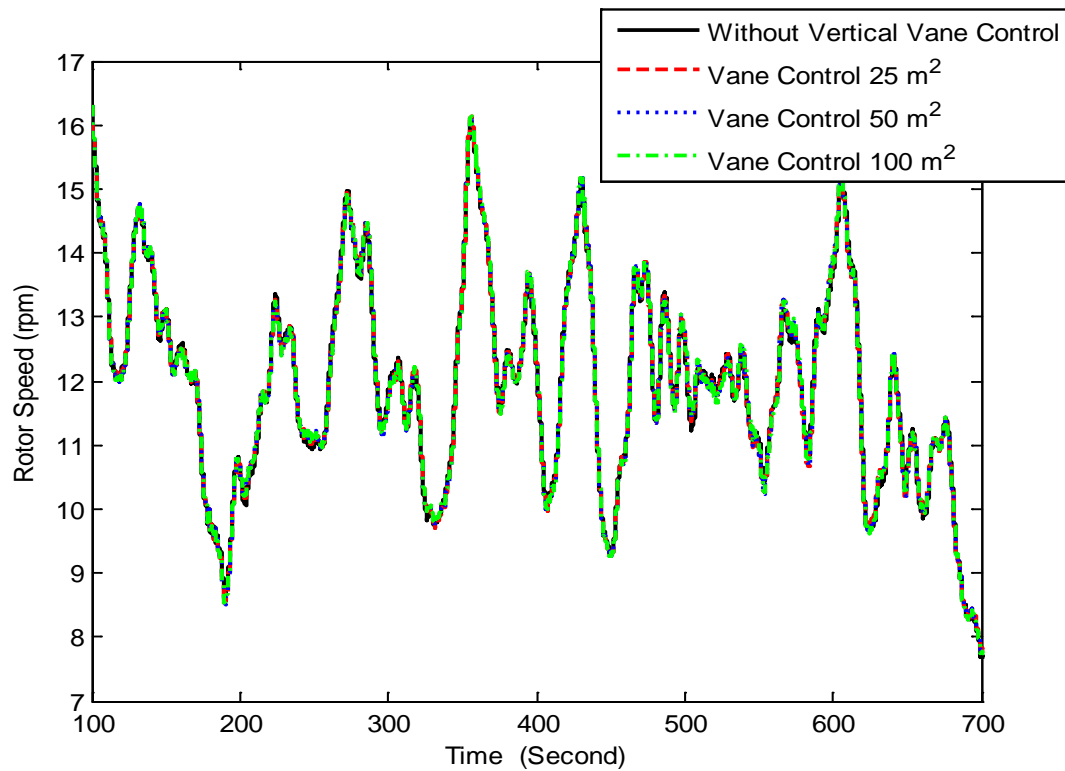


Fig. 7.65 Rotor Speed (Vertical Vane, Highlift Airfoil, Downwind as Benchmark)

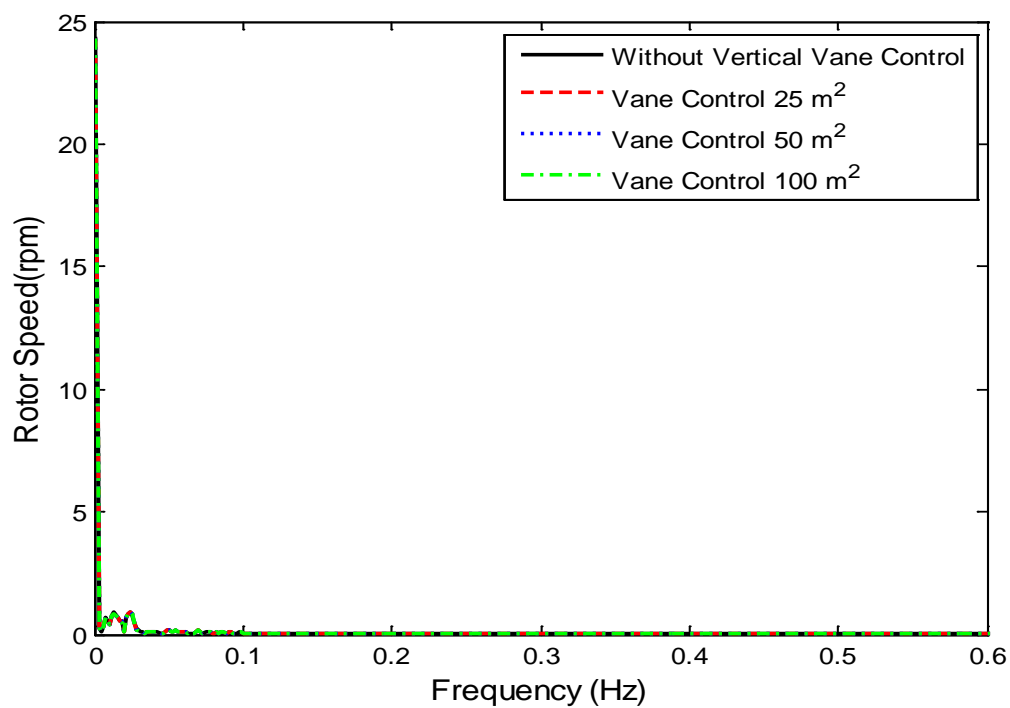


Fig. 7.66 Rotor Speed Spectra (Vertical Vane, Highlift Airfoil, Downwind as Benchmark)

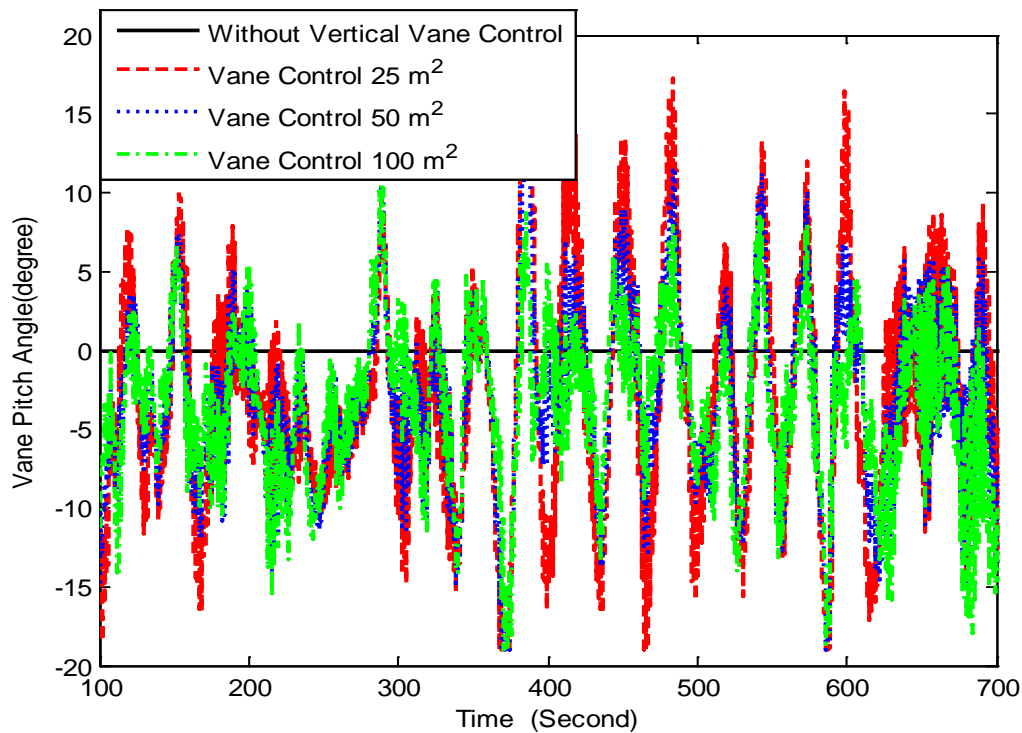


Fig. 7.67 Vane Pitch Angle (Vertical Vane, Highlift Airfoil, Downwind as Benchmark)

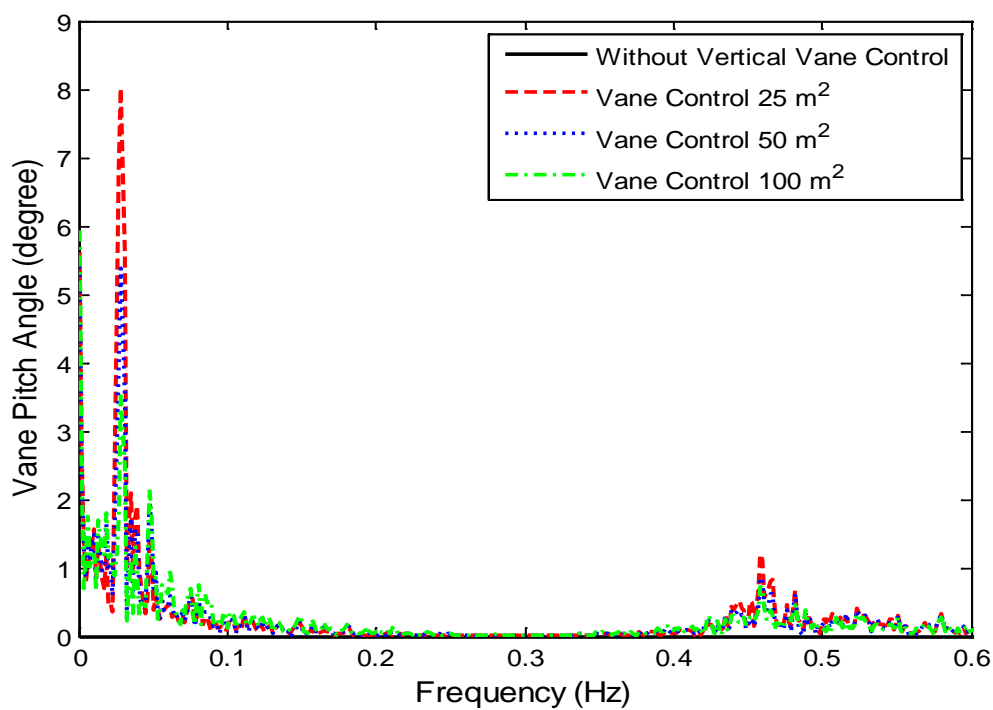


Fig. 7.68 Vane Pitch Angle Spectra (Vertical Vane, Highlift Airfoil, Downwind as Benchmark)

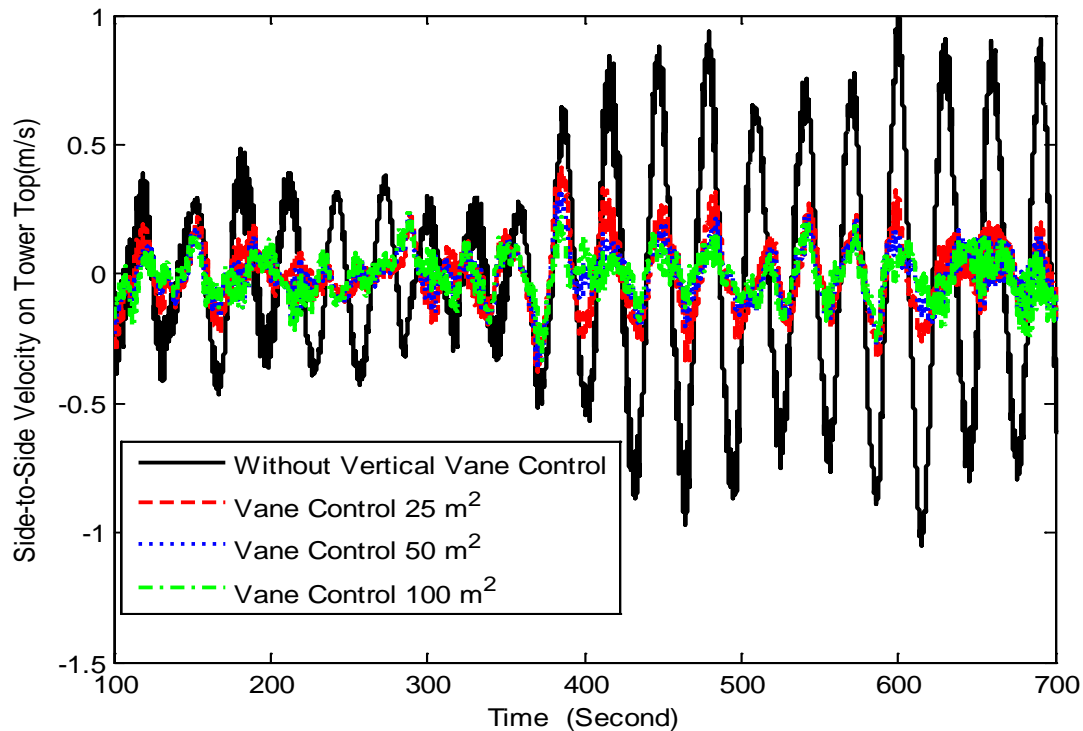


Fig. 7.69 Side-to-Side Velocity (Vertical Vane, Highlift Airfoil, Downwind as Benchmark)

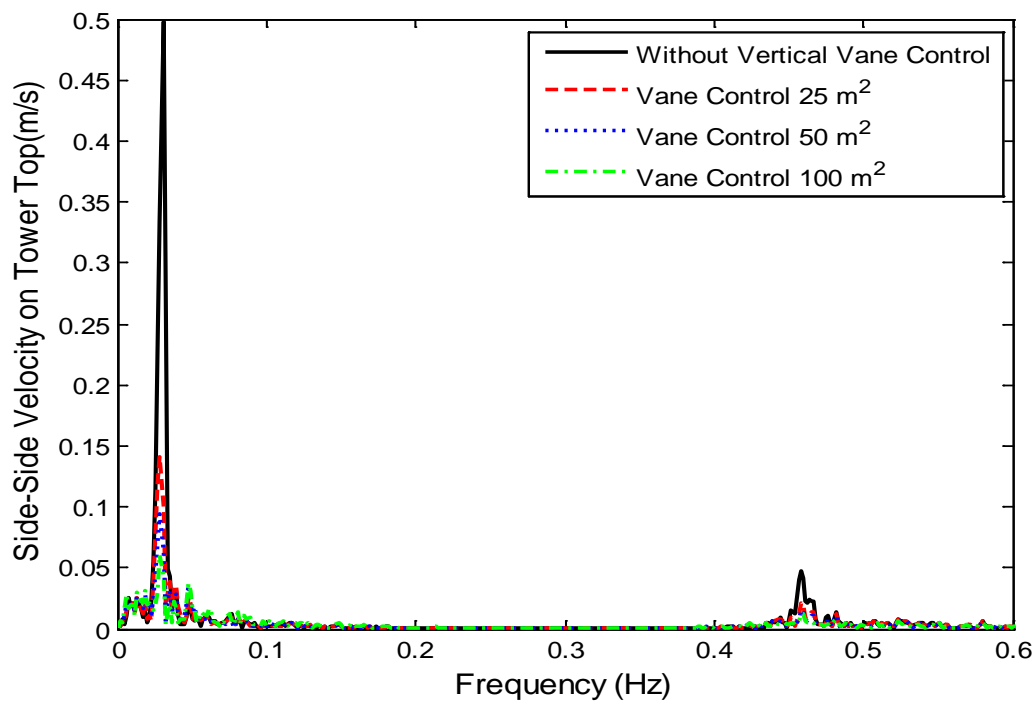


Fig. 7.70 Side-to-Side Velocity Spectra (Vertical Vane, Highlift Airfoil, Downwind as Benchmark)

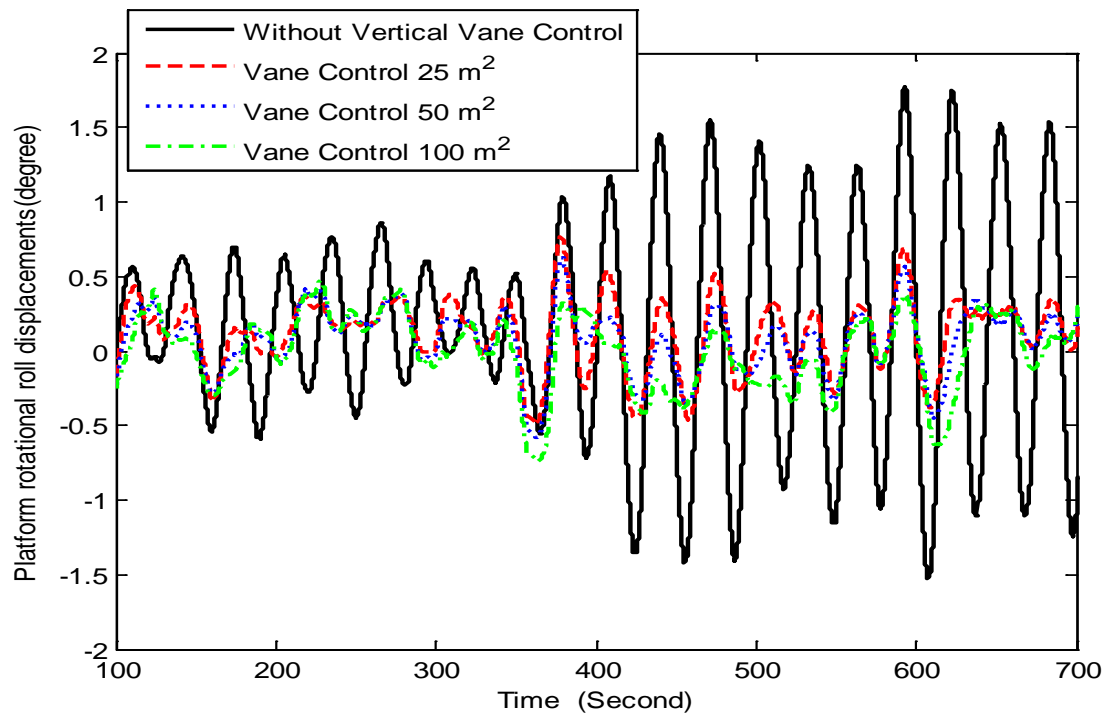


Fig. 7.71 Platform Roll Displacement (Vertical Vane, Highlift Airfoil, Downwind as Benchmark)

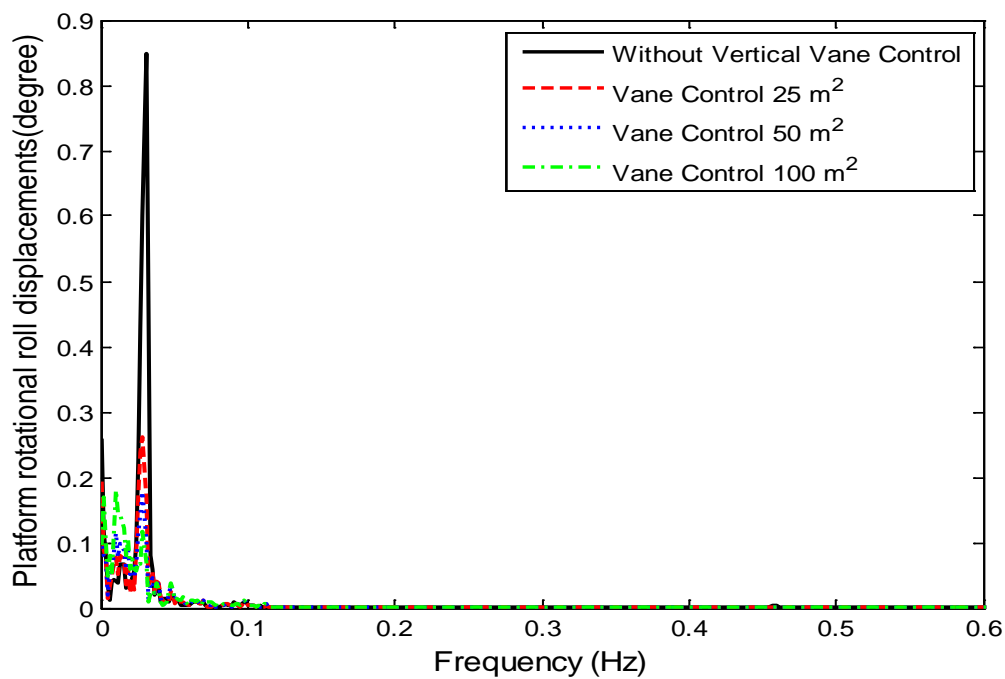


Fig. 7.72 Platform Roll Displacement Spectra (Vertical Vane, Highlift Airfoil, Downwind as Benchmark)

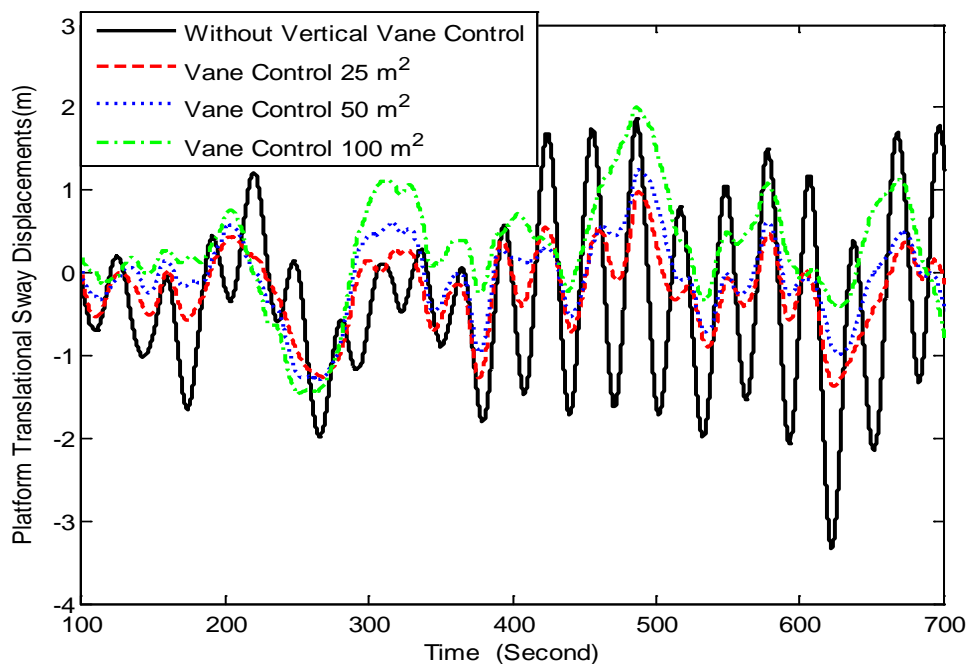


Fig. 7.73 Platform Sway Displacement (Vertical Vane, Highlift Airfoil, Downwind as Benchmark)

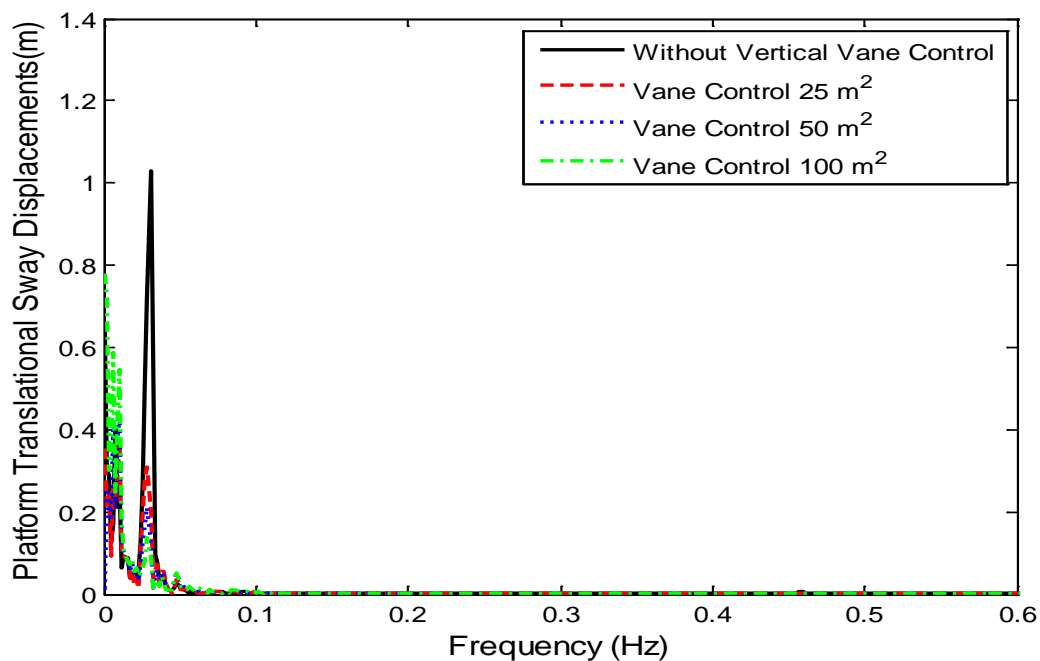


Fig. 7.74 Platform Sway Displacement Spectra (Vertical Vane, Highlift Airfoil, Downwind as Benchmark)

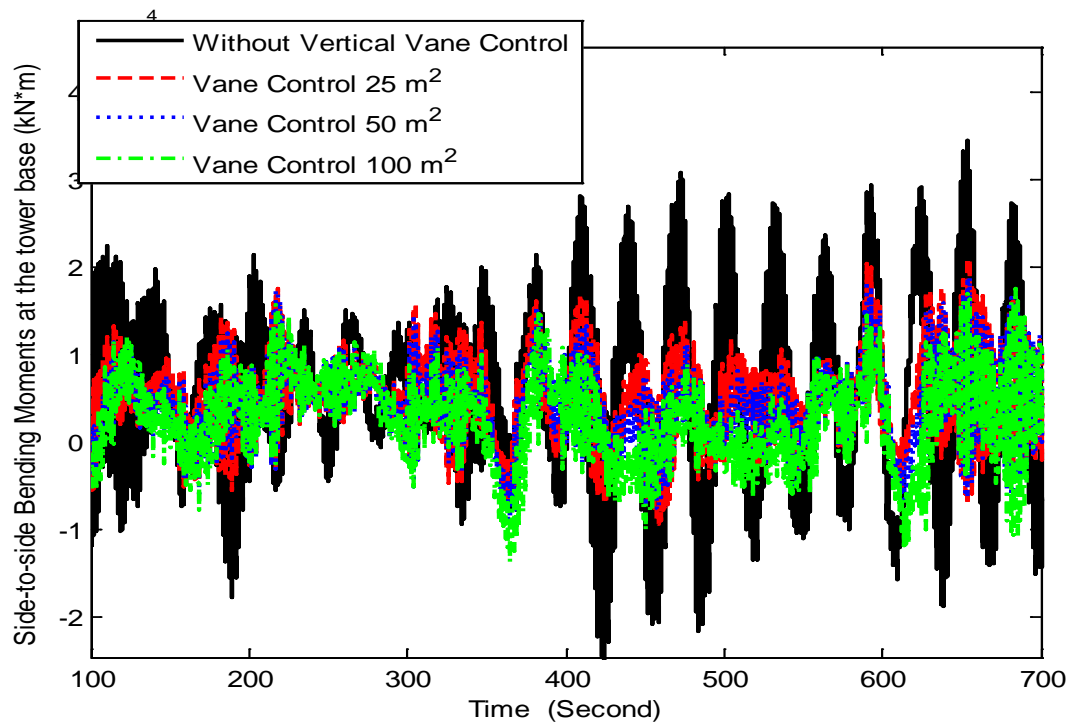


Fig. 7.75 Side-to-Side Bending Moment (Vertical Vane, Highlift Airfoil, Downwind as Benchmark)

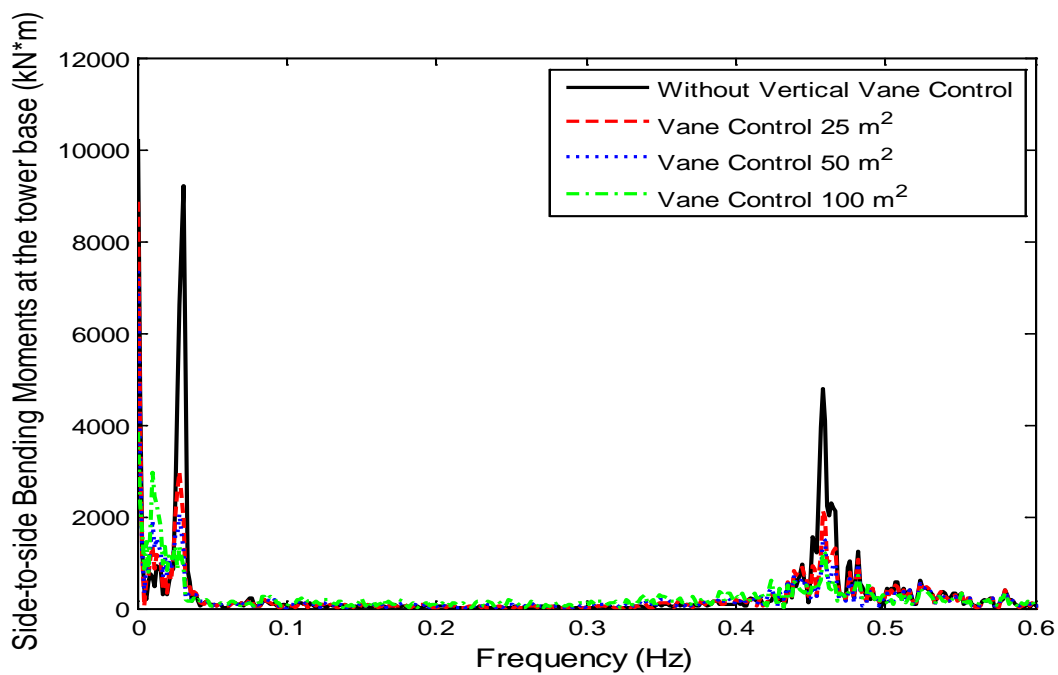


Fig. 7.76 Side-to-Side Bending Moment Spectra (Vertical Vane, Highlift Airfoil, Downwind as Benchmark)

7.3.1.6. Damage Equivalent Loads

When damping in roll direction of floating turbines is increased, loads at tower base in side-to-side direction should be also reduced. In this section, the damage-equivalent loads (DEL) of the moments at tower base in both side-to-side and fore-aft direction are calculated by use of MCrunch [200] and results are listed in Table 7-3.

Table 7-3: Damage Equivalent Loads (DEL) for Vertical Vane

Cases	Airfoil	Vane Area m ²	Feedback Variable	Side-to-Side Moment at Tower Base (kN*m)	Side-to-Side Moment Reduction	Fore-Aft Moment at Tower Base (kN*m)	Fore-Aft Moment Reduction
1 (no vane)	-----	-----	-----	23630.00	0.00%	68200	0.00%
2	NACA0012	25	Velocity	18560	21.46%	67330.00	1.28%
3	NACA0012	50	Velocity	16920	28.40%	67130.00	1.57%
4	NACA0012	100	Velocity	14920	36.86%	67440.00	1.11%
5	NACA0012	100	Acceleration	18730	20.74%	67440.00	1.11%
6	Highlift	25	Velocity	15910	32.67%	67370.00	1.23%
7	Highlift	50	Velocity	14470	38.76%	67540.00	0.97%
8	Highlift	100	Velocity	13410	43.25%	67970.00	0.34%
9	Highlift	100	Acceleration	14900	36.94%	67210.00	1.45%

7.3.1.7. Power Assumption by Vertical Vane Actuator

In this study, it is assumed that vane pitch angle is controlled by electrical motor. Vane dynamics can be used to estimate torque and power which is needed for vane control. Vane dynamics is shown in the below

$$J\ddot{\theta} = T_m - T_{aero} \quad (7.1)$$

where θ is the pitch angle of vertical vane, J is the inertial moment of vertical vane and T_m is electrical torque used for vane pitch control. T_{aero} is the aerodynamic torque of vertical vane according to the pitch axis located at 25% of the chord from the leading edge of the airfoils in the cross-plane. T_{aero} can be calculated by

$$T_{aero} = C_m(\alpha) \cdot \frac{1}{2} \rho v^2 \cdot A \quad (7.2)$$

where C_m is pitching moment coefficients of airfoils, α is angle of attack for vertical vane, A is the vane area, ρ is air density and v is the mean wind speed for vane.

Torque from vane motor can be calculated by use of Eqs. (7.2) and (7.3). Then power is used by vane motor can be estimated by use of the following formula

$$P_m = T_m \cdot \dot{\theta} \quad (7.3)$$

The power assumption of vane actuator and power production of wind turbine for different cases are listed in Table 7-4.

Table 7-4: Power Assumption of Vane Pitch

Cases	Airfoil	Vane Area m ²	Feedback	Wind Turbine Power Production (kWh)	Vane Actuator Power Assumption (kWh)	Percent of Power Assumption
1	Without Vane	-----	-----	1007	0	0.0000%
2	NACA0012	25	Velocity	1007.5	0.0551	0.0055%
3	NACA0012	50	Velocity	1007.3	0.1042	0.0103%
4	NACA0012	100	Velocity	1007	0.1678	0.0167%
5	NACA0012	100	Acceleration	1007.2	39.2684	3.8988%

Table 7-4 shows that:

- a) When side-to-side velocity is used as measurement, the percentage of power assumption ranges from 0.0055% to 0.0167% for vertical vane;
- b) The bigger the vane area is, the higher the power assumption of vertical vane is;
- c) Compared with that with velocity measurement, the power assumption of vertical vane is higher (3.89%) when side-to-side acceleration at tower top is used as measurement.

7.3.2. Simulation Results for Horizontal Vane

In this part, highlift airfoil and fore-aft velocity were proposed for horizontal vane control based on experience of vertical vane control. Conditions of wind speed and wave are the same to that for vertical vane control.

The vane pitch angle and its spectra are shown in Fig. 7.77 and Fig. 7.78. The fore-aft velocity at tower top and its spectra are shown in Fig. 7.79 and Fig. 7.80. The rotational pitch displacement and its spectra are shown in Fig. 7.81 and Fig. 7.82, which shows that the variation of the platform pitch displacement was reduced about 40% near 0.02 Hz. The fore-aft bending moment at the tower base and its spectra are plotted in Fig. 7.83 and Fig. 7.84, which shows that variation of the fore-aft bending moment is reduced by about 50% near 0.02 Hz.

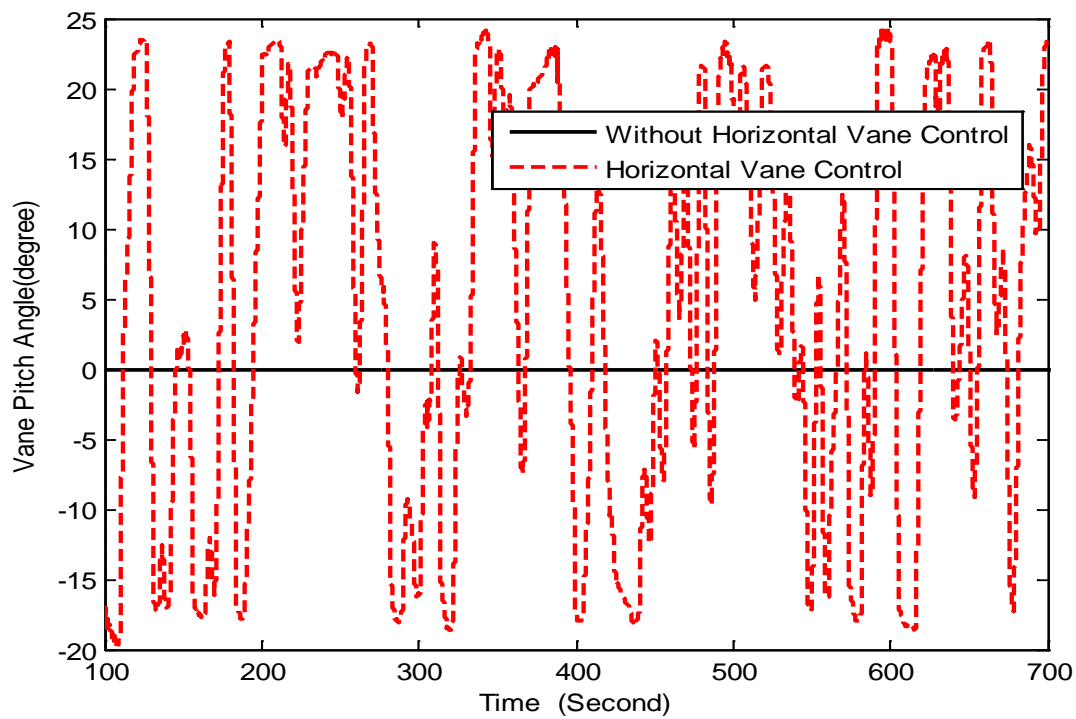


Fig. 7.77 Vane Pitch Angle for Horizontal Vane Control

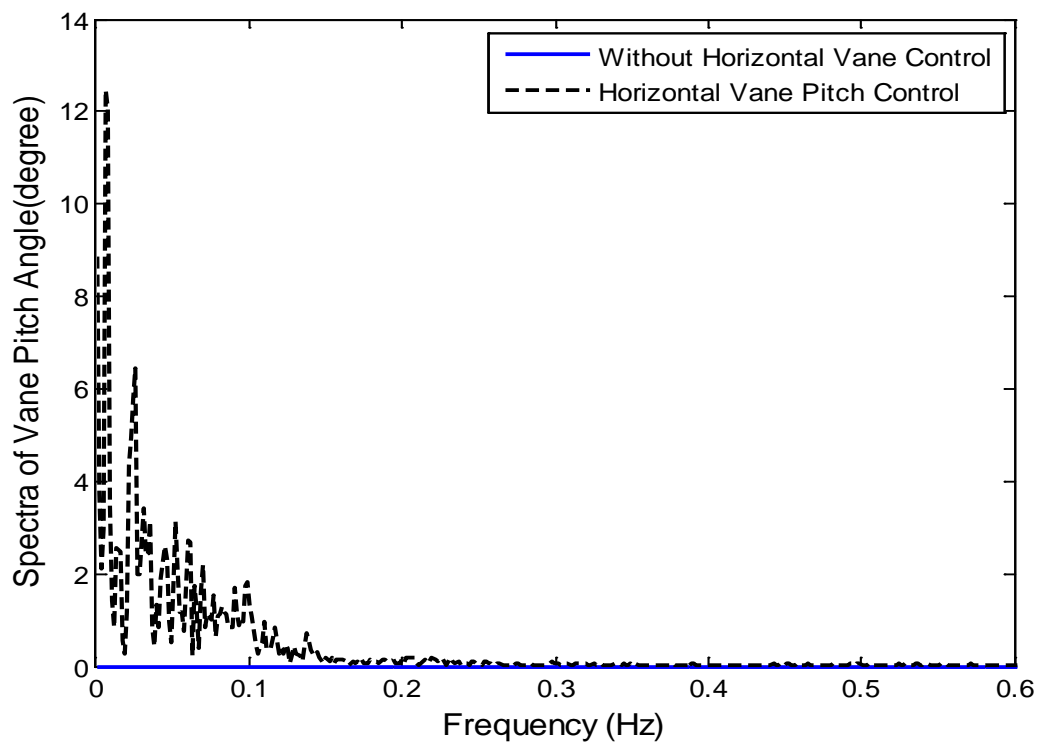


Fig. 7.78 Vane Pitch Angle Spectra for Horizontal Vane Control

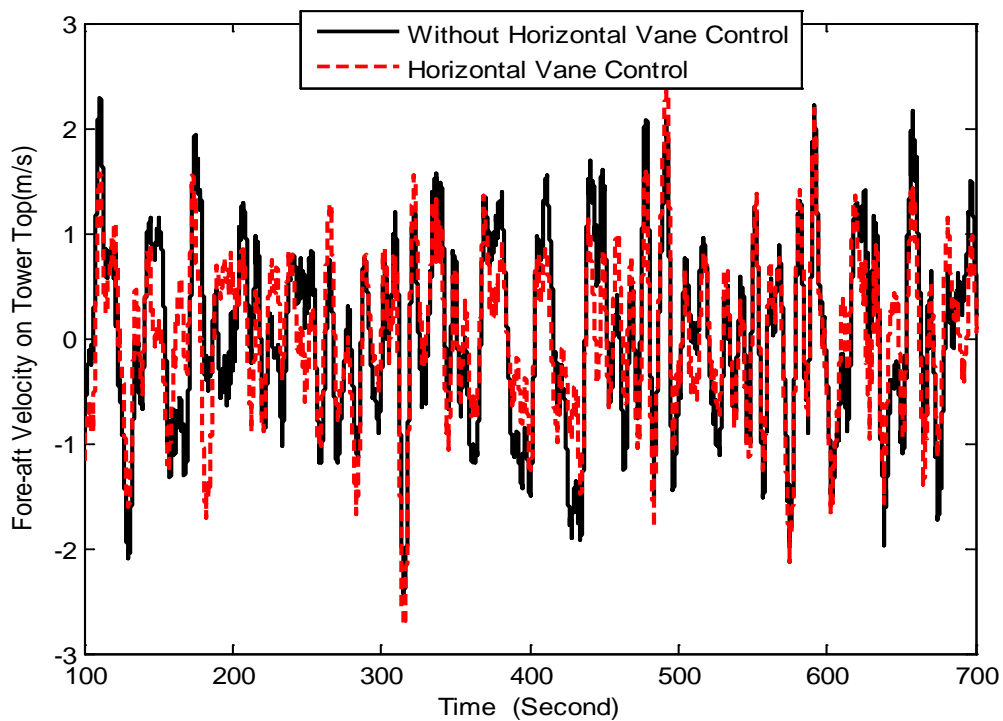


Fig. 7.79 Fore-aft Velocity at Tower Top for Horizontal Vane Control

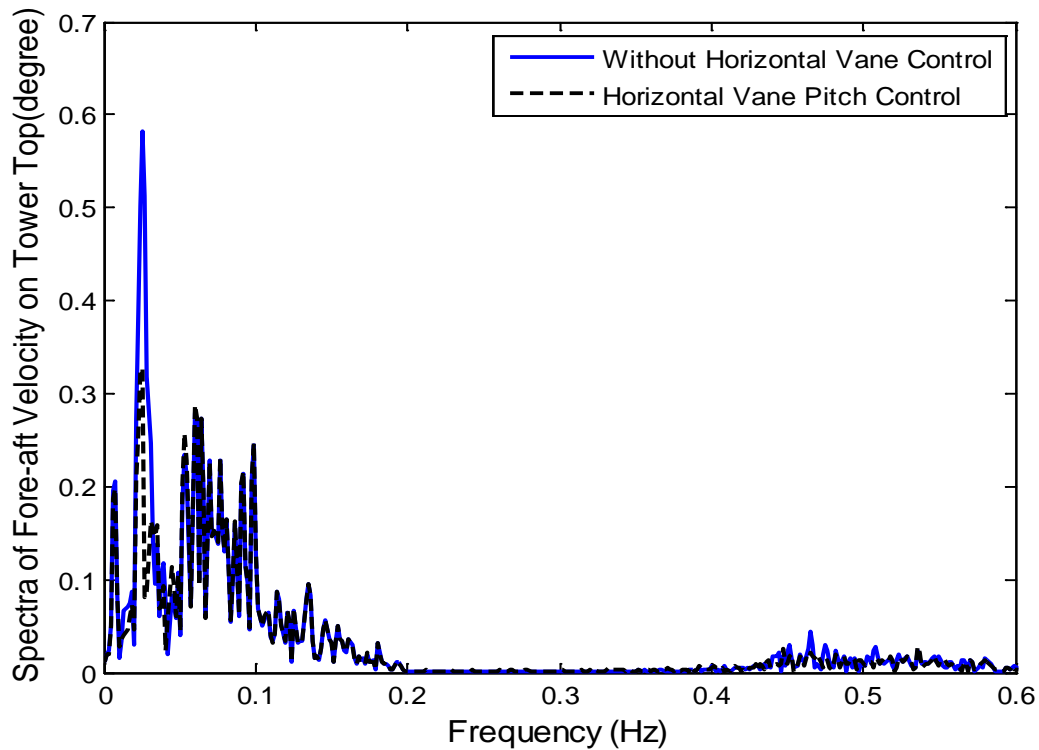


Fig. 7.80. Spectra of Fore-aft Velocity at Tower Top for Horizontal Vane Control

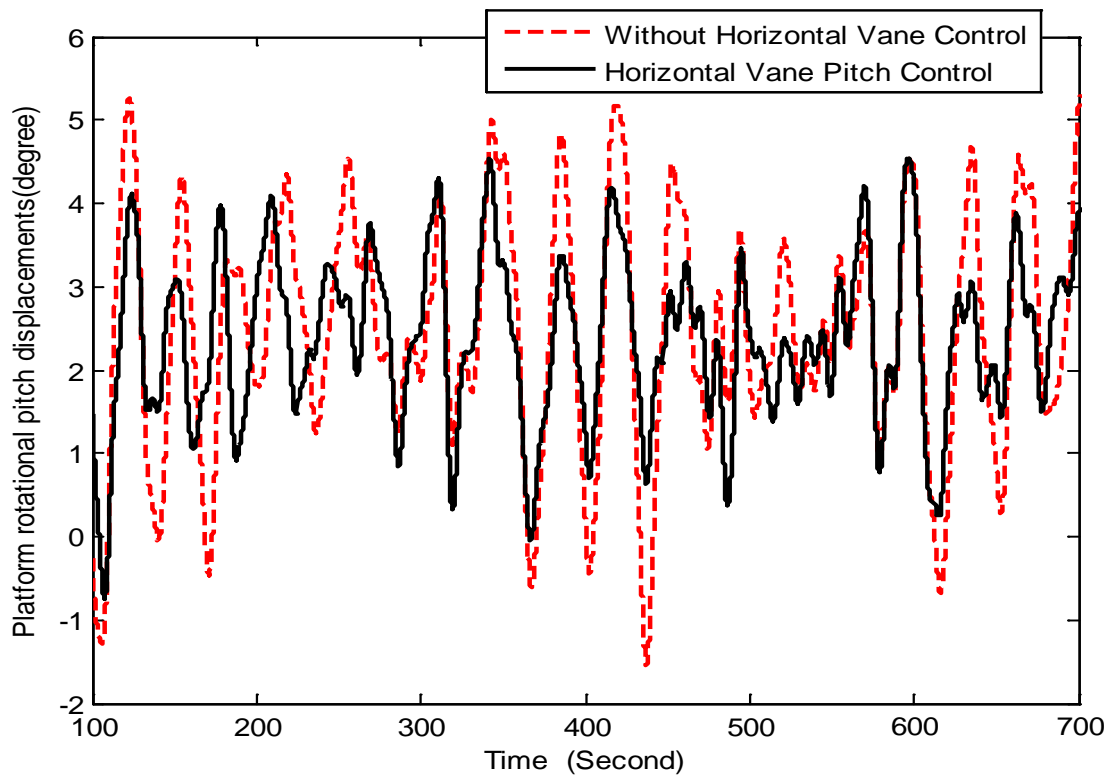


Fig. 7.81. Platform Rotational Pitch Displacement for Horizontal Vane Control

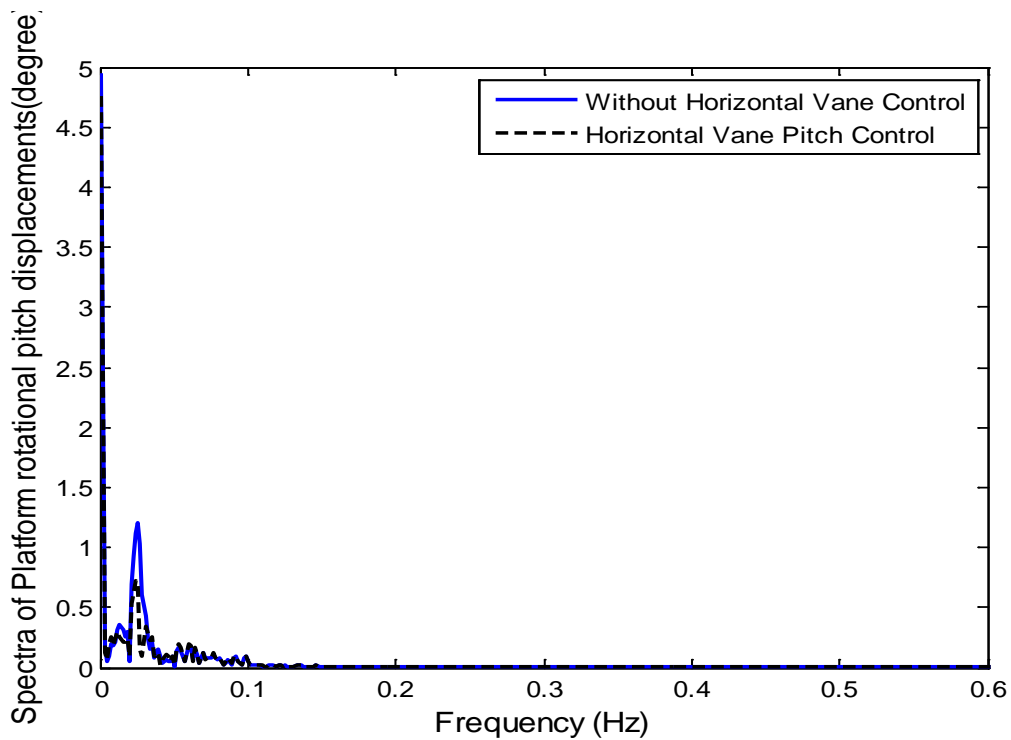


Fig. 7.82. Spectra of Platform Rotational Displacements for Horizontal Vane Control

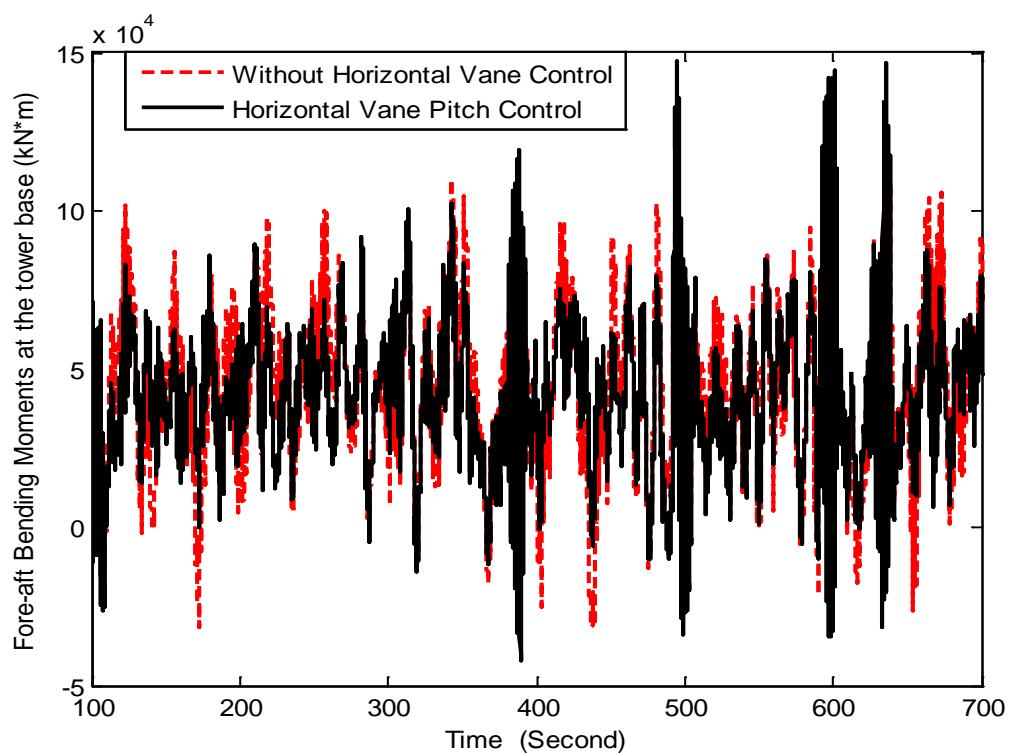


Fig. 7.83. Fore-Aft Bending Moments at Tower Base for Horizontal Vane Control

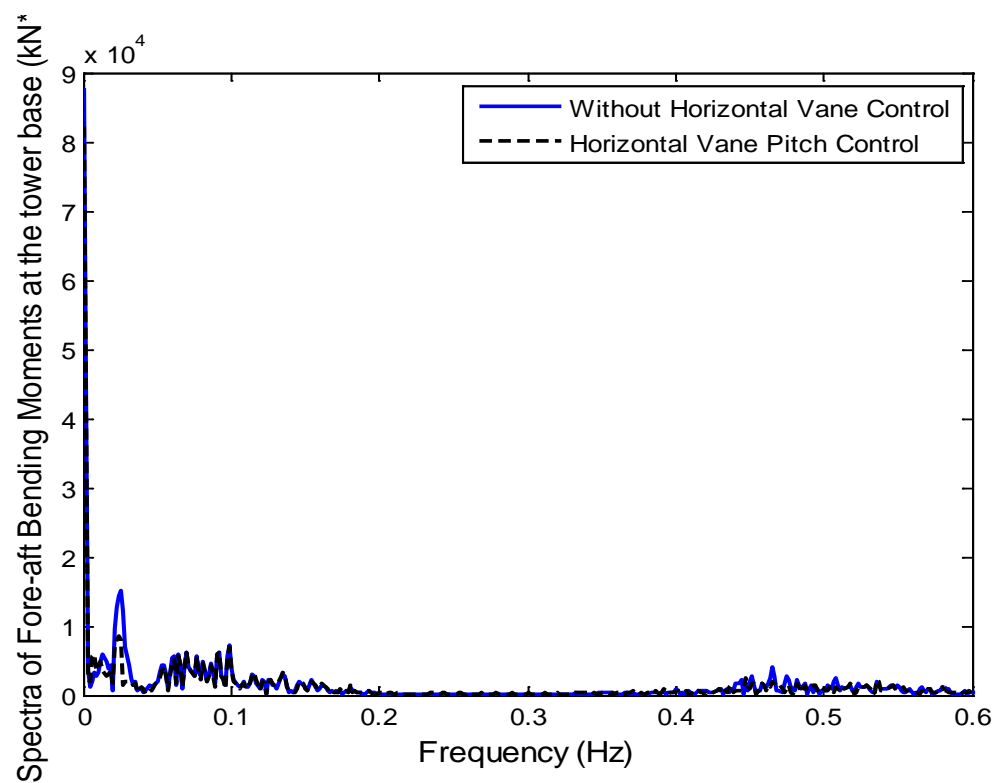


Fig. 7.84. Spectra of Fore-Aft Bending Moments at Tower Base for Horizontal Vane Control

7.4. Summary

In this chapter, a new actuator aerodynamics vane was proposed to increase damping of floating wind turbine in the roll and pitch motion. The basic idea is to move wind turbine back to balance line by use of aerodynamic forces of vertical vane when wind turbines are not located in the balance line along the side-to-side direction. Tail-furling module of FAST software is modified to simulate floating turbine including vanes. The benchmark controller is built by use of PI-based individual pitch controller and variable torque control. The PI-based vertical- and horizontal-vane controllers were designed by use of both velocity and acceleration measurements at tower top. In order to evaluate the capability of vertical vane, both airfoil NACA0012 and a highlift airfoil proposed in [35] are used for vane design. Simulation results show that damping in the roll direction was increased and side-to-side bending moments at tower was reduced from 19% to 42% by use of vertical vane control and the power assumption for vertical vane control is not high. For horizontal vane control, variation of platform pitch displacement was reduced about 40% and variation of fore-aft bending moment reduced about 50% at near 0.02 Hz.

Chapter 8. Contribution and Future Work

This dissertation research addresses several control problems for farm operated and offshore floating turbines, covering both energy capture enhancement and load reduction. As wind farm and offshore operations present the major engineering challenge and opportunity for wind energy, this dissertation research has made more attempts on such regard. This chapter concludes this dissertation by summarizing the major contributions as well as suggesting some aspects of future work.

8.1. Summary of Research Contribution

8.1.1. Individual Pitch Control of Wind Turbine Load Reduction by Including Wake Interaction

The Larsen wake model is chosen to compose the wind profile at the downstream wind turbines under wake interaction, and a switched control strategy is thus developed based on the composite wind profile. The idea of equivalent circular wind profile was proposed to obtain different pitch references along azimuth. When different pitch references along azimuth are used, more accurate state-space models of wind turbine can thus be generated via FAST linearization. Based on such models, the IPC are designed following both the DAC and the periodic control frameworks. Simulation results showed that the tower-base fore-aft bending moment, the tower-base side-to-side bending moment, the rotor speed fluctuation and the blade-tip displacement difference are significantly suppressed.

8.1.2. Model Predictive Control of Wind Turbines including Wake

Meandering

An MMPC based IPC design was presented for load reduction of wind turbine under a wake meandering scenario. The spectral method with a special lateral coherence function is used to generate the initial wind profile at the upstream wind turbine. Then a simplified wake meandering model is used to predict the wake-center position at the downstream wind turbine. Based on the wake center position thus calculated, the wind profile with wake meandering was generated. After obtaining the linearized state-space models via MBC, MMPC are designed in order to ensure smooth controller transition. Simulation results showed that, compared that by use of traditional MPC, the variations in the rotor speed and the blade-root flapwise moment are significantly suppressed by use of MMPC.

8.1.3. Maximizing Wind Farm Energy Capture via Nested-loop

Extremum Seeking Control

A nest-looped ESC controller is evaluated to maximize energy capture in wind farm level. Based on analytical analysis and simulation, it is verified that optimal torque gains exists and do not change with wind speed for maximizing energy capture in wind farm level. For steady wind speed, power summation of all turbines in the wake of a turbine is used as output measurement of this turbine's ESC. For turbulent wind, power coefficients are redefined in wind farm level and they are used for output measurement of ESC. Cross-covariance is used to calculate the delay time of wake transportation. Simulation results show that energy capture can be increased 5% under steady wind and 1.3% under turbulent wind.

8.1.4. Active Vane Control for Stabilization of Floating Offshore Wind Turbine

The active vane concept is evaluated for stabilization of floating wind turbine in both roll and pitch motion. FAST software was modified to simulate floating turbine including vane according to Kane's method. The benchmark controller was built by use of PI-based individual pitch controller and variable torque control. The PI-based vertical and horizontal vane controllers were designed by use of both velocity and acceleration measurements at tower top as feedback. In order to fully test the capability of vertical vane, both airfoil NACA0012 and a highlift airfoil from Stanford were used for vane design. Simulation results showed that side-to-side bending moments at tower was reduced from 19% to 42% by use of the vertical vane control; the power assumption for the vertical vane control is not high; damping of pitch motion for floating turbines was increased by use of horizontal vane control.

8.2. Future Work

For MMPC control of wind turbine including wake meandering, MPC schemes of higher robustness may be combined with MMPC framework in order to enhance stability robustness. If the wake meandering situation can be formulated as a piece-wise affine system, the hybrid MPC scheme can be applied.

The active vane design of higher lift can be investigated and the CFD study can be performed. Coupling of vertical vane and horizontal vane will be a more interesting research topic.

Experimental studies are necessary to further evaluate these above control strategies.

Appendix A. Justification of Nested-loop Optimization for Maximizing Energy Capture of A Cascade of Wind Turbines

In this appendix, the optimal inductor factor relationship from [21, 22] is described and the prove in this section was provided by Prof. Yaoyu Li. All the derivations are based on the 1D Momentum Theory and the Actuator Disc Model of wind turbine. The wind turbine array of interest is the cascaded topology as shown in Fig.A.1, where all the wind turbine disks are lined up against the direction of the prevailing wind. For the ease of the derivation later, the turbines are numbered along the upwind direction, i.e. turbine 1 is at the most the downwind position. For turbine i , U_i indicates its upcoming free-stream wind speed. The row distance of the wind turbine array is designed such that the free-stream average speed of the incoming wind for a downstream turbine can be approximated as the far-wake average speed of an upstream turbine, i.e.

$$U_i = (1 - 2a_{i+1})U_{i+1} \quad (\text{A.1})$$

where a_i is the axial induction factor for the i th wind turbine.

Definition 1: *Array Power Coefficient.* For cascaded wind turbines 1, 2, ..., n , ... (as illustrated in Fig.A.1), the Array Power Coefficient K_n for wind turbine n is defined as

$$K_n = \frac{\sum_{j=1}^n P_j}{(1/2)\rho A U_n^3} \quad (\text{A.2})$$

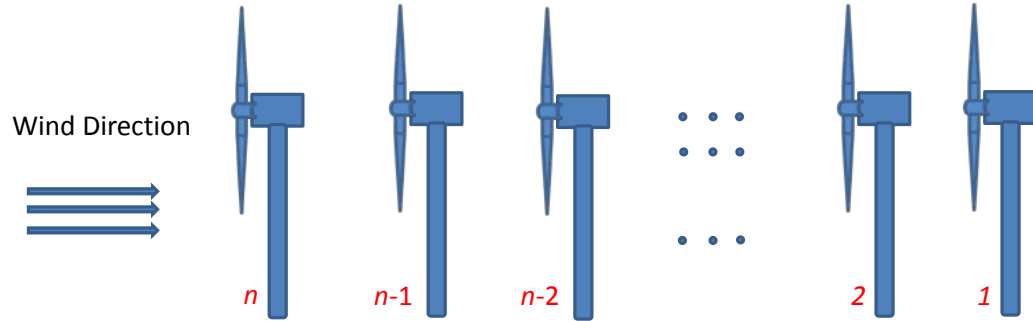


Fig. A.1 A Cascade of Wind Turbines

Lemma 1: For the cascaded wind turbine array as shown in Fig.A.1, when the total power captured by the array is maximized, the optimal values of axial induction factors of adjacent wind turbines, e.g. turbine n and turbine $(n+1)$, are related by

$$a_{n+1}^* = \frac{a_n^*}{2a_n^* + 1} \quad (\text{A.3})$$

where the optimal induction factor of turbine n is

$$a_n^* = \frac{1}{3 + 2(n-1)} \quad (\text{A.4})$$

Also, the array power coefficient of turbine n is

$$K_n^* = \frac{2}{3} (1 - a_n^{*2}) \quad (\text{A.5})$$

Proof: To maximize the total power output of the wind turbine array in Fig.A.1, it is equivalent to maximizing the array power coefficient for an arbitrary sub-array which consists of turbines 1 to n , i.e.

$$K_n = \frac{\sum_{j=1}^n P_j}{(1/2)\rho A U_n^3} = C_{pn} + K_{n-1} \left(\frac{U_{n-1}}{U_n} \right)^3 = C_{pn} + K_{n-1} (1-2a_n)^3 \quad (\text{A.6})$$

where A is the rotor area and ρ is the air density, U_n is the wind speed right in front of the rotor of turbine n , and C_{pn} is the power coefficient of turbine n , i.e.

$$C_{pn} = \frac{P_n}{\frac{1}{2}\rho A U_n^3} = 4a_n (1-a_n)^2 \quad (\text{A.7})$$

Substitute Eq. (A.7) into (A.6) yields

$$K_n = 4a_n (1-a_n)^2 + K_{n-1} (1-2a_n)^3 \quad (\text{A.8})$$

To maximize K_n with respect to a_n , the first-order sufficient condition is

$$\frac{dK_n}{da_n} = 0 \quad (\text{A.9})$$

which leads to

$$K_{n-1} = \frac{2(1-a_n)(1/3-a_n)}{(1-2a_n)^2} \quad (\text{A.10})$$

Substituting Eq. (A.10) into Eq. (A.8) yields

$$K_n^* = \frac{2}{3}(1-a_n^{*2}) \quad (\text{A.11})$$

By extending Eq. (A.11) to K_{n+1} , the effective power efficient is

$$K_{n-1}^* = \frac{2}{3}(1 - a_{n-1}^{*2}) \quad (\text{A.12})$$

Then, substituting Eqs. (A.11) and (A.12) into Eq. (A.8) yields

$$a_n^* = \frac{a_{n-1}^*}{2a_{n-1}^* + 1} \quad (\text{A.13})$$

Based on Eq. (A.10), we can derive

$$a_n^* = \frac{1}{3 + 2(n-1)} \quad (\text{A.14})$$

Proposition 1: For a cascaded wind turbine array in Fig.A.1 , the optimal axial induction factors of turbine $n \geq 2$ follows

$$a_n^* \in \left(0, \frac{1}{3} \right] \quad (\text{A.15})$$

Proof: from Eq. (A.4) in Lemma 1, the optimal axial induction factor for turbines 1, 2, 3, ... , respectively, form a positive and decreasing series $\{1/3, 1/5, 1/7, \dots\}$, which results in Eq. (A.6).

Proposition 2: For a cascaded wind turbine array in Fig.A.1, the optimal array power coefficient of turbine $n \geq 1$ is

$$K_n^* \in \left[\frac{16}{27}, \frac{2}{3} \right) \quad (\text{A.16})$$

Proof: Substituting Eq. (A.6) into Eq. (A.5) yields Eq. (A.16).

Theorem 1: For cascaded wind turbine array as shown in Fig.A.1, the maximum total power of $n+1$ turbines ($n \geq 1$) can be uniquely optimized by optimizing the axial induction factor of the most upwind turbine (i.e. a_{n+1}) and optimizing the array power coefficient of the immediate downwind turbine K_n (i.e. the total power of all downwind turbines).

Proof: For turbine n and $(n+1)$, we have

$$U_n = (1 - 2a_{n+1})U_{n+1}$$

1. The array power coefficient for turbine $(n+1)$ is

$$K_{n+1} = \frac{\sum_{i=1}^{n+1} P_i}{(1/2)\rho A U_{n+1}^3} = \frac{P_{n+1}}{(1/2)\rho A U_{n+1}^3} + \frac{\sum_{i=1}^n P_i}{(1/2)\rho A U_{n+1}^3} = C_{P,n+1} + K_n \left(\frac{U_n}{U_{n+1}} \right)^3$$

Therefore, we have

$$K_{n+1} = 4a_{n+1}(1 - a_{n+1})^2 + K_n(1 - 2a_{n+1})^3 \quad (\text{A.17})$$

Maximizing K_{n+1} relies on both a_{n+1} and K_n . As K_n is function of dimensionless numbers a_1, \dots, a_n , $K_n(a_1, \dots, a_n)$ is invariant with U_{n+1} , and in consequence independent on a_{n+1} . Since $a_{n+1} \in (0, 1/2)$, $4a_{n+1}(1 - a_{n+1})^2 > 0$, and $(1 - 2a_{n+1})^3 > 0$. Also, $K_n > 0$, we have $K_{n+1} > 0$ from Eq. (15). From Eq. (A.16), the limit of K_n is $2/3$, so $K_{n+1}(a_{n+1}, K_n)$ is positive-value function defined on a Cartesian domain $(0, 1/2) \times [16/27, 2/3]$. An important implication for wind turbine array optimization is that, once the operational parameters of a sub-array of wind turbines is optimized (by adjusting the axial induction factors of the involved turbines), adjustment of upwind turbines would not affect such optimality.

2. For any fixed a_{n+1} , attaining the maximum for K_{n+1} (i.e. K_{n+1}^*) will require K_n achieves its maximum, i.e. $K_{n,max}$. An easy proof by contradiction can be set as follows. If the pair (a_{n+1}^*, K_n^*) maximized K_{n+1} , where $K_n^* < K_{n,max}$, we would have

$$4a_{n+1}^*(1-a_{n+1}^*)^2 + K_n^*(1-2a_{n+1}^*)^3 < 4a_{n+1}^*(1-a_{n+1}^*)^2 + K_{n,max}(1-2a_{n+1}^*)^3$$

which results in $K_n^* = K_{n,max}$.

An important implication of this statement is that the optimal choice of K_n regarding to optimizing K_{n+1} is fixed to $K_{n,max}$, which is result of maximizing the total power of all downwind turbines. In other words, it shows a “common-sense” consequence – the total power of $(n+1)$ turbines would be maximized after the total power of the n downwind turbines is optimized.

3. Then the task of maximizing K_{n+1} in Eq. (15) can be simplified as

$$K_{n+1}^* = \arg \max_{a_{n+1}} \left[4a_{n+1}(1-a_{n+1})^2 + K_n(1-2a_{n+1})^3 \right] \quad (\text{A.18})$$

where K_n can be considered as a constant for this optimization problem, which can reach its maximum $K_{n,max}$ by adjusting (a_1, \dots, a_n) in a separate problem. For all the following derivation, the axial inductor factor has permissible range of

$$a_{n+1} \in (0, 1/2)$$

Consider the first-order sufficient condition for optimality,

$$\frac{dK_{n+1}}{da_{n+1}} = 0 \quad (\text{A.19})$$

Since

$$\frac{dK_{n+1}}{da_{n+1}} = (12 - 24K_n)a_{n+1}^2 + (24K_n - 16)a_{n+1} + (4 - 6K_n) \quad (\text{A.20})$$

Eq. (A.19) becomes

$$\begin{aligned} (6 - 12K_n)a_{n+1}^2 + (12K_n - 8)a_{n+1} + (2 - 3K_n) &= 0 \\ \Rightarrow a_{n+1} &= \frac{(8 - 12K_n) \pm \sqrt{16 - 24K_n}}{2(6 - 12K_n)} \end{aligned}$$

This results in

$$a_{n+1} = \frac{(4 - 6K_n) \pm \sqrt{4 - 6K_n}}{(6 - 12K_n)} \quad (\text{A.21})$$

Due to the possible singularity in the denominator in Eq.(A.21) and also different possible solutions, we need to separate three cases:

$$\text{i) } K_n \in \left(\frac{1}{2}, \frac{2}{3}\right): (6 - 12K_n) < 0, \text{ and } (4 - 6K_n) \in (0, 1) \Rightarrow \sqrt{4 - 6K_n} > (4 - 6K_n)$$

$$\Rightarrow a_{n+1} = \frac{(4 - 6K_n) - \sqrt{4 - 6K_n}}{(6 - 12K_n)} \text{ is the only positive solution.}$$

This is the situation when the total power of all the downwind turbines have been optimized, the axial inductor factor of the current turbine can be optimized to a unique solution.

$$\text{ii) For } K_n = 1/2:$$

$$(12 - 24K_n)a_{n+1}^2 + (24K_n - 16)a_{n+1} + (4 - 6K_n) = 0 \Rightarrow a_{n+1} = \frac{1}{4}$$

iii) $K_n \in \left(0, \frac{1}{2}\right)$:

$$(6 - 12K_n) > 0, \text{ and } (4 - 6K_n) \in (1, 4) \Rightarrow \sqrt{4 - 6K_n} < (4 - 6K_n)$$

$$\Rightarrow a_{n+1} = \frac{(4 - 6K_n) \pm \sqrt{4 - 6K_n}}{(6 - 12K_n)} \text{ are two positive real roots.}$$

Now we will test if both roots lie in the permissible range of $(0, \frac{1}{2})$ for axial induction factor.

$$a_{n+1} = \frac{(4 - 6K_n) + \sqrt{4 - 6K_n}}{(6 - 12K_n)} = \frac{1}{6(1 - 2K_n)} + \frac{1}{2} + \frac{\sqrt{4 - 6K_n}}{6(1 - 2K_n)} > \frac{1}{2}$$

This is an impossible solution.

Therefore, only $a_{n+1} = \frac{(4 - 6K_n) - \sqrt{4 - 6K_n}}{(6 - 12K_n)}$ is the possible solution, which is the same as the case i).

4. To show the existence of unique a_{n+1} , we need to verify the following second-order derivative condition to validate an obtained stationary point as maximum:

$$\frac{d^2 K_{n+1}}{da_{n+1}^2} < 0 \tag{A.22}$$

$$\frac{d^2 K_{n+1}}{da_{n+1}^2} = 2(6 - 12K_n)a_{n+1} + (12K_n - 8) \tag{A.23}$$

i) For $K_n=1/2$, $\frac{d^2 K_{n+1}}{da_{n+1}^2} = -2$, i.e. $\frac{d^2 K_{n+1}}{da_{n+1}^2} < 0$ for all a_{n+1} .

ii) Otherwise $K_{n+1} \neq 1/2$, substituting the aforementioned root (for cases i and iii in the part 3) into Eq. (A.23) yields

$$a_{n+1} = \frac{(4-6K_n) - \sqrt{4-6K_n}}{(6-12K_n)}, \quad \frac{d^2 K_{n+1}}{da_{n+1}^2} = -\sqrt{4-6K_n} < 0 \quad \text{and} \quad \frac{d^2 K_{n+1}}{da_{n+1}^2} < 0 \quad \text{since} \quad K_n < 2/3.$$

Combining both case yields that therefore there exist interior point of a_{n+1} that is unique optimal solution.

Appendix B. Specifications of NREL 5MW Turbine Model

In this appendix, main characteristics of NREL 5MW [192] is provided in Table B-1.

Table B-1: Properties of the NREL-5MW Baseline

Rated Power	5 MW
Rotor Orientation	Upwind
Blade number	3 Blades
Rotor, Hub Diameter	126m, 3m
Rotor Mass	110,000 kg
Nacelle Mass	240,000kg
Tower Mass	347,460kg
Rated Tip Speed	80 m/s
Cut-In, Rated Rotor Speed	6.9rpm, 12.1rpm
Cut-In, Rated, Cut-out Wind Speeds	3m/s, 11.4m/s, 25m/s
Gearbox Ratio	97
Generator Efficiency	94.4%

For more detailed description for the characteristics of the NREL 5MW turbine model, the FAST [140] input file is copied as follows:

```

-----
----- FAST INPUT FILE -----
NREL 5.0 MW Baseline Wind Turbine for Use in Offshore Analysis.
Properties from Dutch Offshore Wind Energy Converter (DOWEC) 6MW Pre-Design (10046_009.pdf)
and REpower 5M 5MW (5m_uk.pdf); Compatible with FAST v6.0.
----- SIMULATION CONTROL -----
False   Echo   - Echo input data to "echo.out" (flag)
1       ADAMSPrep - ADAMS preprocessor mode {1: Run FAST, 2: use FAST as a preprocessor to
create an ADAMS model, 3: do both} (switch)

```

1 AnalMode - Analysis mode { 1: Run a time-marching simulation, 2: create a periodic linearized model } (switch)
 3 NumBl - Number of blades (-)
 630.0 TMax - Total run time (s)
 0.0125 DT - Integration time step (s)
 ----- TURBINE CONTROL -----
 0 YCMode - Yaw control mode { 0: none, 1: user-defined from routine UserYawCont, 2: user-defined from Simulink } (switch)
 9999.9 TYCon - Time to enable active yaw control (s) [unused when YCMode=0]
 2 PCMode - Pitch control mode { 0: none, 1: user-defined from routine PitchCntrl, 2: user-defined from Simulink } (switch)
 0.0 TPCOn - Time to enable active pitch control (s) [unused when PCMode=0]
 3 VSContrl - Variable-speed control mode { 0: none, 1: simple VS, 2: user-defined from routine UserVSCont, 3: user-defined from Simulink } (switch)
 1173.7 VS_RtGnSp - Rated generator speed for simple variable-speed generator control (HSS side) (rpm) [used only when VSContrl=1]
 43093.55 VS_RtTq - Rated generator torque/constant generator torque in Region 3 for simple variable-speed generator control (HSS side) (N-m) [used only when VSContrl=1]
 0.0255764 VS_Rgn2K - Generator torque constant in Region 2 for simple variable-speed generator control (HSS side) (N-m/rpm^2) [used only when VSContrl=1]
 10.0 VS_SlPc - Rated generator slip percentage in Region 2 1/2 for simple variable-speed generator control (%) [used only when VSContrl=1]
 1 GenModel - Generator model { 1: simple, 2: Thevenin, 3: user-defined from routine UserGen } (switch) [used only when VSContrl=0]
 True GenTiStr - Method to start the generator { T: timed using TimGenOn, F: generator speed using SpdGenOn } (flag)
 True GenTiStp - Method to stop the generator { T: timed using TimGenOf, F: when generator power = 0 } (flag)
 9999.9 SpdGenOn - Generator speed to turn on the generator for a startup (HSS speed) (rpm) [used only when GenTiStr=False]
 0.0 TimGenOn - Time to turn on the generator for a startup (s) [used only when GenTiStr=True]
 9999.9 TimGenOf - Time to turn off the generator (s) [used only when GenTiStp=True]
 1 HSSBrMode - HSS brake model { 1: simple, 2: user-defined from routine UserHSSBr } (switch)
 9999.9 THSSBrDp - Time to initiate deployment of the HSS brake (s)
 9999.9 TiDynBrk - Time to initiate deployment of the dynamic generator brake [CURRENTLY IGNORED] (s)
 9999.9 TTpBrDp(1) - Time to initiate deployment of tip brake 1 (s)
 9999.9 TTpBrDp(2) - Time to initiate deployment of tip brake 2 (s)
 9999.9 TTpBrDp(3) - Time to initiate deployment of tip brake 3 (s) [unused for 2 blades]
 9999.9 TBDepISp(1) - Deployment-initiation speed for the tip brake on blade 1 (rpm)
 9999.9 TBDepISp(2) - Deployment-initiation speed for the tip brake on blade 2 (rpm)
 9999.9 TBDepISp(3) - Deployment-initiation speed for the tip brake on blade 3 (rpm) [unused for 2 blades]
 9999.9 TYawManS - Time to start override yaw maneuver and end standard yaw control (s)
 9999.9 TYawManE - Time at which override yaw maneuver reaches final yaw angle (s)
 0.0 NacYawF - Final yaw angle for yaw maneuvers (degrees)
 9999.9 TPitManS(1) - Time to start override pitch maneuver for blade 1 and end standard pitch control (s)
 9999.9 TPitManS(2) - Time to start override pitch maneuver for blade 2 and end standard pitch control (s)
 9999.9 TPitManS(3) - Time to start override pitch maneuver for blade 3 and end standard pitch control (s) [unused for 2 blades]
 9999.9 TPitManE(1) - Time at which override pitch maneuver for blade 1 reaches final pitch (s)
 9999.9 TPitManE(2) - Time at which override pitch maneuver for blade 2 reaches final pitch (s)
 9999.9 TPitManE(3) - Time at which override pitch maneuver for blade 3 reaches final pitch (s) [unused for 2 blades]

14.749 BIPitch(1) - Blade 1 initial pitch (degrees)
 14.749 BIPitch(2) - Blade 2 initial pitch (degrees)
 14.749 BIPitch(3) - Blade 3 initial pitch (degrees) [unused for 2 blades]
 0.0 B1PitchF(1) - Blade 1 final pitch for pitch maneuvers (degrees)
 0.0 B1PitchF(2) - Blade 2 final pitch for pitch maneuvers (degrees)
 0.0 B1PitchF(3) - Blade 3 final pitch for pitch maneuvers (degrees) [unused for 2 blades]

----- ENVIRONMENTAL CONDITIONS -----

9.80665 Gravity - Gravitational acceleration (m/s^2)

----- FEATURE FLAGS -----

True FlapDOF1 - First flapwise blade mode DOF (flag)
 False FlapDOF2 - Second flapwise blade mode DOF (flag)
 False EdgeDOF - First edgewise blade mode DOF (flag)
 False TeetDOF - Rotor-teeter DOF (flag) [unused for 3 blades]
 True DrTrDOF - Drivetrain rotational-flexibility DOF (flag)
 True GenDOF - Generator DOF (flag)
 False YawDOF - Yaw DOF (flag)
 True TwFADOF1 - First fore-aft tower bending-mode DOF (flag)
 False TwFADOF2 - Second fore-aft tower bending-mode DOF (flag)
 True TwSSDOF1 - First side-to-side tower bending-mode DOF (flag)
 False TwSSDOF2 - Second side-to-side tower bending-mode DOF (flag)
 True CompAero - Compute aerodynamic forces (flag)
 False CompNoise - Compute aerodynamic noise (flag)

----- INITIAL CONDITIONS -----

0.0 OopDefl - Initial out-of-plane blade-tip displacement (meters)
 0.0 IPDefl - Initial in-plane blade-tip deflection (meters)
 0.0 TeetDefl - Initial or fixed teeter angle (degrees) [unused for 3 blades]
 0.0 Azimuth - Initial azimuth angle for blade 1 (degrees)
 12.1 RotSpeed - Initial or fixed rotor speed (rpm)
 0.0 NacYaw - Initial or fixed nacelle-yaw angle (degrees)
 0.0 TTDspFA - Initial fore-aft tower-top displacement (meters)
 0.0 TTDspSS - Initial side-to-side tower-top displacement (meters)

----- TURBINE CONFIGURATION -----

63.0 TipRad - The distance from the rotor apex to the blade tip (meters)
 1.5 HubRad - The distance from the rotor apex to the blade root (meters)
 1 PSpnEIN - Number of the innermost blade element which is still part of the pitchable portion of the blade for partial-span pitch control [1 to BldNodes] [CURRENTLY IGNORED] (-)
 0.0 UndSling - Undersling length [distance from teeter pin to the rotor apex] (meters) [unused for 3 blades]
 0.0 HubCM - Distance from rotor apex to hub mass [positive downwind] (meters)
 -5.01910 OverHang - Distance from yaw axis to rotor apex [3 blades] or teeter pin [2 blades] (meters)
 1.9 NacCMxn - Downwind distance from the tower-top to the nacelle CM (meters)
 0.0 NacCMyn - Lateral distance from the tower-top to the nacelle CM (meters)
 1.75 NacCMzn - Vertical distance from the tower-top to the nacelle CM (meters)
 87.6 TowerHt - Height of tower above ground level [onshore] or MSL [offshore] (meters)
 1.96256 Twr2Shft - Vertical distance from the tower-top to the rotor shaft (meters)
 0.0 TwrRBHt - Tower rigid base height (meters)
 -5.0 ShftTilt - Rotor shaft tilt angle (degrees)
 0.0 Delta3 - Delta-3 angle for teetering rotors (degrees) [unused for 3 blades]
 -2.5 PreCone(1) - Blade 1 cone angle (degrees)
 -2.5 PreCone(2) - Blade 2 cone angle (degrees)
 -2.5 PreCone(3) - Blade 3 cone angle (degrees) [unused for 2 blades]
 0.0 AzimB1Up - Azimuth value to use for I/O when blade 1 points up (degrees)

----- MASS AND INERTIA -----

0.0 YawBrMass - Yaw bearing mass (kg)
 240.00E3 NacMass - Nacelle mass (kg)
 56.78E3 HubMass - Hub mass (kg)

0.0 TipMass(1) - Tip-brake mass, blade 1 (kg)
 0.0 TipMass(2) - Tip-brake mass, blade 2 (kg)
 0.0 TipMass(3) - Tip-brake mass, blade 3 (kg) [unused for 2 blades]
 2607.89E3 NacYIner - Nacelle inertia about yaw axis (kg m²)
 534.116 GenIner - Generator inertia about HSS (kg m²)
 115.926E3 HubIner - Hub inertia about rotor axis [3 blades] or teeter axis [2 blades] (kg m²)
 ----- DRIVETRAIN -----
 100.0 GBoxEff - Gearbox efficiency (%)
 94.4 GenEff - Generator efficiency [ignored by the Thevenin and user-defined generator models]
 (%)
 97.0 GBRatio - Gearbox ratio (-)
 False GBRevers - Gearbox reversal {T: if rotor and generator rotate in opposite directions} (flag)
 28.1162E3 HSSBrTqF - Fully deployed HSS-brake torque (N-m)
 0.6 HSSBrDT - Time for HSS-brake to reach full deployment once initiated (sec) [used only when
 HSSBrMode=1]
 DynBrkFi - File containing a mech-gen-torque vs HSS-speed curve for a dynamic brake
 [CURRENTLY IGNORED] (quoted string)
 867.637E6 DTTorSpr - Drivetrain torsional spring (N-m/rad)
 6.215E6 DTTorDmp - Drivetrain torsional damper (N-m/(rad/s))
 ----- SIMPLE INDUCTION GENERATOR -----
 9999.9 SIG_SIPc - Rated generator slip percentage (%) [used only when VSContrl=0 and
 GenModel=1]
 9999.9 SIG_SySp - Synchronous (zero-torque) generator speed (rpm) [used only when VSContrl=0
 and GenModel=1]
 9999.9 SIG_RtTq - Rated torque (N-m) [used only when VSContrl=0 and GenModel=1]
 9999.9 SIG_PORT - Pull-out ratio (Tpullout/Trated) (-) [used only when VSContrl=0 and
 GenModel=1]
 ----- THEVENIN-EQUIVALENT INDUCTION GENERATOR -----
 9999.9 TEC_Freq - Line frequency [50 or 60] (Hz) [used only when VSContrl=0 and GenModel=2]
 9998 TEC_NPol - Number of poles [even integer > 0] (-) [used only when VSContrl=0 and
 GenModel=2]
 9999.9 TEC_SRes - Stator resistance (ohms) [used only when VSContrl=0 and GenModel=2]
 9999.9 TEC_RRes - Rotor resistance (ohms) [used only when VSContrl=0 and GenModel=2]
 9999.9 TEC_VLL - Line-to-line RMS voltage (volts) [used only when VSContrl=0 and GenModel=2]
 9999.9 TEC_SLR - Stator leakage reactance (ohms) [used only when VSContrl=0 and GenModel=2]
 9999.9 TEC_RLR - Rotor leakage reactance (ohms) [used only when VSContrl=0 and GenModel=2]
 9999.9 TEC_MR - Magnetizing reactance (ohms) [used only when VSContrl=0 and GenModel=2]
 ----- PLATFORM -----
 0 PtfmModel - Platform model {0: none, 1: onshore, 2: fixed bottom offshore, 3: floating offshore}
 (switch)
 PtfmFile - Name of file containing platform properties (quoted string) [unused when
 PtfmModel=0]
 ----- TOWER -----
 20 TwrNodes - Number of tower nodes used for analysis (-)
 "NRELOffshrBslne5MW_Tower_Onshore.dat" TwrFile - Name of file containing tower
 properties (quoted string)
 ----- NACELLE-YAW -----
 9028.32E6 YawSpr - Nacelle-yaw spring constant (N-m/rad)
 19.16E6 YawDamp - Nacelle-yaw damping constant (N-m/(rad/s))
 0.0 YawNeut - Neutral yaw position--yaw spring force is zero at this yaw (degrees)
 ----- FURLING -----
 False Furling - Read in additional model properties for furling turbine (flag)
 FurlFile - Name of file containing furling properties (quoted string) [unused when Furling=False]
 ----- ROTOR-TEETER -----
 0 TeetMod - Rotor-teeter spring/damper model {0: none, 1: standard, 2: user-defined from routine
 UserTeet} (switch) [unused for 3 blades]

0.0 TeetDmpP - Rotor-teeter damper position (degrees) [used only for 2 blades and when TeetMod=1]
0.0 TeetDmp - Rotor-teeter damping constant (N-m/(rad/s)) [used only for 2 blades and when TeetMod=1]
0.0 TeetCDmp - Rotor-teeter rate-independent Coulomb-damping moment (N-m) [used only for 2 blades and when TeetMod=1]
0.0 TeetSSStP - Rotor-teeter soft-stop position (degrees) [used only for 2 blades and when TeetMod=1]
0.0 TeetHSStP - Rotor-teeter hard-stop position (degrees) [used only for 2 blades and when TeetMod=1]
0.0 TeetSSSp - Rotor-teeter soft-stop linear-spring constant (N-m/rad) [used only for 2 blades and when TeetMod=1]
0.0 TeetHSSp - Rotor-teeter hard-stop linear-spring constant (N-m/rad) [used only for 2 blades and when TeetMod=1]

----- TIP-BRAKE -----
0.0 TBDrConN - Tip-brake drag constant during normal operation, Cd*Area (m^2)
0.0 TBDrConD - Tip-brake drag constant during fully-deployed operation, Cd*Area (m^2)
0.0 TpBrDT - Time for tip-brake to reach full deployment once released (sec)

----- BLADE -----
"NRELOffshrBslne5MW_Blade.dat" BldFile(1) - Name of file containing properties for blade 1 (quoted string)
"NRELOffshrBslne5MW_Blade.dat" BldFile(2) - Name of file containing properties for blade 2 (quoted string)
"NRELOffshrBslne5MW_Blade.dat" BldFile(3) - Name of file containing properties for blade 3 (quoted string) [unused for 2 blades]

----- AERODYN -----
"NRELOffshrBslne5MW_AeroDyn_WM.ipt" ADFile - Name of file containing AeroDyn input parameters (quoted string)

----- NOISE -----
NoiseFile - Name of file containing aerodynamic noise input parameters (quoted string) [used only when CompNoise=True]

----- ADAMS -----
"NRELOffshrBslne5MW_ADAMSSpecific.dat" ADAMSFile - Name of file containing ADAMS-specific input parameters (quoted string) [unused when ADAMSPrep=1]

----- LINEARIZATION CONTROL -----
"NRELOffshrBslne5MW_Linear.dat" LinFile - Name of file containing FAST linearization parameters (quoted string) [unused when AnalMode=1]

----- OUTPUT -----
True SumPrint - Print summary data to "<RootName>.fsm" (flag)
True TabDelim - Generate a tab-delimited tabular output file. (flag)
"ES10.3E2" OutFmt - Format used for tabular output except time. Resulting field should be 10 characters. (quoted string) [not checked for validity!]
0.0 TStart - Time to begin tabular output (s)
1 DecFact - Decimation factor for tabular output {1: output every time step} (-)
1.0 SttsTime - Amount of time between screen status messages (sec)
-3.09528 NcIMUxn - Downwind distance from the tower-top to the nacelle IMU (meters)
0.0 NcIMUyn - Lateral distance from the tower-top to the nacelle IMU (meters)
2.23336 NcIMUzn - Vertical distance from the tower-top to the nacelle IMU (meters)
1.912 ShftGagL - Distance from rotor apex [3 blades] or teeter pin [2 blades] to shaft strain gages [positive for upwind rotors] (meters)
0 NTwGages - Number of tower nodes that have strain gages for output [0 to 9] (-)
TwrGagNd - List of tower nodes that have strain gages [1 to TwrNodes] (-) [unused if NTwGages=0]
3 NBlGages - Number of blade nodes that have strain gages for output [0 to 9] (-)
5,9,13 BldGagNd - List of blade nodes that have strain gages [1 to BldNodes] (-) [unused if NBlGages=0]

OutList - The next line(s) contains a list of output parameters. See OutList.txt for a listing of available output channels, (-)

"WindVxi , WindVyi , WindVzi"	- Longitudinal, lateral, and vertical wind speeds
"GenPwr , GenTq"	- Electrical generator power and torque
"OoPDefl1 , IPDefl1 , TwstDefl1"	- Blade 1 out-of-plane and in-plane deflections and tip twist
"BldPitch1"	- Blade 1 pitch angle
"BldPitch2"	- Blade 2 pitch angle
"BldPitch3"	- Blade 3 pitch angle
"Azimuth"	- Blade 1 azimuth angle
"RotSpeed , GenSpeed"	- Low-speed shaft and high-speed shaft speeds
"TTDspFA , TTDspSS , TTDspTwst"	- Tower fore-aft and side-to-side displacements and top twist
"Spn2MLxb1 , Spn2MLyb1"	- Blade 1 local edgewise and flapwise bending moments at span station 2 (approx. 50% span)
"RootFxc1 , RootFyc1 , RootFzc1"	- Out-of-plane shear, in-plane shear, and axial forces at the root of blade 1
"RootMxc1 , RootMyc1 , RootMzc1"	- In-plane bending, out-of-plane bending, and pitching moments at the root of blade 1
"RootMxc2 , RootMyc2 , RootMzc2"	
"RootMxc3 , RootMyc3 , RootMzc3"	
"RootMyb1"	- flapwise moment at the root of blade 1
"RootMyb2"	- flapwise moment at the root of blade 2
"RootMyb3"	- flapwise moment at the root of blade 3
"RotTorq , LSSGagMya , LSSGagMza"	- Rotor torque and low-speed shaft 0- and 90-degree bending moments at the main bearing
"YawBrFxp , YawBrFyp , YawBrFzp"	- Fore-aft shear, side-to-side shear, and vertical forces at the top of the tower (not rotating with nacelle yaw)
"YawBrMxp , YawBrMyp , YawBrMzp"	- Side-to-side bending, fore-aft bending, and yaw moments at the top of the tower (not rotating with nacelle yaw)
"TwrBsFxt , TwrBsFyt , TwrBsFzt"	- Fore-aft shear, side-to-side shear, and vertical forces at the base of the tower (mudline)
"TwrBsMxt , TwrBsMyt , TwrBsMzt"	- Side-to-side bending, fore-aft bending, and yaw moments at the base of the tower (mudline)
"rotcq"	
"rotpwr"	
"YawBrTDxt"	- Tower-top/yaw bearing fore-aft (translational) deflection
"YawBrTDyt"	- Tower-top/yaw bearing fore-aft (translational) deflection
"TipDxc1 , TipDxc2 , TipDxc3"	- Blade 1, 2, 3 out-of-plane tip deflection (relative to the pitch axis)

END of FAST input file (the word "END" must appear in the first 3 columns of this last line).

Appendix C. Codes of MMPC and dual-mode MPC

C.1 Multiple Model Predictive Control

C.1.1 Source Codes

```
function
[c1,c2,c3]=mmmpc(Weighting,SwS,Est11,Est12,Est13,Est14,Est15,Est16,Est17,Est21,Est22,Est23,Est24,Est25,Est26,Est27,phi,omega,Wy,Wu,A,B,C,PitchRef,pinvM)
%#eml

eml.extrinsic('qpOASES');
% eml.extrinsic('pinv');
Ts=0.1;

% Decide model number
    if SwS-round(SwS)>=0.0
        k=round(SwS)+1;
    else
        k=round(SwS)+1-1;
    end

% Calculate pitch reference

    if k>=11
        ur=PitchRef(11)*180/pi;
    else
        ur=Weighting*PitchRef(k)*180/pi+(1-Weighting)*PitchRef(k+1)*180/pi;
    %   PitchRefW=pi*PitchRefW/180;
    end
```

```

        if k<=0
            k=1;
        end
        if k>11
            k=11;
        end

% Set parameters for MPC design
nc=20;
p=nc;
m=p;
nu=3;
ny=4;
% uc=[p1;p2;p3];
U0=zeros(nu*m,1);

% Extract two models from the model bank
[Cn,Cm,C11]=size(C);
CC1=zeros(Cn,Cm);
CC2=zeros(Cn,Cm);

[Bn,Bm,B11]=size(B);
BB1=zeros(Bn,Bm);
BB2=zeros(Bn,Bm);

[An,Am,A11]=size(A);
AA1=zeros(An,Am);
AA2=zeros(An,Am);
% for nn=1:Cn
%     for mm=1:Cm
%         C1(nn,mm)=C(nn,mm,1);
%     end
% end

if k<11

```

```

for nn=1:Cn
    for mm=1:Cm
        CC1(nn,mm)=C(nn,mm,k);
        CC2(nn,mm)=C(nn,mm,k+1);
    end
end
for nn=1:Bn
    for mm=1:Bm
        BB1(nn,mm)=B(nn,mm,k);
        BB2(nn,mm)=B(nn,mm,k+1);
    end
end
for nn=1:An
    for mm=1:Am
        AA1(nn,mm)=A(nn,mm,k);
        AA2(nn,mm)=A(nn,mm,k+1);
    end
end
else
LL=10;
for nn=1:Cn
    for mm=1:Cm
        CC1(nn,mm)=C(nn,mm,LL);
        CC2(nn,mm)=C(nn,mm,LL+1);
    end
end
for nn=1:Bn
    for mm=1:Bm
        BB1(nn,mm)=B(nn,mm,LL);
        BB2(nn,mm)=B(nn,mm,LL+1);
    end
end
for nn=1:An
    for mm=1:Am
        AA1(nn,mm)=A(nn,mm,LL);
        AA2(nn,mm)=A(nn,mm,LL+1);
    end
end
end

```

```

end

[An,Am]=size(AA1);
[Bn,Bm]=size(BB1);

ModL=2;
xhat1=[Est11;Est12;Est13;Est14;Est15;Est16;Est17;];
xhat2=[Est21;Est22;Est23;Est24;Est25;Est26;Est27;];

%% Formulate the matrix in quadratic programming
% generate Sx
Sx=zeros(ny*p,1);
for nn=1:ModL
    if nn==1
        Cnn=CC1;
        Ann=AA1;
        xhat=xhat1;
        Weightnn=Weighting;
    else
        Cnn=CC2;
        Ann=AA2;
        xhat=xhat2;
        Weightnn=1-Weighting;
    end
    Sx_temp=zeros(ny*p,Am);
    for ii=1:p
        Sx_temp_part=Cnn*Ann^(ii);
        for jj=1:ny
            for kk=1:Am
                Sx_temp(ny*(ii-1)+jj,kk)=Sx_temp_part(jj,kk);
            end
        end
    end
    Sx=Sx+Weightnn*Sx_temp*xhat;
end

```

```

% Generat Sc
Sc=zeros(p*ny,p*nu);
for nn=1:ModL

    if nn==1
        Cnn=CC1;
        Ann=AA1;
        Bnn=BB1;
        Weightnn=Weighting;
    else
        Cnn=CC2;
        Ann=AA2;
        Bnn=BB2;
        Weightnn=1-Weighting;
    end

    Sc_temp=zeros(p*ny,p*nu);
    for ii=1:p
        for jj=1:p
            if ii==jj
                Sc_temp_part=Cnn*Bnn;
            elseif ii>jj
                Sc_temp_part=Cnn*Ann^(ii-jj)*Bnn;
            else
                Sc_temp_part=zeros(ny,nu);
            end

            for kk=1:ny
                for mm=1:nu
                    Sc_temp(ny*(ii-1)+kk,nu*(jj-1)+mm)=Sc_temp_part(kk,mm);
                end
            end
        end
    end
    Sc=Sc+Weightnn*Sc_temp;
end

```

```

% Generate Se
Se=zeros(p*nu,m*nu);
for ii=1:p
    for jj=1:m
        if ii==jj
            for kk=1:nu
                for mm=1:nu
                    if kk==mm
                        Se(nu*(ii-1)+kk,nu*(jj-1)+mm)=1.0;
                    else
                        Se(nu*(ii-1)+kk,nu*(jj-1)+mm)=0.0;
                    end
                end
            end
        elseif ii>jj
            for kk=1:nu
                for mm=1:nu
                    if kk==mm
                        Se(nu*(ii-1)+kk,nu*(jj-1)+mm)=1.0;
                    else
                        Se(nu*(ii-1)+kk,nu*(jj-1)+mm)=0.0;
                    end
                end
            end
        elseif ii<jj
            for kk=1:nu
                for mm=1:nu
                    Se(nu*(ii-1)+kk,nu*(jj-1)+mm)=0.0;
                end
            end
        end
    end
end

% U0=zeros(nu*m,1);

H=2*Wu+2*(Sc*Se)'*Wy*Sc*Se;

```

```
g=2*(Sc*Se)'*Wy*(Sx+Sc*U0);
```

```
%%%%%%%%%% CONSTRAINT HANDLING PART
```

```
umin=(-ur-0)*pi/180;
```

```
umax=(-ur+90)*pi/180;
```

```
ubarmin=-10*pi/180;
```

```
ubarmax=10*pi/180;
```

```
lbA=zeros((m+1)*nu+m*nu,1);
```

```
ubA=zeros((m+1)*nu+m*nu,1);
```

```
for i=1:(m+1)*nu
```

```
    lbA(i)=umin;
```

```
    ubA(i)=umax;
```

```
    if i<=m*nu
```

```
        lbA((m+1)*nu+i)=Ts*ubarmin;
```

```
        ubA((m+1)*nu+i)=Ts*ubarmax;
```

```
    end
```

```
end
```

```
TN=zeros((m+1)*nu,(m+1)*nu);
```

```
M=zeros(m*nu,(m+1)*nu);
```

```
omegar=12.1*pi/30;
```

```
T=zeros(3,3);
```

```
for i=1:m+1
```

```
    phiv=phi+(omega+i*(omegar-omega)/(m*1.0))*Ts*(i-1);
```

```
    T(1,1)=1;    T(1,2)=cos(phiv);    T(1,3)=sin(phiv);
```

```
    T(2,1)=1;    T(2,2)=cos(phiv+pi/3.0);    T(2,3)=sin(phiv+pi/3.0);
```

```
    T(3,1)=1;    T(3,2)=cos(phiv+2.0*pi/3.0);    T(3,3)=sin(phiv+2.0*pi/3.0);
```

```
    TINV=inv(T);
```

```
    TN((i-1)*nu+1,(i-1)*nu+1)=TINV(1,1);    TN((i-1)*nu+1,(i-1)*nu+2)=TINV(1,2);    TN((i-1)*nu+1,(i-1)*nu+3)=TINV(1,3);
```

```
    TN((i-1)*nu+2,(i-1)*nu+1)=TINV(2,1);    TN((i-1)*nu+2,(i-1)*nu+2)=TINV(2,2);    TN((i-1)*nu+2,(i-1)*nu+3)=TINV(2,3);
```

```
    TN((i-1)*nu+3,(i-1)*nu+1)=TINV(3,1);    TN((i-1)*nu+3,(i-1)*nu+2)=TINV(3,2);    TN((i-1)*nu+3,(i-1)*nu+3)=TINV(3,3);
```

```

    if i<m+1
        for j=1:nu
            M((i-1)*nu+j,(i-1)*nu+j)=-1;
            M((i-1)*nu+j,i*nu+j)=1;
        end
    end
end

% TINVMTMMT=TN*inv(M'*M)*M';
% TRFTINVMTMMT=M*TN*inv(M'*M)*M';
TINVMTMMT=TN*pinvM;
TRFTINVMTMMT=M*TN*pinvM;

ATotal=zeros((m+1)*nu+m*nu,m*nu);

for i=1:(m+1)*nu
    for j=1:m*nu
        ATotal(i,j)=TINVMTMMT(i,j);
        if i<=m*nu
            ATotal((m+1)*nu+i,j)=TRFTINVMTMMT(i,j);
        end
    end
end

X = zeros(nc*nu,1);
c = zeros(nc*nu,1);
[obj,c,y,status,nWSRout] = qpOASES(H,g,ATotal,[],[],lbA,ubA);
c1=c(1);
c2=c(2);
c3=c(3);

```

C1.2 Simulink Layout

In the left and up corner of Fig. C.1, “subsystem” is used to extract measurements from “FAST” simulation. In the middle, “Observer” is used for state estimation. In the right and down corner, “MPC” is embedded Matlab code for MMPC.

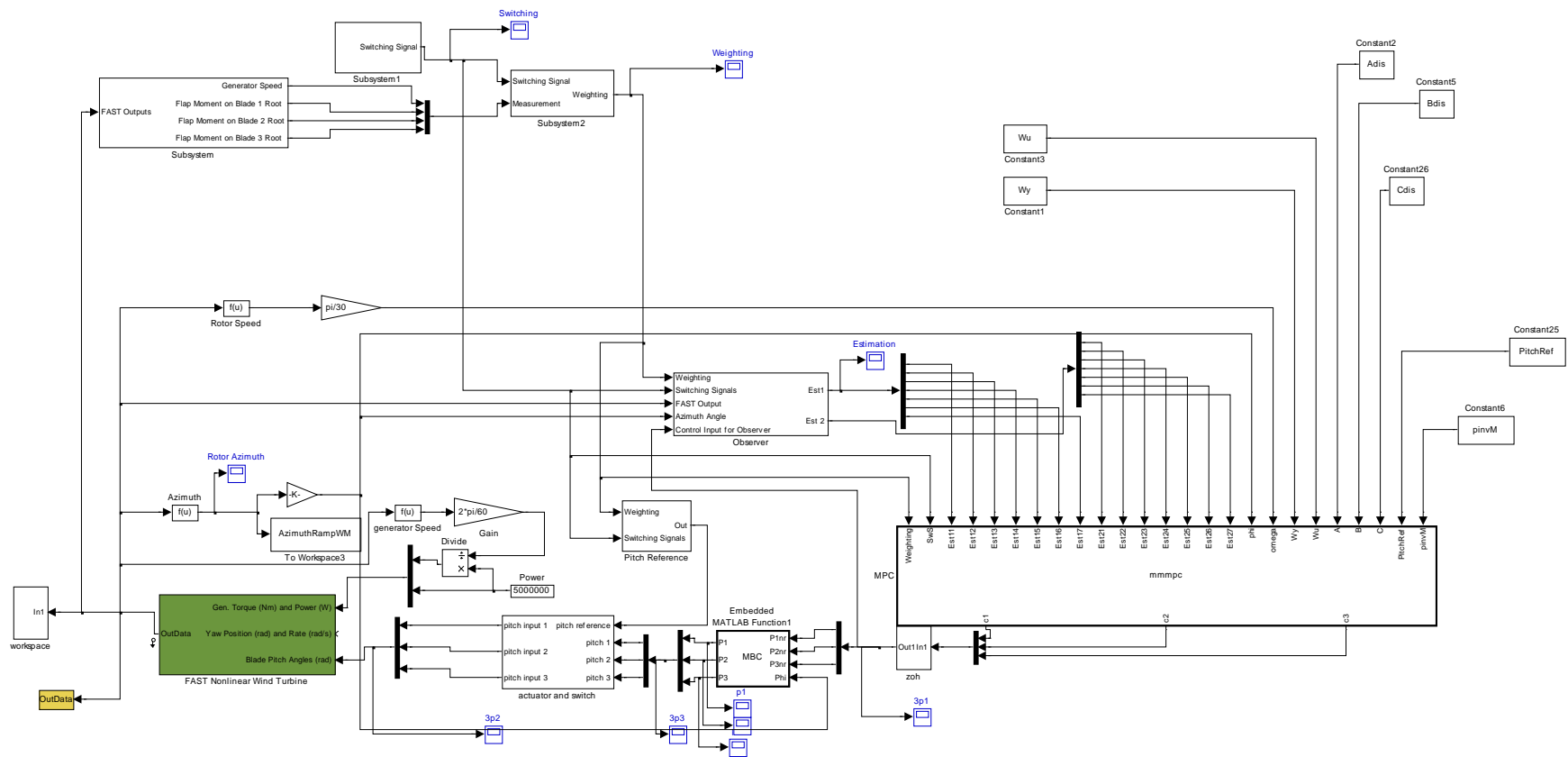


Fig. C.1 Simulink Layout for MMPC

C1.3 Usage

1. Adjust weighting matrix in “StandardMPC.m”;
2. Run Matlab file “MMMPC.m” to extract state-space models from FAST output files for MMPC;
3. Run Matlab file “LoadDataforSimulation.m” to load data for MMPC;
4. In Matlab, input “Simsetup” and the FAST input file name “NRELOffshrBsline5MW_Onshore_WM_BWeighting.fst”;
5. Run Simulink file “MMMPC_AveragedLoadsRef”;

C.2 Dual Mode MPC

C.2.1 Source Codes

```
function [c1,c2,c3]=dmmpc(x1,x2,x3,x4,x5,x6,x7,x8,x9,umin1,umin2,umin3,umax1,umax2,umax3,SS,Pclu,Hcu)
%#eml

% nu  Control input number
% nc  prediction horizon number

eml.extrinsic('qpOASES');
x=[x1;x2;x3;x4;x5;x6;x7;x8;x9];
nc=20;
nu=3;
S=zeros(nc*nu,nc*nu);

for k=1:nc;
    for i=1:nu;
        for j=1:nu;
%            S((k-1)*nu+1:k*nu,(k-1)*nu+1:k*nu)=SS;
```

```

        S((k-1)*nu+i,(k-1)*nu+j)=SS(i,j);
    end
end
end

% lbs=K*x+umin;
% ubS=K*x+umax;
lbs=zeros(nu,1);
ubS=zeros(nu,1);
lbs(1)=umin1;
lbs(2)=umin2;
lbs(3)=umin3;
ubS(1)=umax1;
ubS(2)=umax2;
ubS(3)=umax3;

lb=zeros(nc*nu,1);
ub=zeros(nc*nu,1);

for k=1:nc;
    for i=1:nu;
%     lb((k-1)*nu+1:k*nu)=lbs;
%     ub((k-1)*nu+1:k*nu)=ubS;
        lb((k-1)*nu+i)=lbs(i);
        ub((k-1)*nu+i)=ubS(i);
    end
end

lbA=lb+Pclu*x;
ubA=ub+Pclu*x;

%%%%%%%%%%%%%% CONSTRAINT HANDLING PART
X = zeros(nc*nu,1);
c = zeros(nc*nu,1);
% [obj,c,y,status,nWSRout] = qpOASES(S,X,clb,cub);
[obj,c,y,status,nWSRout] = qpOASES(S,X,Hcu,[],[],lbA,ubA);
ce=zeros(nu,nc*nu);

```

```
for j=1:nu;
    ce(j,j)=1;
end
ci=ce*c;
c1=[1 0 0]*ci;
c2=[0 1 0]*ci;
c3=[0 0 1]*ci;
```

C.2.2 Simulink Layout

The Simulink layout for dual mode MPC is shown in Fig. C.2. In the left and up corner, “subsystem” is used to extract measurements from “FAST” simulation. In the right and middle, “Switched MPC” is switched dual mode MPC for different models.

C.2.3 Usage

1. Adjust weighting matrix in “QRValue.m” and “MPC_WakeMeandering5.m”;
2. Run Matlab file “StateSpaceModelandPredictionModelforMPC.m” to extract state-space models from FAST output files for dual mode MPC;
3. Run Matlab file “LoadDataforSimulation.m” to load data for dual mode MPC;
4. In Matlab, input “Simsetup” and the FAST input file name “NRELOffshrBslne5MW_Onshore_WM_Torq.fst”;
5. Run Simulink file “MPC_MBC_WakeMeandering_Torque_Nonalign61by61.mdl”;

Appendix D. Codes for Jensen Wake Model, Larsen Wake Model and Wake Meandering

D.1 Jensen Wake Model

Subroutine

```
singlewake(NumGrid_Y,NumGrid_Z,GridHeight,HubHt,GridWidth,Zbottom,RotorDiameter,Uhub,Uhubwake,ijshadow,m,ijincoming  
,n,wakesign)
```

! Uhubwake---- the wind speed at the hub in the wake

! ijshadow-----position of points in overlapping

! ijincoming---position of the points not in the wake

implicit none

```
integer Downwindspace,m,n,istep,NumGrid_Y,NumGrid_Z,i,j,II
```

```
integer ijshadow(NumGrid_Y*NumGrid_Z,2),ijincoming(NumGrid_Y*NumGrid_Z,2),wakesign(NumGrid_Y*NumGrid_Z)
```

```
real k, RW,y,z,RotorDiameter,Uhub,Uhubwake,HubHt,GridWidth,GridHeight,Zbottom,Ct
```

real DisAxis !Distance between the axis of downwind and upwind turbine

! Identify the points belong to wake region

!k=0.075 !original 0.1, suggest: 0.075 onshore wind turbine and 0.05 offshore wind turbine

k=0.1

Downwindspace=8 ! mean Downwindspace*Diameter, the distance between wind turbines along downwind

$RW = (\text{RotorDiameter} + k * \text{Downwindspace} * \text{RotorDiameter} * 2) / 2$

DisAxis=0.7*RW !Added for general wake interaction

m=0

n=0

do j=1,NumGrid_Z

Do i=1,NumGrid_Y

$y = -\text{GridWidth} / 2.0 + (i-1) * \text{GridWidth} / (\text{NumGrid_Y} - 1)$

$z = Z_{\text{bottom}} + (j-1) * \text{GridHeight} / (\text{NumGrid_Z} - 1)$

$\text{II} = (j-1) * \text{NumGrid_Y} + i$

if(((y-DisAxis)**2+(z-HubHt)**2).lt.RW**2) then !y-RW has been changed into y-DisAxis July 2nd 2010

m=m+1

ijshadow(m,1)=i

ijshadow(m,2)=j

wakesign(II)=1

else

n=n+1

ijincoming(n,1)=i

ijincoming(n,2)=j

wakesign(II)=0

```

    end if

enddo

enddo

! Compute the mean wind speed within wake region

!U(I,Z) Vinf=15 !above rated wind speed in this case

!Vwake=Vinf*(1-(1-sqrt(1.0-Ct))/(1+2*k*Downwindspace)^2)

Ct=0.7 !Range from 0.0 to about 1.0, when power coefficient reaches its maximum, Ct is about 0.7

Uhubwake=Uhub*(1-(1-sqrt(1.0-Ct))/(1+2*k*Downwindspace)**2)

End

```

D.2 Larsen Wake Model

subroutine

Larsenwake(z0,NumGrid_Y,NumGrid_Z,GridHeight,HubHt,GridWidth,Zbottom,RotorDiameter,Uhub,Uhubwake,ijshadow,ijincomin
g,wakesign,wakev,DisAxis,Ia,DownwindSpace,RW)

! Uhubwake---- the wind speed at the hub in the wake

! ijshadow-----position of points in overlapping

! ijincoming---position of the points not in the wake

implicit none

integer m,n,istep,NumGrid_Y,NumGrid_Z,i,j,II

integer ijshadow(NumGrid_Y*NumGrid_Z,2),ijincoming(NumGrid_Y*NumGrid_Z,2),wakesign(NumGrid_Y*NumGrid_Z)

real k, RW,y,z,RotorDiameter,Uhub,Uhubwake,HubHt,GridWidth,GridHeight,Zbottom,Ct,wakev(NumGrid_Y*NumGrid_Z)

real DisAxis !Distance between the axis of downwind and upwind turbine

real Ia !the ambient turbulence intensity

real Rnb,R9p5,Deff,c1,x0,A,PI,x,DU1

real z0,zeta0,d0,DU2,Downwindspace

write(*,*) 'z0=',z0

!Ia=0.18

Rnb=max(1.08*RotorDiameter,1.08*RotorDiameter+21.7*RotorDiameter*(Ia-0.05))

R9p5=0.5*(Rnb+min(HubHt,Rnb))

Ct=0.7 !Range from 0.0 to about 1.0, when power coefficient reaches its maximum, Ct is about 0.7

Deff=RotorDiameter*sqrt((1+sqrt(1-Ct))/2.0/sqrt(1-Ct))

PI=3.1415926

A=PI*RotorDiameter**2/4.0

$$x0=9.5*\text{RotorDiameter}/((2*R9p5/\text{Deff})^{**3.0}-1.0)$$

$$c1=(\text{Deff}/2.0)^{**2.5}*(105.0/2.0/\text{PI})^{**(-0.5)}*(\text{Ct}*A*x0)^{**(-5.0/6.0)}$$

!Downwindspace=8 ! mean Downwindspace*Diameter, the distance between wind turbines along downwind

$$x=\text{Downwindspace}*\text{RotorDiameter}$$

$$\text{RW}=(35.0/2.0/\text{PI})^{**0.2}*(3.0*c1^{**2})^{**0.2}*(\text{Ct}*A*(x+x0))^{**1.0/3.0}$$

$$\text{DU1}=-\text{Uhub}/9.0*(\text{Ct}*A*(x+x0)^{**(-2.0)})^{**1.0/3.0}*(-(35.0/2.0/\text{PI})^{**0.3}*(3.0*c1^{**2})^{**(-0.2)})^{**2.0}$$

$$\text{zeta0}=(35.0/2.0/\text{PI})^{**0.2}*(3.0*c1^{**2.0})^{**(-2.0/15.0)}$$

$$d0=4.0/81.0*\text{zeta0}^{**6}*(-1.0-3.0*(4.0-12.0*(6.0+27.0*(-4.0+48.0/40.0)/19.0)/4.0)/5.0)/8.0$$

$$\text{DU2}=\text{Uhub}*(\text{Ct}*A*(x+x0)^{**(-2.0)})^{**2.0/3.0}*d0$$

$$\text{UhubWake}=\text{Uhub}+\text{DU1}+\text{DU2}$$

write(*,*) 'Uhub=',Uhub

write(*,*) 'RotorDiameter=',RotorDiameter

```
write(*,*) 'DU1=',DU1
```

```
write(*,*) 'DU2=',DU2
```

```
write(*,*) 'UhubWake=',UhubWake
```

```
write(*,*) 'RW=',RW
```

```
!Uhubwake=Uhub+DU1
```

```
!DisAxis=0.9*RW !Added for general wake interaction
```

```
DO i=1,NumGrid_Y*NumGrid_Z
```

```
wakev(i)=0.0
```

```
END DO
```

```
m=0
```

```
n=0
```

```
do j=1,NumGrid_Z
```

Do i=1,NumGrid_Y

y=-GridWidth/2.0+(i-1)*GridWidth/(NumGrid_Y-1)

z=Zbottom+(j-1)*GridHeight/(NumGrid_Z-1)

II=(j-1)*NumGrid_Y+i

if(((y-DisAxis)**2+(z-HubHt)**2).lt.RW**2) then !y-RW has been changed into y-DisAxis July 2nd 2010

m=m+1

ijshadow(m,1)=i

ijshadow(m,2)=j

wakesign(II)=1

wakev(II)=(Uhub+(DU1+DU2)*exp(-((y-DisAxis)/RW)**2.0)*exp(-((z-HubHt)/RW)**2))*log(z/z0)/log(HubHt/z0) ! In

Crespo's paper, z0 means ground level but in fact we can regard z0 as roughness length.

else

n=n+1

ijincoming(n,1)=i

ijincoming(n,2)=j

wakesign(II)=0

end if

enddo

enddo

end

D.3 Wake Meandering Modeling

WakeCenter(0)=0.0

MaxWakeCenter=WakeCenter(0)

MinWakeCenter=WakeCenter(0)

Alp=TimeStep/(RotorDiameter/Uhub+TimeStep) !Parameters for low-pass filter

WM=0 !Including Wake Meandering or not

Larsen=1 ! Larsen Wake Model or not

NOTURB=1 ! Without Turbulence

WakeCenterSection=10.0 ! Section Number for Wake Range

WakeCenterP=5.0 ! Wake Center Position in Wake Range

DownwindSpace=8.0 ! Distance between Upstream and Downstream Wind Turbine

SWM=1 ! Simplified Wake Meandering Model or not

WRITE(*,*) 'WakeCenterP=',WakeCenterP

IF(WM)THEN

open (unit=15, file='WakeCenter.txt', status='unknown')

END IF

```
9010 format(f10.3,f10.3,f10.3,f10.3)
```

```
DO IT=1,NumSteps
```

```
  II = 0
```

```
  MLV(IT)=0
```

```
  DO IZ=1,ZLim
```

```
    DO IY=1,IYmax(IZ)
```

```
      II = II + 1
```

```
      MLV(IT)=MLV(IT)+V(IT,II,2)
```

```
    ENDDO ! IY
```

```
  ENDDO ! IZ
```

```
  MLV(IT)=MLV(IT)/II
```

```
  !! low-pass filter
```

IF(IT.EQ.1)THEN

$MLV(IT)=(1-A_{lp})*MLV(IT)+A_{lp}*MLV(IT)$! MLV(1) does not change

! $WakeCenter(0)=WakeCenter(0)+MLV(1)*DownwindSpace*RotorDiameter/U_{hub}$

ELSE

$MLV(IT)=(1-A_{lp})*MLV(IT-1)+A_{lp}*MLV(IT)$

END IF

IF(SWM.EQ.1)THEN

$WakeCenter(IT)=MLV(IT)*DownwindSpace*RotorDiameter/U_{hub}$

ELSE

$WakeCenter(IT)=WakeCenter(IT-1)+MLV(IT)*TimeStep$

! $WakeCenter(IT+1)=WakeCenter(IT)+V(IT,HubIndx,2)*TimeStep$

END IF

```
IF(WakeCenter(IT).GT.MaxWakeCenter)THEN
```

```
MaxWakeCenter=WakeCenter(IT)
```

```
END IF
```

```
IF(WakeCenter(IT).LT.MinWakeCenter)THEN
```

```
MinWakeCenter=WakeCenter(IT)
```

```
END IF
```

```
CurrentTime=IT*TimeStep
```

```
IF(WM)THEN
```

```
write(15,9010) CurrentTime,V(IT,HubIndx,2),MLV(IT),WakeCenter(IT)
```

```
END IF
```

```
ENDDO ! IT
```

```
IF(WM)THEN
```

```
CLOSE(15)
```

```
END IF
```

```
WRITE(*,*) 'MaxWakeCenter=',MaxWakeCenter
```

```
WRITE(*,*) 'MinWakeCenter=',MinWakeCenter
```

```
! For get wake radius
```

```
DisAxis=0.0
```

```
call
```

```
Larsenwake(z0,NumGrid_Y,NumGrid_Z,GridHeight,HubHt,GridWidth,Zbottom,RotorDiameter,Uhub,Uhubwake,ijshadow,ijincomin  
g,wakesign,wakev,DisAxis,TurbInt,DownwindSpace,RW)
```

```
DO IT=1,NumSteps
```

```
! Steady wake interaction without wakemeandering model
```

IF(WM.EQ.0)THEN

! For the rotor axis of both upstream and downstream is the same.

! DisAxis=MinWakeCenter+WakeCenterP*(MaxWakeCenter-MinWakeCenter)/WakeCenterSection

! For the rotor axis of both upstream and downstream is not the same.

DisAxis=RW-RotorDiameter/2.0+WakeCenterP*RotorDiameter/WakeCenterSection

ELSE

! For the rotor axis of both upstream and downstream is the same.

! DisAxis=WakeCenter(IT)

! For the rotor axis of both upstream and downstream is not the same.

DisAxis=WakeCenter(IT)+abs(MinWakeCenter)+RW-RotorDiameter/2.0

END IF

!! Larsen Wake Model or not

IF(IT.EQ.1.OR.WM.EQ.1)THEN

IF(Larsen)THEN

call

Larsenwake(z0,NumGrid_Y,NumGrid_Z,GridHeight,HubHt,GridWidth,Zbottom,RotorDiameter,Uhub,Uhubwake,ijshadow,ijincomin
g,wakesign,wakev,DisAxis,TurbInt,DownwindSpace,RW)

ELSE

call

singlewake(NumGrid_Y,NumGrid_Z,GridHeight,HubHt,GridWidth,Zbottom,RotorDiameter,UHub,UHubwake,ijshadow,mshadow,iji
ncoming,nincoming,wakesign)

IF (INDEX('JU', WindProfileType(1:1)) > 0) THEN

Uwake(1:ZLim) = getWindSpeed(UHubwake, HubHt, Z(1:ZLim), RotorDiameter, PROFILE=WindProfileType,
UHANGLE=WindDir_profile)

```

ELSE

    Uwake(1:ZLim) = getWindSpeed( UHubwake, HubHt, Z(1:ZLim), RotorDiameter, PROFILE=WindProfileType)

ENDIF

END IF

END IF

!!! Circular Equivalent Wind Profile or not

CIRCULAR=0

IF(CIRCULAR.EQ.1)THEN

UNITLEN=0.2 !!Section Length (meter) for interpolation

NPoint=(INT(SQRT(1.0*(((NumGrid_Y+1)/2)**2+((NumGrid_Z+1)/2)**2)))+1)/UNITLEN

WRITE(*,*) 'NPoint=',NPoint

AZIMUTH=120 !! Azimuth angle for Circular Equivalent Wind Profile

```

```
DO JJ=1,NPoint

  Y_D=(NumGrid_Y+1)/2-(JJ-1)*UNITLEN*COS(AZIMUTH*PI/180)

  Z_D=(NumGrid_Z+1)/2-(JJ-1)*UNITLEN*SIN(AZIMUTH*PI/180)

  DISRADIUS(JJ)=ABS(JJ-1)*UNITLEN

  DO LL=1,NumGrid_Z

    IF(Z_D.GE.LL.AND.Z_D.LT.(LL+1))THEN

      KKZ=LL

    END IF

  END DO

  IF(Z_D.GE.NumGrid_Z+1)THEN

    KKZ=NumGrid_Z

  END IF
```

```
IF(Z_D.LE.1)THEN
```

```
    KKZ=1
```

```
END IF
```

```
DO LL=1,NumGrid_Y
```

```
    IF(Y_D.GE.LL.AND.Y_D.LT.(LL+1))THEN
```

```
        KKY=LL
```

```
    END IF
```

```
END DO
```

```
IF(Y_D.GE.NumGrid_Y+1)THEN
```

```
    KKY=NumGrid_Y
```

```
END IF
```

```
IF(Y_D.LE.1)THEN
```

```
    KKY=1
```

```
END IF
```

```
II=(KKZ-1)*NumGrid_Y+KKY+1
```

```
IF(KKY.EQ.NumGrid_Y)THEN
```

```
II=(KKZ-1)*NumGrid_Y+KKY
```

```
END IF
```

```
IF(WAKESIGN(II))THEN
```

```
    IF(LARSEN)THEN
```

```
        URADIUSM(1)=wakev(II)
```

```
    ELSE
```

```
        URADIUSM(1)=Uwake(KKZ)
```

END IF

ELSE

URADIUSM(1)=U(KKZ)

END IF

II=(KKZ-1)*NumGrid_Y+KKY

IF(WAKESIGN(II))THEN

IF(LARSEN)THEN

URADIUSM(2)=wakev(II)

ELSE

URADIUSM(2)=Uwake(KKZ)

END IF

ELSE

URADIUSM(2)=U(KKZ)

END IF

II=(KKZ+1-1)*NumGrid_Y+KKY

IF(KKZ.EQ.NumGrid_Z)THEN

II=(KKZ-1)*NumGrid_Y+KKY

END IF

IF(Z_D.LT.0)THEN

II=(1-1)*NumGrid_Y+KKY

END IF

IF(WAKESIGN(II))THEN

IF(LARSEN)THEN

URADIUSM(3)=wakev(II)

ELSE

IF(KKZ.GE.NumGrid_Z)THEN

URADIUSM(3)=Uwake(NumGrid_Z)

ELSE

URADIUSM(3)=Uwake(KKZ+1)

END IF

IF(Z_D.LT.1)THEN

URADIUSM(3)=Uwake(1)

END IF

END IF

ELSE

IF(KKZ.GE.NumGrid_Z)THEN

URADIUSM(3)=U(NumGrid_Z)

ELSE

URADIUSM(3)=U(KKZ+1)

END IF

IF(Z_D.LT.1)THEN

URADIUSM(3)=U(1)

END IF

END IF

II=(KKZ+1-1)*NumGrid_Y+KKY+1

IF(KKZ.EQ.NumGrid_Z)THEN

II=(KKZ-1)*NumGrid_Y+KKY+1

END IF

IF(KKY.EQ.NumGrid_Y)THEN

II=(KKZ+1-1)*NumGrid_Y+KKY

END IF

IF(KKZ.EQ.NumGrid_Z.AND.KKY.EQ.NumGrid_Y)THEN

II=(KKZ-1)*NumGrid_Y+KKY

END IF

IF(WAKESIGN(II))THEN

IF(LARSEN)THEN

URADIUSM(4)=wakev(II)

ELSE

IF(KKZ.GE.NumGrid_Z)THEN

```
URADIUSM(4)=Uwake(NumGrid_Z)

ELSE

URADIUSM(4)=Uwake(KKZ+1)

END IF

IF(Z_D.LT.1)THEN

URADIUSM(4)=Uwake(1)

END IF

END IF

ELSE

IF(KKZ.GE.NumGrid_Z)THEN

URADIUSM(4)=U(NumGrid_Z)

ELSE
```

```
URADIUSM(4)=U(KKZ+1)

END IF

IF(Z_D.LT.1)THEN

URADIUSM(4)=U(1)

END IF

END IF

IF(KKY.GE.NumGrid_Y)THEN

KKY=INT(Y_D)

END IF

IF(KKY.EQ.1.AND.Y_D.LT.0)THEN

KKY=INT(Y_D)-1

END IF
```

```

IF(KKZ.GE.NumGrid_Z)THEN

    KKZ=INT(Z_D)

END IF

IF(KKZ.EQ.1.AND.Z_D.LT.0)THEN

    KKZ=INT(Z_D)-1

END IF

LAMDA1=(Y_D-KKY-1)/(KKY-KKY-1)

LAMDA2=(Z_D-KKZ)/(KKZ+1-KKZ)

URADIUS(JJ)=URADIUSM(1)*(1-LAMDA1)*(1-LAMDA2)+URADIUSM(2)*LAMDA1*(1-
LAMDA2)+URADIUSM(3)*LAMDA1*LAMDA2+URADIUSM(4)*(1-LAMDA1)*LAMDA2

WRITE(*,*) 'JJ=',JJ,'Y_D=',Y_D,'Z_D=',Z_D

WRITE(*,*) 'KKY=',KKY,'KKZ=',KKZ

```

```
WRITE(*,*) (URADIUSM(LL),LL=1,4)
```

```
WRITE(*,*) 'URADIUS(JJ)=',URADIUS(JJ)
```

```
END DO !NPOINT
```

```
END IF
```

```
II = 0
```

```
DO IZ=1,ZLim
```

```
IF ( ALLOCATED( WindDir_profile ) ) THEN ! The horizontal flow angle changes with height
```

```
CHFA = COS( WindDir_profile(IZ)*D2R )
```

```
SHFA = SIN( WindDir_profile(IZ)*D2R )
```

```
ENDIF
```

```
DO IY=1,IYmax(IZ)
```

```
II = II + 1
```

! Add mean wind speed to the streamwise component

IF(CIRCULAR)THEN

 TmpDIS=SQRT(1.0*((IY-(NumGrid_Y+1)/2)**2+(IZ-(NumGrid_Z+1)/2)**2))

! WRITE(*,*) 'IY=',IY

! WRITE(*,*) 'IZ=',IZ

! WRITE(*,*) 'TmpDIS=',TmpDIS

DO IR=1,NPoint-1

 IF(TmpDIS.LT.DISRADIUS(IR+1).AND.TmpDIS.GE.DISRADIUS(IR)) THEN !In some azimuth angle, the distance
may be bigger than DISRADIUS(1)

 LAMDA=(TmpDIS-DISRADIUS(IR+1))/(DISRADIUS(IR)-DISRADIUS(IR+1))

 URADIUSINTERP=URADIUS(IR)*LAMDA+URADIUS(IR+1)*(1-LAMDA)

END IF

END DO

IF(TmpDIS.GT.DISRADIUS(NPoint))THEN

URADIUSINTERP=URADIUS(NPoint)

END IF

TmpU = V(IT,II,1) + URADIUSINTERP

ELSE

IF(WAKESIGN(II))THEN

IF(LARSEN)THEN

IF(NOTURB)THEN

TmpU = wakev(II)

ELSE

$\text{TmpU} = V(\text{IT}, \text{II}, 1) + \text{wakev}(\text{II})$

END IF

ELSE

IF(NOTURB)THEN

$\text{TmpU} = \text{Uwake}(\text{II})$

ELSE

$\text{TmpU} = V(\text{IT}, \text{II}, 1) + \text{Uwake}(\text{IZ})$

END IF

END IF

ELSE

IF(NOTURB)THEN

TmpU = U(IZ)

ELSE

 TmpU = V(IT,II,1) + U(IZ)

END IF

END IF

END IF

IF(NOTURB)THEN

 TmpV=0.0

ELSE

 TmpV = V(IT,II,2)

END IF

IF(NOTURB)THEN

 TmpW=0.0

ELSE

 TmpW = V(IT,II,3)

END IF

 ! Rotate the wind to the X-Y-Z (inertial) reference frame coordinates

V(IT,II,1) = TmpU*CHFA*CVFA - TmpV*SHFA - TmpW*CHFA*SVFA

V(IT,II,2) = TmpU*SHFA*CVFA + TmpV*CHFA - TmpW*SHFA*SVFA

V(IT,II,3) = TmpU*SVFA + TmpW*CVFA

ENDDO ! IY

ENDDO ! IZ

ENDDO ! IT

Appendix E. Codes and Simulink Diagram for Active Vane

E.1 Modified Codes for Building Simulink Interface of FAST

```
SUBROUTINE mexFunction(nlhs, plhs, nrhs, prhs)
```

```
! Purpose: Glue routine for making FORTRAN MEX-file systems and blocks
```

```
! Algorithm: FAST_SFunc is a MEX-file
```

```
USE          FAST_Simulink_Mod
```

```
USE          Output, ONLY: MaxOutPts      ! FAST module
```

```
IMPLICIT     NONE
```

```
!-----
```

```
! define parameters
```

```
!-----
```

```

INTEGER(4), PARAMETER    :: mxREAL    = 0    ! MATLAB uses 0 for REAL numbers; 1 for COMPLEX

INTEGER,  PARAMETER      :: mwPointer = 4    ! Size of pointer variables; replace 4 with 8 on DE! Alpha and the SGI

INTEGER,  PARAMETER      :: mwSize    = 4    ! Size of size variables; replace 4 with 8 on DE! Alpha and the SGI 64-

REAL(mxDB), PARAMETER    :: HUGE      = 1.0E+33

INTEGER(4), PARAMETER    :: NSIZES    = 6    ! Number of elements in the size array

INTEGER,  PARAMETER      :: MaxDOFs   = 24    ! Maximum number of DOFs:  required b/c of MATLAB R2009b

INTEGER,  PARAMETER      :: MaxNumBl  = 3    ! Maximum number of blades:  required b/c of MATLAB R2009b bug

INTEGER,  PARAMETER      :: MaxInputs  = 5+MaxNumBl+2*MaxDOFs  !! 4 modified to 5 by zzy

INTEGER,  PARAMETER      :: MaxOutputs = MaxOutPts + MaxDOFs

INTEGER,  PARAMETER      :: MaxWinds  = MIN( MaxInputs, MaxOutputs )

INTEGER          :: nlhs          ! MATLAB's count of the number of left-hand (output) arguments

```

```

INTEGER          :: nrhs          ! MATLAB's count of the number of right-hand (input) arguments

INTEGER(mwPointer)  :: plhs(*)    ! MATLAB's pointer(s) to left-hand (output) arguments

INTEGER(mwPointer)  :: prhs(*)    ! MATLAB's pointer(s) to right-hand (input) arguments

INTEGER(mwPointer)  :: ptr_T     ! pointer to input (RHS) argument #1 (t)

INTEGER(mwPointer)  :: ptr_X     ! pointer to input (RHS) argument #2 (x)

INTEGER(mwPointer)  :: ptr_U     ! pointer to input (RHS) argument #3 (u)

INTEGER(mwPointer)  :: ptr_Y     ! pointer to output (LHS) argument #1 (outputs)

REAL(mxDB)         :: T          ! input argument #1, TIME

! REAL(mxDB), ALLOCATABLE  :: U   (:)      ! input argument #2, INPUT ARRAY

REAL(mxDB)         :: U (MaxInputs)  ! input argument #2, INPUT ARRAY

INTEGER            :: FLAG      ! input argument #4, FLAG

! REAL(mxDB), ALLOCATABLE  :: Y   (:)      ! output argument #1

```

REAL(mxDB) :: Y (MaxOutputs) ! output argument #1, OUTPUT ARRAY

!-----

! define variables from the MATLAB workspace

!-----

INTEGER(mwPointer) :: ptr_retrn ! pointer to Matlab workspace variable

REAL(mxDB) :: retrn_dp ! real array created from pointer ptr_retrn

INTEGER :: NumBl !! Added by M. Hand

INTEGER :: NDOF !! Added by M. Hand

INTEGER :: NumOuts !! Added by M. Hand

REAL(mxDB) :: Initialized ! Prevents running Simulink model with old FAST input file

CHARACTER(1024) :: InpFile ! Name of the FAST input file, from the MATLAB workspace

!-----

! define internal variables

!-----

INTEGER(mwSize) :: M ! Number of rows in array

INTEGER(mwSize) :: N ! Number of columns in array

INTEGER :: Stat ! Return status

INTEGER(mwSize) :: MDLsizes(NSIZES) ! Local array, containing the SimuLink SIZE array that is required

REAL(mxDB) :: DSIZE (NSIZES) ! Local array = DOUBLE(MDLsizes), used to output the MDLsizes array

REAL(mxDB) :: NXTHIT ! return value for next time (not used)

LOGICAL :: InitStep ! Flag determines if this is an initialization step

LOGICAL, SAVE :: FirstStep = .TRUE. ! Flag to determine if FAST has been initialized

!-----

! define the EXTERNAL MATLAB procedures

!-----

INTEGER(mwPointer), EXTERNAL :: mexGetVariablePtr ! MATLAB routine

EXTERNAL :: mxCopyPtrToReal8 ! MATLAB mex function to create REAL(8) array from pointer to an array

EXTERNAL :: mxCopyReal8ToPtr ! MATLAB mex function to create pointer to copy of a REAL(8) array

INTEGER(mwPointer), EXTERNAL :: mxCreateDoubleMatrix ! pointer [Replace integer by integer*8 on the DE

INTEGER(mwSize), EXTERNAL :: mxGetM ! MATABL mex function get number of rows in array

INTEGER(mwSize), EXTERNAL :: mxGetN ! MATABL mex function to get number of columns in array

INTEGER(mwPointer), EXTERNAL :: mxGetPr ! MATLAB mex function to get the address of the first real number

REAL(mxDB), EXTERNAL :: mxGetScalar ! MATLAB mex function to return a scalar

INTEGER(mwPointer), EXTERNAL :: mxGetString ! MATLAB mex function to get string from its pointer

! Get variables from the Matlab workspace (added by M. Hand)

! these checks would not only be done on initialization instead of each call to FAST_SFunc.

! We could also pass this function the name of the FAST input file and perhaps return the

! values obtained from the input file instead of using Read_FAST_Input.m.

! Get NumBl from workspace

```
ptr_retrn = mexGetVariablePtr('base', 'NumBl')
```

```
IF ( ptr_retrn == 0 ) THEN
```

```
CALL ProgAbort('ERROR: Variable "NumBl" does not exist in the MATLAB workspace.')
```

```
ELSE
```

```
CALL mxCopyPtrToReal8(mxGetPr(ptr_retrn), retrn_dp, 1)
```

```
NumBl = INT(retrn_dp)
```

```
ENDIF
```

```
! Get NDOF from workspace

ptr_retrn = mexGetVariablePtr('base', 'NDOF')

IF ( ptr_retrn == 0 ) THEN

    CALL ProgAbort('ERROR: Variable "NDOF" does not exist in the MATLAB workspace.')

ELSE

    CALL mxCopyPtrToReal8(mxGetPr(ptr_retrn), retrn_dp, 1)

    NDOF = INT(retrn_dp)

ENDIF

! Get NumOuts from workspace

ptr_retrn = mexGetVariablePtr('base', 'NumOuts')

IF ( ptr_retrn == 0 ) THEN

    CALL ProgAbort('ERROR: Variable "NumOuts" does not exist in the MATLAB workspace.')
```

ELSE

CALL mxCopyPtrToReal8(mxGetPr(ptr_retrn), retrn_dp, 1)

NumOuts = INT(retrn_dp)

ENDIF

! Set the MDLsizes vector, which determines Simulink model characteristics

MDLsizes(1) = 0 ! number of continuous states

MDLsizes(2) = 0 ! number of discrete states

MDLsizes(3) = NDOF + NumOuts ! number of outputs: qdotted + NumOuts

MDLsizes(4) = 2 + 2 + 1 + NumBl + NDOF*2 ! Modified by zzy

MDLsizes(5) = 0 ! number of discontinuous roots in the system

MDLsizes(6) = 1 ! Direct feedthrough of U

E.2 Simulink Diagram

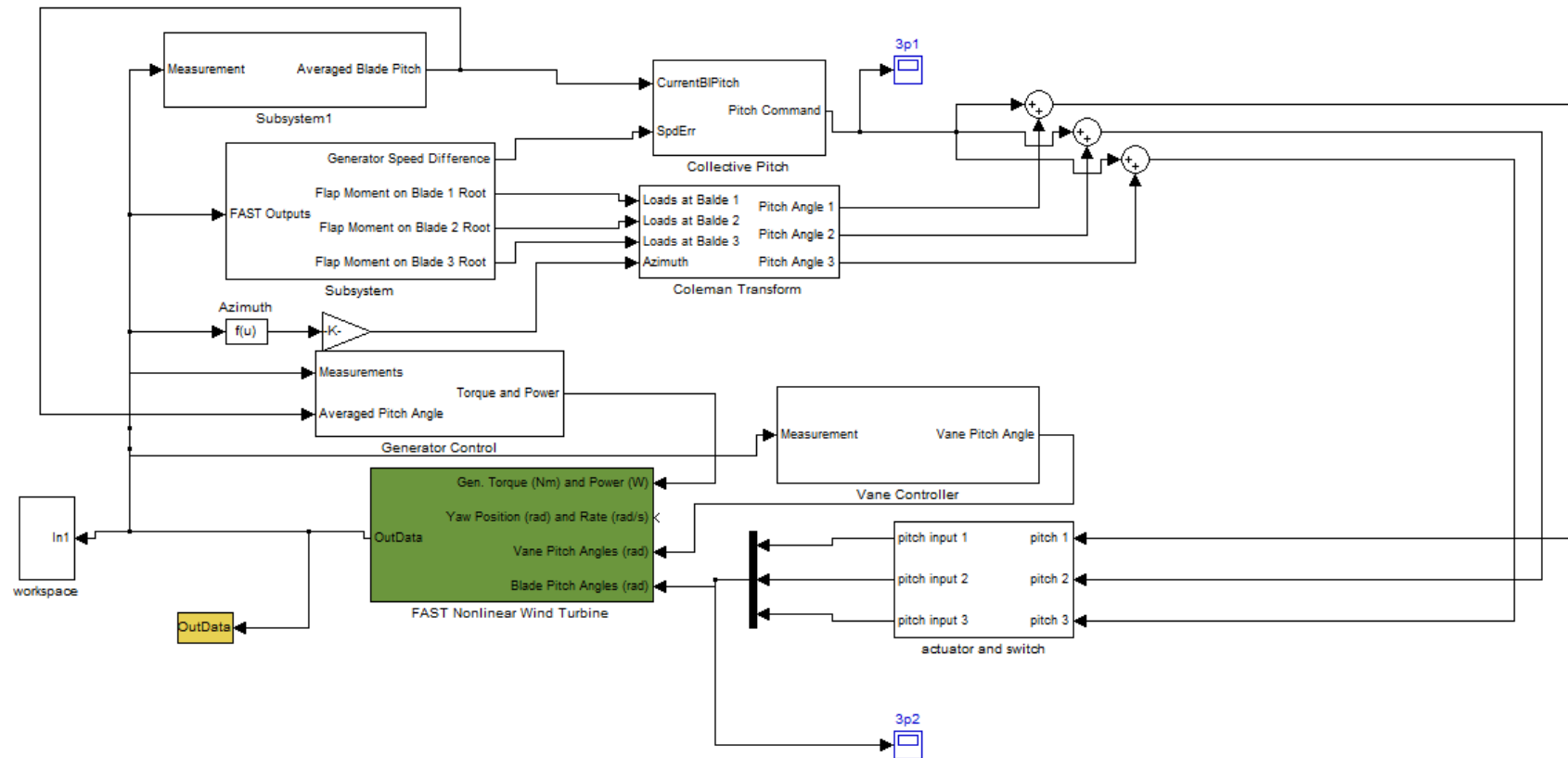


Fig. E.1 Simulink Diagram for Vane Control

Appendix F. Simulation Programs for NLESC Wind Farm Control

The procedure for running the NLESC simulation is illustrated with a case of 8 m/s 5% turbulent wind.

- (1) Run the file “Filterfortorque.m” to generate the parameters for filter parameters;
- (2) Run Simulink file “wind8Turb3TI0p05_ESC_Torque_Taylor_50000s_CrossCorrelation.mdl”.

F.1. Simulink Layout of ESC Implementation

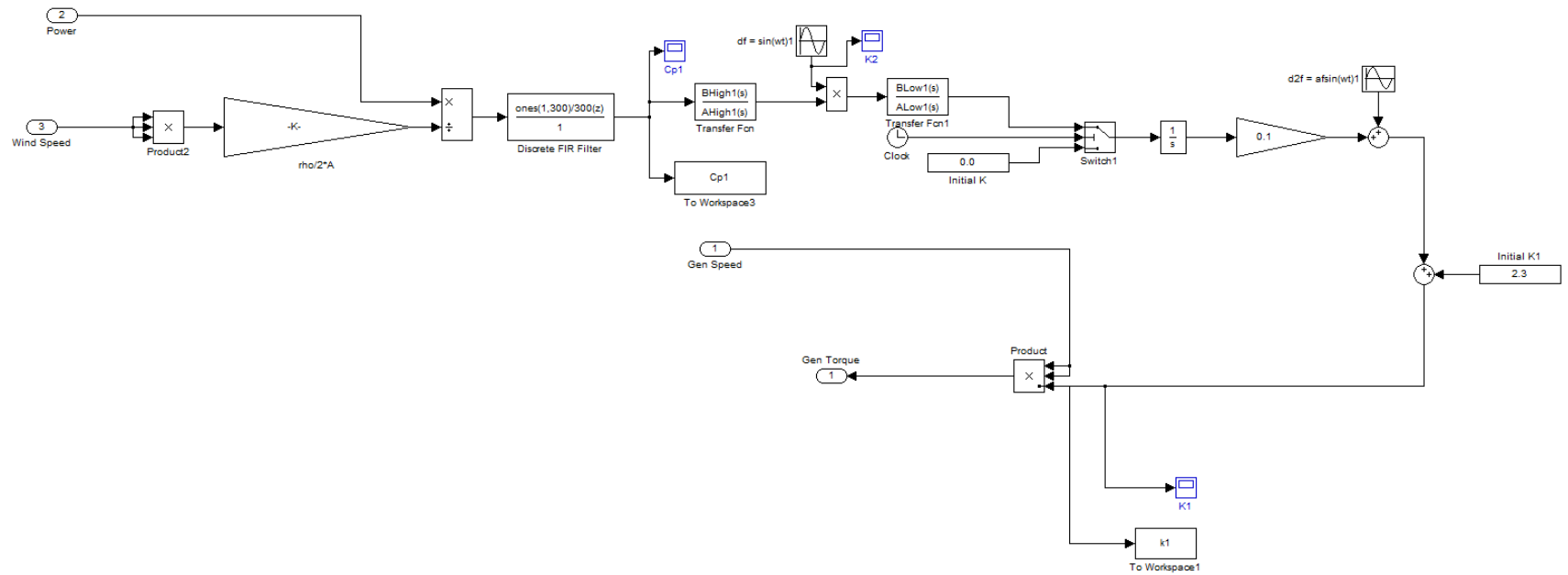


Fig.F.1 Simulink Layout of Individual ESC Implementation

F.2 Simulink Layout for NLESC

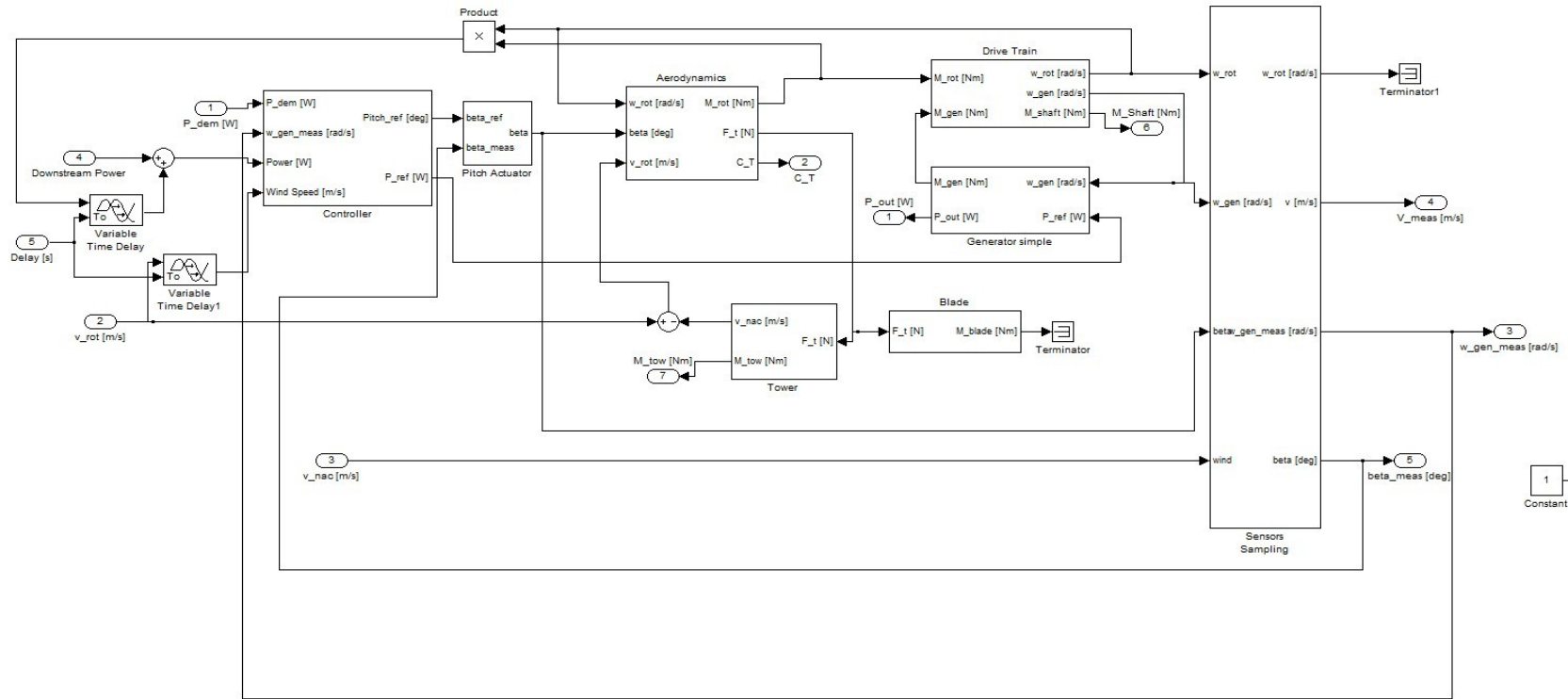


Fig. F.2 Simulink Layout for NLESC

F.3 Simulink Layout Template Generated by SimWindFarm

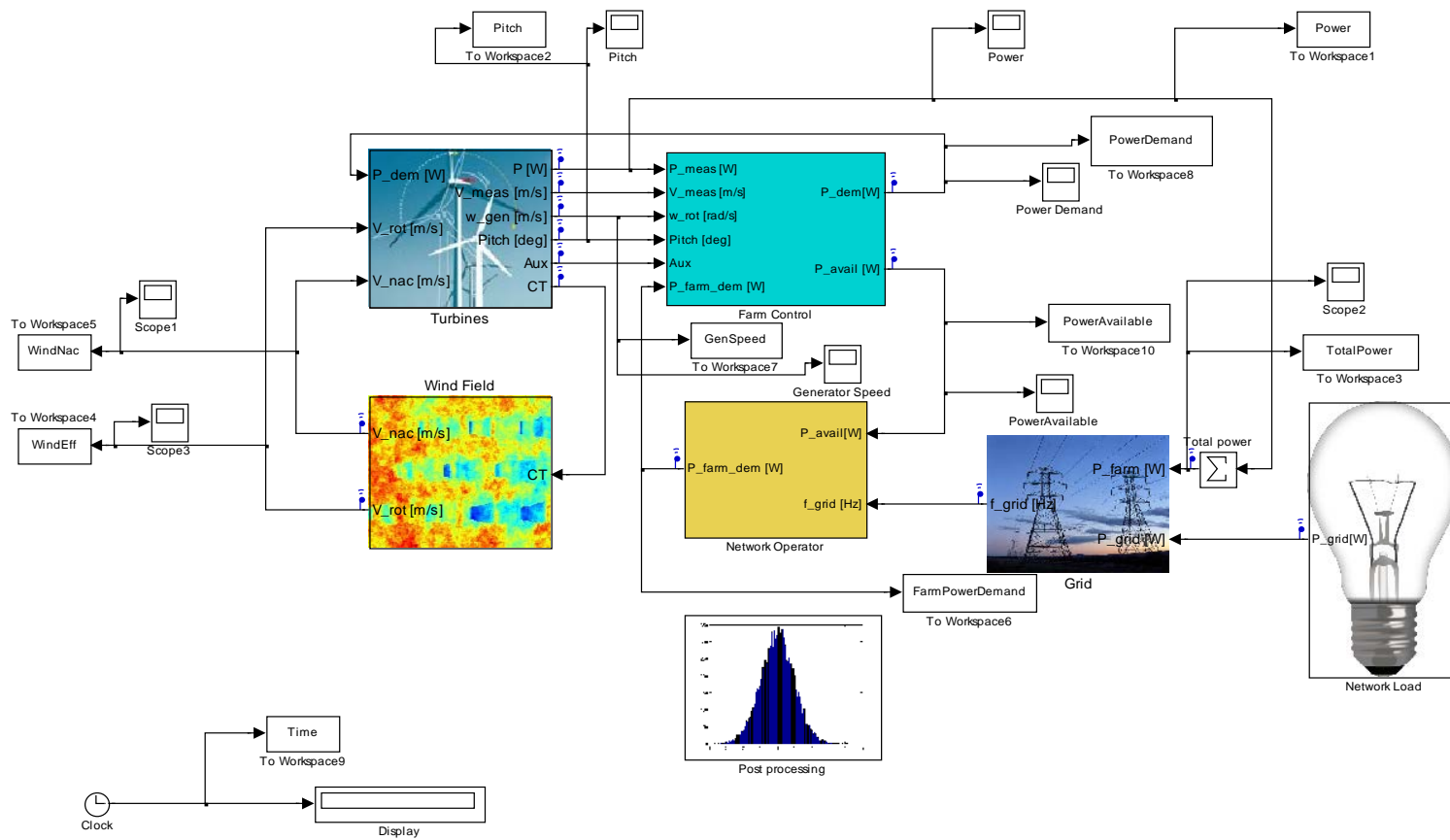


Fig. F.3 Simulink Layout Template Generated by SimWindFarm

Appendix G. Default Wind Farm Controller in SimWindFarm

In default wind farm control of SimWindFarm, the power demands for turbines are proportionally to the available power of every turbine [191]

$$P_{a,i} = \frac{1}{2} \rho A V_i^3 C_{p,\max} \quad (\text{G.1})$$

$$P_a = \sum P_{a,i} \quad (\text{G.2})$$

where $P_{a,i}$ is the available power for turbine i , v_i is the wind speed at the nacelle of turbine i , $C_{p,\max}$ is the maximum power coefficient of the turbine. Note that in reference [191], $C_{p,\max}$ is denoted as maximum thrust coefficient, which the author considers as a typo.

Then, the power demand to the i -th turbine is determined as

$$P_{d,i} = P_d \frac{P_{a,i}}{P_a} \quad (\text{G.3})$$

where P_d is the farm-level power demand.

Reference

- [1] Global_Wind_Energy_Council, "Global wind statistics 2012," *Website*: http://www.gwec.net/wp-content/uploads/2013/02/GWEC-PRstats-2012_english.pdf, 2013.
- [2] "Strengthening America's Energy Security with Offshore Wind," U.S. Department of Energy February 2011.
- [3] Wikipedia. *Wind turbine design*. Available: http://en.wikipedia.org/wiki/Wind_turbine_design
- [4] T. Burton, D. Sharpe, N. Jenkins, and E. Bossanyi, *Wind Energy Handbook*: John Wiley, 2001.
- [5] J. F. Manwell, J. G. McGowan, and A. L. Rogers, *Wind Energy Explained*, 2nd ed.: Wiley Online Library, 2009.
- [6] Wikipedia. *Darrieus Wind Turbine*. Available: http://en.wikipedia.org/wiki/Darrieus_wind_turbine
- [7] J. Creaby, "Maximizing Wind Power Capture Using Multi-variable Extremum Seeking Control," Master of Science, Mechanical Engineering, Universtiy of Wisconsin-Milwaukee, Milwaukee, WI,USA, 2008.
- [8] J. Creaby, Y. Li, and J. E. Seem, "Maximizing wind turbine energy capture using multivariable extremum seeking control," *Wind Engineering*, vol. 33, pp. 361-387, 2009.
- [9] K. E. Johnson, L. J. Fingersh, M. J. Balas, and L. Y. Pao, "Methods for increasing region 2 power capture on a variable-speed wind turbine," *Journal of Solar Energy Engineering*, vol. 126, p. 1092, 2004.
- [10] E. Bossanyi, "Individual blade pitch control for load reduction," *Wind energy*, vol. 6, pp. 119-128, 2003.
- [11] K. Selvam, S. Kanev, J. van Wingerden, T. Van Engelen, and M. Verhaegen, "Feedback–feedforward individual pitch control for wind turbine load reduction," *International Journal of Robust and Nonlinear Control*, vol. 19, pp. 72-91, 2009.
- [12] T. J. Larsen, H. A. Madsen, and K. Thomsen, "Active load reduction using individual pitch, based on local blade flow measurements," *Wind energy*, vol. 8, pp. 67-80, 2005.
- [13] P. Sørensen, A. D. Hansen, F. Iov, F. Blaabjerg, and M. H. Donovan, "Wind farm models and control strategies," Risø National Laboratory Risø-R-1464(EN), August 2005.
- [14] R. Fernandez, P. Battaiotto, and R. Mantz, "Wind farm non-linear control for damping electromechanical oscillations of power systems," *Renewable Energy*, vol. 33, pp. 2258-2265, 2008.
- [15] J. Rodriguez-Amenedo, S. Arnaltes, and M. Rodriguez, "Operation and coordinated control of fixed and variable speed wind farms," *Renewable Energy*, vol. 33, pp. 406-414, 2008.

- [16] K. E. Johnson and N. Thomas, "Wind farm control: Addressing the aerodynamic interaction among wind turbines," in *American Control Conference*, Hyatt Regency Riverfront, St. Louis, MO, US, 2009, pp. 2104-2109.
- [17] N. Jensen, "A note on wind turbine interaction," *Risø National Laboratory, DK-4000 Roskilde, Denmark, Risø-M-2411*, 1983.
- [18] G. C. Larsen, H. A. Madsen, K. Thomsen, and T. J. Larsen, "Wake meandering: a pragmatic approach," *Wind energy*, vol. 11, pp. 377-395, 2008.
- [19] S. J. Qin and T. A. Badgwell, "A survey of industrial model predictive control technology," *Control engineering practice*, vol. 11, pp. 733-764, 2003.
- [20] M. Kuure-Kinsey and B. W. Bequette, "Multiple Model Predictive Control of Nonlinear Systems," in *Nonlinear model predictive control: Towards new challenging applications*. vol. 384, ed: Springer-Verlag New York Incorporated, 2009.
- [21] G. P. Corten and P. Schaak, "More Power and Less Loads in Wind Farms:'Heat and Flux'," in *European Wind Energy Conference*, London,UK, 2004.
- [22] J. E. Seem and Y. Li, "Systems and Methods for Optimizing Power Generation in a Wind Farm Turbine Array," USA Patent, (pending), 2012.
- [23] V. Spudic, "Hierarchical wind farm control for power/load optimization," in *The Science of making Torque from Wind*, 2010.
- [24] M. Soleimanzadeh and R. Wisniewski, "Controller design for a wind farm, considering both power and load aspects," *Mechatronics*, vol. 21, pp. 720-727, 2011.
- [25] J. R. Marden, S. D. Ruben, and L. Y. Pao, "A Model-Free Approach to Wind Farm Control Using Game Theoretic Methods," presented at the Proceedings of the 2012 AIAA/ASME Wind Energy Symposium, Nashville, Tennessee, 2012.
- [26] W. E. Heronemus, "Pollution-free energy from offshore winds," in *8th Annual Conference and Exposition Marine Technology Society*, Washington D.C., 1972.
- [27] D. Biester. (2009). *Hywind: Siemens and StatoilHydro Install First Floating Wind Turbine*. Available: http://www.siemens.com/press/en/pressrelease/?press=/en/pressrelease/2009/renewable_energy/ERE200906064.htm
- [28] J. M. Jonkman, "Dynamics modeling and loads analysis of an offshore floating wind turbine," PhD, University of Colorado, Boulder, 2007.
- [29] R. G. Sullivan, L. B. Kirchler, J. Cothren, and S. L. Winters, "Preliminary Assessment of Offshore Wind Turbine Visibility and Visual Impact Threshold Distances."
- [30] M. Schwartz, D. Heimiller, S. Haymes, and W. Musial, "Assessment of Offshore Wind Energy Resources for the United States," National Renewable Energy Laboratory (NREL), Golden, CO. NREL/TP-500-45889, June 2010.
- [31] S. Butterfield, W. Musial, J. Jonkman, P. Sclavounos, and L. Wayman, "Engineering challenges for floating offshore wind turbines," in *The 2005 Copenhagen Offshore Wind Conference*, Copenhagen, Denmark, 2005.
- [32] T. J. Larsen and T. D. Hanson, "A method to avoid negative damped low frequent tower vibrations for a floating, pitch controlled wind turbine," *Journal of Physics: Conference Series*, vol. 75, p. 012073, 2007.

- [33] M. A. Lackner and M. A. Rotea, "Structural control of floating wind turbines," *Mechatronics*, vol. 21, pp. 704-819, Jun 2011.
- [34] S. Colwell and B. Basu, "Tuned liquid column dampers in offshore wind turbines for structural control," *Engineering Structures*, vol. 31, pp. 358-368, 2009.
- [35] Y. Li, "Active Vane Control for Stabilization of Offshore Floating Wind Turbines," Invention Disclosure, 2013.
- [36] S. J. Johnson, C. Van Dam, and D. E. Berg, "Active load control techniques for wind turbines," *SAND2008-4809, Sandia National Laboratories, Albuquerque, NM*, 2008.
- [37] E. Bossanyi, "The design of closed loop controllers for wind turbines," *Wind energy*, vol. 3, pp. 149-163, 2000.
- [38] T. Olsen, E. Lang, A. Hansen, M. Cheney, G. Quandt, J. VandenBosche, and T. Meyer, "Low Wind Speed Turbine Project Conceptual Design Study: Advanced Independent Pitch Control," National Renewable Energy Laboratory NREL/SR-500-3675, 2004.
- [39] M. Hand, A. Wright, L. Fingersh, and M. Harris, "Advanced wind turbine controllers attenuate loads when upwind velocity measurements are inputs," 2006.
- [40] S. Kanev and T. van Engelen, "Exploring the limits in individual pitch control," in *2009 European Wind Energy Conference (EWEC 2009), Marseille, France*, 2009, pp. 16-19.
- [41] M. Jelavic, V. Petrovic, and N. Peric, "Individual pitch control of wind turbine based on loads estimation," in *Industrial Electronics, 2008. IECON 2008. 34th Annual Conference of IEEE*, 2008, pp. 228-234.
- [42] T. Van Engelen, "Design model and load reduction assessment for multi-rotational mode individual pitch control (higher harmonics control)," in *European Wind Energy Conference*, 2006, pp. 27.2-2.3.
- [43] E. Bossanyi and A. Wright, "Field testing of individual pitch control on the NREL CART-2 wind turbine," in *EWEC2009-European Wind Energy Conference & Exhibition*, 2009.
- [44] E. Bossanyi, A. Wright, and P. Fleming, "Progress with field testing of individual pitch control," in *Conference on the science of making torque from wind, The European Academy of Wind Energy*, 2010.
- [45] E. Bossanyi, A. Wright, and P. Fleming, "Further progress with field testing of individual pitch control," in *Proc. of the European Wind Energy Conference, EWEC*, 2010.
- [46] A. Wright, L. Fingersh, and K. Stol, "Designing and testing controls to mitigate tower dynamic loads in the controls advanced research turbine," National Renewable Energy Laboratory NREL/CP-500-40932, 2007.
- [47] M. Geyler and P. Caselitz, "Individual blade pitch control design for load reduction on large wind turbines," in *Proceeding of the European Wind Energy Conference*, Milan, Italy, 2007, pp. 82-86.
- [48] M. A. Lackner and G. van Kuik, "A comparison of smart rotor control approaches using trailing edge flaps and individual pitch control," *Wind energy*, vol. 13, pp. 117-134, 2010.

- [49] M. J. Balas, Y. J. Lee, and L. Kendall, "Disturbance tracking control theory with application to horizontal axis wind turbines," in *Proceedings of the 17th ASME Wind Energy Symposium*, Reno, NV, 1998, pp. 95-99.
- [50] K. A. Stol, "Dynamics modeling and periodic control of horizontal-axis wind turbines," PhD, Department of Aerospace Engineering Sciences, University of Colorado, 2001.
- [51] M. M. Hand, "Mitigation of wind turbine/vortex interaction using disturbance accommodating control," National Renewable Energy Laboratory NREL/TP-500-35172, 2003.
- [52] A. D. Wright, "Modern control design for flexible wind turbines," PhD, University of Colorado, 2004.
- [53] A. Wright and L. Fingersh, "Advanced Control Design for Wind Turbines," Technical Report NREL/TP-500-42437, National Renewable Energy Laboratory 2008.
- [54] A. Wright and K. A. Stol, "Designing and testing controls to mitigate dynamic loads in the controls advanced research turbine," in *Conference Paper 2008 ASME Wind Energy Symposium*, 2008.
- [55] W. Zhao and K. Stol, "Individual Blade Pitch for Active Yaw Control of a Horizontal-Axis Wind Turbine," in *45th AIAA Aerospace Sciences Meeting and Exhibit*, 2007, pp. 8-11.
- [56] H. Namik and K. Stol, "Individual blade pitch control of a floating offshore wind turbine on a tension leg platform," in *48th AIAA Aerospace Science Meeting and Exhibit*, 2010.
- [57] A. Crespo, J. Hernandez, and S. Frandsen, "Survey of modelling methods for wind turbine wakes and wind farms," *Wind energy*, vol. 2, pp. 1-24, 1999.
- [58] R. Templin, "An estimation of the interaction of windmills in widespread arrays," *National Aeronautical Establishment, Laboratory Report LTR-LA*, vol. 171, 1974.
- [59] B. Newman, "The spacing of wind turbines in large arrays," *Energy Conversion*, vol. 16, pp. 169-171, 1977.
- [60] C. Crafoord, "Interaction in limited arrays of windmills," *NASA STI/Recon Technical Report N*, vol. 83, p. 13608, 1979.
- [61] D. Moore, "Depletion of available wind power by a large network of wind generators," presented at the International Conference on Future Energy Concepts, London, England, 1979.
- [62] E. Bossanyi, G. Whittle, P. Dunn, N. Lipman, P. Musgrove, and C. Maclean, "The efficiency of wind turbine clusters," 1980, pp. 401-416.
- [63] S. Frandsen, "On the wind speed reduction in the center of large clusters of wind turbines," *Journal of Wind Engineering and Industrial Aerodynamics*, vol. 39, pp. 251-265, 1992.
- [64] S. Emeis and S. Frandsen, "Reduction of horizontal wind speed in a boundary layer with obstacles," *Boundary-Layer Meteorology*, vol. 64, pp. 297-305, 1993.
- [65] P. Lissaman, "Energy effectiveness of arbitrary arrays of wind turbines," in *17th American Institute of Aeronautics and Astronautics, Aerospace Sciences Meeting*, New Orleans, LA, 1979.
- [66] P. Vermeulen and P. Bultjes, "Mathematical modelling of wake interaction in wind turbine arrays part II," *MT-TNO Report 81*, vol. 2834, 1981.

- [67] I. Katic, J. Højstrup, and N. Jensen, "A simple model for cluster efficiency," *European Wind Energy Association*, pp. 407-409, 1986.
- [68] S. Frandsen, R. Barthelmie, S. Pryor, O. Rathmann, S. Larsen, J. Højstrup, and M. Thøgersen, "Analytical modelling of wind speed deficit in large offshore wind farms," *Wind energy*, vol. 9, pp. 39-53, 2006.
- [69] G. C. Larsen, J. Højstrup, and H. A. Madsen, "Wind fields in wakes," *EWEC 1996 Proceedings, Goteborg (Sweden)*, 1996.
- [70] H. Schlichting and K. Gersten, *Boundary-layer theory*: Springer; 8th edition (March 22, 2000), 1979.
- [71] P. Sforza, W. Stasi, M. Smorto, and P. Sheerin, "Wind turbine generator wakes," in *17th American Institute of Aeronautics and Astronautics, Aerospace Sciences Meeting*, New Orleans, LA, 1979.
- [72] P. Taylor, "On wake decay and row spacing for WECS farms," in *3rd International Symposium on Wind Energy Systems*, Lyngby, Denmark, 1980, pp. 451-468.
- [73] M. K. Liu, M. Yocke, and T. Myers, "Mathematical model for the analysis of wind-turbine wakes," *Journal of Energy*, vol. 7, pp. 73-78, 1983.
- [74] J. F. Ainslie, "Calculating the flowfield in the wake of wind turbines," *Journal of Wind Engineering and Industrial Aerodynamics*, vol. 27, pp. 213-224, 1988.
- [75] A. Duckworth and R. Barthelmie, "Investigation and Validation of Wind Turbine Wake Models," *Wind Engineering*, vol. 32, pp. 459-475, 2008.
- [76] D. J. Renkema, "Validation of wind turbine wake models," Master, TU Delft, 2007.
- [77] L. Rademakers, F. van Hulle, and W. Stam, *European wind turbine standards*: Netherlands Energy Research Foundation ECN, 1996.
- [78] J. Van Leuven, "The Energetic Effectiveness of A Cluster of Wind Turbines," PhD, Catholic University of Louvain, 1992.
- [79] U. Högström, D. Asimakopoulos, H. Kambezidis, C. Helmis, and A. Smedman, "A field study of the wake behind a 2 MW wind turbine," *Atmospheric Environment (1967)*, vol. 22, pp. 803-820, 1988.
- [80] G. C. Larsen, H. Madsen Aagaard, F. Bingöl, J. Mann, S. Ott, J. N. Sørensen, V. Okulov, N. Troldborg, N. M. Nielsen, K. Thomsen, T. J. Larsen, and R. Mikkelsen, "Dynamic wake meandering modeling," Risø National Laboratory Risø-R-1607(EN) 2007.
- [81] D. Medici and P. Alfredsson, "Measurements on a wind turbine wake: 3D effects and bluff body vortex shedding," *Wind energy*, vol. 9, pp. 219-236, 2006.
- [82] K. Thomsen, Madsen, H., Larsen, G. and Larsen, T., "A Simplified Approach for Simulation of Wake Meandering," Risø National Laboratory RISO Report AED-RB-18, 2006.
- [83] J. J. Trujillo and M. Kühn, "Adaptation of a lagrangian dispersion model for wind turbine wake meandering simulation," in *European Wind Energy Conference (EWEC)*, Marseille, France, 2009.
- [84] A. Jimenez, A. Crespo, E. Migoya, and J. Garcia, "Advances in large-eddy simulation of a wind turbine wake," *Journal of Physics: Conference Series*, vol. 75, p. 012041, 2007.

- [85] P. S. Veers, "Three-dimensional wind simulation," Sandia National Labs., Albuquerque, NM, USA, SAND88-0152, 1988.
- [86] M. Nielsen, G. C. Larsen, and K. Hansen, "Simulation of inhomogeneous, non-stationary and non-Gaussian turbulent winds," *Journal of Physics: Conference Series*, vol. 75, p. 012060, 2007.
- [87] G. Espana, S. Aubrun, and P. Devinant, "Is the Meandering of a Wind Turbine Wake Due to Atmospheric Length Scales?," *Progress in Turbulence III*, pp. 91-94, 2009.
- [88] L. Kristensen and N. Jensen, "Lateral coherence in isotropic turbulence and in the natural wind," *Boundary-Layer Meteorology*, vol. 17, pp. 353-373, 1979.
- [89] A. Davenport, "The prediction of the response of structures to gusty wind," *Safety of Structures under Dynamic Loading*, vol. 1, pp. 257-284, 1977.
- [90] H. A. Madsen, G. C. Larsen, T. J. Larsen, N. Troldborg, and R. Mikkelsen, "Calibration and validation of the Dynamic Wake Meandering model for implementation in an aeroelastic code," *Journal of Solar Energy Engineering*, vol. 132, p. 041014, 2010.
- [91] I. E. Committee, "IEC 61400-1: Wind turbines part 1: Design Requirements," ed: IEC, 2005.
- [92] J. A. Rossiter, *Model-based predictive control: a practical approach*: CRC, 2003.
- [93] E. F. Camacho and C. Bordons, *Model predictive control*: Springer-Verlag London, 2003.
- [94] W. H. Kwon and S. H. Han, *Receding horizon control: model predictive control for state models*: Springer, 2005.
- [95] J. B. Rawlings and D. Q. Mayne, *Model Predictive Control: Theory and Design*: NOB Hill Pub, 2009.
- [96] F. Borrelli, Bemporad, A., and Morari, M., *Predictive control for linear and hybrid systems*: Cambridge University Press, 2012.
- [97] D. Q. Mayne, J. B. Rawlings, C. V. Rao, and P. O. M. Scokaert, "Constrained model predictive control: Stability and optimality," *Automatica*, vol. 36, pp. 789-814, 2000.
- [98] A. Bemporad and M. Morari, "Robust model predictive control: A survey," *Robustness in identification and control*, pp. 207-226, 1999.
- [99] W. Kwon and A. Pearson, "A modified quadratic cost problem and feedback stabilization of a linear system," *Automatic Control, IEEE Transactions on*, vol. 22, pp. 838-842, 1977.
- [100] W. Kwon and A. Pearson, "On feedback stabilization of time-varying discrete linear systems," *Automatic Control, IEEE Transactions on*, vol. 23, pp. 479-481, 1978.
- [101] S. Keerthi and E. G. Gilbert, "Optimal infinite-horizon feedback laws for a general class of constrained discrete-time systems: Stability and moving-horizon approximations," *Journal of optimization theory and applications*, vol. 57, pp. 265-293, 1988.
- [102] J. B. Rawlings and K. R. Muske, "The stability of constrained receding horizon control," *Automatic Control, IEEE Transactions on*, vol. 38, pp. 1512-1516, 1993.

- [103] A. Zheng and M. Morari, "Stability of model predictive control with mixed constraints," *Automatic Control, IEEE Transactions on*, vol. 40, pp. 1818-1823, 1995.
- [104] P. Scokaert and J. B. Rawlings, "Infinite horizon linear quadratic control with constraints," in *Proceedings of the 13th IFAC World Congress, San Francisco*, 1996.
- [105] E. Polak and T. Yang, "Moving horizon control of linear systems with input saturation and plant uncertainty part 1. robustness," *International Journal of Control*, vol. 58, pp. 613-638, 1993.
- [106] Z. Q. Zheng, "Robust Control of Systems Subject to Constraints," PhD, California Institute of Technology, Pasadena, CA, 1995.
- [107] L. C. Henriksen, "Model predictive control of a wind turbine," Technical University of Denmark, DTU, IMM-Thesis, 2007.
- [108] R. A. Santos, "Damage mitigating control for wind turbines," PhD, Department of Aerospace Engineering Sciences, University of Colorado at Boulder, Boulder, 2007.
- [109] A. A. Kumar and K. A. Stol, "Scheduled model predictive control of a wind turbine," ed: American Institute of Aeronautics and Astronautics, 1801 Alexander Bell Dr., Suite 500 Reston VA 20191-4344 USA, 2009.
- [110] J. Laks, L. Y. Pao, E. Simley, A. Wright, N. Kelley, and B. Jonkman, "Model predictive control using preview measurements from lidar," in *49th AIAA Aerospace Sciences Meeting*, Orlando, Florida, 2011.
- [111] M. Soltani, R. Wisniewski, P. Brath, and S. Boyd, "Load reduction of wind turbines using receding horizon control," in *Control Applications (CCA), 2011 IEEE International Conference*, Denver, CO 2011, pp. 852-857.
- [112] Y. Wang and S. Boyd, "Fast model predictive control using online optimization," *Control Systems Technology, IEEE Transactions on*, vol. 18, pp. 267-278, 2010.
- [113] D. Castaignet, N. K. Poulsen, T. Buhl, and J. J. Wedel-Heinen, "Model Predictive Control of Trailing Edge Flaps on a wind turbine blade," in *American Control Conference (ACC), 2011 San Francisco, CA 2011*, pp. 4398-4403.
- [114] A. A. Kumar and K. A. Stol, "Scheduled model predictive control of a wind turbine," in *28th American Society of Mechanical Engineers (ASME) Wind Energy Symposium*, Orlando, Florida, 2009.
- [115] S. Joe Qin, V. M. Martínez, and B. A. Foss, "An interpolating model predictive control strategy with application to a waste treatment plant," *Computers & Chemical Engineering*, vol. 21, pp. S881-S886, 1997.
- [116] D. Dougherty and D. Cooper, "A practical multiple model adaptive strategy for single-loop MPC," *Control engineering practice*, vol. 11, pp. 141-159, 2003.
- [117] D. Dougherty and D. Cooper, "A practical multiple model adaptive strategy for multivariable model predictive control," *Control engineering practice*, vol. 11, pp. 649-664, 2003.
- [118] J. Wang, "Softly Switched Model Predictive Control: Generic Development and Application to Water Supply and Distribution Systems," PhD, Mechanical Department, University of Birmingham, 2006.

- [119] S. Di Cairano, E. Tseng, D. Bernardini, and A. Bemporad, "Steering vehicle control by switched model predictive control," in *Advances in Automotive Control*, 2010, pp. 1-6.
- [120] P. Mhaskar, N. H. El-Farra, and P. D. Christofides, "Predictive Control of Switched Nonlinear Processes with Scheduled Mode Transitions," in *Dynamics and Control of Process Systems 2004 (DYCOPS-7): A Proceedings Volume from the 7th IFAC Symposium, Cambridge, Massachusetts, USA, 5-7 July 2004*, p. 257.
- [121] L. Özkan and M. V. Kothare, "Stability analysis of a multi-model predictive control algorithm with application to control of chemical reactors," *Journal of Process Control*, vol. 16, pp. 81-90, 2006.
- [122] M. Kuure-Kinsey, "Novel Approaches to Nonlinear Model Predictive Control with Application to High Temperature Fuel Cells," PhD, Chemical Engineering, Rensselaer Polytechnic Institute, 2008.
- [123] R. R. Rao, B. Aufderheide, and B. W. Bequette, "Experimental studies on multiple-model predictive control for automated regulation of hemodynamic variables," *Biomedical Engineering, IEEE Transactions on*, vol. 50, pp. 277-288, 2003.
- [124] H. Ferreau, "qpOASES—an open-source implementation of the online active set strategy for fast model predictive control," 2007, pp. 29-30.
- [125] A. Bemporad, M. Morari, V. Dua, and E. N. Pistikopoulos, "The explicit linear quadratic regulator for constrained systems," *Automatica*, vol. 38, pp. 3-20, 2002.
- [126] M. de la Pena, A. Bemporad, and C. Filippi, "Robust explicit MPC based on approximate multi-parametric convex programming," 2004, pp. 2491-2496 Vol. 3.
- [127] H. J. Ferreau, E. Arnold, H. Diedam, H. J. Ferreau, B. Houska, C. Kirches, A. Perrin, A. Potschka, T. Wiese, and L. Wirsching, "qpOASES User's Manual," Optimization in Engineering Center (OPTEC) and Department of Electrical Engineering, K. U. Leuven, 2011.
- [128] G. Associates, "Unique Integration of Mature Technologies," in *16th Offshore Symposium*, Houston, TX, 2010.
- [129] G. R. Fulton, D. J. Malcolm, and E. Moroz, "Design of a Semi-Submersible Platform for a 5MW Wind Turbine," in *Proceeding 44th AIAA/ASME Wind Energy Symposium*, Reno, NV, 2006.
- [130] K. H. Lee, "Responses of floating wind turbines to wind and wave excitation," MSc. Thesis, Massachusetts Institute of Technology, 2005.
- [131] *Sway to Erect 10 MW Offshore Wind Turbine, May 30, 2010*. Available: <http://www.renewableenergyfocus.com/view/7279/sway-to-erect-10-mw-offshore-wind-turbine/>
- [132] B. Bulder, M. T. van Hees, A. Henderson, R. Huijsmans, J. Pierik, E. Snijders, G. Wijnants, and M. Wolf, "Study to feasibility of and boundary conditions for floating offshore wind turbines," ECN, MARIN, Llargerweij the Windmaster, TNO and TUD 2002-CMC-R43, 2002.
- [133] W. Musial, and Ram, B., "Large-Scale Offshore Wind Power in the United States: Assessment of Opportunities and Barriers," National Renewable Energy Laboratory, Boulder, Colorado NREL/TP-500-40745, September 2010.
- [134] PrinciplePower. *Principle Power's WindFloat*. Available: <http://www.youtube.com/watch?v=IO7GXMLR4YUo>

- [135] B. Linde, "Motion of floating wind turbines," M.Sc., Norwegian University of Science and Technology, 2010.
- [136] J. E. Withee, "Fully coupled dynamic analysis of a floating wind turbine system," PhD, Massachusetts Institute of Technology, 2004.
- [137] "ADAMS User's Guide," Mechanical Dynamics, Inc., Ann Arbor, MI2002.
- [138] P. J. Moriarty and A. C. Hansen, "Aerodyn theory manual," National Renewable Energy Laboratory NREL/TP-500-3688, 2005.
- [139] E. Wayman, "Coupled Dynamics and Economic Analysis of Floating Wind Turbine Systems," Master of Science, Mechanical Engineering, Massachusetts Institute of Technology, 2006.
- [140] J. M. Jonkman and M. L. Buhl Jr, "FAST user's guide," National Renewable Energy Lab, Golden, Colorado, USA NREL/EL-500-38230, 2005.
- [141] D. Matha, "Model Development and Loads Analysis of an Offshore Wind Turbine on a Tension Leg Platform with a Comparison to Other Floating Turbine Concepts," Master, University of Colorado, Boulder, 2009.
- [142] C. Cermelli, D. Roddier, and A. Aubault, "WINDFLOAT: a floating foundation for offshore wind turbines Part II: Hydrodynamics analysis," in *Proceedings of the ASME 28th International Conference on Ocean, Offshore and Arctic Engineering*, Honolulu, Hawaii, USA, 2009.
- [143] D. Roddier, C. Cermelli, A. Aubault, and A. Weinstein, "WindFloat: A floating foundation for offshore wind turbines," *Journal of Renewable and Sustainable Energy*, vol. 2, p. 033104, 2010.
- [144] C. H. Lee, *WAMIT theory manual*: Massachusetts Institute of Technology, Dept. of Ocean Engineering, 1995.
- [145] F. G. Nielsen, T. D. Hanson, and B. Skaare, "Integrated dynamic analysis of floating offshore wind turbines," in *Proceedings of the 25th International Conference on Offshore Mechanics and Arctic Engineering*, Hamburg, German, 2006, pp. 671-679.
- [146] T. J. Larsen and A. M. Hansen, "How 2 HAWC2, the user's manual," Risø National Laboratory 8755035833, 2007.
- [147] S. Reinholdtsen and E. Falkenberg, "SIMO General Description," *Marintek Report MTK*, vol. 519614, 1998.
- [148] I. Fylling, C. Larsen, N. Sødahl, E. Passano, A. Bech, A. Engseth, H. Lie, and H. Ormberg, "RIFLEX User's Manual 3.6," 2008.
- [149] J. M. Jonkman, "Influence of control on the pitch damping of a floating wind turbine," in *the 2008 ASME Wind Energy Symposium*, Reno, Nevada, 2008.
- [150] B. Skaare, T. D. Hanson, and F. G. Nielsen, "Importance of control strategies on fatigue life of floating wind turbines," in *26th International Conference on Offshore Mechanics and Arctic Engineering*, San Diego, California, 2007.
- [151] H. Namik and K. Stol, "Individual blade pitch control of floating offshore wind turbines," *Wind energy*, vol. 13, pp. 74-85, 2010.
- [152] H. Namik and K. Stol, "Performance analysis of individual blade pitch control of offshore wind turbines on two floating platforms," *Mechatronics*, vol. 21, pp. 691-703, 2011.
- [153] M. A. Lackner and M. A. Rotea, "Passive structural control of offshore wind turbines," *Wind energy*, vol. 14, pp. 373-388, 2011.

- [154] N. Luo, C. Bottasso, H. Karimi, and M. Zapateiro, "Semiactive Control for Floating Offshore Wind Turbines Subject to Aero-hydro Dynamic Loads," presented at the International Conference on Renewable Energies and Power Quality, Las Palmas de Gran Canaria, Spain, 2011.
- [155] Z. Yang, Y. Li, and J. E. Seem, "Individual Pitch Control for Wind Turbine Load Reduction Including Wake Modeling," *Wind Engineering*, vol. 35, pp. 715-738, 2012.
- [156] Z. Yang, Y. Li, and J. E. Seem, "Load Reduction of Wind Turbines under Wake Meandering with Model Predictive Control for Individual Pitching," in *50th AIAA Aerospace Sciences Meeting including the New Horizons Forum and Aerospace Exposition*, Nashville, Tennessee, 2012.
- [157] C. J. Spruce, "Simulation and control of windfarms," PhD, University of Oxford, 1993.
- [158] F. Borrelli, *Constrained optimal control of linear and hybrid systems* vol. 290: Springer Verlag, 2003.
- [159] M. Soltani, T. Knudsen, and T. Bak, "Modeling and Simulation of Offshore Wind Farms for Farm Level Control," in *European Offshore Wind Conference and Exhibition (EOW) 2009*, Stockholm, Sweden, 2009.
- [160] M. Soleimanzadeh and R. Wisniewski, "An optimal control scheme to minimize loads in wind farms," in *Control Applications (CCA), 2012 IEEE International Conference on*, 2012, pp. 986-990.
- [161] D. Madjidian and A. Rantzer, "A stationary turbine interaction model for control of wind farms," in *IFAC 18th World Congress*, Milano, Italy, 2011.
- [162] A. J. Brand, "A Quasi-Steady Wind Farm Control Model," in *European Wind Energy Conference*, Brussels, Belgium, 2011.
- [163] A. J. Brand and J. W. Wagenaar, "A quasi-steady wind farm flow model in the context of distributed control of the wind farm," in *European Wind Energy Conference*, 2010.
- [164] T. Knudsen, T. Bak, and M. Soltani, "Distributed control of large-scale offshore wind farms," in *European Wind Energy Conference*, Marseille, France, 2009.
- [165] M. Kristalny and D. Madjidian, "Decentralized feedforward control of wind farms: prospects and open problems," in *Decision and Control and European Control Conference (CDC-ECC), 2011 50th IEEE Conference on*, 2011, pp. 3464-3469.
- [166] D. Madjidian, K. Martensson, and A. Rantzer, "A distributed power coordination scheme for fatigue load reduction in wind farms," in *American Control Conference (ACC)*, 2011, pp. 5219-5224.
- [167] D. Madjidian, M. Kristalny, and A. Rantzer, "Dynamic Power Coordination for Load Reduction in Dispatchable Wind Power Plants," in *2013 European Control Conference*, Zürich, Switzerland, July 2013.
- [168] B. Biegel, D. Madjidian, V. Spudic, A. Rantzer, and J. Stoustrup, "Distributed low-complexity controller for wind power plant in derated operation," in *IEEE Multi-Conference on Systems and Control*, Hyderabad, India, 2013.
- [169] R. Zhao, W. Shen, T. Knudsen, and T. Bak, "Fatigue distribution optimization for offshore wind farms using intelligent agent control," *Wind energy*, vol. 15, pp. 927-944, 2012.

- [170] T. Horvat, V. Spudic, and M. Baotic, "Quasi-stationary optimal control for wind farm with closely spaced turbines," in *MIPRO, 2012 Proceedings of the 35th International Convention*, 2012, pp. 829-834.
- [171] E. Bitar and P. Seiler, "Coordinated control of a wind turbine array for power maximization," in *American Control Conference (ACC), 2013*, 2013, pp. 2898-2904.
- [172] J. Park, S. Kwon, and K. H. Law, "Wind farm power maximization based on a cooperative static game approach," in *SPIE Smart Structures and Materials+ Nondestructive Evaluation and Health Monitoring*, 2013, pp. 86880R-86880R-15.
- [173] Y. Guo, W. Wang, C. Y. Tang, J. N. Jiang, and R. G. Ramakumar, "Model predictive and adaptive wind farm power control," in *American Control Conference (ACC), 2013*, pp. 2890-2897.
- [174] E. Bossanyi, T. Burton, D. Sharpe, and N. Jenkins, "Wind Energy Handbook," *John Wiley*, 2000.
- [175] P. Vermeulen, "An experimental analysis of wind turbine wakes," in *3rd International Symposium on Wind Energy Systems*, 1980, pp. 431-450.
- [176] B. J. Jonkman, "TurbSim User's Guide: Version 1.50," National Renewable Energy Laboratory NREL/TP-500-46198, 2009.
- [177] M. Harris, M. Hand, and A. Wright, "Lidar for turbine control," National Renewable Energy Laboratory, Golden, CO NREL/TP-500-39154, 2006.
- [178] F. Haugen. (2008). *Derivation of a Discrete-Time Low pass Filter*. Available: http://techt teach.no/simview/lowpass_filter/doc/filter_algorithm.pdf
- [179] K. A. Stol, "Disturbance tracking and blade load control of wind turbines in variable-speed operation," in *22nd ASME Wind Energy Conference*, Reno, NV, 2003, pp. 317-322.
- [180] L. J. Fingersh and K. E. Johnson, "Controls advanced research turbine (CART) commissioning and baseline data collection," National Renewable Energy Laboratory NREL/TP-500-32879, 2002.
- [181] G. Bir, "Multiblade coordinate transformation and its application to wind turbine analysis," in *Proceedings of 2008 ASME Wind Energy Symposium, Reno, Nevada, USA, Jan. 7, 2008*.
- [182] L. C. Henriksen, N. K. Poulsen, and H. H. Niemann, "Constraint handling within a multi-blade coordinate framework of a wind turbine," in *Decision and Control and European Control Conference (CDC-ECC), 2011 50th IEEE Conference on*, 2011, pp. 5825-5830.
- [183] W. Johnson, *Helicopter theory*. New Jersey: Princeton University Press, 1980.
- [184] M. Kuure-Kinsey and B. W. Bequette, "Multiple model predictive control: a state estimation based approach," in *American Control Conference, 2007. ACC'07*, 2007, pp. 3739-3744.
- [185] J. Jonkman, S. Butterfield, W. Musial, and G. Scott, "Definition of a 5-MW reference wind turbine for offshore system development," *National Renewable Energy Laboratory, NREL/TP-500-38060*, 2009.
- [186] J. M. Jonkman and M. L. Buhl Jr, "FAST user's guide," *Rep. No. NREL/EL-500-38230, NREL, Golden, Colorado, USA*, 2005.

- [187] M. A. Rotea, "Analysis of Multivariable Extremum Seeking Algorithms," in *Proceeding of 2000 American Control Conference*, Chicago, IL, 2000, pp. 433-437.
- [188] I. Munteanu, A. I. Bratcu, and E. Ceangă, "Wind turbulence used as searching signal for MPPT in variable-speed wind energy conversion systems," *Renewable Energy*, vol. 34, pp. 322-327, 2009.
- [189] T. Pan, Z. Ji, and Z. Jiang, "Maximum power point tracking of wind energy conversion systems based on sliding mode extremum seeking control," in *Energy 2030 Conference, 2008. ENERGY 2008. IEEE*, Atlanta, GA, 2008, pp. 1-5.
- [190] T. Hawkins, W. N. White, G. Hu, and F. D. Sahneh, "Region II wind power capture maximization using robust control and estimation with alternating gradient search," in *American Control Conference (ACC)*, San Francisco, CA, 2011, pp. 2695-2700.
- [191] J. D. Grunnet, M. Soltani, T. Knudsen, M. Kragelund, and T. Bak, "Aeolus toolbox for dynamic wind farm model, simulation and control," in *Proceedings of the European Wind Energy Conference*, Warsaw, Poland, 2010.
- [192] J. Jonkman, S. Butterfield, W. Musial, and G. Scott, "Definition of a 5-MW reference wind turbine for offshore system development," *National Renewable Energy Laboratory, NREL/TP-500-38060*, 2009.
- [193] D. G. Alciatore and M. B. Hestand, *Introduction to mechatronics and measurement systems*: McGraw-Hill New York, 2007.
- [194] J. Schepers and S. Pijl, "Improved modelling of wake aerodynamics and assessment of new farm control strategies," *Journal of Physics: Conference Series, The Science of Making Torque from Wind*, vol. 75, p. 012039, 2007.
- [195] J. Jonkman, "Definition of the Floating System for Phase IV of OC3," *National Renewable Energy Lab, NREL/TP-500-47535*, May 2010.
- [196] J. M. Jonkman and A. C. Hansen, "Development and validation of an aeroelastic model of a small furling wind turbine," in *43 rd AIAA Aerospace Sciences Meeting and Expedition*, Reno, Nevada, 2005.
- [197] T. R. Kane and D. A. Levinson, *Dynamics: Theory and Applications McGraw-Hill*, 1985.
- [198] R. E. Sheldahl and P. C. Klimas, "Aerodynamic characteristics of seven symmetrical airfoil sections through 180-degree angle of attack for use in aerodynamic analysis of vertical axis wind turbines," Sandia National Labs., Albuquerque, NM (USA), SAND80-2114, 1981.
- [199] S. Kim, J. J. Alonso, and A. Jameson, "Multi-Element High-Lift Configuration Design Optimization Using Viscous Continuous Adjoint Method," *Journal of Aircraft*, vol. 41, pp. 1082-1097, 2004.
- [200] G. Hayman, "NWTC Design Codes (MCrunch by Greg Hayman), <http://wind.nrel.gov/designcodes/postprocessors/mcrunch/>." 2012.

CURRICULUM VITAE

Zhongzhou Yang

Place of birth: Linfen, Shanxi, China

Dissertation Title: Wind Turbine Controls for Farm and Offshore Operation

Education:

Bachelor of Engineering, Taiyuan University of Technology, China, June 2004
Major: Engineering Mechanics

Master of Engineering, Beihang University, China, January 2008
Major: Fluid Mechanics

Ph.D., University of Wisconsin-Milwaukee, December 2013
Major: Mechanical Engineering

Employment:

Zhongzhou Yang was working as a Mechanical Engineer at a wind turbine supplier GoldWind Science and Technology in Beijing, China from April 2007 to September 2008. From October 2008, Zhongzhou started working at the University of Wisconsin-Milwaukee as research assistant of Prof. Yaoyu Li. From September 2011, Zhongzhou Yang moved to the University of Texas at Dallas and worked as visiting research assistant of Prof. Yaoyu Li. From May 2013, Zhongzhou Yang started working as a Systems Modeling and Control Engineer at Exa Corporation, Livonia, Michigan.

Publications:

- [1] Li, Y., **Yang, Z.**, and Seem, J.E., "Active Horizontal Vane Control for Stabilizing Platform Pitch Motion of Floating Offshore Turbines", will be presented at AIAA SciTech 2014, January 13-17th, 2014, National Harbor, Maryland

- [2] **Yang, Z.**, Li, Y. and Seem, J.E., “Maximizing Wind Farm Energy Capture Via Nested-Loop Extremum Seeking Control”, *Proceedings of 2013 ASME Dynamic Systems and Control Conference (DSCC’2013)*, October 21-23, 2013, Stanford University, Palo Alto, CA
- [3] **Yang, Z.**, and Li, Y., “Active Vertical-Vane Control for Roll Motion of Floating Offshore Wind Turbines”, *51th AIAA Aerospace Sciences Meeting including the New Horizons Forum and Aerospace Exposition*, AIAA 2013-0452, January 9-12th, 2013, Grapevine (Dallas/Ft. Worth Region), Texas
- [4] **Yang, Z.**, Li, Y. and Seem, J.E., “Load Reduction of Wind Turbines under Wake Meandering with Model Predictive Control for Individual Pitching”, *50th AIAA Aerospace Sciences Meeting including the New Horizons Forum and Aerospace Exposition*, AIAA 2012-1150, January 9-12th, 2012, Nashville, Tennessee
- [5] **Yang, Z.**, Li, Y. and Seem, J.E., “Individual Pitch Control for Wind Turbine Load Reduction Including Wake Modeling,” *Journal of Wind Engineering*, 2012, 35(6):715-738
- [6] **Yang, Z.**, Li, Y. and Seem, J.E. “Improved Individual Pitch Control for Wind Farm Turbine Load Reduction via Wake Modeling,” *49th AIAA Aerospace Sciences Meeting including the New Horizons Forum and Aerospace Exposition*, AIAA 2011-820, January 4-7th, 2011, Orlando, Florida
- [7] **Yang, Z.**, Li, Y. and Seem, J.E., “Individual pitch control for wind turbine load reduction including wake interaction”, *American Control Conference (ACC)*, June 29-July 1st, 2011, pp. 5207-5212, San Francisco, CA

- [8] **Yang, Z.**, Li, Y. and Seem, J.E. "Individual Pitch Control For Wind Turbine Load Reduction Including Wake Modeling," *Proceedings of 2010 ASME Dynamic Systems and Control Conference (DSCC'2010)*, September 13-15, 2010, Cambridge, MA
- [9] Wu, X., Li, Y., Li, F. and **Yang, Z.** "Adaptive Estimation Based Leakage Detection for Wind Turbine Hydraulic Pitching System," *IEEE Transactions on Mechatronics*, 2012, V17(5): 907-914
- [10] Wu, X., Li, Y., **Yang, Z.**, Lu, B. "Model Based Fault Diagnosis for Wind Turbine Hydraulic Pitching Systems," *2010 American Control Conference*, June 30-July 2, Baltimore, Maryland.
- [11] Lu,B., Li,Y., Wu, X. and **Yang, Z.** "A review of recent advances in wind turbine condition monitoring and fault diagnosis", *Power Electronics and Machines in Wind Applications*, June 24-26th, 2009, Lincoln, Nebraska
- [12] Chen, Q., Li, Y., Seem, J.E., **Yang, Z.** and Creaby., J. "Self-Optimizing Robust Control of Wind Power Generation with Doubly-Fed Induction Generator", accepted by *ASME Journal of Solar Energy Engineering*